Strontium optical lattice clocks : clock comparisons for timescales and fundamental physics applications

Slawomir Bilicki

THÈSE DE DOCTORAT
DE L'UNIVERSITÉ PIERRE et MARIE CURIE

Spécialité: Physique Fondamentale et Appliquée

École Doctorale : Physique en Île de France (ED 564)

réalisée
au SYRTE
laboratoire des SYstèmes de Référence Temps-Espace

présentée par

Sławomir BILICKI

pour obtenir le grade de:
Docteur de l'Université Pierre et Marie Curie

sujet de Thèse:

Horloges à réseau optique au strontium : comparaisons d'horloges pour des applications en physique fondamentale et échelles de temps

Strontium optical lattice clocks:
clock comparisons for timescales and fundamental physics applications

Soutenance le 10 novembre 2017, devant le jury composé de :

Mme. Agnès Maître	Président du jury
Mme. Mathilde Fouché	Raporteur
M. Davide Calonico	Raporteur
M. Michał Zawada	Membre invité
M. Sébastien Bize	Directeur de thèse
M. Jérôme Lodewyck	Co-encadrant

Paris 2017

If I have seen further, it is by standing on the shoulders of giants.
Isaac Newton

Acknowledgements

This PhD work was funded through the Future Atomic Clock Techonology (FACT) project Initial Training Network (ITN) supported by the European Commission's 7th Framework Programme under Grant Agreement Number 607493.

We acknowledge funding support from Centre National d'Études Spatiales (CNES), Conseil Régional Île-de-France (DIM Nano'K), Agence Nationale de la Recherche (Labex First-TF ANR-10-LABX-48-01)

Support has been received from the project EMPIR 15SIB03 OC18. This project has received funding from the EMPIR programme co-financed by the Participating States and from the European Union's Horizon 2020 research and innovation programme.

Remerciements

En premier lieu, je tiens à remercier ma famille, en particulier mes parents Beata et Bogusław, pour leur soutien et leur compréhension de mon besoin de grande disponibilité afin de me consacrer à la science au quotidien.
Quand je suis arrivé au SYRTE, trois personnes sympatiques m'ont accueilli: Sébastien Bize, Jérôme Lodewyck et Rodolphe Le Targat.
Sébastien, le chef du groupe de fréquence optique, a accepté ma candidature et je me suis donc joint à son groupe de doctorants. Je le remercie d'avoir dirigé ma thèse.
Jérôme, co-encadrant a toujours pris du temps pour répondre à mes questions. Son esprit scientifique m'a permis d'avoir tout sous contrôle grace à deux options possibles. Sans lui, cette thèse n'aurait pas été . Mais j'ose espèrer qu'il n'aura pas de nouveaux cheveux blancs après avoir lu toutes les versions de ma thèse !!! Son humanité m'a permis de poser toutes les questions possibles même les plus naives, Je pouvais compter sur lui comme sur un père. Il m'a aidé à gérer tous les problèmes du quotidien. Sa femme et ses filles ont de la chance d'avoir un tel mari et un tel père.
Rodolphe, s'est révélé non seulement capable de franches "rigolades" dans le cadre du laboratoire mais aussi de trouver du «plaisir» dans l' administration de mon projet, Cela, a nécessité parfois du travail le soir et le week-end. Néanmoins, nous avons toujours eu le temps de regarder de beaux matchs de football. Enfin et surtout, il a le sens de l'humour et ses blagues sont aussi drôles que celles de Jérôme.
Au cours de mon travail, j'ai partagé mon bureau et le laboratoire avec deux autres tigres du strontium: Eva Bookjans et Grégoire Vallet.
Eva, post-doc dans notre équipe, sa loquacité et są patience m'ont permis d'améliorer mes compétences linguistiques. Merci beaucoup pour le «babysitting commun» des horloges pendant les étalonnages TAI. J'espère que son équipe de volleyball va gagner la le titre de la ligue la saison prochaine.
Grégoire, le doctorant le plus ouvert d'esprit que j'ai rencontré. C'était intéressant d'une part de l'entendre parler de sujets autres que ceux de la physique et d'autre part d'écouter son explication de la physique dure de manière très simple. J'espère que tu vas de l'avant avec un système de détection non destructif pour faire des expériences de spin-squeezing.

Je tiens à remercier toutes les autres personnes que j'ai pu rencontrer au SYRTE pour l'atmosphère familiale qui y règne . Ainsi, j'ai pu me sentir comme chez moi.
J'ai des remerciements particuliers pour : Chunyan Shi et Jean-Luc, ex post-doctorants, qui m'ont fait entrer au laboratoire Sr au début de mon séjour à Paris ,
Michel Abgrall et Luca Lorini qui m'ont expliqué la complexité des étalonnage TAI,
Pacôme Delva qui m'a décrit les détails du test d'invariance de Lorentz,
Mesdames du département administratif: Christel Comte, Francia Decostier et Marine Pailler pour une aide administrative sans faille,
Frédéric Meynadier et Stéphane Guerandel qui ont pris soin de la machine la plus importante au SYRTE - la machine à café.

Je tiens à remercier tous les membres du jury de ma thèse: Agnès Maitre qui a accepté le rôle du jury président, Mathilde Fouché et Davide Calonico qui ont fourni les efforts liés à la lecture et la relecture de mon manuscrit et Michał Zawada qui a accepté l'invitation à mon jury.

Je voudrais également rendre hommage aux personnes sans lesquelles je n'aurais pas pu me trouver parmi vous:
Michał Zawada et Roman Ciuryło qui m'ont fait confiance au début de ma «carrière scientifique» et qui m'ont offert l'opportunité de travailler dans leur équipe au KL FAMO de Toruń, où j'ai commencé mes études,
Mme Halina Formela, qui, au lycée, m'a encouragé à faire la physique et m'a donné des cours de physique supplémentaires tous les mercredis à 7 heures du matin .

Ce fut trois années intensives , mais cela a été un plaisir et un privilège de travailler ici. J'ai fait du mieux que je pouvais. Merci!

CONTENTS

CHAPTER 1

INTRODUCTION

Over the years, astronomy was responsible for timekeeping because time has been determined from the diurnal changes in the appearance of the sky. The need for a precise modeling of the Earth's motions is the basis of modern calculus and classical mechanics. With the technological progress, society has needed more and more precise measurements in shorter time periods. Pendulum clocks have been for a long time used to measure time in short term time periods. During the electronic revolution, the quartz clocks could measured mega or gigahertz oscillations, and they have already allowed to observe the tiny weekly variations of the Earth's rotational speed. Due to the insufficient uniformity of the Earth's rotation, the stability of time provided by the Earth is limited to ms at a day [1]. However, modern society needs more precise and appropriate timescales, that would be independent of the variability of the Earth's rotational speed. Therefore, the scientific community had to choose another physical phenomenon, that can be as least as stable than the Earth's motions.

James Clerk Maxwell postulated that atomic transitions have the potential to be a good frequency standard due to their invariance and resonance properties [2]. With the progress of quantum mechanics and atomic spectroscopy, the embodiment of these desires was the first calibration, with respect to ephemeris time, of electronic transition between two hyperfine ground states of the cesium-133 atoms with an uncertainty of ± 20 Hz in 1955 by L. Essen and J. V. L. Parry at National Physical Laboratory and W. Markowitz from United States Naval Observatory [3, 4]. In 1967, the atomic second era has been initiated, when the 13th General Conference on Weight and Measures (CGPM) adopted time not determined by astronomical observations of the Earth's rotation. Since that time, the second has been defined as «the duration of 9 192 631 770 periods of the radiation corresponding to the transition between the two hyperfine levels of the ground state of the cesium 133 atom». Over the next decades, the second based on the cesium transition has been realized with more and more precision, 1 order of magnitude higher in 10 years. Together with the progress in time transfer methods, it has been possible to establish robust atomic timescales based on the large number of clocks in operation worldwide, which have a fundamental importance to science and technology. Currently, after more than 50 years of development and experience, the microwave standards, which use a cloud of laser-cooled atoms have achieved their state-of-the-art performances with an accuracy at the 10^{-16} level and a frequency stability at 1.6×10^{-14} at 1 s limited by quantum projection noise limit [5].

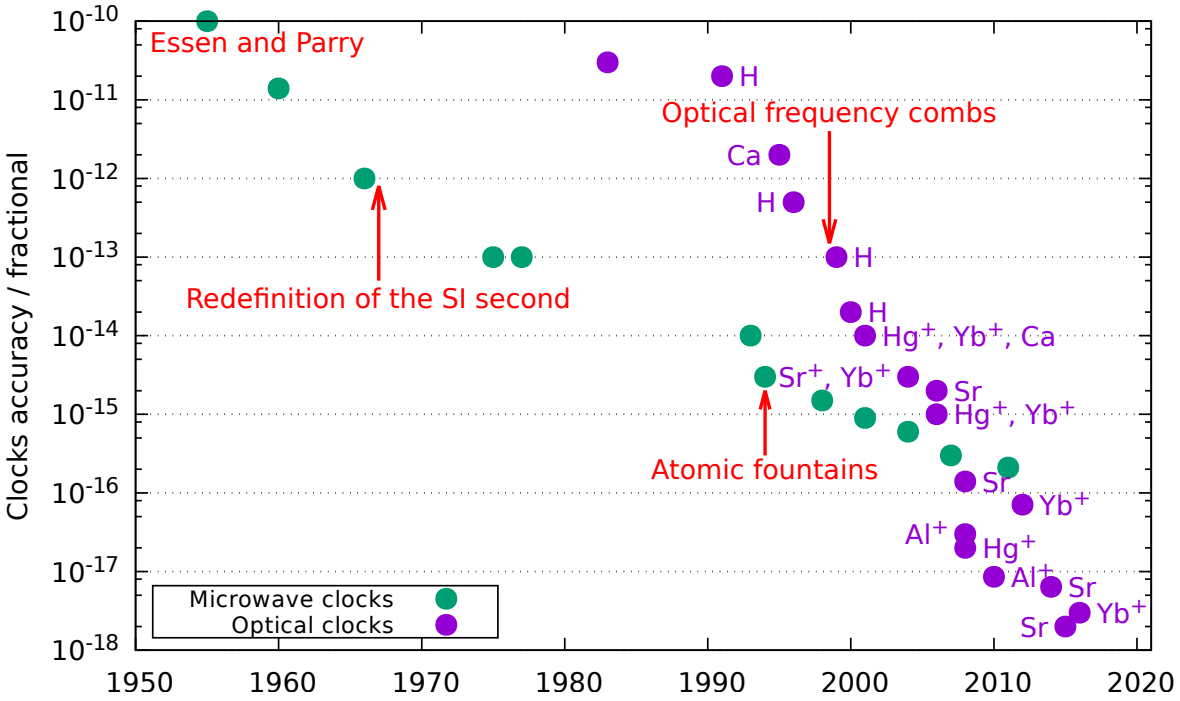

Figure 1.0.1. Evolution of the fractional systematic uncertainty of atomic clocks over years. The best Sr optical lattice clock reaches a systematic uncertainty of 2×10^{-18} [6].

The development of new standards based on optical transitions with frequencies higher than several hundreds of gigahertz was blocked by the inability to measure optical frequencies with electronic devices. Measurement techniques using multiple doublings of a coherent microwave signal, were inefficient and complicated [7]. The real revolution in the optical standards has begun with the optical frequency comb, which allows for a simple transfer of optical frequencies to the optical and microwave domains, and, more importantly, maintaining a high stability of the optical signal [8,9]. Since that moment, a strong acceleration in the development of optical frequency standards has been observed. Together with the development of ultra-cold atomic and laser physics, with the aid of which atoms or ions can be well controlled, the accuracy of optical clocks improved by one order of magnitude every 3 years. Nowadays, almost 20 years after the invention of the optical frequency comb, the optical frequency standards have surpassed the microwave standards by 2 orders of magnitude, both in terms of stability and accuracy (see figure 1.0.1).

In the near future, a redefinition of the SI second via optical clock transitions is expected. The Working Group of Frequency Standards (WGFS), formed in 2001, recommended and defined «secondary representations of the second», that can realize the SI second in parallel to the Cs primary standard. This recommendation shows that many transitions are now as suitable as the Cs standard to act as a frequency reference. In 2006, the International Committee for Weights and Measures (CIPM) officially accepted the first five representations. In 2015, the list of recommended representations was updated and extended [10].

1.1 Characterization of Optical Frequency Standards

A frequency standard[1] is a device, that delivers a periodic physical signal whose frequency is stable and constant in time. To have a precise clock, the periodic event must be well described and controlled. In the atomic frequency standards, the realization of the reference is based on the detection of a change of state of the atomic sample. The atomic reference is prepared in one of two quantum states that are associated with the atomic transition. A local oscillator then interrogates the atoms, so that they can be excited. The local oscillator is locked with an atomic transition when the probability of excitation is maximal. Clocks work in a cycle because after each interrogation, the transition probability measurement is required. Then, the new interrogation can be performed in the new cycle (see figure 1.1.2).

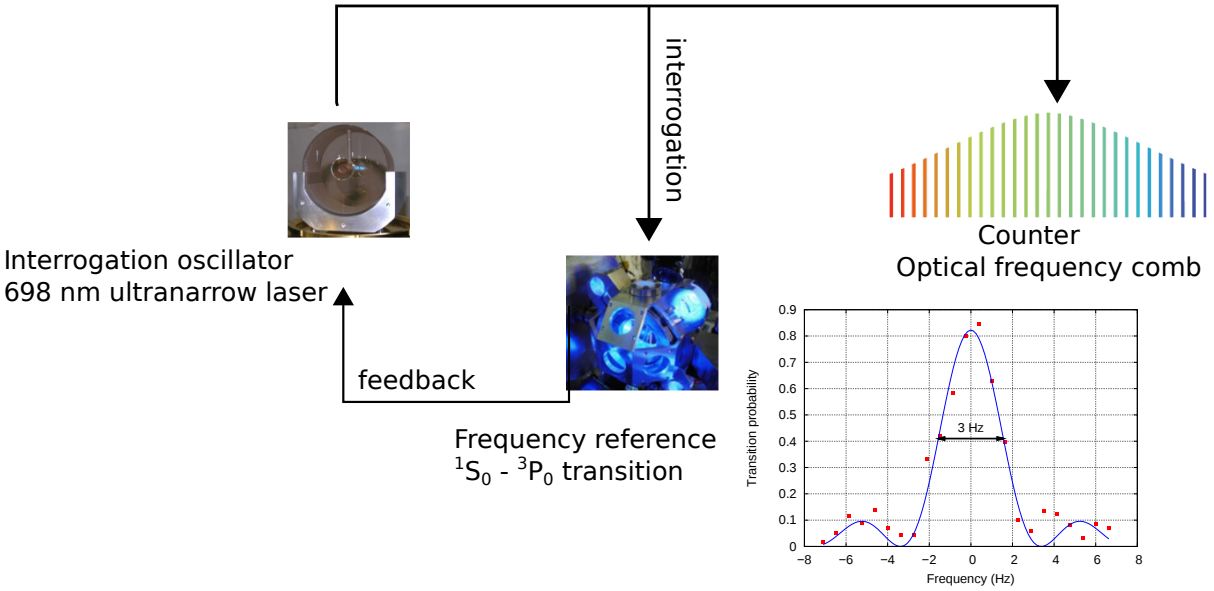

Figure 1.1.2. Principle of operation of an optical atomic clock, using the strontium optical lattice clock as an example. The frequency of a local oscillator is stabilized to a resonance of the atomic reference. The counter synthesizes the optical signal to the microwave domain.

The frequency ω_L of an atomic resonance is perturbed by environmental effects and the real realization is affected by two kinds of perturbations:

$$\omega_L = \omega_0[1 + \varepsilon + y(t)], \tag{1.1.1}$$

where ω_0 is the unperturbed frequency of the reference. ε is the fractional frequency correction for systematic effects, and its uncertainty tells how well the unperturbed transition frequency can be determined. It shows the state of the understanding of all effects that can shift the clock transition. $y(t)$ is the fractional frequency fluctuation of the output signal which determines the statistical resolution of the frequency measurement. It tells how much the frequency of the standard varies (is stable) over some period of time[2]. According to the Institute of Electrical and Electronic Engineers (IEEE), to appropriately

[1] In general, the term 'clock' means the frequency standard which is continuously operated. Therefore, 'optical lattice clock' is a bit incorrect. Nevertheless, we will use it alternately.

[2] We will use the fractional frequency uncertainty and stability, which are defined as a ratio of the uncertainty/stability and frequency of the clock transition.

evaluate the stability of the frequency measurement and the averaging of the noise after the total integration time τ, we use the Allan variance [11]:

$$\sigma_y^2(\tau) = \left\langle \frac{1}{2}(\bar{y}_{k-1} - \bar{y}_k)^2 \right\rangle, \tag{1.1.2}$$

where the $\bar{y}_k$ is the mean value of the fractional frequency deviation around t_k:

$$\bar{y}_k = \frac{1}{\tau}\int_{t_k}^{t_k+\tau} y(t)dt = \frac{1}{\tau}\int_{t_k}^{t_k+\tau} \frac{\nu(t) - \nu_0}{\nu_0}dt, \tag{1.1.3}$$

where ν_0 is the nominal frequency over τ. The Allan deviation is defined as a square root of the Allan variance. For atomic clocks, the fractional stability limited by a white frequency noise source, can be expressed by:

$$\sigma(\tau) = \frac{1}{Q_0}\frac{\eta}{(S/N)\sqrt{\tau}}, \tag{1.1.4}$$

where Q_0 is the experimental quality factor, defined as a ratio of the absolute frequency of the clock transition to its linewidth $Q_0 = \frac{\nu_0}{\Delta\nu}$, η is parameter of order of one, which depends on the shape of the resonance, S/N is the signal to noise ratio of the transition measurement and τ is the averaging time. The fundamental limitation for the clock stability is a quantum projection noise limit (QPN) [12], which comes from the quantum fluctuations of the transition probability measurements. For this noise $S/N = \sqrt{N}$, where N is the number of atoms. For optical lattice clocks it is below 10^{-17} at one second for the typical number of atoms larger than 10^4. Because the QPN limit is so low that the frequency stability of optical clocks is limited by another effect, the so-called Dick effect [13]. It is a degradation of the stability of the atomic signal due to the non-continuous probing of the atoms. The clock transition is interrogated once every clock cycle, corresponding to a characteristic frequency $f_c = 1/T_c$, where T_c is the total duration of the clock cycle. Due to the inability to low-pass filter spectral components of the oscillator at harmonic frequencies of the clock cycle, the atomic response down-converts the high frequency laser noise to the detection bandwidth by and aliasing effect. During the clock operation, the aliased frequencies are not distinguishable from the excitation measurement, and therefore the S/N ratio of the atomic resonance is degraded. The Dick effect is a common problem for all clocks, working in a cycle way. Nevertheless, there are solution to reduce this effect and reach better stability.

The first option to reduce the Dick effect and therefore improve the clock stability is reducing the dead time of the clock sequence (faster preparation of the atomic sample). Then, the interrogation time occupies proportionally a larger fraction of the clock cycle. Other option is the implementation a non-destructive detection method, which does not expel lattice-trapped atoms after detection [14, 15]. Then, trapped atoms are re-used several times for several interrogations. In this case, the loading time, which takes usually a half of a clock sequence, is significantly eliminated from a cycle and the need to reload atoms is limited to the lifetime of atoms in the trap. Prospectively, clocks with realizing the non-destructive detection method are able to demonstrate a frequency stability not only beyond the Dick effect limit, but also beyond the QPN limit [16, 17]. The second option is reducing the frequency noise of the clock laser to make it more stable. With a reduced laser noise, a clock transition with a narrower linewidth can be observed. As a result, the Q quality factor is higher, and the stability can achieve lower value. Moreover,

a low noise laser has a longer coherence time and therefore, it can probe atoms longer - meaning that the interrogation takes a larger fraction of the total time in the cycle of the clock. Currently, many groups make efforts to develop high finesse ultra-stable optical Fabry-Pérot cavities, to which lasers can be stabilized at sub-Hz level linewidth. The best frequency stabilities of ultra-stable lasers obtained so far, on the order of 10^{-16}, are limited by the thermal Brownian noise, which originates from mirror coatings. To reduce this noise, the cavity length can be increased [18–20], the temperature of the cavity can be decreased to the cryogenic temperatures [21, 22] or the size of a cavity mode can be increased [23]. In parallel, other alternative methods are developed to improve the clock stability limit. New mirror coatings like crystalline coatings with thermally limited noise floor [24] are investigated, and spectral hole burning in cryogenically cooled crystals with long-term stability [25, 26], a new protocol of locking scheme [27] and an active light source, based on lattice-trapped alkaline-earth atoms [28] look promising.

The Dick effect can also be reduced without any improvement in the clock cycle (shorter preparation or longer interrogation). By using several atomic samples that can be consecutively interrogated by one oscillator, it is possible to largely reduce or eliminate the Dick effect [20, 29–31]. Because it involves several atomic references, the experiment becomes more complex.

1.2 State-of-the-Art Optical Clocks

Optical clocks can be divided in two groups, according to the type of the interrogated particle - ions or neutral atoms. Historically, ion optical clocks were developed first. Because an ion is a charged particle, its manipulation is relatively easy. An ion is stored in a Paul-type trap in which a time-varying quadrupolar potential is used to keep the ion in a balance between the Coulomb force and inertia of ion. In these conditions, it can be cooled, confined, separated from external perturbations in a stable position. Trapped ions have extremely long lifetimes (several days or even months), limited by chemical reactions with background gases. However, using an ion also implies some problems. Ions strongly interact with other ions or particles, then, in a single point-like field-free region, it is possible to trap only a few ions, which significantly limits the potential achievable stability. The linear Paul trap, in which several ions can be trapped and interrogated, could improve the stability, but the realization of the linear trap with the zero-field point is technologically demanding [32]. There are several ion clocks being developed based on various atomic species: Al^+ [33], Ca^+ [34, 35], Sr^+ [36, 37], In^+ [38], Yb^+ [39–41] and Hg^+ [42]. Nowadays, the best Yb^+ ion clock at PTB can reach an accuracy of 3×10^{-18} in fractional units [41].

In contrast to ion clocks, the second type of clocks - optical lattice clocks - is based on the trapping of ultra-cold neutral atoms in a dipole potential. Because interactions of neutral atoms between each other are much weaker than the ion-electric field interactions, it is possible to interrogate many atoms in a trap. On the other hand, the atom-light interactions are much weaker than for ions, which makes the trapping process more difficult. But the opportunity to improve the clock stability by the simultaneous interrogation of an atomic ensemble composed of several thousands of atoms is very attractive. For optical clocks, alkaline earth(-like) atoms have drawn attention due to their simple atomic structure, which allows for efficient cooling, and narrow intercombination lines, in particular the doubly forbidden $^1S_0$-$^3P_0$ transition in isotopes with nuclear spin. This transition is very narrow with a sub-Hertz linewidth at technological accessible frequencies. Cur-

rently, the observed linewidth of the clock transition is Fourier limited, because of the interrogation time up to 1 s limited by the coherence time of the clock laser. But presented recently, the ultra-stable laser [22] can push forward this limit so that it will be possible to resolve the natural linewidth of the Sr clock transition. The main problem - the AC Stark shift of atomic energy levels is solved by the so-called «magic» wavelength concept [43, 44]. Nowadays, optical lattice clocks are operated mostly with Sr [6, 45–50], Yb [51–55] and Hg [56, 57] in several group worldwide. The best optical lattice clock based on Sr atoms has already reached an estimated total systematic uncertainty in the low 10^{-18} [6]. This thesis is dedicated to strontium optical lattice clocks, therefore, we will describe the current status of this type of clocks in more details.

1.2.1 ^{87}Strontium Optical Lattice Clocks

Among all optical lattice clocks (OLCs), clocks based on Sr atoms are the most popular choice in the laboratories worldwide. In ^{87}Sr clock, the clock transition is realized by the very weak electric dipole resonance, doubly forbidden ($\Delta S = 0, \Delta J = 0$) ^{1}S$_0$-^{3}P$_0$ at 698 nm with a natural linewidth of $\sim$ 1 mHz. It is weakly allowed due to the hyperfine interaction [58]. The Sr atoms are cooled in two steps. The dipole allowed transition

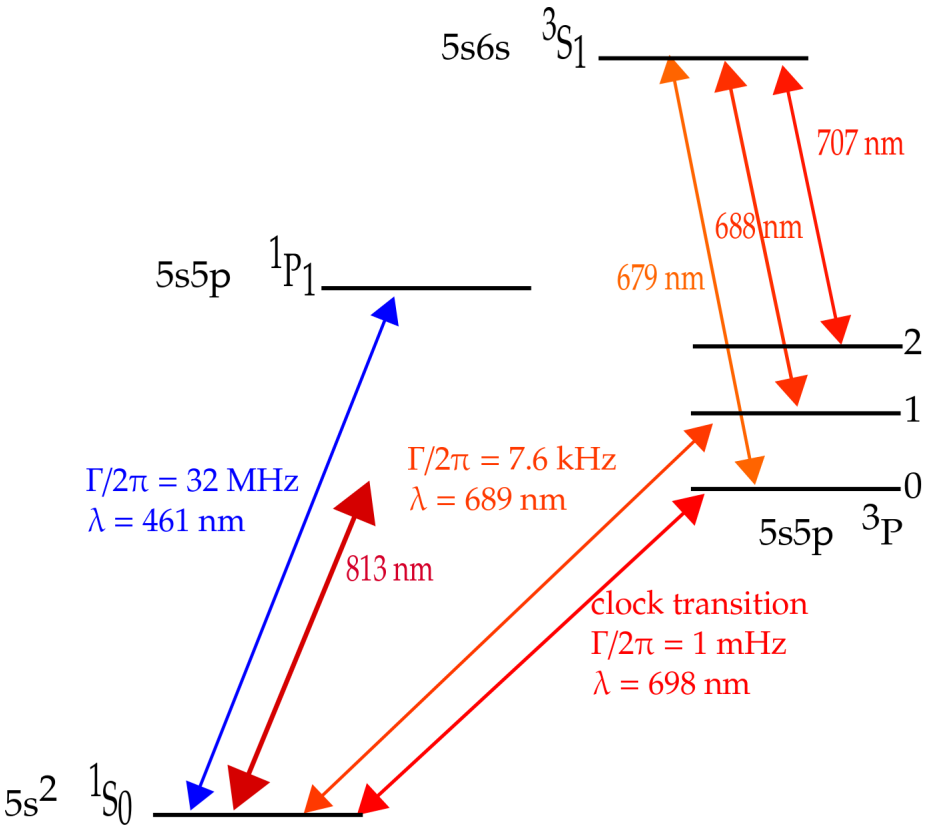

Figure 1.2.3. Energy levels of Sr which are important in the clock operation.

between the ground state $5s^2$ ^{1}S$_0$ and the $5s$ $5p$ ^{1}P$_1$ state at 461 nm is used for the first stage cooling of Sr atoms. The second stage cooling below the Doppler limit of the first stage cooling transition is achievable using the intercombination transition ^{1}S$_0$ - ^{3}P$_1$ at 689 nm. Finally, atoms are trapped in an optical lattice at the magic wavelength of

813 nm. A reason for the common choice of Sr for OLCs is the availability of the laser sources required for the clock operation.

Currently, the Sr clocks equipped with the best ultra-stable lasers show a fractional stability at the low 10^{-16} level at 1 second [6]. The fractional uncertainty of the best clocks is evaluated to be a few of 10^{-18} by operating with an ambient temperature environment [6] or in a vacuum housing cooled down to cryogenic temperatures [48].

At SYRTE, two ^{87}Sr OLCs have been already constructed and successfully operated [14,46,59,60] for several years. The fractional stability of two non-synchronized clocks is $1\times\ 10^{-15}$ at 1 second and it averages down into the low 10^{-17} range after 2 hours. The fractional uncertainty of clocks is estimated to be a few of 10^{-17} [61]. A clock performance and an accuracy budget are described in details in section 5.4 and chapter 4 respectively. In the near future, a new ultra-stable cavity will be implemented for the Sr clocks, with an expected improvement of 1 order of magnitude on the clock stability.

In the last years, several measurements of the Sr clock transition with respect to the primary Cs frequency standard have been performed as shown in figure 1.2.4. Comparisons were carried out locally or remotely by using a satellite or fiber links, which connect spatially separated clocks. The recommended frequency of the ^{87}Sr clock tran-

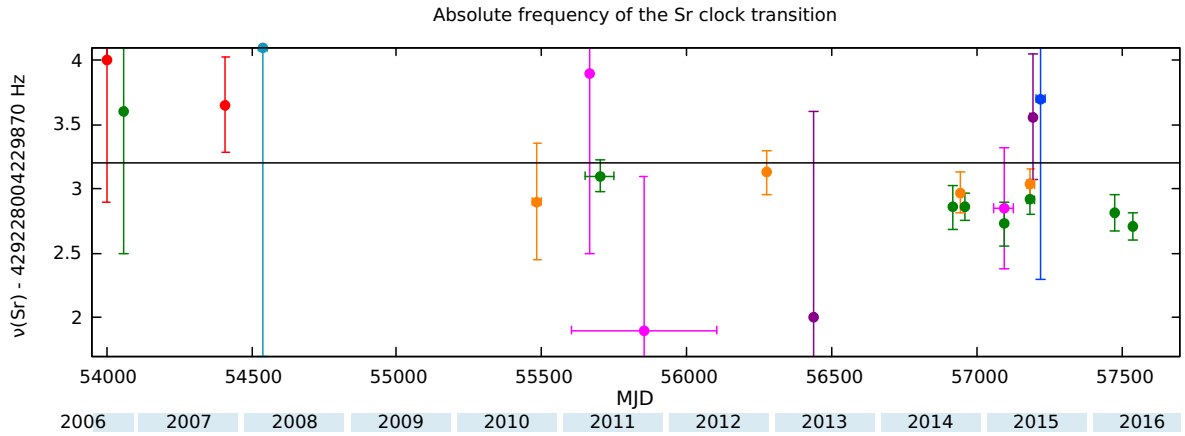

Figure 1.2.4. The absolute frequency of the Sr clock transition of LNE-SYRTE (green • [46,62]) over the years in comparison with similar measurements of other institutes in the world: red • JILA [63,64], light-blue • Tokyo University [65], orange • PTB [47,66,67], pink • NICT [35,65,68,69], purple • NMIJ [49,70], blue • NIM [71]. The black line indicates the recommended value $\nu_{^{87}Sr}$.

sition for secondary representation of the SI second is based on a part of these comparisons [62,63,65,67,69,72] and its value is $\nu_{^{87}Sr} = 429\ 228\ 004\ 229\ 873.2$ Hz with a fractional standard uncertainty of 5×10^{-16} [3] which was approved by the CIPM in 2015. On June 2017, the Consultative Committee for Time and Frequency (CCTF) recommended a new value $\nu_{^{87}Sr} = 429\ 228\ 004\ 229\ 873.0$ Hz. On October 2017, during the 106th meeting of the CIPM, this value was accepted[4]. In the future, a larger number of independent comparisons will allow us to have a higher confidence in the determined frequency. Therefore, the CIPM will be able to recommend more precise value with reduced uncertainty. Nevertheless, the ratio Sr/Cs is already the best reproducible frequency ratio between an optical and a microwave frequency by various institutions in the world.

To compare optical clocks beyond the SI second, it is necessary to implement a better

[3] https://www.bipm.org/utils/en/pdf/CIPM/CIPM2015-II-EN.pdf

[4] The final report is not published online yet.

remote comparison technology than the satellite link, currently used to compare microwave clocks. So far, direct satellite comparison between two remote Sr clocks was solely limited by the satellite link [73]. Therefore, the satellite technology can not support optical clock comparisons in the 10^{-18} accuracy range. The alternative is the optical transfer by telecommunication fibers [74,75], which does not limit clock comparison down to the 10^{-19} level. Currently, new fiber connections are being developed rapidly in France, Germany, Italy and Poland [76–79]. In the future, optical clocks, connected by optical fibers, can be frequently compared with each other. As results of these comparisons, optical clocks will regularly contribute to the International Atomic Time (TAI), replacing the microwave clocks, making a significant step forward the redefinition of the SI second.

There are other possibilities to establish an «optical atomic time scale». The first option is the Atomic Clock Ensemble in Space (ACES) mission, which will place a cold atomic cesium clock and a hydrogen maser on board of the International Space Station in order to be able to compare space and ground clocks with a frequency instability less than 10^{-17} after a few days of averaging [80]. The second project is a space-based optical clock. Launched to space optical clock could be compared with other clocks on the Earth by using a high-performance frequency link like in the ACES mission. Such Sr space clock is developed within the Space Optical Clock project[5] (SOC) [81]. In both projects, the access would not be limited by a lack of the fiber connection. However, space or transportable applications require a higher degree of compactness and reliability of components and additional tremendous amount of engineering work must be performed.

But before optical clocks, in particular Sr clocks, massively contribute to international timescales, great efforts are currently focused on the fundamental physics tests and other basic research. Sr clocks have already been involved, for instance, in the monitoring of the variation of fundamental constants [64] or probing atomic interactions [82,83], test of Special Relativity [84] or searching on the topological-defect dark matter [85]. These applications and others are expected by be enhanced by optical clocks connected by a network.

1.2.2 ^{88}Strontium Optical Lattice Clocks

On the other hand, some efforts have been made to extend optical lattice clocks to stable bosonic isotope ^{88}Sr. Its simpler atomic structure, the absence of total nuclear spin and and much higher abundance make the clock operation easier with ^{88}Sr than with fermionic isotopes, which was, in particular, important at the beginning of development of optical lattice clocks. In the presence of no hyperfine interactions, the clock transition is insensitive for lattice light polarization effects (no a tensor lattice shift). But the absence of hyperfine coupling implies that the clock transition $J = 0 \rightarrow J = 0$ is strictly forbidden for all one photon excitations. To experimentally excite this transition, a high magnetic mixing field or probe light intensity are required (higher than for fermionic isotopes) to observe the clock resonance. With these conditions, a larger second order Zeeman shift or a larger probe light light shift is induced, respectively. Now, this issue can be mitigated by implementing a hyper-Ramsey-type interrogation protocol, immune for the probe light shift [41]. Additionally, bosons interact each other much stronger than fermions therefore, to suppress the collisional shift, a 3D lattice must be applied, because in a 1D lattice, this shift is one order of magnitude larger than for fermionic type clocks and it is the main limitation of the total accuracy budget at low 10^{-17} level [86]. Nevertheless, a bosonic

[5] www.soc2.eu

strontium clock is considered as a candidate for a transportable clock [81]. ^{88}Sr clock has been developed and presented in a few laboratories [50, 86–89].

1.3 Thesis At-a-Glance

Naturally, it is not the first dissertation about optical frequency standards [90–96] and there are as well several excellent reviews dedicated to optical frequency standards [97–102], which the author (carefully) reads and widely used during the writing of his own thesis. When I arrived at SYRTE, two Sr OLCs had already been constructed and successfully operated [14, 29, 46, 103, 104].

This thesis describes the latest progresses regarding the Sr optical lattice clocks at LNE-SYRTE, Observatoire de Paris, from October 2014 to September 2017. In the expectation of a redefinition of the SI second, we show that optical clocks are progressing towards replacing the microwave time and frequency architecture currently realizing the SI second, once optical clocks are proven to be as reliable and reproducible as their microwave counterparts. This thesis presents three decisive steps in this direction. First, we demonstrate nearly continuous Sr clocks over several weeks with a total uptime larger than 80% [61]. Second, local and remote frequency comparisons against various microwave and optical frequency standards show that OLCs are reproducible over time, and by independent laboratories [61, 105]. We notably demonstrated the first all-optical agreement between fully independent optical clocks at the continental scale with a relative agreement in the 10^{-17} range [106]. Third, the Sr clocks were used to calibrate the Temps Atomique International. The five calibration reports we produced, were validated by the BIPM, as the first contributing to TAI by optical clocks [107]. In addition, some of these results were used to improve bounds on a putative violation of the Lorentz invariance by testing the stability of the frequency ratio between remote spatially separated clocks. As a result, the constraint is improved by 2 orders of magnitude compared to the previous limit obtained by clock comparisons and it is 2 times better than the best constraint by using accelerated ions [84]. Finally, we conducted a full characterization of the frequency shifts associated with semi-conductor laser sources for the trapping light, including optical measurements and frequency shift measurements, with applications for transportable and space clocks.

CHAPTER 2

ATOMS IN THE DIPOLE TRAP POTENTIAL

We aim at performing the ultra-precise spectroscopy of the ultra-narrow optical transition $^1S_0$-$^3P_0$. To do that, the motion of atoms must be extremely well controlled much better than in the magnetic-optical trap, where the atomic motions leads to significant velocity dependent Doppler and recoil shifts, which limit the accuracy of the free-atomic microwave and optical standards to 10^{-16} [108]. Fortunately, with the novel cooling and trapping techniques, we can overcome these problems. Cooled atoms, whose the energy is smaller than the harmonic oscillator spacing of the trap in energy scale: $k_B T < \hbar\Omega$, occupy only a few of the lowest motional states of the trapping potential. Motional degrees of freedom are quantized (Lamb-Dicke regime) and the motional effects are maximally dwarfed far below 10^{-16} level. The residual motional effects such as the second order Doppler shift and the tunneling of atoms between lattice sites are negligible and estimated to be below 10^{-18} level [6]. Although, atomic energy levels are strongly perturbed by the trapping laser field, by the so-called ac Stark shift, the «magic» conditions can largely cancel this shift. In this chapter, we describe interactions between atoms and off-resonant light, assuming some approximations and simple models. In our experiment, we use the dipole potential to trap atoms in a 1D optical lattice, which is widely used in the clock community. In particular, we are interested into how the dipole potential shifts the clock energy states away from the unperturbed values and how we can minimize such effects, how motional effects are suppressed in the dipole potential.

This chapter is organized as follows. At first, we assume that atoms have enough low temperature to be trapped in the dipole potential. At the beginning, we describe an atom placed in an off-resonant laser field. Next, we explain the concept of the control of the AC Stark shift by the implementation of the «magic» wavelength and the control of the motional effects of atoms in the lattice by the Lamb-Dicke regime. Finally, we consider the spectroscopic interrogation of atoms trapped in the optical lattice.

2.1 Dipole Trap

The optical dipole force is a well-known concept in experimental physics. In this section, we consider the basic physics of dipole traps with far-detuned light which guarantees a low photon scattering rate. This section is based mostly on prof. Rudolf Grimm's paper [109]. At the beginning, we consider the atom as a simple oscillator, placed in a laser

light field with amplitude $\mathcal{E}_0$, and polarization $\boldsymbol{\epsilon}$ and frequency ω

$$\boldsymbol{\mathcal{E}}(\boldsymbol{r},t) = \boldsymbol{\mathcal{E}} = \boldsymbol{\epsilon}\mathcal{E}_0(\boldsymbol{r})\exp(i\omega t) + c.c. \tag{2.1.1}$$

The laser electric field $\boldsymbol{\mathcal{E}}$ induces on the atom a dipole moment $\boldsymbol{d}$ with amplitude d_0 in the atom, given by following formula:

$$\boldsymbol{d}(\boldsymbol{r},t) = \boldsymbol{d} = \boldsymbol{\epsilon}d_0(\boldsymbol{r})\exp(i\omega t) + c.c. \tag{2.1.2}$$

The averaged interaction potential can be expressed as the effect of the coupling between atom and laser field:

$$U_{dip}(\boldsymbol{r},t) = -\frac{1}{2}\langle \boldsymbol{d}\cdot\boldsymbol{\mathcal{E}}\rangle. \tag{2.1.3}$$

The factor 1/2 is introduced because the dipole moment is induced. Usual frequencies ω of the laser are on the order of 100s of THz, therefore, the rapid oscillating terms are negligible and the stationary term can be used only.

Due to its conservative character, the dipole force f_{dip} can be expressed as the gradient of the interaction potential:

$$\boldsymbol{f}_{dip}(\boldsymbol{r}) = -\nabla U_{dip}(\boldsymbol{r}). \tag{2.1.4}$$

The scattering rate is defined as the photon absorption rate P_{abs} by the atom from the laser field:

$$\Gamma_{sc}(\boldsymbol{r}) = \frac{P_{abs}}{\hbar\omega} = \frac{\langle \dot{\boldsymbol{d}}\cdot\boldsymbol{\mathcal{E}}\rangle}{\hbar\omega}, \tag{2.1.5}$$

where $\hbar\omega$ is the energy of absorbed photons.

The interaction potential $U_{dip}(\boldsymbol{r})$ and the scattering rate $\Gamma_{sc}(\boldsymbol{r})$ are the main quantities, that describe the dipole trap. These general expressions are valid for any polarizable particle and any near-resonance or far off-resonance driving field. In the case of the rotating-wave approximation, for which the counter-rotating term is negligible, the general expressions for the interaction potential $U_{dip}(\boldsymbol{r})$ and the scattering rate $\Gamma_{sc}(\boldsymbol{r})$ simplify to:

$$U_{dip}(\boldsymbol{r}) = \frac{3\pi c^2}{2\omega_0^3}\frac{\Gamma}{\Delta}I(\boldsymbol{r}) = -\frac{\Re[\alpha(\omega)]}{2\varepsilon_0 c}I(\boldsymbol{r}), \tag{2.1.6}$$

$$\Gamma_{sc}(\boldsymbol{r}) = \frac{3\pi c^2}{2\hbar\omega_0^3}\left(\frac{\Gamma}{\Delta}\right)^2 I(\boldsymbol{r}) = \frac{\Im[\alpha(\omega)]}{\hbar\varepsilon_0 c}I(\boldsymbol{r}), \tag{2.1.7}$$

where α is the polarizability, $I(\boldsymbol{r})$ is the field intensity, ω_0 is the frequency of the atomic resonance, Γ is the linewidth of the resonance and $\Delta = \omega - \omega_0$ is the detuning from the resonance, c is the speed of light, ε_0 the vacuum permittivity and $\hbar$ is the Planck's constant divided by 2π. Based on these equations, the relation between the interaction potential and scattering rate can be expressed as:

$$\hbar\Gamma_{sc} = \frac{\Gamma}{\Delta}U_{dip}. \tag{2.1.8}$$

According to equations above, we can see that the dipole force is proportional to the intensity of the driving field and its gradient. To induce a large dipole force, we need a high gradient and a high intensity for the trapping light. To have low scattering rate, a large detuning is preferred. Dipole traps can be divided on two main classes. We can say that the dipole trap is red detuned, when $\Delta < 0$. Then, atoms are attracted to the

maximum of the light intensity. When $\Delta > 0$, the trap is blue detuned and the atoms are trapped in the minimum of the light intensity.

The dipole force is a standard practice to confine thousands of ultracold atoms. On the other hand, considering the induced dipole moment by off-resonance trapping light as a second order perturbation, atom-light interactions leads to an energy shift, the so-called light-shift (or an ac Stark shift) of atomic state. The energy shift δE depends on the polarizability $\alpha(\omega)$, that describes the dispersive properties of atom-light interactions, given the local intensity $I(\bar{r})$ of the trapping light. The energy shift can be written:

$$\delta E = -\frac{\alpha(\omega)}{4}\mathcal{E}^2(\boldsymbol{r}) = -\frac{\alpha(\omega)}{2\varepsilon_0 c}I(\boldsymbol{r}). \tag{2.1.9}$$

In the metrological point of view, it means that the fundamental and excited clocks states experience different light shifts, because they have different polarizability.

2.2 Dipole Polarizability

In previous section, we modeled the atom by a simple oscillator, but a real atom is more complicated. Due to the complex sub-structure of electronic transitions, the dipole potential depends on the given atomic sub-state. In this section, a multi-level atom will be described with an irreducible operator of polarizability $\alpha(\omega)$, depending on the trapping light polarization and the orientation of the quantization axis. Calculations are based on refs [60, 98, 110]. We consider an atom with a ground state $|g, \{n, J, F, m_F\}\rangle$ and an exited state $|e, \{n', J', F', m'_F\}\rangle$, with unit angular momentum along the quantization axis, parallel to the bias magnetic field $\boldsymbol{B}_s$. Atom is placed in the dipole potential with the presence of $\boldsymbol{B}_s$. The Hamiltonian of that system is:

$$\hat{\mathcal{H}}_{tot} = \hat{\mathcal{H}}_Z + \hat{\mathcal{H}}, \tag{2.2.10}$$

where $\hat{\mathcal{H}}_Z$ is the Hamiltonian describing the Zeeman interactions:

$$\hat{\mathcal{H}}_Z = \frac{g\mu_B}{\hbar}\hat{\boldsymbol{F}} \cdot \boldsymbol{B}_s, \tag{2.2.11}$$

where g is the Landé factor and μ_B is the Bohr magneton. The Hamiltonian of the electric dipole interaction between atom and the off-resonance trapping light is as follows:

$$\hat{\mathcal{H}} = -\hat{\boldsymbol{d}} \cdot \boldsymbol{\mathcal{E}}(\boldsymbol{r}, t), \tag{2.2.12}$$

which, in the second-order perturbation theory can be expressed as [111]:

$$\hat{\mathcal{H}} = -\frac{1}{4}\hat{\alpha}|\mathcal{E}|^2, \tag{2.2.13}$$

where the polarizability operator $\hat{\alpha}$ is defined as a sum of the atom-light interactions of all excited states:

$$\hat{\alpha} = \frac{1}{\hbar}\sum_{|e\rangle}\frac{\boldsymbol{\epsilon}^* \cdot \hat{\boldsymbol{d}}|e\rangle\langle e|\boldsymbol{\epsilon} \cdot \hat{\boldsymbol{d}}}{\omega_0 - \omega} + \frac{\boldsymbol{\epsilon} \cdot \hat{\boldsymbol{d}}|e\rangle\langle e|\boldsymbol{\epsilon}^* \cdot \hat{\boldsymbol{d}}}{\omega_0 + \omega}. \tag{2.2.14}$$

The matrix elements of the polarizability operator depends on the electric dipole moment $\hat{d}$ and polarization $\hat{\epsilon}$ and it can be expressed as a expansion in the irreducible

tensor products $[\boldsymbol{\epsilon} \otimes \boldsymbol{\epsilon}^*]_{jM}$ of the polarization $\boldsymbol{\epsilon}$ and conjugate $\boldsymbol{\epsilon}^*$ of the tensor rank $j = 0, 1, 2$:

$$\langle m_2|\hat{\alpha}|m_1\rangle = \sum_{j=0}^{2} K_j \sum_{M=-j}^{j} (-1)^M C^{Fm_2}_{Fm_1 j-M} [\boldsymbol{\epsilon} \otimes \boldsymbol{\epsilon}^*]_{jM}. \tag{2.2.15}$$

The expansions coefficients: Clebsch-Gordan coefficients $C^{Fm_2}_{Fm_1 j-M}$ depend on the m_F, while the atomic parameter K_j depend on the excited states $|e\rangle$. It can be written as:

$$K_j = \frac{1}{\hbar} \sum_{|n',J',F'\rangle} k_j \left(\frac{1}{\omega_0 - \omega} + \frac{(-1)^j}{\omega_0 + \omega} \right), \tag{2.2.16}$$

where k_j is expressed by using the standard Wigner 6j-symbols and the reduced dipole matrix elements:

$$k_j = (-1)^{j-F-F'} \sqrt{\frac{2j+1}{2F+1}} \begin{Bmatrix} F & F & j \\ 1 & 1 & F' \end{Bmatrix} |(F'||d||F)|^2. \tag{2.2.17}$$

By rescaling these coefficients, we can decompose α as the sum of the scalar α_s, vector α_v, and tensor α_t polarizabilities:

$$\alpha(\omega) = \alpha_s(\omega) + (\hat{k} \cdot \hat{B}) \mathcal{A} \frac{m_F}{2F} \alpha_v(\omega) + \frac{1}{2}(3|\hat{\boldsymbol{\epsilon}} \cdot \hat{\boldsymbol{B}}_s|^2 - 1) \frac{3m_F^2 - F(F+1)}{F(2F-1)} \alpha_t(\omega), \tag{2.2.18}$$

where

$$\alpha_s = -\frac{1}{\sqrt{3}} K_0 \tag{2.2.19}$$

$$\alpha_v = \sqrt{\frac{2F}{F+1}} K_1 \tag{2.2.20}$$

$$\alpha_t = \sqrt{\frac{2F(2F-1)}{3(F+1)(2F+3)}} K_2, \tag{2.2.21}$$

and $\mathcal{A}$ describes the circular polarization of the light. The matrix of the polarizability operator (equation 2.2.15) can be described by α_s, α_v and α_t, which corresponds to values of $j = 0, 1, 2$, respectively. The main contribution, the scalar polarizability α_s is independent of the total angular momentum F. The vector polarizability α_v makes contribution to the matrix if $F \geq 1/2$ and non-linear polarization of the light: $\mathcal{A} = \pm 1$ for a $\sigma_\pm$ polarized light. α_v vanishes for a perfect linear polarization, $\mathcal{A} = 0$. It can be treated as a fictitious magnetic field parallel to the light wave vector $\hat{k}$. In particular, in optical clocks, in which two extreme m_F states are interrogated, the vector component drops out regardless of the polarization, but if it is too big the vector component can broad the line. The tensor polarizability α_t is non zero for $F \geq 1$, and can be interpreted as a polarized dependent polarizability with even dependence on m_F. Here, we apply this formalism to the clock transition $5s^2\ {}^1\mathrm{S}_0$ - $5s5p\ {}^3\mathrm{P}_0$ in the strontium atom (see figure 1.2.3. Both clock states have $J = 0$, then their polarizability does not depend on the magnetic sub-levels m_F and the polarization of the trap light $\boldsymbol{\epsilon}$. But the hyperfine interactions in the fermionic isotopes induce the state mixing mechanism for states with the same total F. The pure excited clock state is mixed with ${}^1\mathrm{P}_1$, ${}^3\mathrm{P}_1$ and ${}^3\mathrm{P}_2$. Then the wave function of the ${}^3\mathrm{P}_0$ state is modified and the weak dependence of polarizability of the clock states on m_F and $\boldsymbol{\epsilon}$ appears. Vector and tensor components α_v and α_t exist due to the state

mixing between clock state $^3P_0$ and $^3P_1$ and $^3P_2$. The ratio between them and α_s is on the same order of magnitude as the ratio between the hyperfine splitting frequency ν_{hfs} and frequency of the clock transition ν_{clock}:

$$\frac{\alpha_{v,t}}{\alpha_s} \approx \frac{\nu_{hfs}}{\nu_{clock}}. \tag{2.2.22}$$

2.3 The Magic-Wavelength

In the previous section, the considerations were limited to the electric-dipole approximation. Naturally, in the real atom, the energy shift δE must be considered with higher orders corrections associated within dipole approximation, higher-order multipole corrections such as magnetic dipole (M1) or electric quadrupole (E2) and two photon processes (hyperpolarizability). In a general view, the light shift of the energy of a given level in the presence of the trapping field can be expressed in an order-by-order expansion [43]:

$$\delta E = -\frac{1}{4}\alpha_{E1}\mathcal{E}^2 - \frac{1}{64}\gamma\mathcal{E}^4 - \frac{1}{4}\alpha_{M1}\frac{\mathcal{B}^2}{c^2} - \frac{1}{4}\alpha_{E2}\left(\frac{\partial\mathcal{E}}{\partial k_l z}\right)^2, \tag{2.3.23}$$

where the $\alpha_{E1} = \alpha$ described in equation 2.2.18 and γ describes the hyperpolarizability term. For metrological applications, the ability of the control of the light shift is cru-

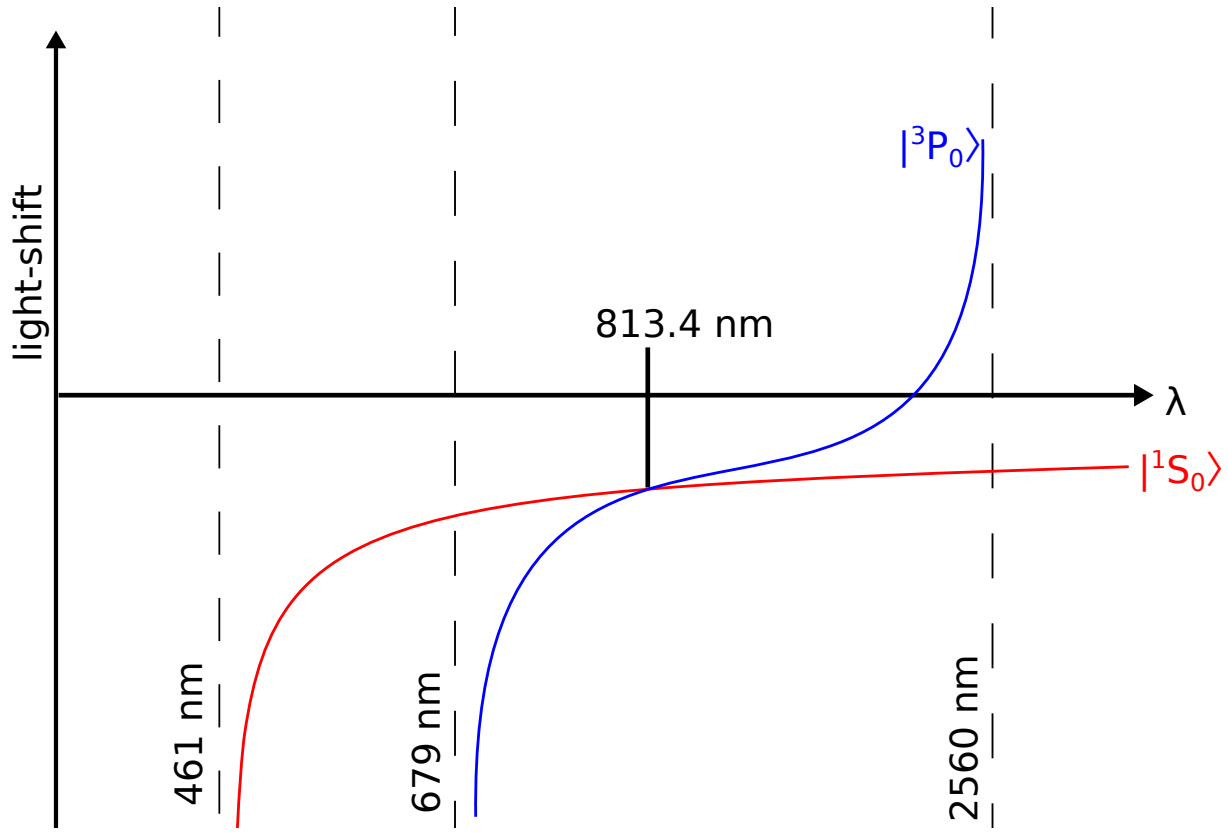

Figure 2.3.1. The light-shift of the ground and excited clock states of Sr atoms as a function of the trapping laser wavelength as an example. Intersection of two curves around 813.4 nm indicates the magic wavelength [43].

cial because the electric dipole term, which dominates the total light shift perturbation, corresponds to a shift on the order of MHz (10^{-9} in fractional units), that in the past

seriously limited any development of optical clocks. Fortunately, there is a smart solution, the so-called «magic» wavelength, which largely reduces this problem.

The prof. Katori's concept [43] is shown on figure 2.3.1. The magic wavelength λ_{magic} is the wavelength for which the light shift of the electric dipole term for the fundamental $|g\rangle$ and the excited $|e\rangle$ state are the same, so that the differential polarizability of the two clock states $\Delta\alpha_{E1} = \alpha_e - \alpha_g = 0$:

$$\hbar\omega_{clock} = \hbar\omega_0 - \frac{1}{4}\Delta\alpha_{E1}\mathcal{E}^2 - \frac{1}{64}\Delta\gamma\mathcal{E}^4 - \cdots \tag{2.3.24}$$

By canceling out the electric-dipole term of the polarizability, the frequency of the clock transition should be equal to the unperturbed frequency of the clock transition, which is independent of the intensity of the trapping light (assuming that the higher orders can be neglected). But with the development of optical lattice clocks, the other terms must be considered for a proper evaluation of the light-shift. Over the years, the residual ac multipole polarizability and dipole hyperpolarizability were considered in more and more precise theoretically calculations of the total light-shift [110,112,113] and were determined experimentally [45,59,60,103,114–116].

Currently, the light shift due to the presence of the trapping light is fully controlled at low the 10^{-18} level [6] and it is not the main effect limiting the total clock accuracy.

2.4 1D Optical Lattice

The 1D optical lattice is widely used because atoms are confined in a stable periodic potential. The optical lattice can be realized by two counter-propagating laser beams with the same intensity $I = \varepsilon_0 c|\mathcal{E}|^2/2$ along an axis Ox. In this standing wave configuration, the intensity nodes are separated by $\lambda/2$. In our experiment, the waist of the laser beam is

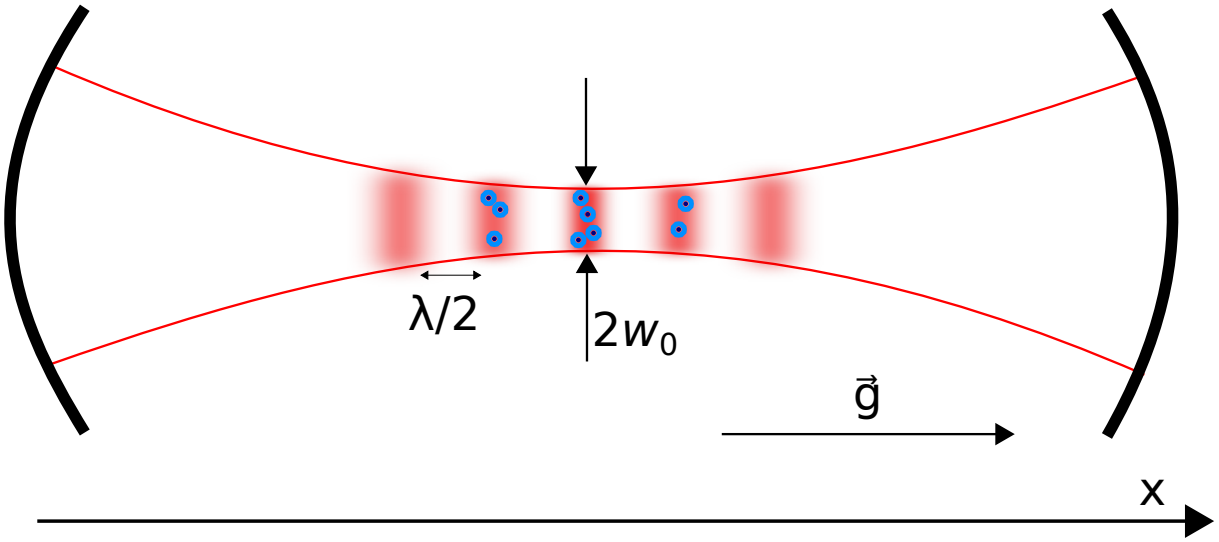

Figure 2.4.2. Schematic concept of the lattice trap build-up cavity with a tight focused laser beam at 813 nm. As it is a red-detuned trap, atoms are attracted in the maxima of the intensity of the light.

focused on 90 μm. The Rayleigh range $z_0 = \pi w_0^2/\lambda$ of the beam is equal to 30 mm, which is much larger than the size of the blue MOT (0.7 mm standard deviation). Therefore we assume that atoms are collected in the spot where the laser beam has the constant waist

and they experience the periodic potential:

$$U(x,r) = U_0 \sin^2(kx), \qquad U_0 = -\frac{1}{2c\varepsilon_0}\alpha(\omega) I \exp\left(\frac{-2r^2}{w_0^2}\right), \tag{2.4.25}$$

where the r is the radial coordinate in the transverse direction, w_0 is the waist of the beam and $k = 2\pi/\lambda$ is the wave vector. We can see that the potential depends on the polarizability $\alpha(\omega)$. At the magic wavelength condition, both clock states are shifted by the same amount, then they experience the same trapping potential.

To increase the light intensity, an experimental implementation is based on the laser beam built-up in an optical cavity (see figure 2.4.2). With the finesse of the cavity 100, the intensity is roughly 30 times larger than the retroreflected lattice. The 1D lattice is created in the vertical orientation along the gravity field in order to suppress site-to-site tunneling. For this orientation of the lattice, it can be shown that the corresponding shift due to the tunneling effect is less than 10^{-18} [117] for the first band down to $U_0 = 5\ E_r$.

2.5 Lamb-Dicke Regime

Close to the bottom of the wells, the potential is harmonic with oscillation frequency expressed by:

$$\hbar\Omega = 2\sqrt{U_0 E_r}, \tag{2.5.26}$$

where Ω is the Rabi frequency and E_r is the energy recoil defined as:

$$E_r = \hbar\omega_r = \frac{\hbar^2 k^2}{2m}, \tag{2.5.27}$$

m is the mass of the atom. In the harmonic potential, energy levels are equally spaced in the energy scale by $(n+1/2)\hbar\Omega$, as is shown on figure 2.5.3, and the atomic wave function has a finite standard deviation given by the harmonic oscillator characteristic length a_{oh}:

$$a_{oh} = \sqrt{\frac{\hbar}{m\Omega}}. \tag{2.5.28}$$

The Lamb-Dick parameter η [118] describes the relation between this characteristic length and the trapping laser field with wave vector k:

$$\eta \equiv k\sqrt{\frac{\hbar}{2m\Omega}} = k\frac{a_{oh}}{\sqrt{2}} = \sqrt{\frac{E_r}{\hbar\Omega}} \ll 1, \tag{2.5.29}$$

which establishes relations between the energies in the potential:

$$E_r \ll \hbar\Omega \ll U_0. \tag{2.5.30}$$

During the clock interrogation along the lattice axis, a trapped atom absorbs the photon's momentum $p = \hbar k$ and gains internal and kinetic energy. In the Lamb-Dicke regime, the recoil energy E_r is much smaller than the energy separation $\hbar\Omega$ of the harmonic potential, and the atom is well confined in the trap, such that the atomic motional spread in the trap $ka_{oh} \ll 1$. In these conditions, the laser spectroscopy of the atom in the dipole trap shows a central carrier at ω_0 and weak sidebands, which are separated by $\pm\Omega$. The frequency of the light absorbed by the atom is equal to internal atomic frequency and atom remains

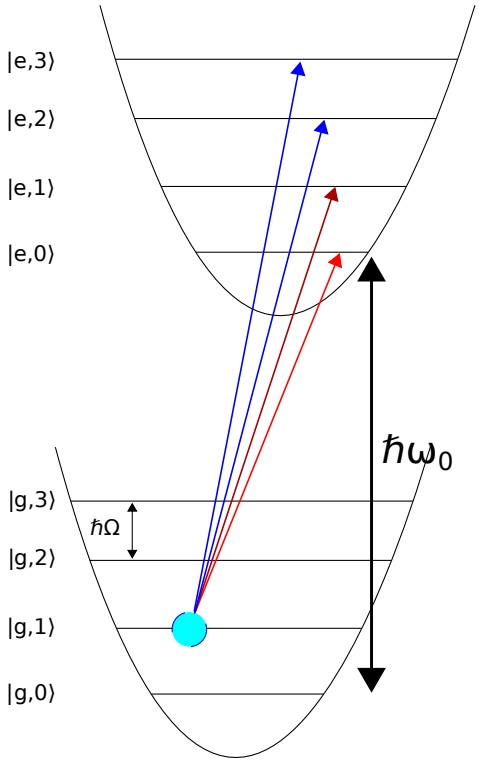

Figure 2.5.3. An atom in the harmonic potential. In the Lamb-Dicke regime, the transition is realized without change of the motional state, and the Doppler shift is removed.

in the same motional state. Moreover, in the well-resolve-sideband regime, $\Gamma \ll \Omega$ (where Γ is the width of the clock transition) so that the carrier is well discriminated from the motional sidebands. The atomic motion in the trap is quantized.

As the results of the interrogation, we obtain a spectra with an unperturbed carrier and two sidebands distributed at the trapping frequency on both sides of the carrier. Because the atomic confinement is realized only in one dimension, longitudinal sidebands are more visible than the transverse sidebands. The typical sideband spectrum is shown in figure 2.5.4. The amplitude of the carrier at zero detuning has maximum amplitude. The amplitude of the sidebands is reduced, because motional excitations are realized with the low probability $\eta^2(n+1)$ for blue sideband and $\eta^2 n$ for red sideband.

The separation between sidebands gives information about the trap frequency Ω along the longitudinal direction for the probe beam aligned along the lattice. Due to the fact that the blue sideband is always stronger and more visible than red sideband, in the experiment is usually used only blue sideband to determine Ω.

The other trapping parameters can be calculated by assuming that the state population of atoms is distributed according to the Boltzmann distribution. The longitudinal temperature of the trap can be estimated by comparing the height of the blue and red sidebands:

$$T_x = \frac{\hbar\Omega_x}{k_B \ln(b_{br})}, \tag{2.5.31}$$

where the k_B is the Boltzmann constant, and b_{br} is the height ratio between blue and red sidebands. The trapping potential U_0 can be calculated from the formula:

$$U_0 = \frac{\hbar^2\Omega_x^2}{4E_r}, \tag{2.5.32}$$

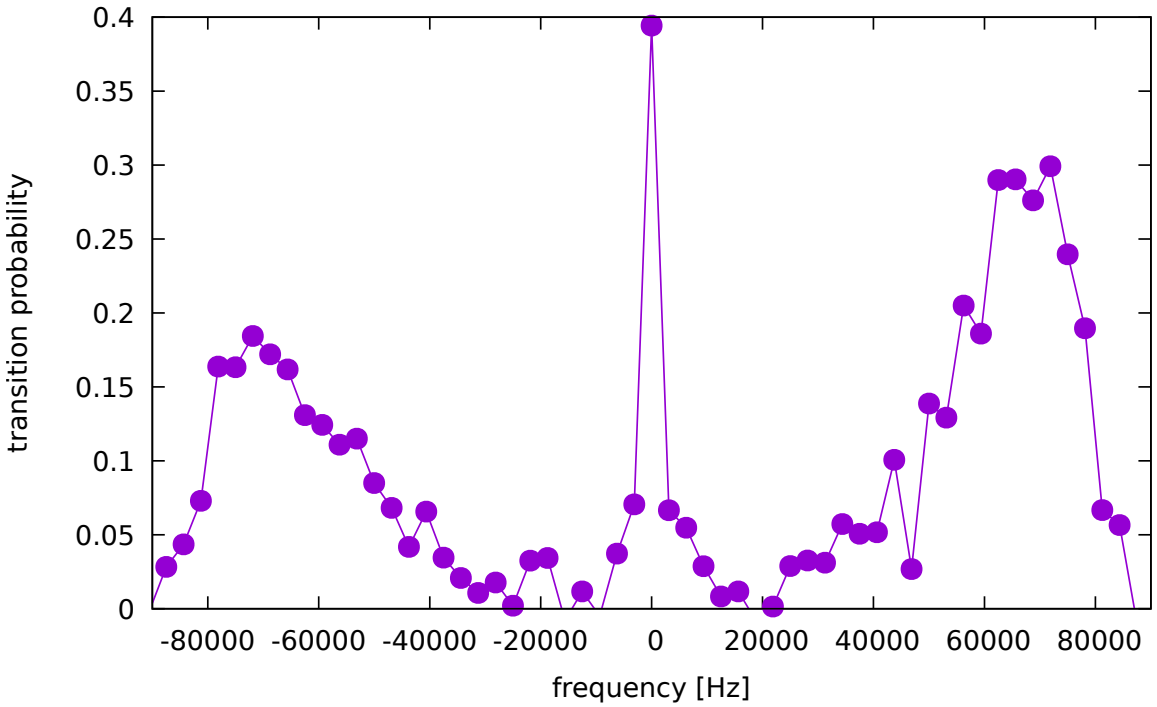

Figure 2.5.4. The sideband spectroscopy, a trap depth of $U_0 = 141\ E_r$ and longitudinal temperature $T_x = 8.1\ \mu K$. On the center, the carrier frequency corresponds to the clock transition.

The radial frequency of the trap is given by:

$$\Omega_r = \frac{\Omega_x \lambda}{\sqrt{2}\pi w_0}, \tag{2.5.33}$$

where the w_0 is the waist of the laser beam.

In the Lamb-Dicke regime, the atom is free of the first order Doppler shift, assuming that the clock laser beam is aligned along the stable lattice and that the optical phase of the lattice and the clock beam is referenced to the same mirror. Mechanical noise, which can make the cavity unstable with respect to atoms, is removed by using the Doppler cancellation technique (see section 3.5). The second order Doppler shift related to the relativistic effects proportional to $v^2/(2c^2)$ is present, but it is estimated to be far below the 10^{-18} level [6].

2.6 Ultrahigh Resolution Spectroscopy

The ultra-narrow clock transition is the ultimate goal of the atomic clocks. Thanks to the Lamb-Dicke and well-resolved sidebands regimes, the pure electronic excitation is minimally perturbed. At the low saturation limit (below unity) the amplitude of sidebands are smaller at least by factor of 10. As a result of the clock interrogation, the absorption signal is Rabi-shaped. An example of the observed resonance is shown in figure 2.6.5. For negligible broadening effects, the linewidth of the absorption line is Fourier limited by interrogation time, itself limited by the coherence time of the probe ultra-stable laser. But the phase coherent signal, generated by ultra stable laser, should be longer than time of the single clock interrogation and it extends over several spectroscopy probings. Longer coherence times allow to obtain narrower resonances. Currently, observed resonances

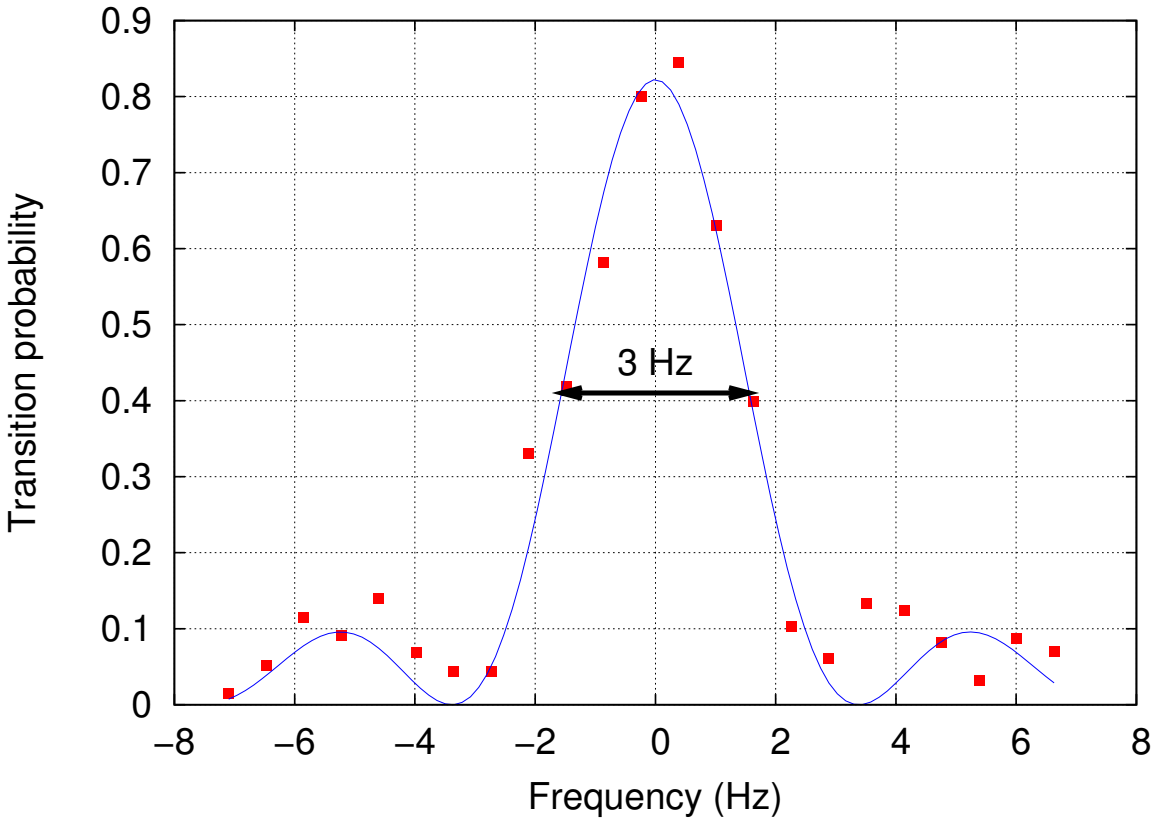

Figure 2.6.5. Rabi spectroscopy of the $^1S_0$-$^3P_0$ clock transition of the ^{87}Sr atoms for probe time of 250 ms. The width of the resonance is Fourier-limited.

have linewidth at sub-Hz level by using state-of-the-art laser [119]. But recent progress in ultra-stable lasers pushed forward the linewidth of the atomic spectrum [22]. The stability of cryogenic-stabilized Fabry-Pérot cavities is thermal noise limited at 4×10^{-17} with a coherence time up to 55 s. The linewidth of the laser can be then as small as sub-mHz level, which is comparable with predicted atomic linewidth.

CHAPTER 3

CLOCK OPERATION

SYRTE is one of the first institution where optical frequency standards have been developed as a future definition of the SI second. As the result of all the efforts, there are currently at SYRTE two ^{87}Sr clocks which are fully operational - Sr2 and SrB. SrB is the updated version of Sr1 version of the clock. In this chapter, we will focus on experimental details of the Sr2 clock not only because that I have pleasure to work with it but also because Sr2 has not been described since 2010. Sr2 was built by Jérôme Lodewyck, Arnaud Lecallier, Luca Lorini and Michał Zawada.

Clocks work in cycles because atoms are expelled from the trap during the fluorescent detection. Therefore, after each detection, a new atomic ensemble must be prepared in the trap for the next cycle. The typical cycle of Sr2 clock is shown in figure 3.0.1 and it is composed of the main parts: cooling, state preparation, interrogation and detection. The total time of the cycle is 800 ms with 200 ms for the clock interrogation time. In parallel to the first stage cooling, which employs the ^{1}S$_0$-^{1}P$_1$ transition, atoms are collected in the dipole potential. The temperature of trapped atoms in the lattice direction is proportional to the trap depth during the loading time 2500 E_r: $T_x = U_0/k_B \approx 300$ μK. The Doppler broadening for this temperature is at sub-MHz level, which makes hard any observation of ultra-narrow transition. To reduce broadening effects, it is necessary to quantize motional state of trapped atoms in the Lamb-Dicke regime.

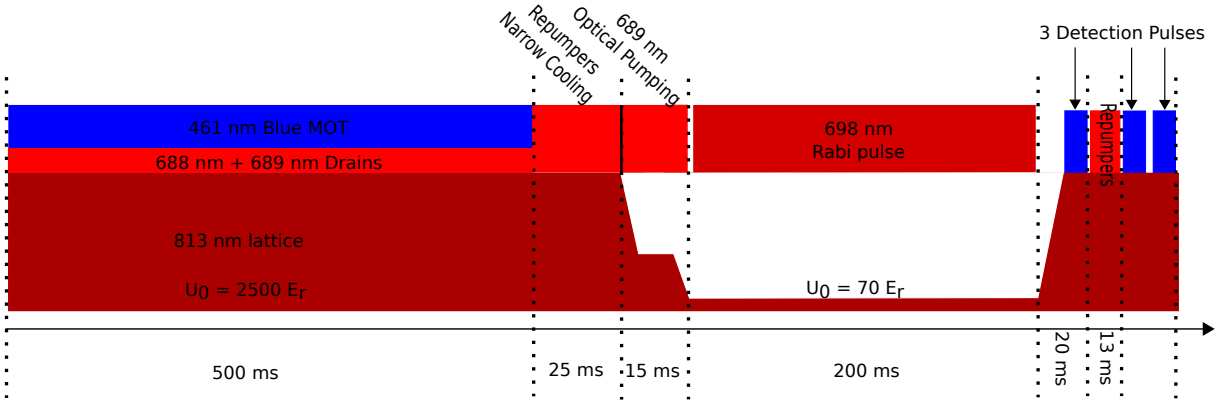

Figure 3.0.1. The time sequence of the Sr2 clock at SYRTE. Timings of following parts of the cycle can be slightly different. The total time of the sequence is smaller than 800 ms.

The chapter is organized as follows. Because the theoretical description of the dipole

potential and the clock spectroscopy is already described in chapter 2, we focus only on the experimental realization of the clock operation. The first section describes the first stage cooling and trapping methods. The next sections are focused on the mechanism of loading atoms to the dipole trap, the so-called «atomic drain», and laser systems which generate the lattice dipole potential. Finally, the state preparation and detection will be shown.

3.1 Cooling and Trapping Sr Atoms

To obtain ultra-cold Sr atoms, we need to heat them up to temperature 500 °C - 600 °C in an effusive oven, due to the low vapor pressure of Sr. The hot atomic flux (10^{12} atoms/s) is cooled down by using the $^1S_0 - ^1P_1$ transition at 461 nm. In the first step, atoms are cooled in a Zeeman slower in order to be trapped in a 3D magneto-optical (MOT). The cooling transition with linewidth $\Gamma = 2\pi \cdot 32$ MHz is fully allowed by electric dipole selection rules and guarantees efficient cooling of atoms to a Doppler limit of $T_{Dopp} = \frac{\hbar\Gamma}{2k_B} = 720\ \mu$K, where $\hbar$ and k_B are the Planck's and Boltzmann's constants respectively. In practical realization, the obtained temperatures are higher - a few mK due to the extra-heating mechanism, induced by transverse spatial intensity fluctuations of the optical molasses [120]. To generate the 461 nm light, a doubling ring cavity with PPKTP crystal (periodically poled potassium titanyl phosphate) is used. An infrared beam at 922 nm is amplified by a tapered amplifier (TA) before the cavity. The injection beam is provided to the TA from the SrB system. The laser system is locked to the $^1S_0 - ^1P_1$ transition via spectroscopy in an independent Sr oven with a feedback loop to the 922 nm master laser. The cavity is digitally locked by using a RedPitaya (FPGA - field-programmable gate array). We can obtain 250-350 mW of optical power from 1 W of infrared light. Then the output beam is divided on the deflection, MOT and Zeeman beams. The general scheme of the distribution of blue beams is shown in figure 3.1.2.

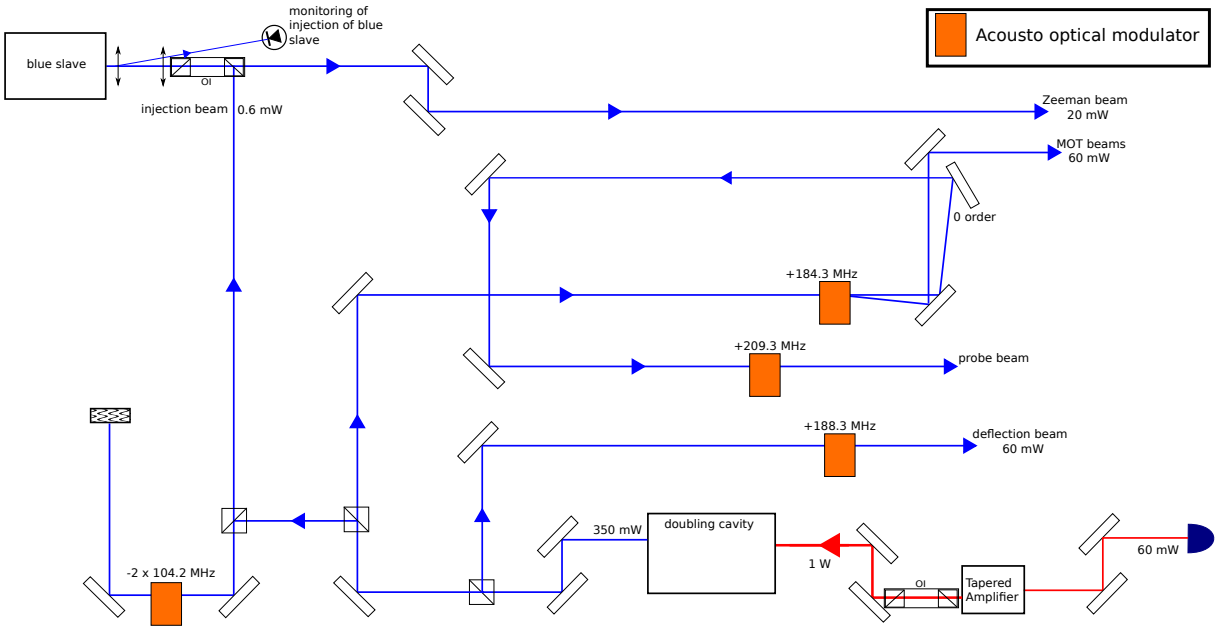

Figure 3.1.2. The distribution of blue beams.

In a typical ultra-cold experiment, the source of atoms - the effusive oven - is usually

in the view axis of the magneto-optical trap. In our system, which is developed for metrological applications, we need to suppress collisions with background hot atoms and hide the hottest point of black body radiation (BBR) which trapped atoms can see. We have implemented optical beams on the output of the oven which deflect and collimate the hot atomic flux in 2 directions, in such a way that the oven and the trapped atoms are not aligned. The angle between the axis of the output of the oven and the axis of the Zeeman laser beam is around 30 mrad. By using deflection beams we can trap up to 4 times more atoms than without these beams [29].

When I started my PhD, the laser setup for the first stage blue cooling was already in place. However, I brought two significant additions : a laser diode at 461 nm injection locked to the master laser, and re-designed coils for the Zeeman slower.

In the past to generate 461 nm, the doubling cavity was employed only. For well aligned cavity, the output power was enough in the short term but any degradation of the output power limited the performance of the clock over longer operation. Therefore, to have a bit of margin of optical power in the longer clock operation, we decided to employ a new laser diode, which is currently commercially available. The laser diode with peak wavelength at 460 nm, provided by NICHIA corporation (type NDB4216E), has a maximum optical output power CW of 100 mW with a threshold current of 30 mA. In our setup, the diode works in the laser injection locking scheme. The blue diode is injected by detuned beam from the doubling cavity (see figure 3.1.2). In such way we can save a lot of optical power. In the new setup, only 2-3 mW of optical power is sent to a double pass acousto-optical modulator because to inject the blue slave, 0.5 mW of optical power is necessary. The injection current depends on the temperature of the diode, therefore

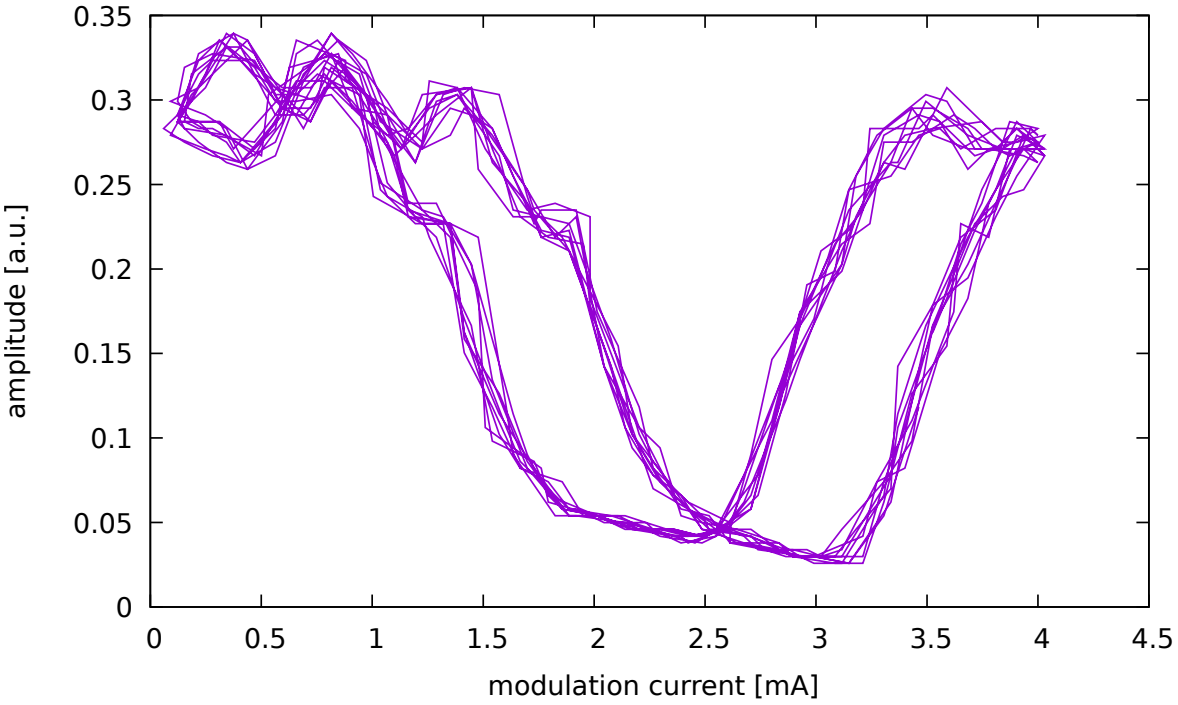

Figure 3.1.3. Plateau of the injected blue diode. The injection point is negative.

it is possible to have only few possible operational points. At the beginning, to lock the slave diode, we made a beat note between the injected beam (output) and injecting beam (intput) but we realized that the shape of the output beam changes, when it is injected

properly. Therefore, this feature is employed in order to discriminate the frequency of the diode. To monitor the status of the injection, a photodiode is inserted in a spot, in which a change of power can be distinguished, which corresponds to the change of the shape of the beam. To observe the quality of the injection, the current of the diode is scanned and a characteristic plateau is visible, as shown in figure 3.1.3. In our case, the plateau is negative, because at the injection point the output beam changes the shape in such way that the monitor photodiode can see a smaller signal. In the stable thermal conditions the diode can stay at the injection point for at most a few hours. For long operation of the clock (longer than a few hours), automatic re-locking system has been implemented to tune the diode current. The system is based on an Arduino micro-controller and it automatically re-scans the current of the diode, when the amplitude of the signal differs more than 10% from the injected value. To have a visible plateau, no more than 600 μW of injection power is necessary. Normally, the diode works at injection point with output optical power around 24 mW, which corresponds to the saturated value of the MOT fluorescent signal, as shown in figure 3.1.4. With the slave diode set-up, it is possible

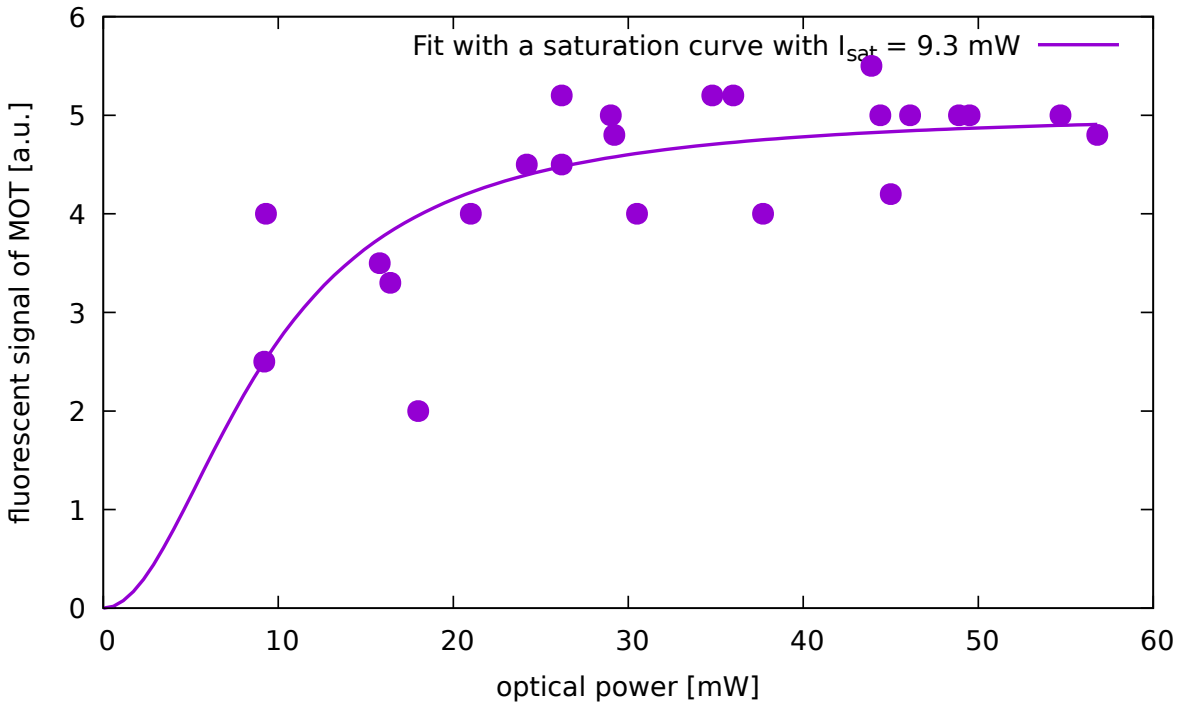

Figure 3.1.4. MOT fluorescent signal as a function of the optical power in the Zeeman slowing beam. To the experimental points, function $f(x) = Ab^2/(1+b^2)$ is fitted, where $b = x/I_{sat}$. For output power larger than 20 mW the fluorescent signal does not change a lot.

to have a 2 times larger MOT than before and to reach optimal power for other beams, which was not possible in the past. Currently, there is 60 mW of optical power in the deflection and MOT beams (detuned in the right order) with even some margin of power.

Moreover, we changed the design of the Zeeman slower coils. The previous Zeeman slower consumed a lot of power and therefore emitted a lot of heat to the surrounding vacuum elements. In normal working conditions, its temperature was around 60°C with water cooling applied. Therefore, one side of vacuum chamber had a temperature significantly higher than the opposite and it was hard to reach high temperature homogeneity of the vacuum components (spread less than 1 K), which is important to have a precise estimation of BBR shift. Before the replacement of the old Zeeman slower, the magnetic

field of the new Zeeman slower was verified with the theoretical model as shown in figure 3.1.5. The new Zeeman slower does not heat up as previous coils. It consumes 10 times

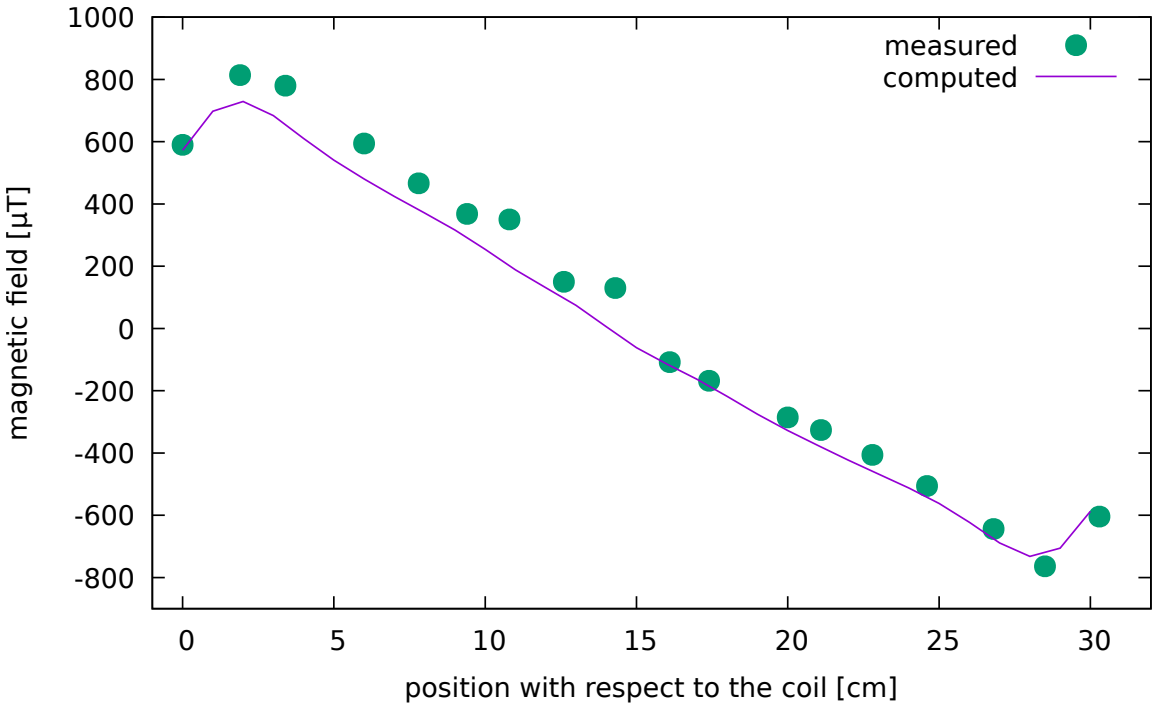

Figure 3.1.5. The longitudinal profile of the magnetic field induced by new Zeeman slower and the theoretical simulation. The position '0 cm' corresponds to position where hot atoms enter the Zeeman slower to be cooled down.

less power and the applied water cooling is sufficient that the temperature of the vacuum system is around ambient temperature and the vacuum system can achieve higher temperature homogeneity.

3.2 Lattice Laser Systems

The lattice dipole potential for both clocks is provided by a Titanium-Sapphire (TiSa) laser (MSquared SolsTiS), which generates more than 2 W of output power at the magic frequency at 813 nm. The TiSa crystal is pumped by a Verdi laser at 532 nm (provided by Coherent) with 10 W output power. Optionally, the Sr2 clock can still work with the previous set-up, based on semiconductor sources: an external cavity diode laser (ECDL) 813 master, an injected slave diode and a tapered amplifier (TA). The general view of both laser systems is shown in figure 3.2.6. Nevertheless that possibility, only the TiSa laser is used only in daily clock operation due to the incoherent background spectrum of the semiconductor sources. But in specific situations, both systems can be employed separately or jointly on the Sr2 clock by a flip-flop mirror, which allows us to combine the TiSa beam with the TA beam and perform, for instance, differential measurement of the laser spectral purity by using atoms. chapter 7 is dedicated to this comparison. In order to tune the frequency of the lattice laser to the magic wavelength, the TiSa laser is frequency offset locked to the 813 ECDL master laser. The 813 master laser is referenced to the $^1S_0$-$^3P_1$ transition via a transfer cavity. Then all lasers are locked to an absolute reference and regular measurements of the lattice light shift. Both beams (separated

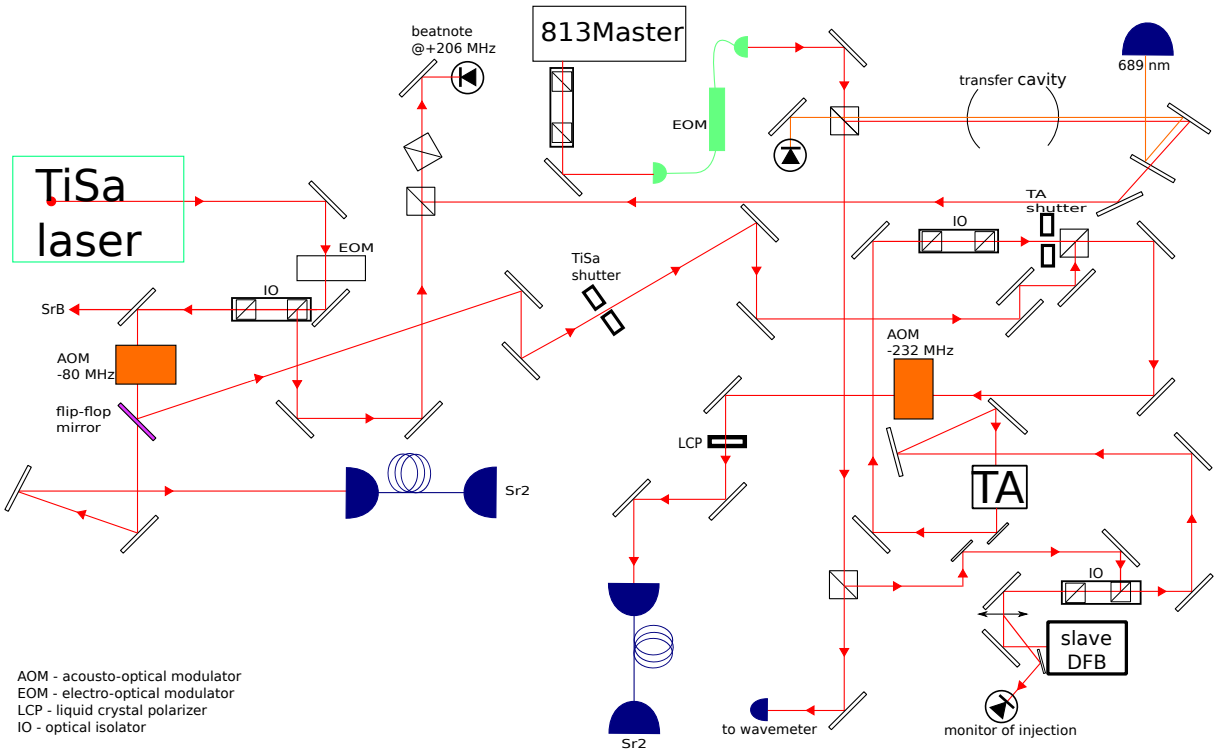

Figure 3.2.6. The laser systems which provides the lattice potential for the Sr2 clock.

or combined) are transferred to the Sr2 clock by a photonic crystal fiber, which due to its large mode area suppresses possible Brillouin scattering. The lattice is built-up in a Fabry-Perot cavity with finesse $\mathcal{F} = 120$, which enhances the optical power by factor 40. The waist of the lattice beam is localized at the center of the atomic sample and can induce the trap depth up to 2500 E_r (for TiSa laser). The length of the cavity is actively stabilized by the Pound-Drever-Hall method. Moreover, an intra-cavity power stabilization is implemented in order to actively control the trap depth during the clock cycle.

3.3 Loading Atoms in the Dipole Trap

Cold atoms, collected in the MOT, must be transferred to the dipole trap. At SYRTE, the loading technique, the so-called «atomic drain» is used. It is based on pumping the atoms to the metastable states $^3P_0$ and $^3P_2$ via the $^1S_0$–$^3P_1$ (689 nm) and $^3P_1$-$^3S_1$ (688 nm) transitions. The relevant transitions are depicted in figure figure 3.3.7. The technique is in contrast to all other laboratories, which employ the second stage MOT based on the narrow $^1S_0$-$^3P_1$ transition as a second stage cooling (the so-called «red-MOT»). The atomic drain method has several advantages. The first one, very low power (4 μW for 689 nm and 20 μW for 688 nm) is necessary to implement this method. The red-MOT needs around 20 mW of power. The 689 nm laser in the atomic drain method requires only one frequency as opposed to the red-MOT, where, in order to effectively collect atoms, trapping and stirring frequencies are necessary due to the large hyperfine splitting of the $^3P_1$ state. Moreover, the red-MOT cooling and trapping take more time. With the atomic drain method, the loading to the dipole trap is performed in parallel to the first stage blue cooling and only the coldest atoms of the Maxwell distribution

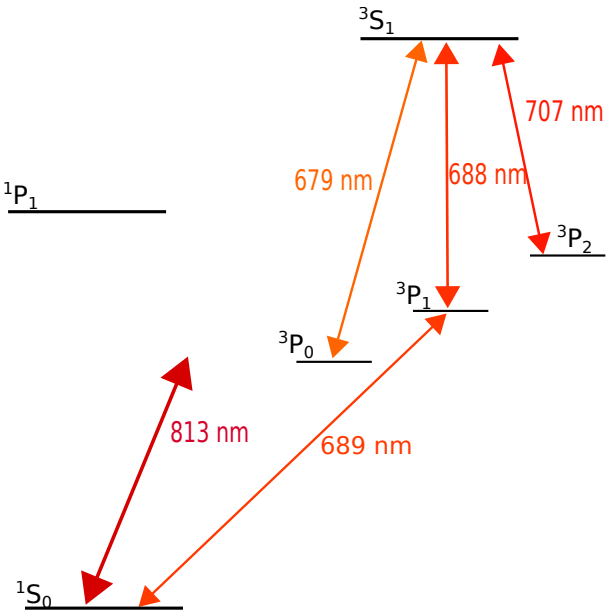

Figure 3.3.7. Relevant transitions used in the atomic drain method.

are transferred to the dipole trap, where they are cooled by short second stage cooling (section 3.4). Finally, because the blue MOT is ten times bigger than the red-MOT, the atoms are spread in more lattice sites and therefore, the atomic density in the lattice potential is low (1-2 atoms per site), the interaction between atoms are small and the density shift of the clock transition is reduced. On the other hand, the atomic drain method employs one extra laser at 688 nm.

As mentioned before, atoms are loaded to the dipole potential during the blue MOT phase. At this time, the trap depth is set to its maximum value in order to capture as many atoms as possible. Two drain lasers are tuned to the $^1S_0$–$^3P_1$ (689 nm) and $^3P_1$-$^3S_1$ (688 nm) transitions, overlapped and tightly focused at the center of the dipole trap. When cold enough atoms pass through the region of the dipole potential, they are transferred by the drain lasers to the metastable $^3P_0$ and $^3P_2$ states via the $^3S_1$ state. In these states, atoms can be trapped in the dipole potential and they become invisible to the blue cooling transition. The MOT dynamics does not kick out them from the dipole trap. The transfer process is repeated, as the cloud of cold atoms thermalizes and new cold atoms are produced in the MOT. To have efficient transfer, the drain lasers operate at the nominal power 4 μW for 689 nm laser and at least 20 μW for 688 nm laser. Both lasers are locked to the corresponding atomic transitions in an independent Sr oven : the 689 nm laser via saturation spectroscopy and 688 nm via absorption spectroscopy. The transfer process is finished with the end of the blue cooling stage. Then, atoms in the metastable states are repumped by using two repumper lasers : $^3P_0$–$^3S_1$ at 679 nm and $^3P_2$–$^3S_1$ at 707 nm during 15 ms. Atoms confined in the dipole potential take part in the further preparation process.

3.4 State Preparation

To cool atoms to the lower motional states, a second stage cooling is employed by using the intercombination $^1S_0$–$^3P_1$ transition. It is a narrow transition of linewidth $\Gamma = 2\pi \cdot 7.6$ kHz and photon recoil temperature limit of 460 nK [121]. Parallel to the

repumping lasers, a detuned 689 nm laser beam is applied. Along the direction of the atomic confinement of the lattice, sideband cooling is applied. In the transverse directions Doppler cooling is employed, because the motional sidebands are not resolved in these directions. After the red cooling, the temperature of the atoms is reduced to a few μK. Figure 3.4.8 shows the dependence of the temperature of the atoms with trap depth.

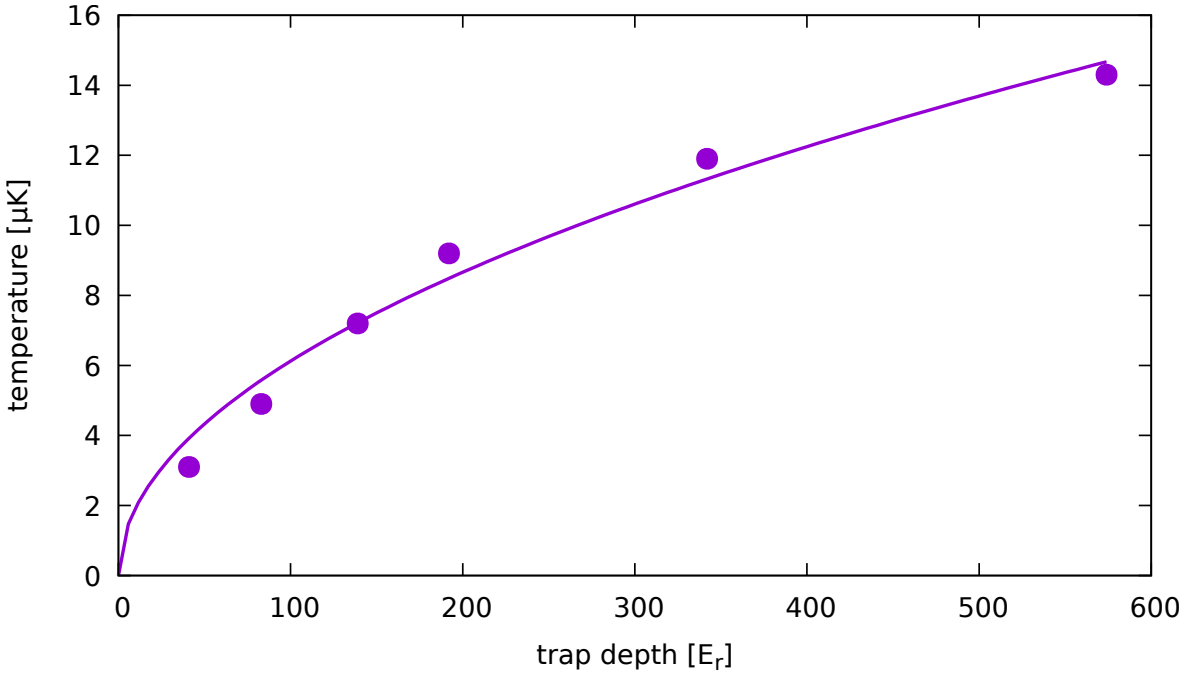

Figure 3.4.8. The temperature of the atoms in the dipole trap as a function of the trap depth. In the shallow trap, the temperature of the atoms is smaller, because only the coolest atoms can stay in the trap.

The frequency of the Sr transition is the average frequencies of the stretched Zeeman components. But atoms in the lattice are in random m_F sub-levels of the ground $^1S_0$ state. This is not a suitable ensemble of atoms to do high precision spectroscopy, because the frequency of m_F sub-levels depend differently on external fields [58]. Hyperfine interactions of states with the same total spin F cause that the $^3P_0$ state is not pure and g factor is not equal for both clock states. This causes that the line shape of the clock transition is broadened, which depends on the stability and the accuracy of the clock. Therefore, to perform the precise coherent clock interrogation of the atoms, all atoms are prepared in extreme spin $m_F = \pm 9/2$ states. In the presence of bias magnetic field, orthogonal to the axis of the lattice bias magnetic field, we resolve the Zeeman m_F sub-levels and optically pump atoms to extreme sub-levels $m_F = \pm 9/2$ of the ground $^1S_0$ state by using the intercombination transition at 689 nm and applying alternating σ^+ or σ^- polarized laser beam parallel with the direction of the magnetic field as shown in figure 3.4.9. The value of the magnetic field is larger (a few Gauss) than during the clock spectroscopy in order to have high efficiency of the optical pumping. To interleaving circular polarizations, the initial beam is divided into two parts with orthogonal linear polarization. Each beam has own AOM which drives the optimal frequency modulation. In the end, beams are combined back and go through a polarization-maintaining fiber. At the output, a quarter waveplate is installed to adjust the right circular polarization. The efficiency of the optical pumping (OP) weakly depends on the value of the bias field, the trap depth

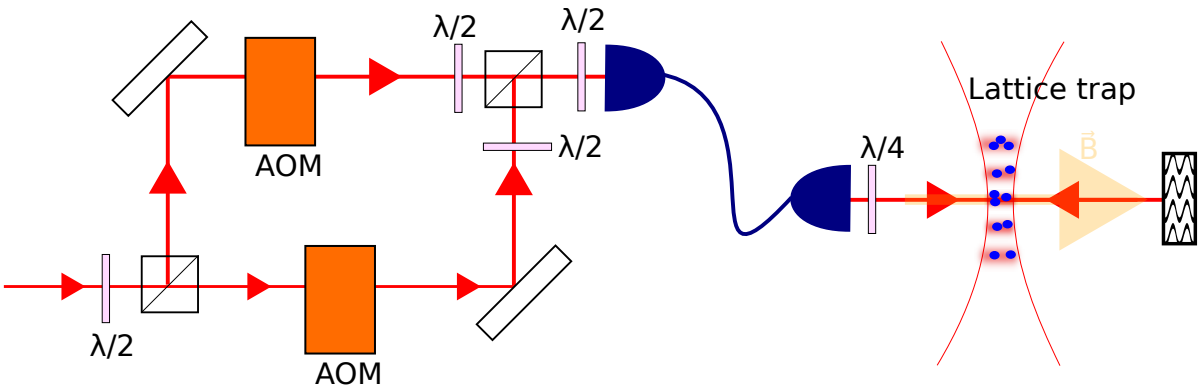

Figure 3.4.9. Scheme of optical pumping in Sr2. With two AOMs we can independently control the frequency and modulation amplitude of the laser beams to reach the optimum of clock resonance.

and modulation frequency that this these parameters were optimized to maximize the OP efficiency. For a given clock cycle, atoms are interrogated only in one sub-level. In the next cycle, the polarization of the laser beam is swapped and atoms are prepared in the opposite sub-level. Optical pumping takes 15 ms of clock cycle and 20 mW of the optical power. Most of problems with efficiency of optical pumping is related to the alignment of the beam in the science chamber and select of the right polarization.

3.5 Stabilization of the Clock Light

The phase of the clock laser beam is stabilized to reduce the impact of external perturbations for clock light and preserve an ultrahigh stable frequency reference to the interrogated atoms. This can be reached by implementing an active phase noise cancellation method, the so-called Doppler cancellation [122]. The principle of operation of this technique is shown on figure 3.5.10. The incoming laser beam with phase φ_{ref} is

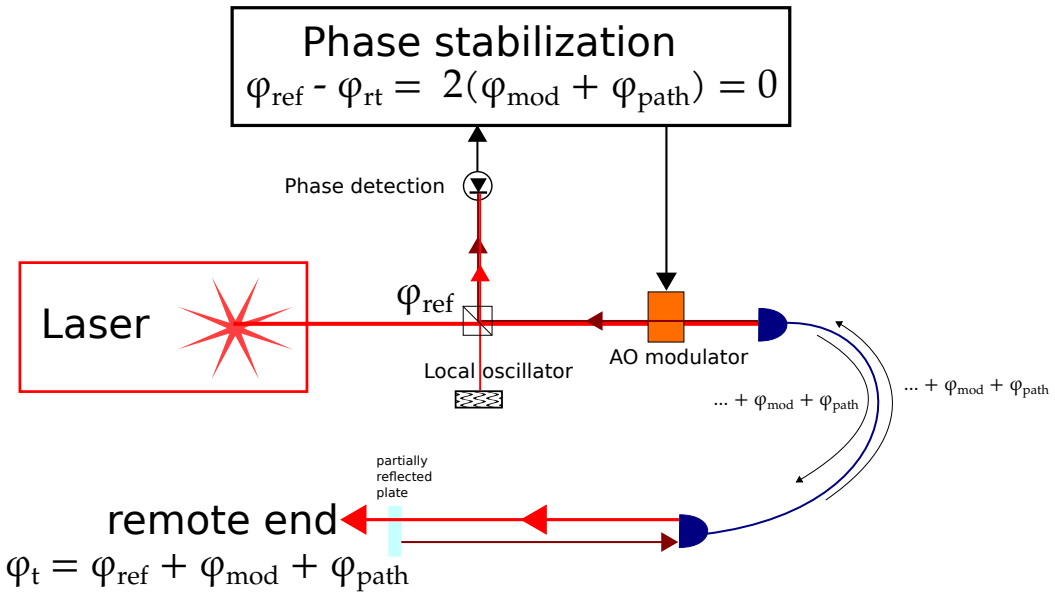

Figure 3.5.10. Actively compensation technique of the phase noise. The part of the light on the remote end is back reflected. A beat note between a local oscillator and backreflected light gives the error signal which feeds back an AO modulator.

modulated by an AO modulator. Through the optical path, the light accumulates the phase noise φ_{mod} and φ_{path} related with a modulation process and the path noise due to environmental fluctuations, respectively. At the remote end, the phase of the incident light is $\varphi_t = \varphi_{ref} + \varphi_{mod} + \varphi_{path}$. To actively compensate noise noise, a part of the light is back reflected and it makes round trip giving phase φ_{rt}. At the reference point, the phase difference between a local oscillator light and the round trip light is $\varphi_{ref} - \varphi_{rt} = 2(\varphi_{mod} + \varphi_{path})$. On the end, this phase difference is measured by a local heterodyne detection, and is canceled by a servo-loop acting on the frequency of the AOM. At no compensation conditions, the phase noise limits the clock stability at mid 10^{-16} level for a 10 m long fiber. Therefore, in our set-up the phase noise of each beam in clock distribution is actively compensated as the longest optical path as possible. For compensated clocks beams, the phase noise does not degrade the clock signal.

3.6 Clock Spectroscopy and Detection

To perform the final clock interrogation, the trap depth is reduced to around 70 E_r in order to have only the coldest atoms and the low frequency shift related with the presence of the trapping light. The magnetic field is adjusted to separate the extreme Zeeman sub-levels by 1 kHz. To interrogate the atoms a Rabi π pulse is applied with a time duration usually no longer than 200 ms. The clock beam with linear π polarization has a broad waist in order to illuminate all atoms homogeneously. We can reach a visible signal with maximum 0.8 contrast. The ultra-narrow laser is preliminarily stabilized to the high finesse cavity with finesse $\mathcal{F} = 20000$ and then is locked to very high finesse cavity with finesse $\mathcal{F} = 568000$. More details about the distribution of the clock laser is described in the section 5.4.

In the end of the cycle it is necessary to measure the result of the interrogation of the clock transition. On Sr2, the normal fluorescent detection method is applied, which is based on a probe beam tuned to the $^1S_0$–$^1P_1$ transition. The effects of the clock excitation are measured by taking 3 pictures with an EMCCD camera. The first picture is proportional to the number of atoms in the fundamental state (N_1). Before the second picture, the excited atoms are pumped back to the fundamental state by using a pair of repumpers 707 nm and 679 nm. Therefore, the second picture is proportional to the number of the excited atoms (N_2). The last picture takes the background signal (N_3). After each detection pulse, atoms in the $^1S_0$ state are expelled from the trap due to the high scattering rate of the $^1S_0$–$^1P_1$ transition. The transition probability for the clock excitation is obtained from the formula:

$$P = \frac{N_e}{N_e + N_f}, \tag{3.6.1}$$

where the net number of atoms in the excited state is $N_e = N_2 - N_3$ and the net number of atoms in the fundamental state is $N_f = N_1 - N_3$. In this way, the ratio does not depend on the fluctuations of the number of atoms.

CHAPTER 4
EVALUATION OF SYSTEMATIC EFFECTS

The frequency of the clock transition is affected by several effects which shift and perturb the «true» clock frequency. Thus, a careful evaluation of all systematic effects must be performed. The majority of effects arises from the interactions between trapped atoms and the electromagnetic field that surrounds the atoms. Thanks to the magic wavelength, the AC Stark shift, which would have the largest contribution to the accuracy budget, can be well suppressed, and additionally controlled by well-known theory [59,60]. However, the atoms experience also other electro-magnetic radiations. The blackbody radiation shift induced by the thermal environment around the atoms has been for a long time the main limitation to the accuracy budget. Now it is controlled with superior precision [6,48,123]. Moreover, the clock transition is shifted by the probe laser itself. The influence of static magnetic and electric fields must also be examined. The first order of Zeeman shift is cleverly canceled out by interleaving probing opposite Zeeman sub-levels. The second order of the Zeeman shift and the static electric field are accurately evaluated by magnetic and electric field measurements respectively. At current state-of-the-art, performance, the collision shift becomes relevant and its precise estimation is based on many-body calculations [83]. We need to consider the imperfection of the measurement process itself and servo data acquisition. Nowadays the best optical lattice clock realizes the optical frequency with the uncertainty at low 10^{-18} level [6, 48, 51].

4.1 The Zeeman Shifts

The first-order Zeeman shift is a result of the coupling of the fermion's nuclear spin with the magnetic field B. The existence of the hyperfine state mixing between the excited clock state $^3\mathrm{P}_0$ and other states with the same F number leads to a difference in the Landé factor between the fundamental and the excited states. For a π linear polarized, (with states $m_F = m'_F$), the difference of the energy of atomic levels is:

$$\Delta\nu_Z^{(1)} = -\frac{\mu_B \delta_g}{h} m_F B, \tag{4.1.1}$$

where μ_B is the Bohr magneton, δ_g the differential Landé factor. As it is described in the previous chapter, the magnetic field and optical pumping are applied to separate and prepare atoms in only the one of the extreme sub-level, because it is an easy way to cancel the first-order Zeeman shift. By interleaving interrogations with opposite spin states and

taking the average of frequencies of both Zeeman components, the first order Zeeman shift is canceled.

But using resolved sub-levels by applying external bias field, the second order shift $\Delta\nu_Z^{(2)}$ must be considered. The second order term proportional to B^2 is 4 orders of magnitude smaller than the first order. In contrast, it is related to the fact that clocks states have $J = 0$ so the level separated in energy by the fine structure splitting contributes significantly to the second order shift. The main contribution comes from excited clock state $^3\mathrm{P}_0$ and the closest level $^3\mathrm{P}_1$ because the fundamental state is separated from all other states by optical frequencies. The total second order shift can be approximated as follows:

$$\Delta\nu_Z^{(2)} \cong -\frac{2\mu_B^2}{3\Delta\nu_s h^2}B^2, \tag{4.1.2}$$

where the $h\Delta\nu_s$ is the energy separation between $^3\mathrm{P}_0$ and $^3\mathrm{P}_1$ states.

The calibration of the second order Zeeman shift is performed by applying different values of the magnetic field for both Zeeman sub-levels with respect to the linear Zeeman shift coefficient and with a quadratic fit of type $aB^2 + c$ to the experimental data. The quadratic coefficient a, measured in 2011, is -23.59(25) MHz/T^2 [59] which is in the good agreement with other Sr clocks [58, 67]. The uncertainty of the coefficient establishes the uncertainty of the Zeeman effect. The typical splitting between extreme sub-levels m_F is 2 kHz which corresponds to 100 μT of applied magnetic field. Since last June, the Zeeman splitting has been reduced to 1 kHz.

4.2 The Black Body Radiation Shift

The environment surrounding the interrogated atoms emits thermal radiation around room temperature (a few of ten of THz). This far detuned radiation causes a frequency shift, called the blackbody radiation shift. The shift is described as a power series of T^4, T^6 and T^8. The first static term $\Delta\nu_{stat}$ is proportional to the difference $\Delta\alpha$ between the static polarizabilities of both clock states and the mean thermal field of the environment radiation. It corresponds to 90% of the total BBR shift. The second term, $\Delta\nu_{dyn}$, is the dynamic correction to the static polarizability and it includes the frequency dependence of polarizabilities of all states through the BBR spectrum:

$$\Delta\nu_{BBR} = \Delta\nu_{stat}\left(\frac{T}{T_0}\right)^4 + \Delta\nu_{dyn}\left(\frac{T}{T_0}\right)^6 + \mathcal{O}\left(\frac{T}{T_0}\right)^8, \tag{4.2.3}$$

where $\Delta\nu_{stat} = -2.13013(6)$ Hz and $\Delta\nu_{dyn} = -147.6(23)$ mHz are the shifts at the temperature $T_0 = 300$ K [124]. This correction is applied in our clock.

The estimation of the BBR shift is based on the precise measurement of the thermal environment around the atoms. The temperature around the atoms is measured continuously by 6 calibrated pt100 sensors. The temperature of the science chamber is not homogeneous, mostly due to the heating of the MOT coils. Although, they are cooled, they dissipate heat and warm up the vacuum chamber. Therefore, sensors are spread in pairs in the hottest points - around each MOT coil - and coldest points - far away from coils - of the science chamber. The last pair is placed in the mid temperature points. The temperature of the chamber shows inhomogeneity as large as 0.9 K. Except the points where the temperature is measured, we do not have any other information about the temperature gradient in the chamber. We simply, but pessimistically assume that the

effective temperature is not larger or smaller than the extreme measured temperatures and it is equally distributed in this range. The associated uncertainty is $1/\sqrt{12}$ of the total spread, so it is equal to 0.26 K [47,125]. However, our vacuum chamber has two large view ports, one on each side of the atomic ensemble. Windows have larger emissivity than the metallic part of the chamber and occupy a large solid angle. Moreover, the measured temperature does not differ from the temperatures of mid points.

We need to include in the total BBR induced shift the fact that the atoms can see the hot effusive oven. Due to the implementation of the deflection beam, atoms do not share common sight axis with the oven. The distance between the source of hot atoms and the trap of cold atoms is 700 mm. Hot atoms are transferred via 5 mm diameter aperture. As in the case of the vacuum chamber, we do not have a precise model of potential reflections and the possible distribution of this radiation. We use a simple model that assumes the worst case scenario that atoms are covered by a sphere of 700 mm radius and emissivity 0.1[1] at room temperature. On its surface, we consider a small BBR source which has the same characteristics as the oven. The small source emits the thermal radiation which is uniformly reflected by the big sphere. Using this model the BBR shift in the center of the sphere is 10^{-17}, which we take as the uncertainty of the BBR shift induced by the hot oven. The model does not include that indirect emission of the BBR of the oven to the atoms is shielded. It takes into account only homogeneous emissivity of the solid angle from the atoms, which is additionally higher than assumed 0.1. Therefore this model overestimates the uncertainty of the shift.

To get 10^{-18} level of the uncertainty more sophisticated work must be done. Various groups in the world have different ideas. The first approach takes advantage of the strong dependence on temperature. Trapped atoms are interrogated in a special cryogenic chamber at 95 K. At this temperature, the 10^{-18} level of the uncertainty requires temperature sensors accurate at the 0.5 K level because of the BBR correction is a few mHz [48]. At room temperature, we need devices precise at mK level to measure temperatures. In the Yb clock experiment at NIST, the atoms are surrounded by a radiative enclosure which is composed of highly conductive radiative materials [123]. The enclosure is inserted in a high vacuum and several temperature sensors monitor its temperature. The system guarantees the high temperature uniformity. Moreover, enclosure internal surfaces are coated by high-emissivity carbon-nanotube paint which minimizes the influence of the BBR radiation outside the enclosure.

In the future at SYRTE, the approach similar to NIST will applied to control BBR shift at 10^{-18} level. A single vacuum chamber only will be employed. The chamber will be made of highly conductive materials to have high temperature uniformity.

4.3 The Lattice Light Shifts

In the previous chapter, we shown that the differential light-shift due to the present of the trapping light is as follows:

$$\hbar\Delta\omega = -\Delta\alpha(\omega)\left(\frac{\mathcal{E}}{2}\right)^2 - \Delta\alpha'(\omega)\left(\frac{\mathcal{E}}{2}\right)^4 + \mathcal{O}(\mathcal{E}^6). \tag{4.3.4}$$

[1]Emissivity is the ratio between the radiation emitted by a material and a black body with the same shape. Its value varies from 0 (perfect reflector) to 1 (ideal black body). It depends on the wavelength, the angle of incidence, the temperature, the nature of the material and its surface roughness.

The evaluation of lattice light-shift is based on a differential measurement of the clock frequency for various trap depths from 50 E_r to 1000 E_r. At the magic wavelength, hyperpolarizability effects, proportional to the square of the average trapping potential, are visible and the data are fitted to a parabola $f(U_0) = aU_0^2 + bU_0 + c$. The correction and the uncertainty of the light-shift at the normal clock operation (70 E_r) are taken from the parameters of the fit. However, based on only the single measurement the uncertainty of the coefficient a is rather large, which leads to a large uncertainty on the extrapolation to zero trap depth. Over years, repeated lattice light-shift measurements show that the value of a is fully reproducible for different lattice sources, atomic densities and the lattice polarizations. Therefore, the value of $a = (0.457 \pm 0.066)\mu\text{Hz}/E_r^2$ taken to extrapolate the lattice light-shift at zero trap depth (figure 4.3.1), is fixed at the average value, which allows us to decrease the associated uncertainty. The typical value of the correction and uncertainty are at low 10^{-17} level (the accuracy budget is at the end of the chapter). During the last campaign in June 2017, the Sr2 clock operated with the trap depth at 25 E_r and the associated uncertainty goes down to 3×10^{-18}. We observed also the additional light-shift due to the incoherence of the background spectrum of the semiconductor sources. This shift depends on the given tapered amplifier chip and it changes with the aging of the chip. To avoid this problem, we resigned from using semiconductor sources, and for the measurements described in the next chapters we use a Titanium Sapphire (TiSa) laser. Nevertheless, we investigated the problem, and the separated chapter 7 is dedicated to describe the light-shift that arises from the spectrum background.

4.3.1 The Scalar and Tensor Shifts

In the previous chapter, we have shown that the dipole polarizability $\alpha(\omega)$ can be split in three terms: scalar α_s, vector α_v and tensor α_t. The polarizability depends on the trap polarization, therefore, the evaluation of the clock accuracy needs to include this dependence. To be more adapted to the experimental conditions, we define the trap depth $U_0 = \alpha_s|\mathcal{E}/2|^2$ and introduce the differential $\Delta\kappa^{s,t}$ coefficients:

$$\Delta\kappa^s = -\frac{1}{h}\frac{\Delta\alpha_s}{\alpha_s}, \tag{4.3.5}$$

$$\Delta\kappa^t = -\frac{\Delta\alpha_t}{\alpha_s}\frac{1}{h}\frac{1}{2F(2F-1)}, \tag{4.3.6}$$

where the $\Delta\kappa^{s,t} = \kappa^{s,t}(^3P_0) - \kappa^{s,t}(^3S_0)$. Now, we consider both scalar $\Delta\kappa^s$ and tensor $\Delta\kappa^t$ coefficients, because they depend linearly on the average trap potential:

$$\Delta\nu^{E1} = (\Delta\kappa^s + \beta\Delta\kappa^t)U_0. \tag{4.3.7}$$

The determination of their values is based on the observation of the frequency transition in one clock, on the trap depth as a function of $\beta = (3|\vec{\epsilon}\cdot\vec{e}_Z|^2 - 1)(3m_F^2 - F(F+1))$, where $\vec{e}_Z$ is the vector unit along the quantization axis and $\vec{\epsilon}$ is the polarization of the trapping light. The second clock works as the reference. The average trap depth U_0 is determined from motional sidebands which give the longitudinal and transverse temperature of the trapped atoms. Assuming that the Zeeman shift is larger than vector and tensor shift, β can be changed by the orientation of the quantization axis defined by the magnetic field $\vec{e}_Z$ or the linear polarization of eigen-modes of the lattice cavity ϵ, probing different Zeeman

stretched states $m_F = \{-7/2, 7/2\}, \{-9/2, 9/2\}$. $\Delta\kappa^s = 0$ gives the «conventional» magic wavelength, but due to the presence of the tensor component $\Delta\kappa^t$ we need to find the «operational» magic wavelength for which the sum of $\Delta\kappa^s + \Delta\kappa^t = 0$. Naturally, we can vanish $\Delta\kappa^t$ by setting $\beta = 0$. For this we need to find the right «magic» angle between $\vec{\epsilon}$ and $\vec{e}_Z$ for which the term $3|\vec{\epsilon}\cdot\vec{e}_Z|^2 - 1 = 0$. But in the normal clock operation we rather avoid that configuration. The «magic» angle is around 54°. Due to the high value of the derivative, the «magic» angle introduces the high sensitivity on the fluctuation of the polarization of the lattice cavity, what is potentially hard to control. Therefore, we set the angle such that $\cos^2[\angle(\epsilon; \vec{e}_Z)] = 1$, where the derivative is minimum. Then we detune the «conventional» magic wavelength in such a way that the total value of $\Delta\kappa^s + \beta\Delta\kappa^t = 0$ and we obtain the «operational» magic wavelength.

In Sr2 the magic wavelength is detuned by -268 MHz to balance scalar and tensor components. The determination of the values of coefficients $\Delta\kappa^s$, $\Delta\kappa^t$ and magic wavelength ν_{magic} is valuable. The measurements performed over the years show the consistent results [59, 60]:

$$\begin{aligned}\frac{\partial\Delta\kappa^s}{\partial\nu_{latt}} &= (-15.5 \pm 1.1)\ \mu\text{Hz/E}_\text{r}/\text{MHz},\\ \Delta\kappa^t &= (-57.7 \pm 2.3)\ \mu\text{Hz/E}_\text{r},\\ \nu^{\beta=0}_{\text{magic}} &= (368554725 \pm 3)\ \text{MHz}.\end{aligned}$$

4.3.2 The Vector Shift

In the similar fashion as in the previous subsection we introduce the differential $\Delta\kappa^v$ coefficient:

$$\Delta\kappa^v = -\frac{\Delta\alpha_v}{\alpha_s}\frac{1}{h}\frac{1}{2F}, \tag{4.3.8}$$

Then the vector component of the AC Stark shift is following:

$$\Delta\nu^v = (\Delta\kappa^v m_F \xi \vec{e}_k \cdot \vec{e}_B)U_0, \tag{4.3.9}$$

and due to the dependence on m_F, it can be interpreted as a fictitious magnetic field. The differential vector polarizability coefficient $\Delta\kappa^v$ is determined by measuring the Zeeman splitting ΔZ of $m_F = \pm 9/2$ clock states for various trap depths U_0 with circular polarization of the trapping light $|\xi| = 1$ and different orientation of the bias field $\vec{e}_B$. The value obtained in the ref [60] is:

$$|\Delta\kappa^v| = (0.22 \pm 0.05)\ \text{Hz/E}_\text{r}$$

In the normal clock operation, the vector shift does not shift the average clock frequency directly. Due to the odd dependence of $\Delta\kappa^v$ with m_F, the cancellation of the vector shift is performed in the same way as the first order Zeeman shift by interleaving interrogation extreme clock resonances. Moreover, with the linear polarization, $\vec{e}_k \cdot \vec{e}_B$ is close to zero and the vector shift is reduced.

4.3.3 Hyperpolarizability

The hyperpolarizability is the second order light-shift proportional to U_0^2. The measurement of the hyperpolarizability coefficient is performed by measuring the clock frequency for different lattice trap depths and polarizations - up to 2500 E_r - averaged long

time. The curvature of these measurements for a given polarization is shown in figure 4.3.1. The measurement is repeated for various polarizations. The obtained coefficients

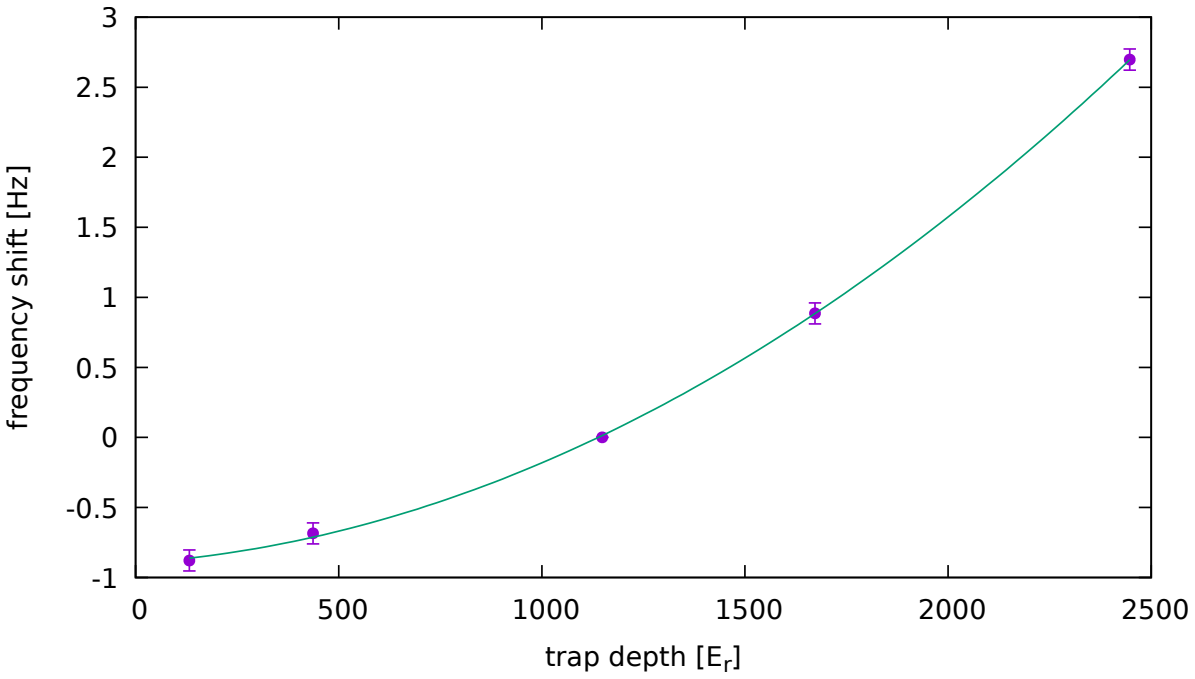

Figure 4.3.1. The typical light shift measurement when the hyperpolarizability effect is visible. The trap depth $U \approx 1200\ E_r$ is used as a reference.

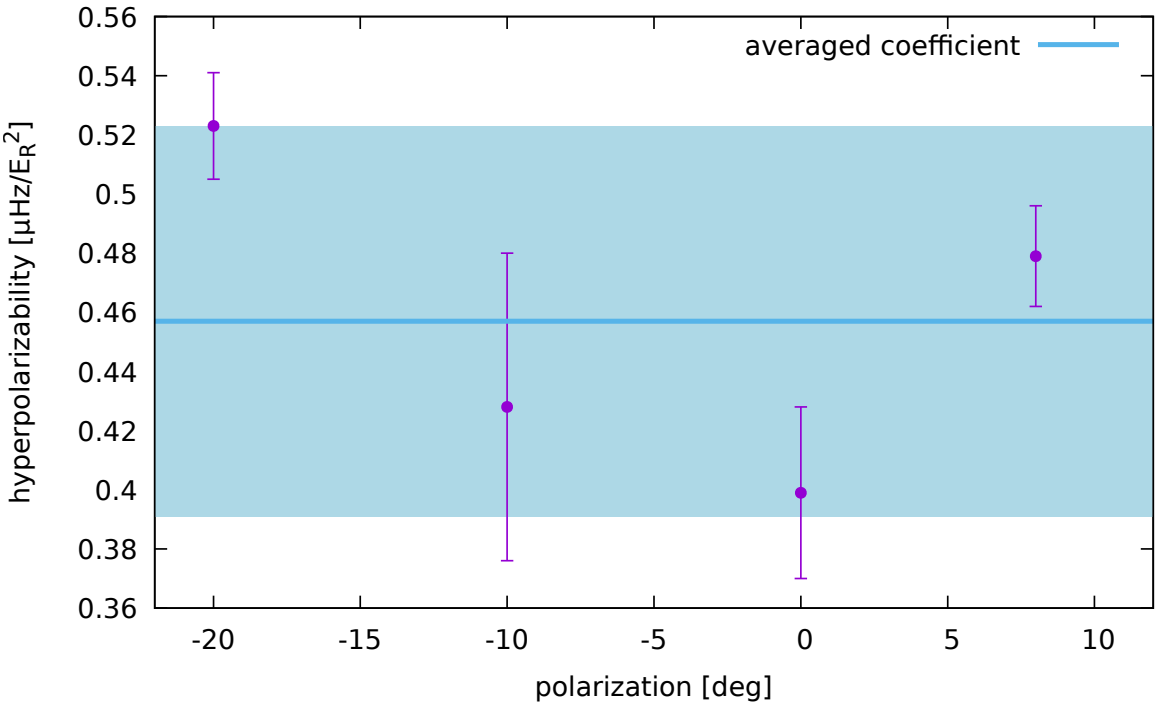

Figure 4.3.2. The hyperpolarizability coefficient for various polarization of the trapping light. The light blue area represents the uncertainty of the averaged value.

as a function of the polarization is shown in figure 4.3.2. The averaged hyperpolarizability quadratic coefficient is $(0.457 \pm 0.066)\ \mu\text{Hz}/E_r^2$.

4.4 The Density Shift

In contrast to ion clocks in OLCs, several thousands of atoms can be interrogated simultaneously, which improves the clock stability. But atoms stored in the trap can interact with each other due to the high atomic density and long coherence times, and therefore can induce an interaction-frequency shift. For ultracold fermions, s-wave collisions, which corresponds to head on collisions, are forbidden by the Pauli exclusion principle. But the inhomogeneous optical excitations cause that an ensemble of fermions becomes distinguishable, and then, allow for s-wave collisions and density-related frequency shift. Nevertheless, for a homogeneous enough clock excitation the s-wave collisions are well suppressed. The higher, p-waves inelastic collisions are suppressed by the thermal energy of the atoms, but are not forbidden. In the high density regime (about 20 atoms per site), atoms reach the strong interaction regime and a density related frequency shift at 10^{-16} level can be induced [82, 126]. With decreased Rabi frequency the number of inelastic collisions should increase and it is possible to determine the loss rate coefficient. They were observed in Sr as well as in Yb clock but using different methods [127, 128].

At SYRTE we have performed experiments to evaluate the density shift. We adapted our experimental conditions to the theoretical model of the JILA group [82]. We assume that the density in the given lattice site has a Gaussian distribution:

$$n(\mathbf{r}) = \frac{N_{site}}{\pi^{3/2} L_x L_y L_z} \exp\left(- \frac{x^2}{L_x^2} - \frac{y^2}{L_y^2} - \frac{z^2}{L_z^2} \right), \tag{4.4.10}$$

where the N_{site} is the number of atoms in the given lattice site and $L_{x,y,z}$ are the $1/e$ lengths given by:

$$L_i = \sqrt{\frac{\hbar}{m\Omega_i}} \sqrt{2\langle n_j \rangle + 1}, \tag{4.4.11}$$

where $\Omega_{j=x,y,z}$ is the trap oscillation in the j direction and $\langle n_j \rangle$ is occupancy factor given by:

$$\langle n_j \rangle = \frac{1}{\exp(\frac{\hbar\Omega_j}{k_B T}) - 1}, \tag{4.4.12}$$

which can be interpreted as a interpolating factor between the high temperature limit ($k_B T > \hbar\Omega_j$) where atomic distribution is Gaussian and the low temperature limit ($k_B T \leq \hbar\Omega_j$), where atoms occupy mostly the ground state of the trap. The number of atoms in the given site N_{site} is estimated using Poissonian lattice filling model [82].

In our experiment, the typical conditions are as follow: $\nu_x = 120$ kHz, $\nu_{z,y} = 250$ Hz with temperatures $T_x = 4\ \mu$T and $T_{z,y} = 15\ \mu$K, the density per particle $\rho_{particle} = 1.4 \times 10^9$ cm^{-3} and the average atoms in the site is $\bar{N}_{site} \approx 1.9$ and the average site density $\bar{\rho}_{site} = 2.7 \times 10^9$ cm^{-3}. We can obtain such low site density, because in the atomic drain technique the transfer of atoms to the dipole trap is performed directly from the blue MOT, which is 10 times larger than, widely used, the red MOT. Therefore, the atoms occupy larger lattice volume. In the JILA experiment Sr1 clock with $\nu_x = 80$ kHz, $\nu_{z,y} = 450$ Hz and temperatures $T_{z,y,x} = 3\ \mu$K, achieves the strong interacting regime with $N_{site} \approx 23$, $\rho_{particle} = 1.7 \times 10^{10}$ cm^{-3}. The average site density $\bar{\rho}_{site} = 3.9 \times 10^{11}$ cm^{-3} is

145 larger than in our experiment. According to the model we should expect density shift at low 10^{-18}, beyond our current precision of measurement. Repeated measurements of interleaved clock operations at various atom number in the trap, shows consistent zero density shift with a statistical uncertainty of 8×10^{-18}. For confirmation, the theory and our observations, the new JILA's Sr clock - Sr2, whose the total accuracy budget is evaluated at 2×10^{-18} level [6], has similar average site density (3×10^9 cm^{-3}). The measured density shift is estimated $(-3.5 \pm 0.4) \times 10^{-18}$ [6].

4.5 The Probe Light AC Shift

Atoms not only experience the AC Stark from the dipole trap light but as well the probe clock beam, which is far detuned from the magic wavelength. The light shift induced by the probe clock laser itself is calculated by the well-predicted theory successfully applied to calculations of the magic wavelength. The shift is counted as a result of the difference of polarizabilities of the clock levels at the wavelength of clock laser. We assume that the pure π pulse interrogates the atoms with known light intensity $I = 50$ mW m^{-2}. The theory, which is based on the dynamic polarizability of clock states, gives that the clock transition is shifted by 0.4×10^{-18} with a conservative uncertainty of 0.4×10^{-18}. The probe light AC shift is small, because the applied optical power is small. In the future, when ultra-stable lasers reach coherence times longer than several seconds, the necessary power will be lower. For a 1 s interrogation time, the probe light shift should be in the low 10^{-20} based on the theoretical model.

The other groups estimate the probe light shift using experimental methods. At JILA for instance, the probe light shift is determined by interrogating the atoms with two different durations of π pulses: 20 ms and 180 ms. Modulation of the intensity of clock beam gives the linear behavior of the probe light shift. For extrapolation to the π pulse with 1 s time duration the shift is $(-3.2 \pm 1.7) \times 10^{-20}$ [6] which is consistent with theory model used above.

The situation is a bit different for the bosonic isotope ^{88}Sr. The true $J = 0 \rightarrow J = 0$ clock transition is completely forbidden to all orders of single photon excitations because in bosonic Sr there is no hyperfine mixing of states. Therefore, the clock interrogation in ^{88}Sr is possible only in the presence of a supplementary coupling magnetic field. Due to the extremely narrow clock linewidth (lifetime 1000 years [58]), the power necessary to interrogate the atoms is much higher, 400 mW cm^{-2}, than in fermionic Sr clock and the related light shift is several of Hz with applied B field 2.43 mT [89]. Obviously, it is possible to reduce the optical power of the interrogating pulse by applying larger coupling magnetic field, but then we need to balance between the probe light shift and the second order Zeeman shift. A good option for the bosonic optical clocks can be a method, which actively cancels the probe light shift [129]. The interrogation scheme is implemented in Yb^+ ion clocks based on the hyper-Ramsey method with time-separated pulses with different durations, frequencies and phases. This method suppresses the probe shift and the associated uncertainty by 2 to 4 orders of magnitude in comparison with the normal Rabi or Ramsey interrogation.

4.6 The Line Pulling Shift

The line pulling shift is a result of the presence of the residual population in other $\pm 7/2$ m_F components which can change the shape of the resonance background and then shift the maximum of the unperturbed clock line. We can remove completely all residual sub-levels by applying the so-called cleaning pulse before the main interrogation clocks pulse. After optical pumping, a short clock pulse (at proper Rabi amplitude) excites atoms in $m_F = \pm 9/2$ to the $^3P_0$ clock state. Next, a short blue pulse (at 461 nm) is applied to clean all residuals Zeeman sub-states. In the end, the main interrogation clock pulse transfers atoms back to the fundamental state, giving inverted resonance. In Sr2 the resonance amplitude is not higher than 0.7, which can suggest that some parts of atoms are not pumped to extreme Zeeman sublevels. But using this method we checked, that the contrast of the resonance reaches a value close to 100% (the residuals come from the coherence time of the laser) which means that there is no problem with optical pumping. The cleaning pulse is used from time to time and it is not integral part of the usual clock sequence, because any extension in the sequence degrades the clock stability. Also, in the particular case of an incorporated cleaning pulse, the clock is less robust for unattended operation. Nevertheless, in a situation where the line pulling effect limits the clock accuracy, the cleaning pulse can be used. On the other hand, we can suppress the line pulling by increasing the separation between neighboring Zeeman sub-levels. But applying larger magnetic field usually increases the uncertainty of the quadratic Zeeman shift. Therefore, some compromise between the line pulling and quadratic Zeeman shift must be found. We simply assume that because of difficult with OP efficiency, one of the $\pm 7/2$ m_F sub-level is larger than opposite counterpart. Then, we use a simple model of Rabi resonance (9/2 sublevel), which is perturbed by another, detuned Rabi resonance (7/2 sublevel) with excited fraction of 10%. The sum of them corresponds to the total

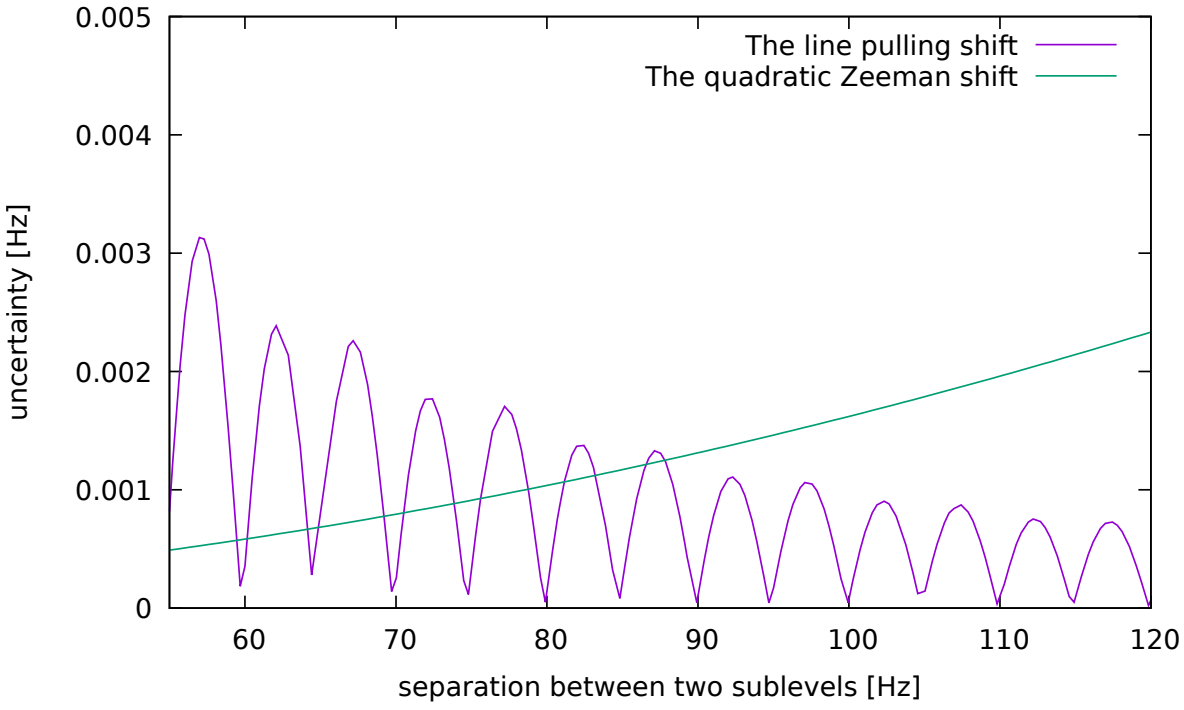

Figure 4.6.3. The uncertainty due the quadratic Zeeman shift and the line pulling as a function of separation between neighboring Zeeman sublevels.

observable resonance. As the uncertainty we take the value of the frequency shift due to the presence of the second resonance. Uncertainties of the quadratic Zeeman shift and the line pulling are shown in figure 4.6.3. For separation of 90 Hz between neighboring Zeeman sub-levels, the cross point for both uncertainties is around 0.0015 Hz which gives fractional shift 4×10^{-18} shift for both quadratic Zeeman and the line pulling shifts. So far we have worked with a separation two times larger.

As the other groups, we take into account not only the pure π excitations but also possible weak σ-transitions due to the imperfect alignment of the clock beam to the quantization axis. Then, the line pulling shift is described as a three level scheme with coherent driven π and σ transitions. The upper bound limit obtained from time dependent Schrödinger equation is 2×10^{-19} [47].

4.7 The Background Gas Collision Shift

Although atoms in the dipole trap are well confined, they can collide with the hot vacuum background gas and induce a frequency shift due to van der Waals interactions. We expect that for a higher vacuum, the lifetime of atoms in the trap should be longer. In ultra-high vacuum, the largest fraction of the background gas is hydrogen, but we have not performed any measurement in this direction due to the fact that the coefficients for van der Vaals coefficients have similar value. The background gas collision shift is estimated by using the procedure described in ref [130]. Trapped cold atoms, which collide due to the long-range interactions with room-temperature atoms, become too hot and go away from the trap and in general are not detected in the clock cycle. However, this scattering process introduces a phase shift in the cold atomic ensemble. Despite that the paper [130] is dedicated to cesium atoms, we can adopt it to Sr. The combination of the observed

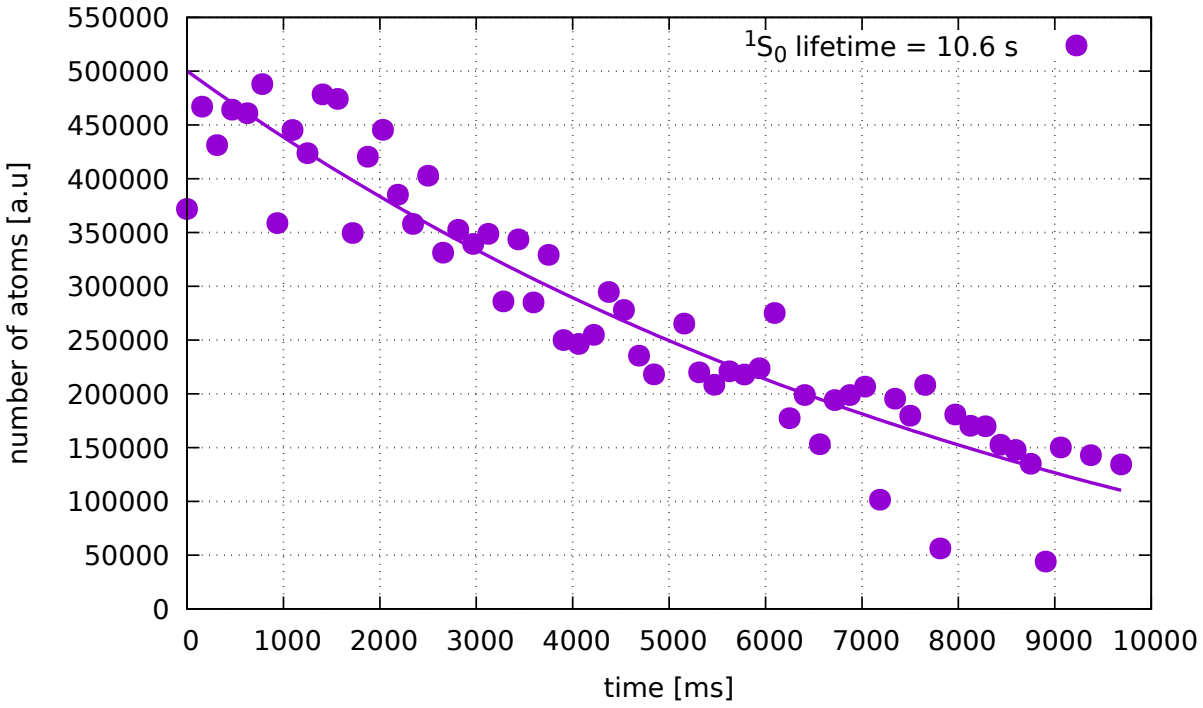

Figure 4.7.4. The lifetime measurement of the atoms in the fundamental state in the dipole trap.

lifetime of atoms in the dipole trap, which in our case is 10 s (see figure 4.7.4), and C_6

coefficient of long-range van der Vaals interactions for the ground and excited states of the clock transition give the expected frequency shift. Based on these calculations, we obtain the upper bound limit of the uncertainty of 8×10^{-18}. To have better estimation of the background gas collision shift, it would be necessary to perform the atomic trapping lifetime measurement for various pressures and extrapolate a correction for zero vacuum.

4.8 AOM Phase Chirp

Because the clock is operated in cycles, in which atoms are not interrogated continuously, the AOM, which drives the frequency of a clock laser beam, works in a pulsed regime. This switching of the AOM introduces a deformation of the optical phase of the clock pulses due to thermal effects in the AOM. This effect is measured with an interferometer by beating the phase of pulsed light with the non-pulsed local oscillator and using a counter. We observed that the effect that critically depends on the optical alignment of the beam. Therefore, to suppress this effect, we can reduce the RF power which drives the AOM as is shown of figure 4.8.5. The low RF power is compensated by higher optical power. For 5 dBm sent to the clock AOM, the related correction and the associated uncertainty is $(-8 \pm 8) \times 10^{-18}$. When the clock improves and the AOM chirp effect limits the clock accuracy, a detail evaluation will be necessary, using for instance mechanical shutter to block the clock beam.

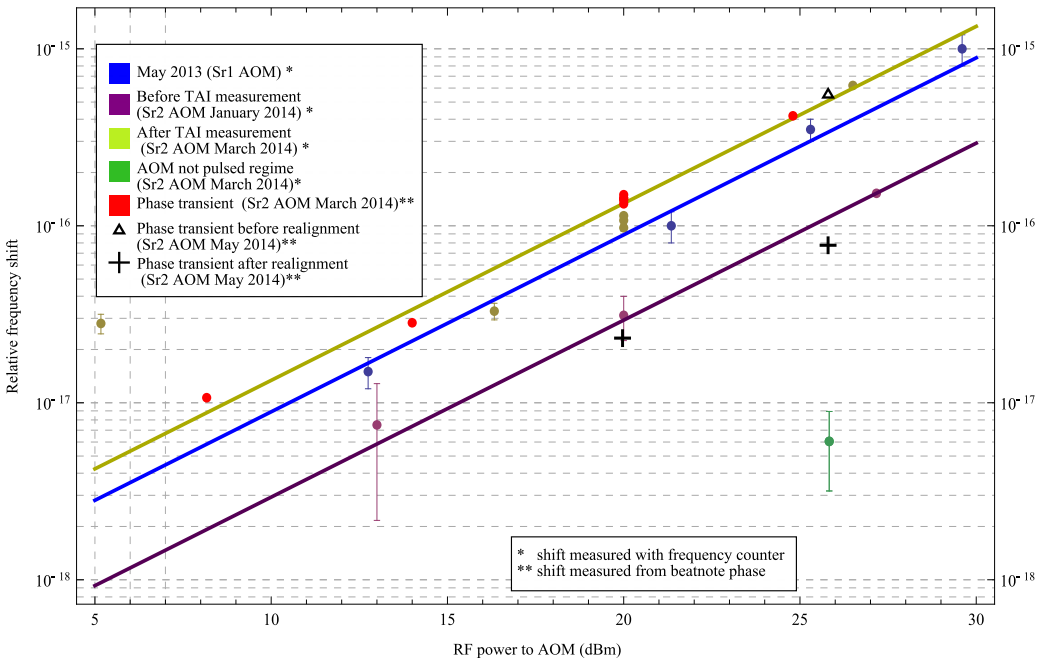

Figure 4.8.5. The AOM phase chirp frequency shift as a function of the applied RF power of the clock AOM for different alignment of the beam in the AOM.

4.9 The DC Stark Shift

The DC Stark shift is induced by static charges which can accumulate on the surface of the dielectric components of the vacuum chambers (cavity mirrors, windows etc.). Such accumulation of charges can shift the frequency of the clock transition even by 10^{-13}. For instance, it was detected by the direct comparison of two Sr clocks in our lab [104]. To remove charges, we illuminate the science chamber with UV light during several hours to get zero frequency offset between clocks within the accuracy budget. Then the stray electric field can be measured. The evaluation of the residual electric field is based on applying an external electric field close to the atoms. Because the shift is proportional to the square of applied electric field, the extremum of the function should be at zero for zero applied field for both polarizations of the electrode. Otherwise, there is a residual electric field, which shifts the resonance. The performed measurements in ref [104] give the uncertainty of 1.5×10^{-18} with any corrections.

Over long time we have not observed any shift induced by electric charges. Then suddenly on May 2015 during the preparation of the clock to the international comparison against the PTB Sr clock, the charges came back. The induced frequency shift was large - 120 Hz. Therefore, we had to use the UV lamp (type 825-1574, ILH XS01 S3365 SC211) for several nights to solve this problem again. It seems that the new charges accumulate after the application the new PT100 on the window surface. Recently, we changed the PT100 at SrB and the same effect was observed.

4.10 Servo Error

The natural drift of the ultra-stable cavity for the clock laser is largely removed by DDS-dedrifting system, which is based on the 3rd order polynomial. The coefficients are updated every 15 minutes and are determined from the frequency correction of the clock as a function of time. The residual drift is smaller than 1 mHz/s, which corresponds to an uncertainty less than 3×10^{-18} in fractional units. However, during the TAI calibration campaign on March 2016 we observed an unusually drift with high amplitude oscillations with a period of few hours. In this situation, the fitting servo could not follow the drift and we had to apply an uncertainty for the servo error 2 order of magnitude larger as usual - 2×10^{-16}. In this particular campaign, the servo error contributed significantly in the total accuracy budget. The effect had an incidental character.

4.11 The Accuracy Budget

Table 4.11.1 summarizes all systematic effects and their associated uncertainties. The main contribution comes from the blackbody radiation. Improving this effect requires the design of new vacuum environment, in which the temperature is well known and more homogeneous. The possible options are described in the section dedicated black body radiation. The rest of the effects are limited by statistics. In June 2016, the Sr2 clock reaches an accuracy of 4×10^{-17} [61].

The accuracy budget was reevaluated in June 2017 during last measurements. A total uncertainty goes down to 2×10^{-17}, thanks to an operation at shallow trap depth (25 E_r) and a better statistics of the Zeeman splitting, the line pulling shift and the density shift. In this time we reached also a better homogeneity of the temperature of the vacuum

Table 4.11.1. The accuracy budget for Sr2 clock in 2016 [61] and 2017.

Systematic effect	Correction $[10^{-18}]$		Uncertainty $[10^{-18}]$	
	2016	2017	2016	2017
Black body radiation shift	5208	5088	20	12
Quadratic Zeeman shift	1317	644	12	5
Lattice light shift	-30	17	20	6
Lattice spectrum	0	0	1	1
Density shift	0	0	8	3
Line pulling	0	0	20	4
Probe light shift	0.4	0.4	0.4	0.4
AOM phase chirp	-8	-8	8	8
Servo error	0	0	3	3
Static charges	0	0	1.5	1.5
Black body radiation oven	0	0	10	10
Background collisions	0	0	8	8
TOTAL	**6487.4**	**5744.4**	**41**	**21**

chamber.

CHAPTER 5

COMPARISONS OF OPTICAL CLOCKS

Nowadays, optical lattice clocks have already outperformed the best cesium microwave clocks, which realize the SI second, in terms of accuracy and stability both by two and three orders of magnitude respectively. Furthermore, their limits are not established yet. On the other hand, microwave clocks with comparison methods suitable and adequate to its accuracy and stability still play an important role in the worldwide timekeeping [108] and tests of fundamental physics [5, 131] due to its robust design and reliable operation over long time. In this chapter, we will show that a new «optical» architecture with optical clocks has well progressed and can lead to an exploration inaccessible, so far, in the fields of timekeeping, geodesy, astronomy or fundamental and applied physics. This promising outlook of OCLs can conduct to new definition of the SI second.

5.1 Applications of Clock Comparisons

Cutting-edge local and remote clock comparisons are able to give important information in many basic and applied research. Some experiments have been already conducted and have shown unprecedented accuracy, and, moreover, it can be improved in the future. In this section, we will describe potential applications that would benefit from comparisons of optical lattice clocks. In the second part of this section, we will present results of the last experiments which involve Sr clocks at SYRTE.

5.1.1 Confirmation of an Accuracy Budget

To characterize the performance of clocks, the systematic and statistic uncertainties must be evaluated. The accuracy budget is established separately for each clock. The procedure includes the differential measurement on single clock, interleaving clock operations for two clock configurations with different parameters. The frequency difference between these states removes not only the frequency drift of the clock laser, but also long-term drift of systematic effects. Therefore, this measurement determines the short-term stability of the clock. But some effects can be hidden in self-comparison of a single clock [104]. Rigorous evaluations require a direct comparison between two clocks based on the same atomic transition. It can be proved that there is no overlooked systematic shifts and show zero offset between clocks. By comparing two Sr clocks at SYRTE, two

overlooked systematic shifts have been discovered: effect of stray charges [52, 104], described in the previous chapter or effect of the incoherent background of semi-conductor sources [46, 52, 132]. The separated chapter 7 is dedicated to the latter effect.

The comparison between clocks is also necessary to evaluate the long term-stability of a clock. In this case, we need to have two clocks with similar performances. The long-term stability constraints often the systematic uncertainty. Currently, optical clocks reach a stability of 10^{-16} at 1 s and their frequency difference averages down to 10^{-18} after only few hours which makes a faster investigation of such systematic shifts as higher lattice light shifts [59], collisional shift [18] or black-body radiation shift [48]. With these evaluations, clocks can reach the 10^{-18} level of uncertainty [48, 52], and it shows that key systematic effects are well controlled beyond the SI second limit [48, 51, 132]. In this chapter, we will present new steps in the comparisons of optical frequencies that confirm the clock's performances and clock's reproducibility: comparison of Sr vs. Hg OLC [105] with a consistent result with an independent measurement performed in Japan [133], and the first agreement between two completely independent Sr clocks [106].

5.1.2 Variation of Fundamental Constants

An optical clock, as a very precise device, is a very convenient system to test the fundamental postulates of physics [134, 135]. Unification theories beyond the Standard Model propose a possibility of temporal variations of fundamental constants in the expanding Universe. Experiments have paid attention on variations of the fine-structure constant α_{EM}, the electron-proton mass ratio $\mu = m_e/m_p$ and the light quark masses m_q over the quantum chromodynamic scale $X_q = m_q/\Lambda_{QCD}$. Astrophysical observations in cosmological time scales, such as quasar absorption spectra, suggest a variation of the fine structure constant α_{EM}, but observation of distant astrophysical objects is encumbered by systematic effects like light blending, differential isotopic saturation, hyperfine splitting, variation of the Earth's velocity, etc. [136–138]. Independent of cosmological models, laboratory experiments based on atomic clocks do not have these drawbacks because various transitions of different atoms are related to fundamental constants and have different sensitivity to them. Therefore, it is possible to test various combinations of the fundamental constants by using frequency ratio measurement of various atomic transitions. All the constraints involve 3 quantities (α_{EM}, μ, X_q) and the time dependent frequency shift between two clocks x and y can be expressed:

$$\frac{\Delta(\nu_x/\nu_y)}{\nu_x/\nu_y} = k_{\alpha_{EM}}\frac{\delta\alpha_{EM}}{\alpha_{EM}} + k_\mu\frac{\delta\mu}{\mu} + k_{X_q}\frac{\delta X_q}{X_q}, \tag{5.1.1}$$

where k are coefficients which describe the sensitivity of the given frequency ratio [139–141]. The drift of α_{EM} can be found from optical-optical comparisons of optical frequency standards because electronic optical transitions have the same k_μ and k_{X_q} coefficients. Despite that comparisons are fixed in short time scales, by a systematic monitoring of frequency ratios between different optical and microwave clocks over time, it is possible to achieve a better uncertainty, accuracy, reliability and reproducibility of measurement. These comparisons allow us to establish new limits on possible variations. So far, several frequency ratio measurements have been performed [5, 33, 39, 46, 64, 142, 143]. Currently the constraints on variation of α_{EM}, μ, X_q are as follows [39, 139]:

- $d\ln(\alpha_{EM})/dt = (-0.7 \pm 2.1) \times 10^{-17}$ yr^{-1}

- $d\ln(\mu)/dt = (0.2 \pm 1.1) \times 10^{-16}$ yr^{-1}
- $d\ln(X_q)/dt = (7.1 \pm 4.1) \times 10^{-15}$ yr^{-1}

In section 5.5, we will show the last results of constraints on variations of fundamental constants which we have obtained at SYRTE using long-term comparisons between Cs fountains and Sr clock.

5.1.3 Dark Matter

Dark matter, together with dark energy, is one of the mysterious problems of science. Observations of gravitational effects on the galaxy scale suggest the existence of dark matter [144]. Rotating galaxies should have shattered a long time ago, their gravity can not hold matter with such velocities. It seems that galaxies have some extra yet undetected mass that they can withstand as galaxies. The direct detection of dark matter is extremely hard due to the fact that it is dark for observation – it does not emit, absorb and reflect the electromagnetic radiation. Theories beyond the Standard Model include the dark matter (and energy as well) with a dominating contribution in the total mass ratio of the Universe. Currently, dark matter effects are a crucial part of simulations of the formation and evolution of galaxies, and can also explain anisotropies in the cosmic microwave background. Nowadays, some groups have suggested and already performed experiments which can establish new constraints of detection of dark matter [145–147] including atomic clocks [85, 131, 148].

It is generally assumed that dark matter is a scalar field which is coupled with general relativity. This scalar field should oscillate and therefore can induce corresponding harmonic variations of the fine structure constant α_{EM}, the mass of fermions m_{fer} and the quantum chromodynamic mass scale Λ_{QCD} [149]. By long-term observations of the locally measured frequency ratio of atomic transitions, it should be possible to observe these oscillations or obtain constraints on the coupling between the dark matter scalar field and the standard matter [131].

Finally, it is possible to use a single optical clock, but only to detect some classes of dark matter objects formed in monopoles (0D object), strings (1D object) or domain walls (2D) [85]. These objects can perturb the standard model parameters, for instance the fine structure constant α_{EM}, which interacts differently with non-relativistic atoms ($\omega \sim \alpha_{EM}^2$) and electromagnetic field in a cavity ($\omega \sim \alpha_{EM}$). Monitoring the transient in time variations of the frequency of the clock transition and a given mode of an ultra-stable cavity makes a single clock responsive to hypothetical dark matter objects. Because clocks can be compared locally, a network of clocks used to detect the dark matter, does not need to be connected by phase coherent links but just synchronized like gravitational wave detectors.

5.1.4 Astronomy

Very Long Baseline Interferometry (VLBI) is the common radio-astronomical technique used to define and maintain celestial and terrestrial reference frames, the high-resolution imaging in radio-domain or Earth's rotation and tectonics studies [150]. It is based on collecting a radio-frequency signal from quasars by at least two spatially separated radio telescopes on the Earth. The signal arrives at different times to each antenna. Time delays are precisely recorded at picosecond level with respect to a local ultra-stable

time standard. VLBI stations make an 'off-line' network and they are not synchronized in real time. After the measurement session all data are sent to a correlation center where data are synchronized. This inconvenience in collecting data will go away in the near future. Combining the e-VLBI where the synchronization of telescopes can be done in real time, and the fiber link technique, allows all antennas to have an access to more precise time scale like TAI or optical clocks, without relying solely on own local H-maser, whose its residual phase fluctuations are the main limitation in order to reach higher resolution at mm wavelength [151]. Additionally, the coherence of atomic clocks allows to properly acquire and time tag the data. Currently, some institutions partially solved the problem and have already replaced H-masers by Cryogenic Sapphire Oscillators to have better short term stability [152]. Nevertheless, employing optical clocks with the stability of 1×10^{-16} after 1 h as a reference improves the short- and long term stabilities, with the aid of which new observables like fast radio bursts or high-stability millisecond pulsars are possible [153]. In geodetic VLBI applications, optical clocks can improve the positioning accuracy at the sub-millimeter level. The first results shown that the replacement of the frequency standard from local to remote does not limit the performance and reliability of the session [154, 155].

5.1.5 Special Relativity Theory

Einstein's relativity theory changed our understanding of space, time, energy and mass [156–158]. Einstein based his theory on two tenets. First, the laws of physics are the same for all non-accelerating observers. Second the speed of light has a defined and finite value c which is independent of the motions of observers. He has shown that space and time are coupled that they can be treated as a continuum - space-time. One of the embodiment of Einstein's theory is the time dilation. It means that clocks do not tick at the same rate for all observers. In special relativity theory, a moving clock runs more slowly with respect to an inertial frame of observation. The effect is bilateral according to the Lorentz transformation. For two speeding clocks in relative uniform motion, from the point of view of each clock, the 'second' clock is always ticking more slowly than the local clock. In each reference frame clocks work normally according to the Lorentz symmetry. But unification theories predict that local Lorentz invariance (LLI) must be broken at some energies, in order to unify all the interactions of nature. Nowadays, experiments like Michelson-Morley type, Kennedy-Thornlike type [159] and Ives-Stilwell type show that the last type, using accelerated ion in storage ring, gives the best constraint on the LLI violation parameter $\alpha \leq 2.0 \times 10^{-8}$ [160]. But the recent test performed by comparing four separated state-of-the-art Sr clocks in Paris, Braunschweig and London composed of a fiber network [84] establishes the new limit of constraint of Lorentz invariance parameter $\alpha \leq 1.1 \times 10^{-8}$, which improved by 2 orders of magnitude the previous limit obtained by clock comparisons [161] and is 2 times better than the best determined by using accelerated ions. This test is described in the dedicated section 5.9.

The Einstein theory assumes not only that measurement is independent of the velocity of clocks, but as well as the location in space-time and the type of clock. Again, theories of the unification of gravity with other forces of nature predict that local position invariance (LPI) must be broken. Gravitational potential can couple with α_{EM} and μ and change their values during the annual Earth's elliptical movement in the solar gravitational potential. The test of violation of LPI can be observed by monitoring the frequency shift

between two clocks x and y $\delta(\nu_x/\nu_y)/(\nu_x/\nu_y)$, which can vary periodically during the year:

$$\frac{\delta(\nu_x/\nu_y)}{\nu_x/\nu_y} = [k_{\alpha_{EM}} + k_\mu + k_{X_q}]\frac{Gm_{sun}}{ac^2}\epsilon\cos(\Omega t), \tag{5.1.2}$$

where G is the gravitational constant, m_{sun} is the solar mass, a is the semi-major orbital axis of the Earth's orbit, c is the speed of light, ϵ is the orbital ellipticity and Ω is the angular velocity of Earth around the Sun. All these parameters are well known and only $k_{\alpha_{EM}}$, k_μ and k_{X_q} coefficients of coupling for α_{EM}, μ and X_q are unknown. Currently combined Hg^+/Cs and Sr/Cs ratios give the limit $k_{\alpha_{EM}} = 2.5(3.1) \times 10^{-6}$ and $k_\mu = -1.3(1.7) \times 10^{-5}$ [64]. Over many years, SYRTE has provided regular monitoring of LPI [108, 139, 162] and we will show the last results in section 5.5. In the near future, it will be possible to obtain better results from regular optical-optical comparisons.

5.1.6 General Relativity Theory

Assuming that the general relativity theory is correct, clock ticks more slowly near a massive object as compared to a similar clock far from this object. In the weak-field approximation, the fractional frequency shift between two clocks $\Delta\nu/\nu_0$ is proportional to the gravity potential difference ΔW and the height difference Δh between them [163] and it is expressed by gravitational red shift formula:

$$\frac{\Delta\nu}{\nu_0} = \frac{\Delta W}{c^2} = \frac{g\Delta h}{c^2}, \tag{5.1.3}$$

where the g is the local gravitational acceleration and c is the speed of light. At the surface of the Earth, the fractional frequency difference between two clocks shifts by 10^{-16} per 1 meter of height difference. If we separate two clocks connected by phase-coherent link that one clock is placed on the top of the Eiffel Tower (325 m of height) and the second clock under the tower, the fractional frequency difference between clocks should be equal to 3.25×10^{-14} as is shown of figure 5.1.1. The redshift should be independent of the type of clock, then comparing clocks at the same location should give a null redshift measurement. Both observers agree that they can see a difference and sign of clock ratio, but observers are convinced that own local clock runs correct. In some theories time dilation does not depend on the height difference only, but also on a given atomic species. Then, the equation 5.1.3 includes a clock dependent parameter β, which for general relativity is equal to zero, and the frequency ratio should vary as:

$$\frac{\Delta\nu}{\nu_0} = (1+\beta)\frac{\Delta W}{c^2}. \tag{5.1.4}$$

When the general relativity is broken, then the frequency ratio should depend on local potential. Nevertheless, many experiments confirm the relativistic time dilation and the correctness of general relativity [163–165], but they need to employ velocities near the speed of light or large vertical separation. Optical clocks can determine a small relativistic shift and perform experiments with unprecedented precision and accuracy. Currently, at Laboratoire Souterrain de Modane (LSM), the German National Metrology Institute (PTB) and the Italian National Metrology Institute (INRIM) perform experiments which involved the Sr mobile optical clock developed by PTB and the stationary Yb clock operated at INRIM[1]. The transportable Sr clock is moved to Fréjus tunnel (LSM) and

[1] http://www-lsm.in2p3.fr/activites/INRIM/INRIM_Eng.htm

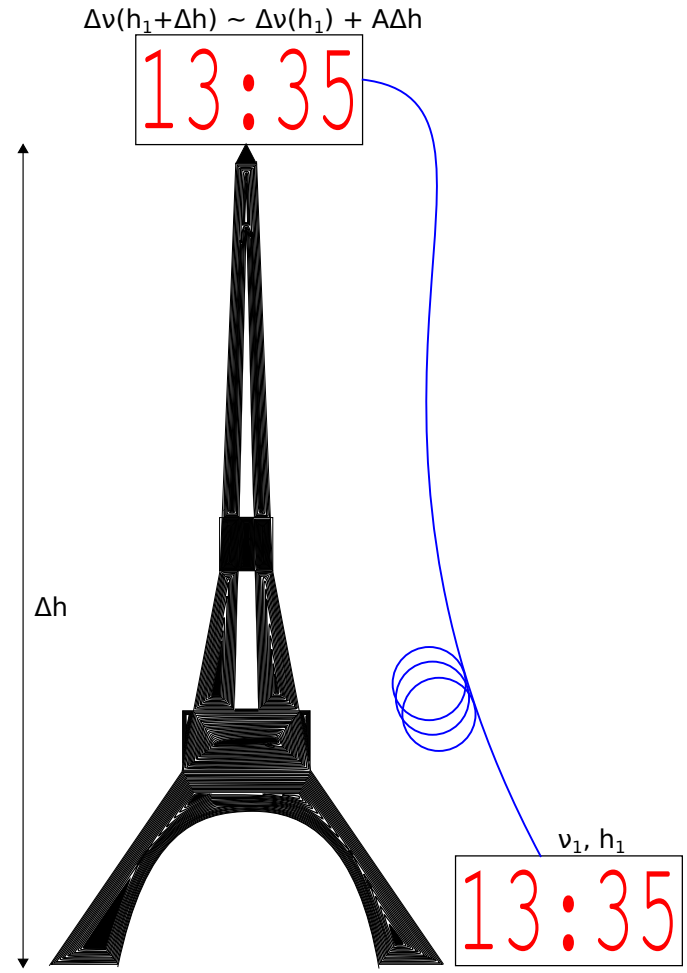

Figure 5.1.1. Gravitational time dilation. Moving a clock by Δh causes that its frequency of ticking is faster by the factor $A\Delta h$ (where $A = g\nu_0/c^2$) than it would stay on the high h_1.

connected by fiber link and at the end will be compared with Yb clock placed at INRIM in Turin. Both clocks are separated by only 90 km in horizontal direction and 1 km in vertical direction. The obtained results will be confronted with Geo-potential differences measured by geodesist of Hannover University and Politecnico di Torino [166]. This is the exceptional experiment with large height-difference between high accuracy clocks on the relativistic effects. On the other hand, it is possible to inverse this problem and measure a height difference by monitoring the frequency shift of clocks. It is a very attractive feature for Geo-science and hydrology. Further improvement of the accuracy of clocks composed in a network can lead to clock-based «chronometric» geodesy.

The term «chronometric» geodesy, first proposed by Martin Vermeer, includes an area of research which employs optical clocks for the measurement of the Earth [167]. Clocks connected by a network would measure the Earth's surface with the geoid [168,169]. The geoid is an hypothetical equipotential surface of the Earth's gravity, that is the nearest to the mean sea level. To achieve centimeter precision of the height, clocks need to be improved to 10^{-18} in fractional units. This level of accuracy is already reached by the best clocks in the world. The network should operate with high daily and Geo-spatial resolution at the clock locations and support other available geodetic levelling networks by replacing a lacks of gravity data with accurate clock measurements. It can monitor not only the gravity potential differences (~ 0.1 m^2/s^2) between clocks, but also variations of

the gravitational potential differences (~ 0.1 m^2/s^2 at 7 h). Weather, tides, climate effects or movement of plate tectonics can change the Geo-potential corresponding to the level of 10^{-17}s of frequency shift. It is essential to understand the behavior of the dynamics of the Geo-potential in order to establish in the future international timescale based on optical clocks.

5.1.7 Time Scales

Nowadays, cesium microwave clocks realize the SI second standard, which means that they calibrate and keep time scales such as TAI. Since optical clocks have provided a frequency signal with better accuracy and stability, first discussions about a possible re-definition of the SI second have arose. In 2006, the Consultative Committee for Time and Frequency (CCTF) established Sr as a Secondary Representation of SI second. Updated in 2015, the recommended value $\nu^0_{\mathrm{Sr}} = 429\ 228\ 004\ 229\ 873.2$ Hz with relative uncertainty 5×10^{-16}, is based on the measurement from 4 institutes (LNE-SYRTE, PTB, JILA and University of Tokyo). Currently among all other accepted second representations, only Rb microwave fountains regularly contribute to TAI [108]. Experiments with optical clocks presented above are focused rather on short integration times limited to few hours per day which makes such potential contribution to TAI useless. However, some efforts to employ short integration clock operations to timescale are done [66, 170]. LNE-SYRTE has already performed the first calibration of TAI with quasi continuous Sr optical clocks. chapter 6 is dedicated to this contribution.

5.2 Methods for Frequency Transfer

Described in the previous sections, clock comparisons have applications in science and international time technology, but it has not been mentioned yet how the frequency of a clock is transferred to other clocks. We can expect that the development of frequency transfer needs to follow (or even surpass) the development in optical clocks in order to be able to efficiently compare clocks. Here, we will briefly describe methods for comparing between local clocks and remote clocks by using local link, satellite and more recently optical fiber links.

Every time-frequency laboratory is equipped in standard time and frequency installations, by which the frequency difference between atomic clocks and time difference between time scales can be measured continuously. Two techniques are mostly used: two-way satellite time and frequency transfer (TWSTFT) and transfer supported by global navigation satellite systems (GNSS) like GPS, GLONASS, BEIDOU or Galileo [171]. Currently, satellite techniques allow to compare clocks at the ultimate level of 10^{-16} (in a reasonable time) by using broadband TWSTFT which is suitable for state-of-the-art microwave frequency standards. This level of uncertainty means a fundamental limitation for the comparison of optical clocks. Nevertheless, satellite techniques, due to the common availability, are used for the comparison of remote clocks in continental, intercontinental and global scale. In the future, within the Atomic Clock Ensemble in Space (ACES), a cold atomic cesium clock and an hydrogen maser will be launched to the International Space Station in order to be able to transfer frequency and time to many laboratories with a frequency in stability less than 10^{-17} [80] after a few days of averaging. But the project is not finished yet. The alternative to satellite techniques is a frequency transfer with superior accuracy through a point-to-point fiber connection. Experiments show that

the fiber technique can support clock comparison until clocks reach an accuracy of low 10^{-19} [106, 172] but this method is rather limited to continental scale.

5.2.1 Local Comparisons

Comparisons between two clocks based on the same atomic transition is relatively easy to perform because they operate at the same frequency, and therefore does not require sophisticated electronics. For two independent clocks, it is necessary to monitor the beat note between two clock lasers which are at resonance with the atomic references. The comparison between two clocks based on different atomic species is more difficult. If the frequency difference between the clock transitions was larger than the available electronics bandwidth (more than 100 GHz), then the comparison against primary cesium standard was performed via an optical frequency comb. The optical frequency comb is a femtosecond mode-locked laser which produces a train of pulses with constant spectral separation ω_r [8]. The frequency of each comb line ω_n can be described by the following equation:

$$\omega_n = n\omega_r + \omega_{CEO}, \tag{5.2.5}$$

where the ω_r is called the repetition frequency and ω_{CEO} is the carrier envelope offset frequency. The frequency comb can be treated as a simple optical synthesizer, which can convert coherently a given frequency phase into the microwave or optical domains. When ω_{CEO} and ω_r are phase-locked to a stable and accurate reference, then frequencies of the comb lines are ultra stable. Therefore, the beat note between a comb line and a given (clock) laser allow us directly to know frequency of this laser:

$$\omega_{laser} = N\omega_r + \omega_{CEO} \pm \omega_{beat}. \tag{5.2.6}$$

During the comparison against microwave standards, the femto comb transfers the stabilities between standards. Therefore, such a system is limited by the less stable standard in this case by microwave standards. An optical frequency comb also allows us to compare directly frequencies of optical transitions without relying on the microwave standards. In this way, a direct optical-optical comparison is possible by monitoring the beat notes between given comb lines and clock lasers, with a stability and accuracy limited by clocks themselves only [173, 174].

5.2.2 Comparisons by Satellite

The TWSTFT method based on the exchange of signals between two remote stations is the most accurate satellite comparison method of time scales with a fractional instability of 10^{-15} after one day of integration. Signals are propagated simultaneously in two ways along the same path and most effects that can cause time delays such as perturbations in the ionosphere and troposphere, can be canceled to first order. Usually, the frequencies of the up-link and the down-link are different because the corresponding propagation delays are not exactly the same. For instance an ionospheric delay depends more strongly on frequency. Information from time interval counters (TIC) contains data of all delays, clock differences and additionally the Sagnac effect:

$$\mathrm{TIC(A)} = \mathrm{t_A} - \mathrm{t_B} + \mathrm{d_{TB}} + \mathrm{d_{BS}} + \mathrm{d_{SBA}} + \mathrm{d_{SA}} + \mathrm{d_{RA}} + \mathrm{S_B} \tag{5.2.7}$$

$$\mathrm{TIC(B)} = \mathrm{t_B} - \mathrm{t_A} + \mathrm{d_{TA}} + \mathrm{d_{AS}} + \mathrm{d_{SAB}} + \mathrm{d_{SB}} + \mathrm{d_{RB}} + \mathrm{S_A}, \tag{5.2.8}$$

where TIC(A) and TIC(B) are read outs from time interval counters, t_A and t_B time at given clocks, $d_{TA/TB}$ and $d_{RA/RB}$ delays in Earth station equipment, $d_{SA/AS}$ and $d_{SB/BS}$ delays in propagation path, $d_{SAB/SBA}$ delays in the satellite, S_A and S_B are Sagnac corrections as described in figure 5.2.2 (Sagnac corrections are not included on figure). A geostation-

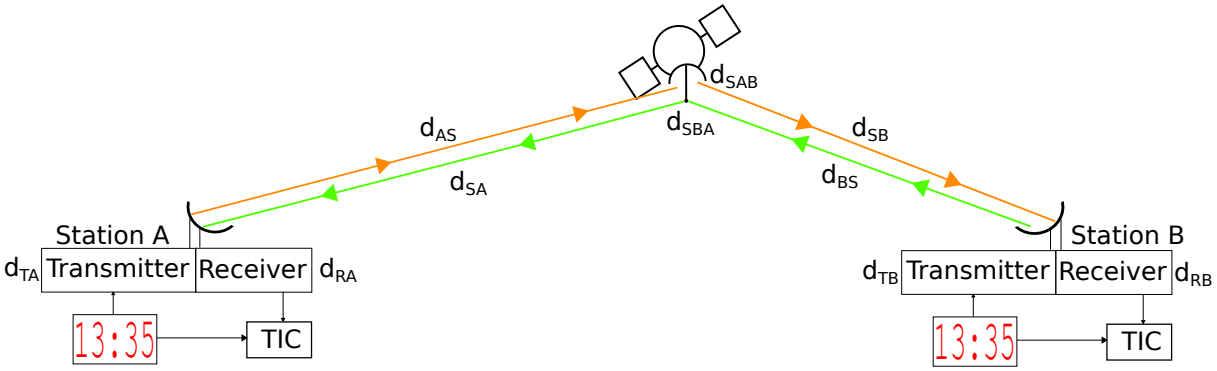

Figure 5.2.2. Two-way satellite time and frequency transfer. Signals from a station is transmitted to another station via satellite.

ary telecommunication satellites mainly employ the signal in the Ku-band (10.7 GHz - 14.5 GHz) which limits the spatial range to 10000 km but an accurate knowledge about the position of the stations is not required. Unfortunately, the required equipment is expensive (100 000 euro) and the cost increases if a commercial communication satellite is used. The clock comparison is immediately available (in quasi real time) after the determination of the time difference between the emission of a signal and the receiving of a signal from the opposite station. In this aspect, TWSTFT differs from GNSS-assisted frequency transfer.

Common View GPS time transfer is the second satellite based technique which is used to establish time scales. Global Positioning System (GPS) is mainly used because it covers almost each location on the Earth. The frequency signal is sent only in one way. Satellites equipped with atomic clock (Cs or Rb) with known orbit transmits signals in microwave L-band to receivers at a fixed and defined position. Ground clocks are compared to the GPS time with respect to propagation delay. The time difference of two clocks is obtained by exchanging data between stations by using, for instance, file transfer protocol (FTP) method. GPS time t_{GPS} is dropped out according to the following equation:

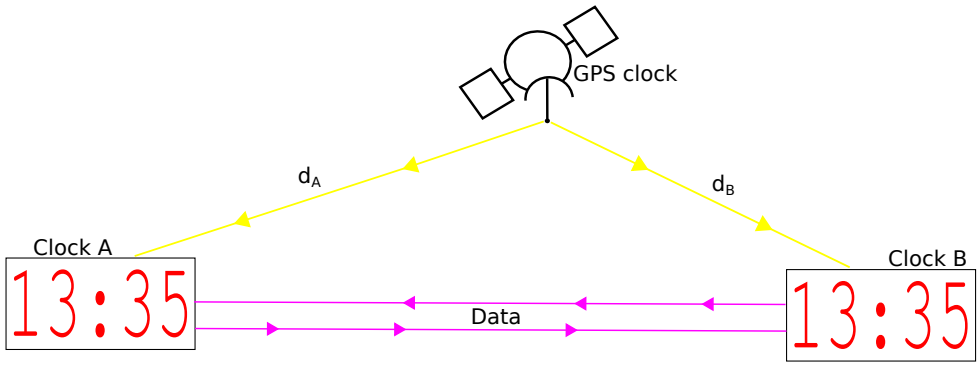

Figure 5.2.3. GPS Common View Method. Signals from a satellite is transmitted to receivers. To compare two clocks posteriori data transfer is necessary.

$$(t_A - d_A - t_{GPS}) - (t_B - d_B - t_{GPS}) = t_A - t_B - (d_A - d_B), \tag{5.2.9}$$

where t_A and t_B are the time at a given clock, and d_A and d_B are the propagation delays as shown figure 5.2.3.

Transmission can be operated in various accuracy modes. Currently, GPS can provide a signal with an instability at the 10^{-15} level after one day [175]. The more precise Integer Precise Point Positioning (IPPP) technique allows for a frequency comparison at the 1×10^{-16} level after a few days [176].

5.2.3 Comparisons by Fiber Link

The alternative to satellite methods is a point-to-point fiber link where the optical phase of an optical carrier at the telecommunication window at 1.55 μm is used to frequency transfer. In the past, this window has been already used to transfer signals in the radio or the microwave domain. The transmission was based on intensity modulation of optical carriers at 1.55 μm [74, 177]. Remote optical clock comparisons have been already performed in short distances ([116] transfer realized at 1064 nm) but, in principle, there is no difference with local comparisons. Currently, the phase of an optical carrier is used to transfer the frequency reference with a high accuracy, but for larger separation between clocks, a remote clock comparison is more challenging due to the attenuation of the light in the fiber, limited noise rejection amplitude, low control bandwidth and high fiber noise. For instance, the bandwidth of the phase noise correction decreases linearly with length of the link and it is limited by the propagation delay through the fiber. It is necessary and essential to develop methods for coherent amplification of an optical carrier and also for compensating optical phase fluctuation over long distances [178]. Furthermore, efficient phase compensation requires bidirectional operation along the same optical path, because the signal must be back reflected (see figure 5.2.4). There are two main techniques which have been extensively investigated in the last years by using 1) fiber Brillouin amplifiers [75, 77] and 2) bidirectional amplifiers [76, 172, 179] realized in a dark fiber or a dark channel. Connected amplifiers (of both types) are composed in a cascaded link and can be remotely controlled. The first method was demonstrated in the dark fiber approach [77]. It means there is a fiber dedicated only for frequency transfer and only frequency information is sent through this fiber. Brillouin amplifiers allow for intermedi-

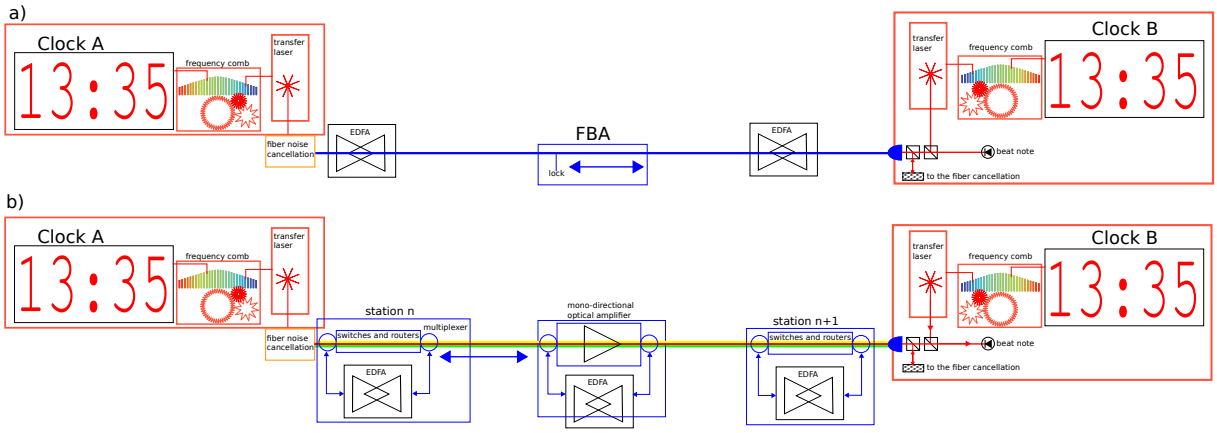

Figure 5.2.4. Two main techniques for transfer by the fiber link. a) fiber Brillouin amplifiers (FBA) in the dark fiber b) bi-directional amplifiers (EDFA) in the dark channel in the public network.

ate amplification through the fiber with 10^{-20} long-term stability level over continental scale [172]. The problem with the dark fiber approach is the availability of dedicated

fiber connections between laboratories and the relative high cost of this infrastructure. Due to this inconvenience the other method - dark channel - has been developed. In this approach, the frequency transfer is realized in a channel of the telecommunication network parallel to the normal Internet traffic [76, 179]. In France this method is using the National Research & Education Network - RENATER[2]. Because the telecommunication transfer is unilateral and employs unidirectional Erbium Doped Fiber Amplifiers (EDFA) only, it is required to bypass EDFAs and other conversion electronics (routers, switches) in order to implement full fiber phase noise cancellation. The incoming signal of a new laser diode is phase locked to feed the signal which is repeated and forwarded to the next station. This method of cascaded link within a public network is competitive with the dark channel technique and reaches a stability of 4×10^{-16} at 1 second and even 10^{-20} in longer integration time, but it is much cheaper [76]. Both techniques mentioned above were involved in the first international clock comparison between the Sr clock at LNE-SYRTE and another Sr clock at PTB [106].

5.3 Gravitational Redshift Corrections

For the comparison of clocks, we need to take into account the gravitational redshift corrections due to the different altitude of the clocks. As shown in the previous section a clock at the gravity potential W (including gravitational and centrifugal potentials) experiences a fractional frequency shift $\Delta\nu/\nu_0 = (W - W_0)c^{-2}$ with respect to the conventional reference zero level surface W_0. A shift of 1×10^{-17} corresponds to a 10 cm difference between the clocks. Therefore, the evaluation of the height position of the atoms with respect to reference level must be measured with centimeter precision.

For the local comparisons, the height difference between the atoms of each clock and the reference point is determined by the geometric leveling and the local measurements of Earth's gravity acceleration. The height difference can be measured with at least 1 cm precision.

To have an accurate height measurement for remote clock comparisons, we used the GNSS/Geoid leveling method, which is composed of a regional Geo-potential model and spatial positions of the clocks with respect to an Earth-fixed reference frame, given from GNSS observations. As a model we applied the European Gravimetric Quasigeoid EGG2015 developed by H. Denker at IfE/LUH (Institut für Erdmessung, Leibniz Universität Hannover). This model was developed in the framework of the ITOC Project and it is an up-dated version of EGG2008. In 2013 a local leveling measurement was performed by P. Delva and Institute Géographique National (IGN). The reference surface $W_0^{IERS} = 62636856.0(5)\ m^2/s^2$ defined in 2010 by the International Earth Rotation and Reference Systems Service (IERS) is based on the definition of the relativistic scale constant L_G of the International Astronomical Union (IAU), which defines the relation between Terrestrial Time (TT) and Geocentric Coordinate Time (GCT). Using the GNSS/Geoid leveling method with the EGG2015 model, the height difference between reference point and clock can be evaluated with 2-3 cm uncertainty. Independently to GNSS/Geoid method, we used the classical geometric leveling, which is based on the data from the Coordinate Reference System and EGG2008. The fractional frequency difference of these two methods is 1.14×10^{-17}[3].

[2] https://www.renater.fr

[3] The value was derived as part of the ITOC by LUH and SYRTE with the contribution of IGN, and that the value was reported in a deliverable of this project. A publication is underway.

5.4 Sr-Sr Comparison

As mentioned in the previous section, an important step in the proper evaluation of a clock stability is a confrontation of two clocks with similar performances. Many laboratories have built a pair of clocks [18, 48, 61] or developed fiber links between two close separated clocks [47, 116] to be able to verify the clock performance. Our group at SYRTE, as other clock groups has two Sr OLCs (SrB and Sr2). Faster evaluation of systematic shifts and detection of new shifts can be done with a better stability. Currently, the best clocks reach stabilities at low 10^{-16} level at 1 second with an ultimate accuracy at the low 10^{-18} level [6, 48] after a few hours of averaging. Clocks at SYRTE are not

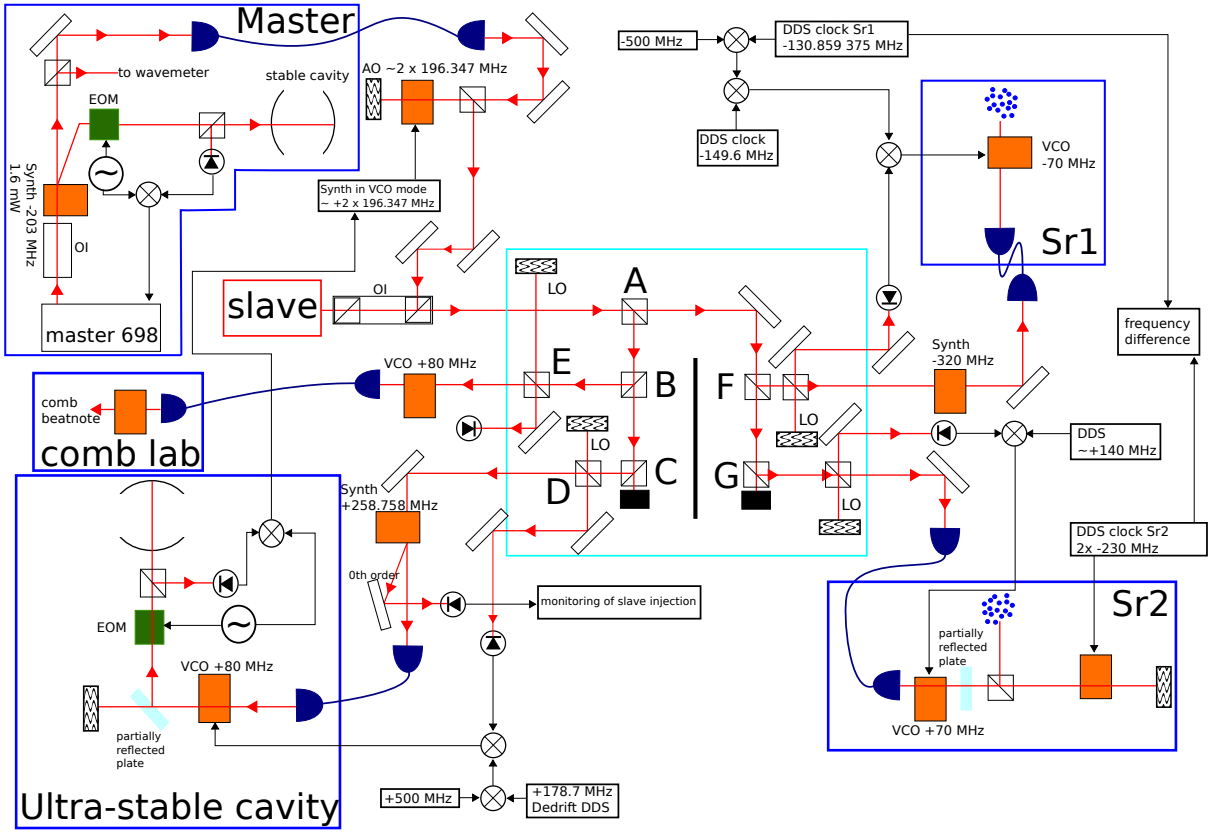

Figure 5.4.5. Optical distribution of clock laser. Clock laser (master) at 698 nm is shared between two Sr clocks: Sr1 and Sr2. The correction signals of clocks are digitally subtracted to see frequency difference. The light blue area indicates the non-compensated optical paths.

completely independent because they share the TiSa laser which is used to generate a lattice dipole potential and as well as the probe clock laser for which the full set-up of distribution of clocks beams is shown in figure 5.4.5. Nevertheless, clocks are built in a slightly different fashion. The design of the vacuum components is varied. In the new set-up, SrB, the science chamber is more compact than Sr2, in order to have more homogeneous temperature around atoms. Instead of the deflection beam in the hot atomic flux, a mechanical shutter that blocks the atomic beam after loading atoms to the MOT is installed. Another difference in the clocks is the distribution of the drain beams. In Sr2 drain beam is counter-propagated with the lattice beam. To effectively load atoms to the trap, both beams must be carefully aligned and, over time, drain beams must be regularly adjusted. In SrB, to increase reliability of the clock operation, the dipole trap and drain beams are coupled into the same fiber, and therefore aligned themselves in the common

fiber mode. The last difference is a better control of the polarization of the lattice light. In the new setup, the light polarization has improved linearity. These changes should improve the clock performance and reliability of the new set-up.

The clock laser (master) which is located in another room in the first step is locked to the high finesse cavity $\mathcal{F} = 20\,000$. Next, the light is transferred to the Sr laboratory and it is amplified by (slave) diode using an injection locking method which guarantees low noise level [180]. After amplification, the light is distributed to the atomic references, the frequency combs and finally to the ultra-stable cavity of very high finesse of $\mathcal{F} = 568\,000$. The phase fluctuations in each beam are compensated by PLL Doppler cancellation. Each beam in clock distribution is locked in phase lock loop (PLL). Uncompensated optical paths are separated in a chamber in which it will be possible to isolate them from ambient fluctuations of temperature, pressure, etc. Two independent acousto-optic modulators (AOMs), driven by DDSs, control the frequency of the clock beam going to each clock. Locking the clock laser to the atomic transition is performed by interleaving excitations of each side of the resonance. Then, the error signal is obtained by subtracting excited fractions of both measurements. To compare both clocks, we monitor the frequency

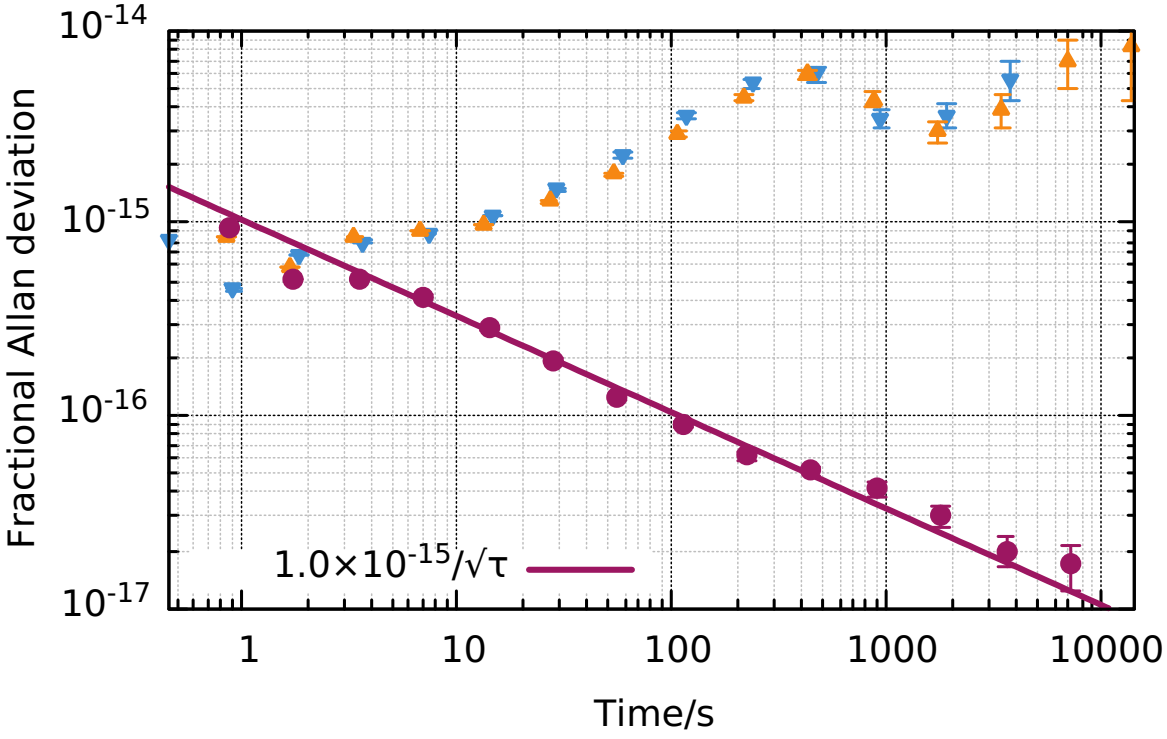

Figure 5.4.6. Frequency stability of two Sr OLCs. Blue • (and orange •) dots show the Allan deviation of frequency different between Sr1 (or Sr2) and ultra-stable-cavity. The purple • is the Allan deviation between two clocks for the asynchronously integration.

difference of the correction signals of the digital servo: $\mathcal{D} = y_{\mathrm{Sr2}} - y_{\mathrm{Sr1}}$, where y is the fractional frequency $\nu(t)$ measured at time t with the nominal frequency ν_0: $y(t) = [\nu(t) - \nu_0] \cdot \nu_0^{-1}$. The typical comparison of asynchronous clocks is shown in figure 5.4.6. The fractional Allan deviation of the frequency difference between each clock and the ultra-stable cavity is stable over time and is limited by the flicker noise of the ultra-stable cavity mirrors at 7×10^{-16}. Nevertheless, the short-term stability of the clocks is limited by the Dick effect and achieves $1 \times 10^{-15}/\sqrt{\tau}$, where τ is the averaging time. Mid 10^{-17} level is reached after 1000 s.

The frequency offset during the comparison performed in June 2016 is:

$$\mathcal{D} = (2.3 \pm 7.1) \times 10^{-17},$$

where the uncertainty includes systematic uncertainties of both clocks and statistical uncertainty of the comparison. The results are 2 times better in term of stability and almost 2 times better in term of accuracy as compared to previous performed measurement with old version of Sr1 and Sr2 [46].

5.5 Sr-Microwave Standards Comparisons

SYRTE, as a department of the Laboratoire National de Métrologie et d'Essais (LNE), is the national institution responsible of the official national time and frequency. Due to this fact, at SYRTE there are microwave fountains. The first one operates with cesium atoms (FO1) and the second one - the dual fountain FO2 - uses simultaneously cesium and rubidium atoms (FO2-Cs and FO2-Rb). Both fountains contribute to the calibration of Temps Atomique International (TAI), and, the cesium fountains, to the realization of the SI second under the direction of Bureau International des Poids et Mesures. Cs fountains naturally participate as an official representation of the SI second (see chapter 6). The general scheme of the distribution of the optical and microwave signals is shown in figure 5.5.7. The ultra-stable microwave signal for fountains is provided by a free running cryogenic sapphire oscillator (CSO), which produces directly a 11.98 GHz signal and down-converted 1 GHz, 100 MHz signals, which go to the microwave standards and the H-maser, and 8.985 GHz, which goes to the optical frequency comb. The CSO is phase locked to the reference hydrogen maser H_{ref} with the time constant of the order of 1000 s. This combination allows us to combine the excellent short-term stability of the CSO and the mid-term and the long-term stability of H_{ref}. Cold atomic microwave fountains

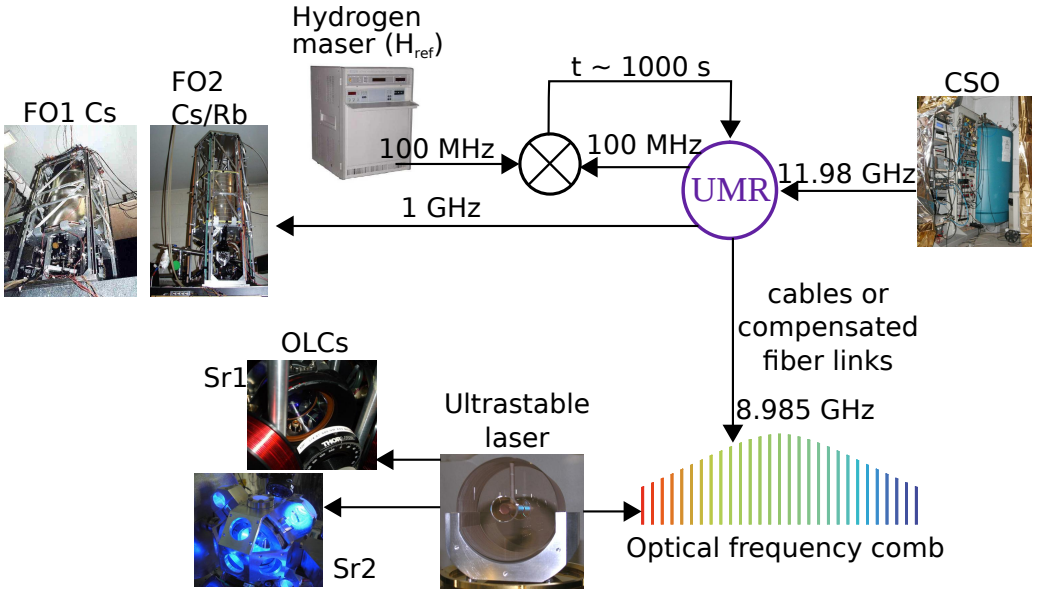

Figure 5.5.7. Optical and microwave clocks optical-microwave frequency comparison scheme.

are based on an atomic ensemble which is interrogated in an optical molasses. Using ultrastable microwave frequency reference (UMR) guarantees that fountains share the same high stability and purity and they can work at quantum projection noise (QPN)

limit and their statistical stabilities are at the 10^{-14} level at 1 second [5]. The optical signal from the Sr clock is down-converted to the 36th harmonics around 9 GHz of the optical frequency comb. Then, the 8.985 GHz signal from the CSU is used to lock the down-converted frequency around 9 GHz.

During the last years, several comparison campaigns were performed. Although, fountains operate in the QPN regime, OLCs have overtaken microwave clocks in terms of both uncertainty and stability. Due to this fact, each comparison is limited by the fountains. The Allan deviation of the frequency difference between Sr2 and the fountain is shown in figure 5.5.8. Both fountains have similar stabilities at 10^{-14} at 1 second. Several

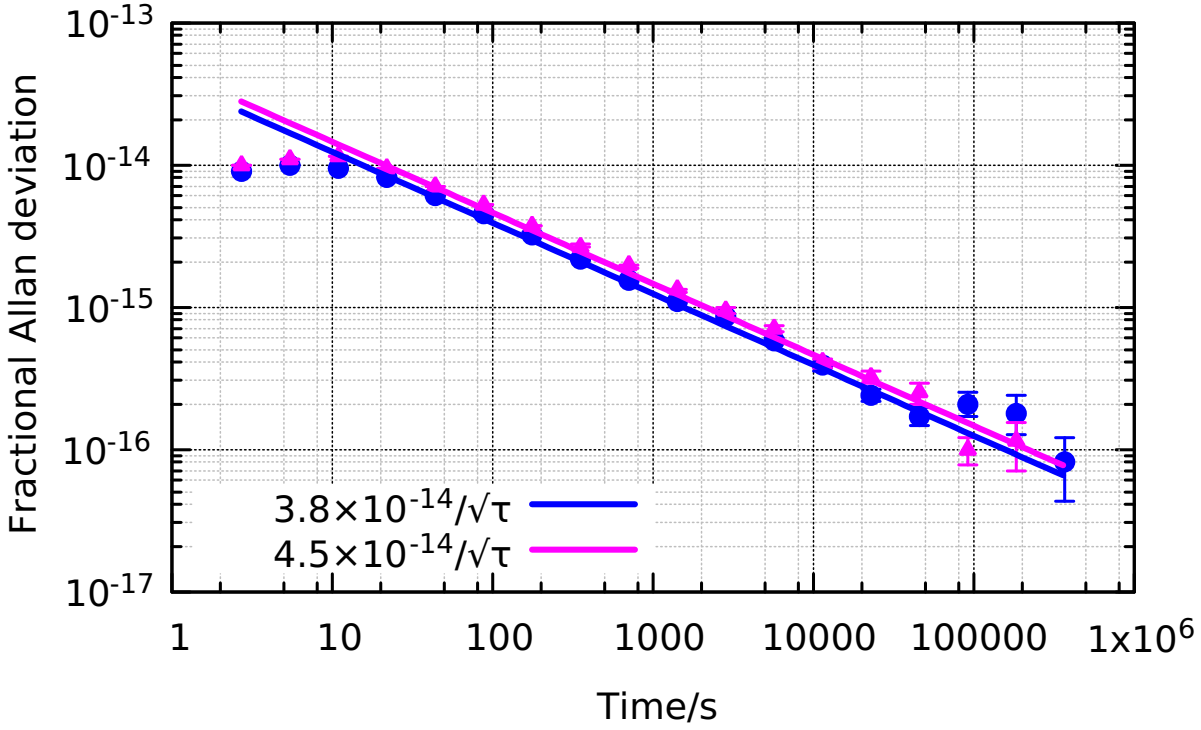

Figure 5.5.8. Frequency stability of the comparison between the Sr2 clock and the FO2. Blue • shows the comparison between Sr2 and Cs atoms and pink ▲ Rb atoms. The 10^{-16} level is reached after a few days of averaging.

days of integration are necessary to reach a statistical resolution at the 10^{-16} level. Long time comparisons with Sr clock were possible because all clocks work reliable and quasi-continuous. The measured frequency ratios of Sr and Cs and Rb are shown in table 5.5.1 and presented over the years in figure 5.5.9. The ratio $\mathcal{R} = \nu_{Sr}/\nu_{Rb}$ has been determined

Table 5.5.1. Frequency ratio measurement between Sr2 and each atomic fountain. The value ν_X^0 is the recommended frequency of the given secondary standard (Sr or Rb) or the definition for Cs. For the average fit with the total uncertainty of FO2 (both Cs and Rb) for which we have the largest data set, we show the reduced χ^2. Value lower than 1 means that systematic frequency shift is stable over time.

Fountain	$\frac{\nu_{\mathrm{Sr}}}{\nu_{\mathrm{X}}}$	$\frac{\nu_{\mathrm{Sr}}}{\nu_{\mathrm{X}}}\frac{\nu_{\mathrm{X}}^0}{\nu_{\mathrm{Sr}}^0} - 1$	absolute frequency ν_{Sr}(Hz)	χ^2
FO1	46 692.613 711 630 600(18)	$-3.0(39) \times 10^{-16}$	429 228 004 229 873.07(17)	
FO2-Cs	46 692.613 711 630 580(13)	$-7.2(28) \times 10^{-16}$	429 228 004 229 872.89(12)	0.6
Cs total	46 692.613 711 630 583(13)	$-6.5(28) \times 10^{-16}$	429 228 004 229 872.92(12)	
FO2-Rb	62 801.453 800 512 435(21)	$-10.9(33) \times 10^{-16}$		0.5

for the first time. The average absolute frequency of the clock transition obtained from all measurement campaigns is

$$\nu_{Sr} = 429228004229872.92(12) \text{ Hz}$$

including the total statistical uncertainty and the systematic uncertainties of the clocks, the fiber link, the frequency comb and the red shift correction. It is clearly presented

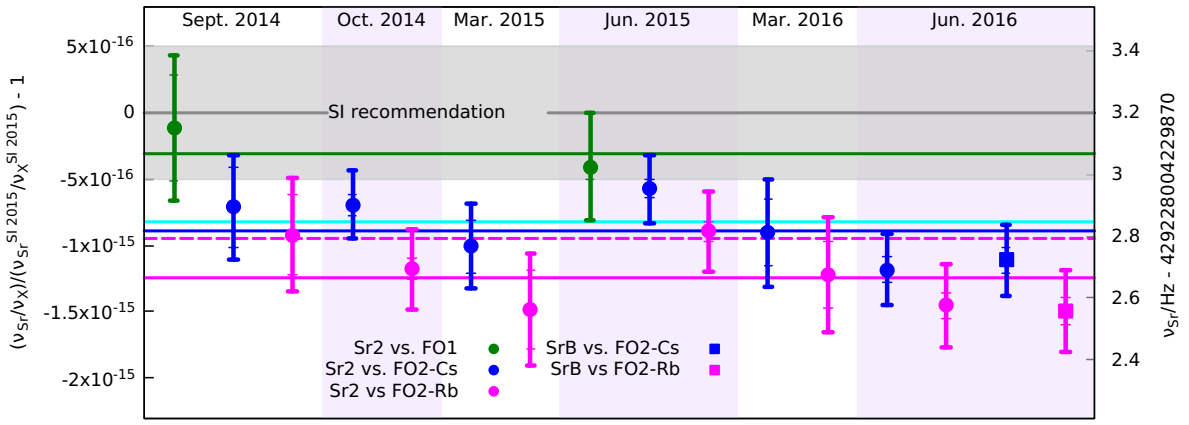

Figure 5.5.9. Frequency ratio measurements between strontium and cesium or rubidium clock transitions. The statistical uncertainty of each point includes a thin error bar, and the total uncertainty in a thick error bar. Gray area shows the uncertainty of the SI recommendation of BIPM. The left axis shows the relative offset between the measured frequency ratio and the frequency ratio given by the secondary representations of the SI second for strontium and rubidium ($\nu_{\mathrm{Sr}}^{\mathrm{SI}\ 2015} = 429228004229873.2$ Hz, $\nu_{\mathrm{Rb}}^{\mathrm{SI}\ 2015} = 6834682610.904310$) Hz. The right axis shows the absolute frequency of the strontium clock transition (with respect to cesium). The colored lines indicate the per-fountain average. The dashed magenta line represents the frequency ratio between Sr and Rb with respect to the Rb frequency measured at LNE-SYRTE ($\nu_{\mathrm{Rb}} = 6834682610.904312$ Hz). The cyan line is the average over the two Cs fountains. In addition to the calibration interval, two other measurements of the Sr/Cs and Sr/Rb frequency ratios are reported in this figure (Sept 2014 and March 2015). However, the overlap of these measurements with TAI segments is too poor to produce a valuable calibration of TAI.

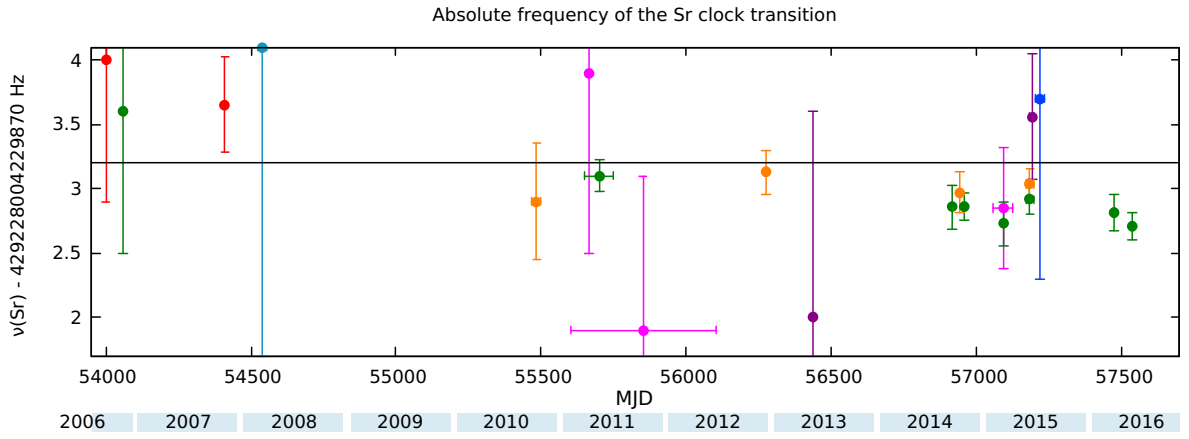

Figure 5.5.10. The absolute frequency of the Sr clock transition of LNE-SYRTE (green • [46,62]) over the years in comparison with similar measurements of other institutes in the world: red • JILA [63,64], light-blue • Tokyo University [65], orange • PTB [47, 66, 67], pink • NICT [35, 65, 68, 69], purple • NMIJ [49,70], blue • NIM [71]. The black line indicates the Sr recommended value.

in figure 5.5.9 that the obtained ratio Sr/Cs is consistent, reliable and reproducible over time and it is a good agreement with other absolute frequency measurements of other laboratories as shown on figure 5.5.10. It makes strontium really strong candidate for a future definition of the SI second. Worldwide and regular frequency ratio measurements against primary standard have another advantage. They allow us to monitor time and gravity dependence variations of the frequency ratio, which can prove for putative variations of fundamental constants. Current results show a time depended linear drift of Sr/Cs ratio: $d\ln(\nu_{\mathrm{Sr}}/\nu_{\mathrm{Cs}})/dt = (-2.3 \pm 1.8) \times 10^{-16}$ yr^{-1}, and a variation with gravity potential U: $c^2 d\ln(\nu_{\mathrm{Sr}}/\nu_{\mathrm{Cs}})/dU = (-1.3 \pm 1.5) \times 10^{-6}$ [108].

5.6 Sr-Hg Comparison

Frequency ratio measurements using microwave frequency standard are limited to a few 10^{-16}. To validate the proper evaluation of systematic shifts, it is necessary to investigate rigorous frequency measurements beyond the SI second between optical clocks based on different atomic species and finally find agreement on frequency ratio. At SYRTE, beside the Sr clocks, there is a Hg OLC in another room [105, 181, 182]. OLCs based on mercury atoms have several advantages over Sr clocks. Mercury atoms have high vapor pressure and we do not need to heat up atoms and it is about 30 times less sensitive to the blackbody radiation. ^{199}Hg isotope, which is used for clock applications, has no tensor light shift due to the spin 1/2 of the clock levels. The high nuclear charge Z makes mercury attractive to explore variations of the fine structure constant α_{EM} [56]. To cool and trap Hg atoms, 2 lasers are necessary. Unfortunately, all of them, together with the clock laser, are in the UV domain. This causes technical problems with efficiency and stability of the UV light sources. To get the clock laser at 266 nm, the 1062.5 nm laser which is locked to the USC must be doubled twice. In spite of these issues, Sr clocks were directly compared against the Hg clock by using an optical frequency comb [105, 133]. It is not the first frequency measurement between Sr and Hg at SYRTE [183] but it is the first optical-to-optical frequency comparison, not limited by the stability of microwave clocks. The scheme of the distribution of the clock lasers is shown on figure 5.6.11. The ultra-stable light at 698 nm and 1062.5 nm from the Sr and the Hg laboratories respectively is sent to the comb laboratory where the beat note of each clock laser is measured simultaneously. Clocks work in asynchronous cycles. The Allan deviation of the frequency difference between the clocks is shown on figure 5.6.12 with a total overlapped up-time 36.6 hours. The frequency stability comparison is 4×10^{-15}, one order of magnitude better than the frequency stability of optical and microwave comparison. After two hours of averaging, the stability reaches the mid 10^{-17} level, below the accuracy of the Hg clock, and is drifting with flicker noise. The total accuracy budget of Hg clock is estimated at 1.7×10^{-16}. The uncertainty budget of Sr is 4×10^{-17}. It means that the uncertainty associated with mercury limits the total uncertainties of frequency ratio measurement. The gravitational red-shift is included in the calculations of the comparison. The height difference of 3(1) cm between clocks (Hg lies higher than Sr) contributes to less than 10^{-17}. The frequency ratio $\mathcal{R} = \nu_{\mathrm{Hg}}/\nu_{\mathrm{Sr}}$ obtained from this data, including systematic and statistical uncertainties, is [105]:

$$\mathcal{R} = 2.62931420989890915(46)$$

which shows a progress by more than 1 order of magnitude to the last frequency ratio measurement performed in 2012, however, the ratio was measured by using microwave

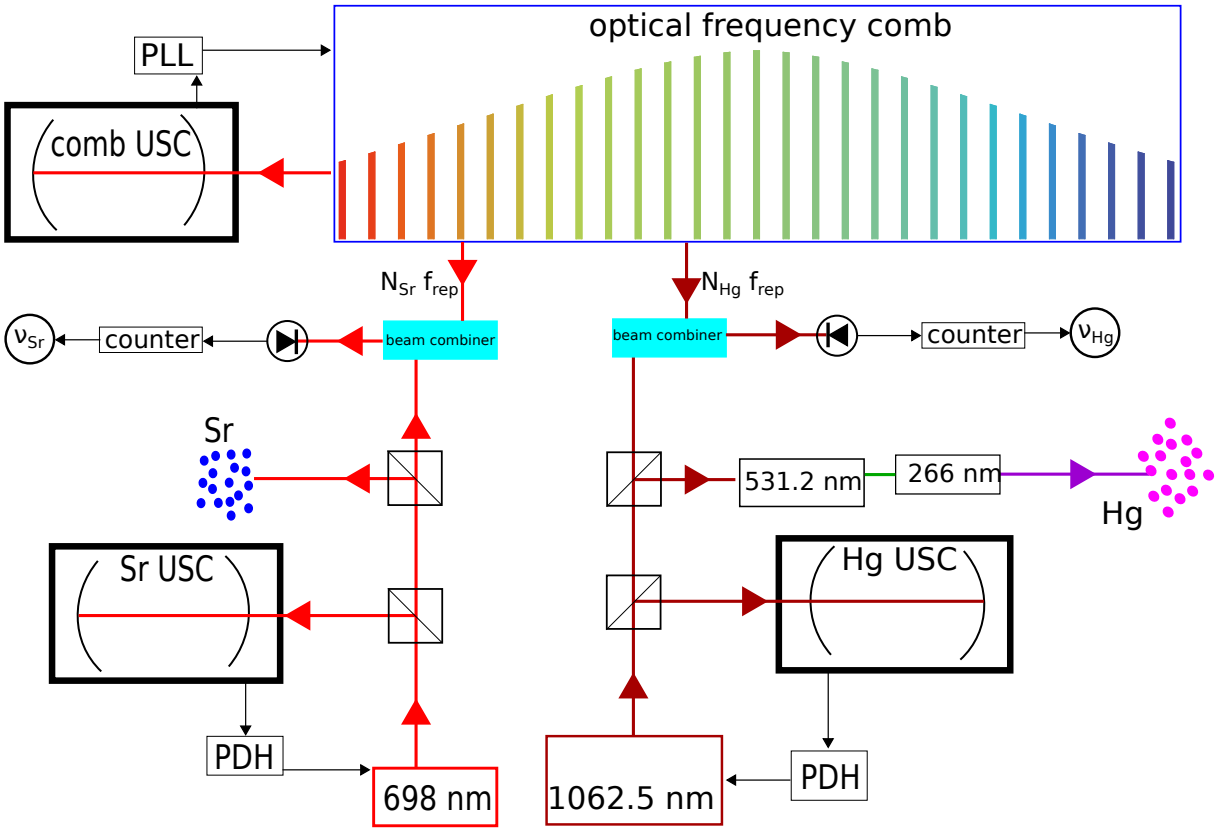

Figure 5.6.11. The strontium and mercury optical-optical frequency comparison scheme.

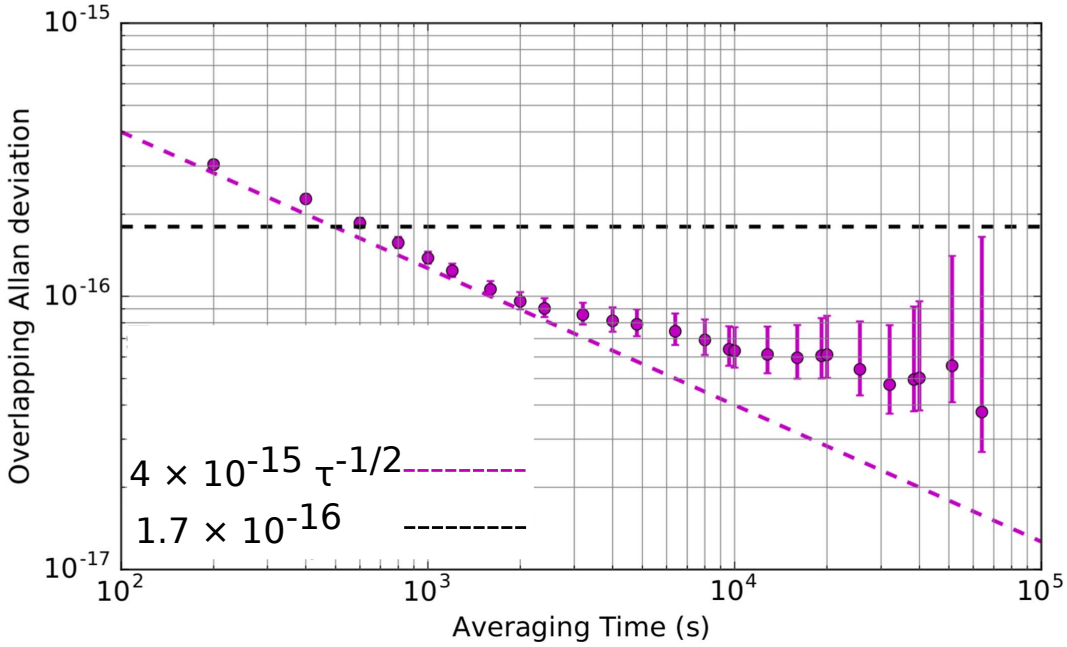

Figure 5.6.12. Frequency stability of comparison of Sr2 clock and Hg clock. The dotted black line indicates the accuracy of the mercury clock. The resolution at mid 10^{-17} level is reached after 1000 s and it is limited by flicker noise.

Cs fountains [183]. The ratio $\mathcal{R} = \nu_{\mathrm{Hg}}/\nu_{\mathrm{Sr}}$ measured at SYRTE is one of the most precisely reproduced quantity between two independent laboratories within an uncertainty. The actual result shows the first inter-continental consistent agreement with an-

other completely independent frequency ratio measurement of RIKEN group from Japan, $\mathcal{R}_{RIKEN} = 2.62931420989890960(22)$ [133], with an accuracy beyond the SI second.

5.7 SYRTE-PTB

The comparison between Sr and Hg, described above, is limited to a single building. A comparison of optical clocks separated by hundreds of kilometers is more challenging. Comparison developed by independent groups in different laboratories and working in different environmental conditions and with different equipment can make a rigorous test of the reproducibility of clocks. LNE-SYRTE, together with Laboratoire Physique de Laser (LPL, Université Paris 13) and PTB (Braunschweig, Germany) have performed the first international comparison between two independent Sr optical clocks by using a cascaded fiber link. Results show that the comparison is not limited by the noise of the fiber link of 1,415 km length [106], and, additionally, it is 10 times better and 4 orders of magnitude faster than other (satellite, TWSTFT) long-distance comparison methods which was performed simultaneously with the optical fiber comparison. The clocks were compared twice - in March and June 2015. Over years, Sr lattice clocks at SYRTE and PTB have been built independently [46, 47, 61, 67]. We will describe the main differences between these two clocks. In principle, both clocks operate at the same frequency using the same atoms but their realization is quite different, starting from the preparation of the cold atoms and finishing with the implementation of the lattice dipole trap. The Sr clock at SYRTE is described in the previous chapters, we will focus mainly on the PTB clock. Sr atoms are heated up in an effusive oven. Then, hot atoms are collimated by a 2 mm diameter pinhole instead of a differential pumping tube like at SYRTE. 2D MOT optical molasses beams deflect and collimate the atomic flux after the Zeeman cooling, not in the hot atomic beam as done at SYRTE. Both approaches guarantee that there is no direct sight axis between the interrogated atoms and the hot oven. MOT coils are fixed on different sides of science chamber- at PTB there are inside the chamber, on the other hand, at SYRTE, there are outside the vacuum. The first cooling stage takes 300 ms, it is 2 times faster than in Parisian set-up. Due to the different method for loading atoms in the dipole trap, the repumping process and the second stage cooling are organized in another way. Repumpers laser at 679 nm, 707 nm are applied during a blue cooling stage. The second stage magneto-optical cooling is realized by using the intercombination line at 689 nm by using resonance between total angular momentum $F = F' + 1$. To avoid problems with optical pumping effects from the trapping laser, a second laser is used, the so-called «stiring laser» between the $F = F'$ states, which ensures the randomization of the spin states of atomic populations in the red MOT, and thus increases the efficiency of the cooling. The second stage cooling takes a maximum 140 ms, and it is longer by almost 5 times than the analogous process in the SYRTE clock. In both clocks, atoms cooled in the micro kelvin regime are loaded into a 1D optical lattice at the magic wavelength. In Braunschweig, the lattice is oriented horizontally and is realized by a retro-reflected mirror. In each site of the lattice, 5 to 10 atoms can be trapped. In contrast to the Sr clock at SYRTE, the lattice is built-up in a vertically oriented optical cavity and controlled by a PDH lock. In this case, 1 or 2 atoms can be stored at each site of the lattice. In Germany, the lattice TiSa laser is pumped by a multi-mode pump laser and its frequency is stabilized to a frequency comb. At SYRTE the TiSa is pumped by a single-mode pump and it is locked to the 689 nm transition via a transfer cavity. At PTB, the waist of the lattice beam is only 34 μm, and is smaller by a factor 1.5 as compared to the waist of the lattice

at SYRTE (56 μm). The PTB clock laser is based on a 48 cm long cavity with a flicker noise level at 8×10^{-17} [19]. In Paris, a shorter (10 cm) ultra-stable cavity is used with a flicker noise at 7×10^{-16} level. Both clocks operate with Rabi interrogation pulses but with different time durations: 580 ms and 200 ms in PTB and SYRTE respectively. The same fluorescence method for detection is applied in both clocks. Some effects which can shift the clock transition, are evaluated in different ways. The estimation of the first order lattice light shift is performed in the same way, but the difference in the range of available trap depths, used for calibration, varies from 70 E_r to 150 E_r in PTB clock and from 50 E_r up to 500 E_r for the SYRTE clock. The higher-order light shifts are evaluated by a correction of data (PTB) or a non-linear regression (SYRTE). At SYRTE, line pulling shift is measured by changing the linewidth of the clock laser during the operation. At PTB the same effect is evaluated by possible spurious excitation amplitude. The measurement of the black body radiation shift is based on monitoring the temperature from pt100 thermometers, which are spread around the science chamber. The PTB chamber is a bit more homogeneous with a temperature range of 0.6 K. The temperature of SYRTE chamber varies by about 0.9 K.

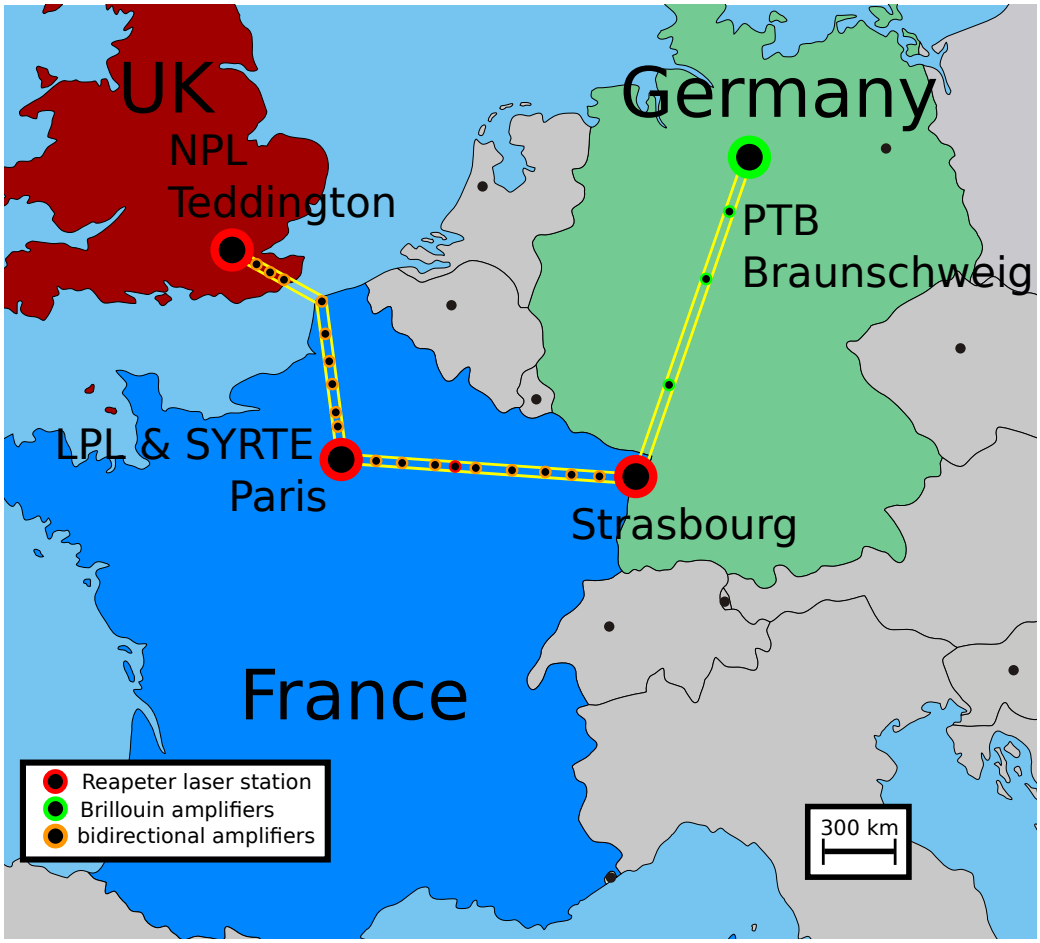

Figure 5.7.13. The optical-optical clock comparisons in Europe. The first comparison was performed between two Sr OLCs at SYRTE and PTB in March 2015 and it was repeated in June 2015. In June 2016 SYRTE and NPL compared own Sr clocks (see the next section). Used map of Europe is available at http://d-maps.com/m/europa/europemin/europemin35.svg

The total uncertainty budgets of both clocks are as follows: 1.9×10^{-17} for the PTB clock and 4.1×10^{-17} for the SYRTE clock, and with respective stabilities 3×10^{-15} and

5×10^{-16} at 1 second. The great number of differences referred above show that the clocks are completely independent and systematic and statistical uncertainties are fully uncorrelated.

Such clocks built with completely different designs are connected by a fiber link by which the frequency information is sent as shown on figure 5.7.13. The frequency transfer is realized by a narrow linewidth laser at 1.542 μm in the telecommunication band at 194.4 THz [184]. In the first step, optical frequency combs at each institute count the frequency ratio (beatnote) of the local clock laser and the transfer laser with an uncertainty less than 10^{-18}. Next, from both ends of the fiber connection (meaning from Paris and from Braunschweig) the light is sent through a cascaded fiber link to a connecting point at Strasbourg. The main difficulties in the operation of such long fiber links are preserving the phase coherence over whole distance, and the attenuation of the optical power. To maximally preserve the phase of the transfer laser, which is perturbed by environmental dependent variation of the refractive index of the fiber, the link is composed of repeating stations, in which part of the light is reflected back to previous station. The round trip phase-noise between stations is detected and rejected by more than 5 orders of magnitude. From both sides of the connection, the fiber attenuates the optical power by about 20 orders of magnitude (205 dB in Paris-Strasbourg part and 178 dBm in Braunschweig-Strasbourg part). The power losses are compensated in two different approaches. French and German parts employ different methods of amplification of the signal. The French side of the link - Paris-Strasbourg, 705 km long - is equipped with 2 repeater laser stations in Paris and Reims and 8 bi-directional amplifiers, which are assembled in a cascaded fiber link. The frequency information is sent through a dark channel available within the public RENATER fiber network. At each laser station, the signal is amplified by a phase-locked laser and signal is sent forward to the next station, and to the previous station as well for phase-cancellation. Due to the operation within the public Internet network, amplifiers and other necessary equipment have to be bypassed. On the other hand, the German side - Braunschweig-Strasbourg, 710 km long - uses dedicated dark fibers with only 3 Brillouin high-gain bi-directional amplifiers. Both signals from Paris and Braunschweig meet at the University of Strasbourg. The beat note between the two transfer lasers from SYRTE and PTB is measured at the dedicated repeater laser station, in which local lasers are phase-locked with incoming signals and give the final result. The counting of the frequency difference is performed with respect to low-noise, ultra-stable radio frequency quartz oscillator disciplined to a GPS signal.

Both sides of the link, despite the differences in design, have similar performances. The fractional stability at 1 s are 8×10^{-16} and 1×10^{-15} for French and German part respectively. The systematic uncertainty is estimated at the low 10^{-19} level for each part of the link (2×10^{-19} for the French part and 1.5×10^{-19} for the German part). The uncertainty of the relative frequency difference between the links in Strasbourg is negligible, and it is evaluated at 2×10^{-20}. Over the whole time of the comparison, the stability of fiber link does not limit the Allan deviation of the frequency difference of the clocks as shown in figure 5.7.14.

Frequency ratios are measured in 3 places: in Paris and Braunschweig between each clock laser and transfer laser and in Strasbourg between the two transfer lasers. Therefore, the final frequency ratio $\mathcal{R} = \nu_{Sr}^{\mathrm{PTB}}/\nu_{Sr}^{\mathrm{SYRTE}}$ (where expected value is equal to 1) must include these 3 terms:

$$\mathcal{R} = \frac{\nu_{Sr}^{\mathrm{PTB}}}{\nu_{Sr}^{\mathrm{SYRTE}}} - 1 \approx y_{Sr}^{PTB} - y_{Sr}^{\mathrm{SYRTE}} =$$

$$= \underbrace{y_{Sr}^{\mathrm{PTB}} - y_{Trans}^{\mathrm{PTB}}}_{\text{measured at PTB}} + \underbrace{y_{Trans}^{\mathrm{PTB}} - y_{Trans}^{\mathrm{SYRTE}}}_{\text{measured at Strasbourg}} + \underbrace{y_{Trans}^{\mathrm{SYRTE}} - y_{Sr}^{\mathrm{SYRTE}}}_{\text{measured at SYRTE}}, \tag{5.7.10}$$

where y is the given fractional frequency measured at time t with nominal frequency ν_0: $y(t) = [\nu(t) - \nu_0] \cdot \nu_0^{-1}$.

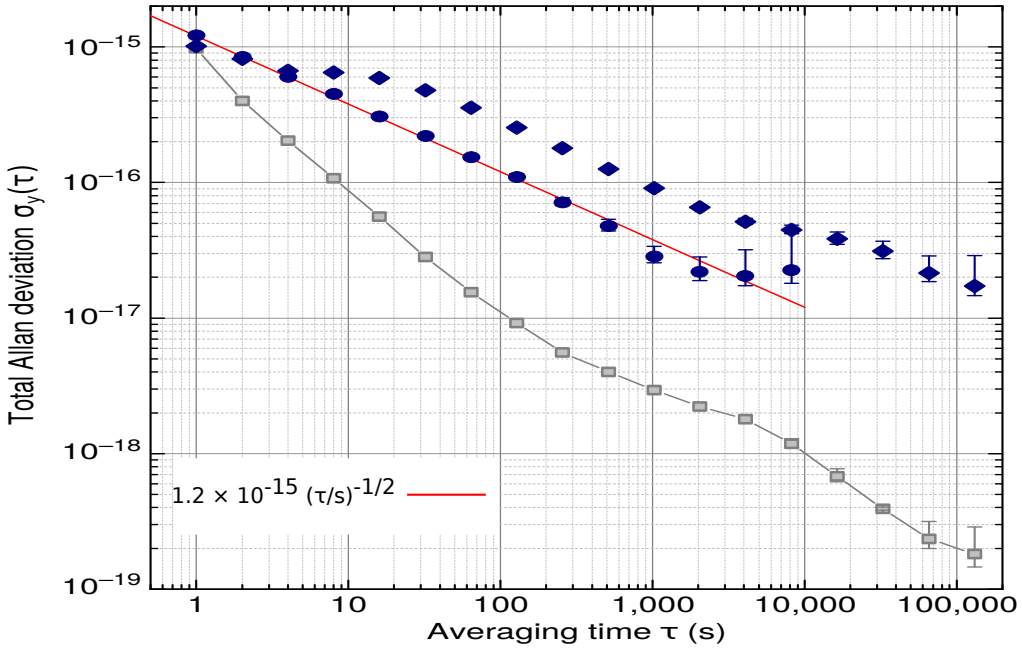

Figure 5.7.14. Frequency stability of comparison between the LNE-SYRTE Sr clock and the PTB Sr clocks. Dots • show the Allan deviation of the first campaign, diamonds ♦ second campaign and squares ■ the frequency link during the second campaign. The low 10^{-17} level is reached after 3000 s.

In order to avoid any undesirable frequency offset and contribution in the stability due to the complexity of the frequency ratio measurement, the accurate synchronization of the clocks is crucial and needs a synchronization procedure. The clocks must indicate the same time for the same events, differing, in our case, by no more than an uncertainty of 1 ms. The synchronization in Strasbourg is made by a GPS receiver which provides a pulse-per-second signal. In Paris and Braunschweig, local realizations of UTC generate a pulse-per-second signal and synchronize the local counters. Unfortunately, during the first measurement session (March 2015), the synchronization of counters at Paris failed. Therefore, indirect methods were applied to obtain and retrieve the missing synchronization of counters. The frequency of the beat note measured over the whole duration of the campaign represents the time dependent frequency drift of the transfer lasers. In case when data are not fully synchronized, the phase noise is not fully canceled. Therefore, by shifting the datasets, it is possible to minimize the short term instability of transfer laser noise and then get back missing counter synchronization with an uncertainty 10 ms. This problem largely resulted in the accuracy budget with uncertainty of 1×10^{-16} in fractional units (see table 5.7.2). During the second campaign all counters were synchronized with uncertainty 0.2 ms and the associated uncertainty is well bellow 10^{-18} level.

Comparisons at 10^{-17} level mean that it is necessary to take into account the relativistic redshift effects and determine the height difference between clocks better than 10 cm, which for two spatially long-separated clocks, is not trivial. To get a as high as possible height resolution, a combination of GPS, spirit leveling and local gravity measurement were involved. The total height difference between clocks is 247.4 m with an uncertainty of 4 cm, which corresponds to fractional uncertainty of 0.4×10^{-17}.

Table 5.7.2. Uncertainty budget of the comparisons between the Sr clocks of SYRTE and PTB.

Ratio Sr_{PTB}/Sr_{SYRTE}	Campaign 1 Unc. $[10^{-17}]$	Campaign 2 $[10^{-17}]$
Systematics Sr_{SYRTE}	4.1	4.1
Systematics Sr_{PTB}	2.1	1.9
Statistical uncertainty	2.0	2.0
Frequency comb	0.1	0.1
Link uncertainty	<0.1	0.03
Counter synchronization	10.0	<0.01
Gravity potantial correction	0.4	0.4
Total clock comparison	**11.2**	**5.0**

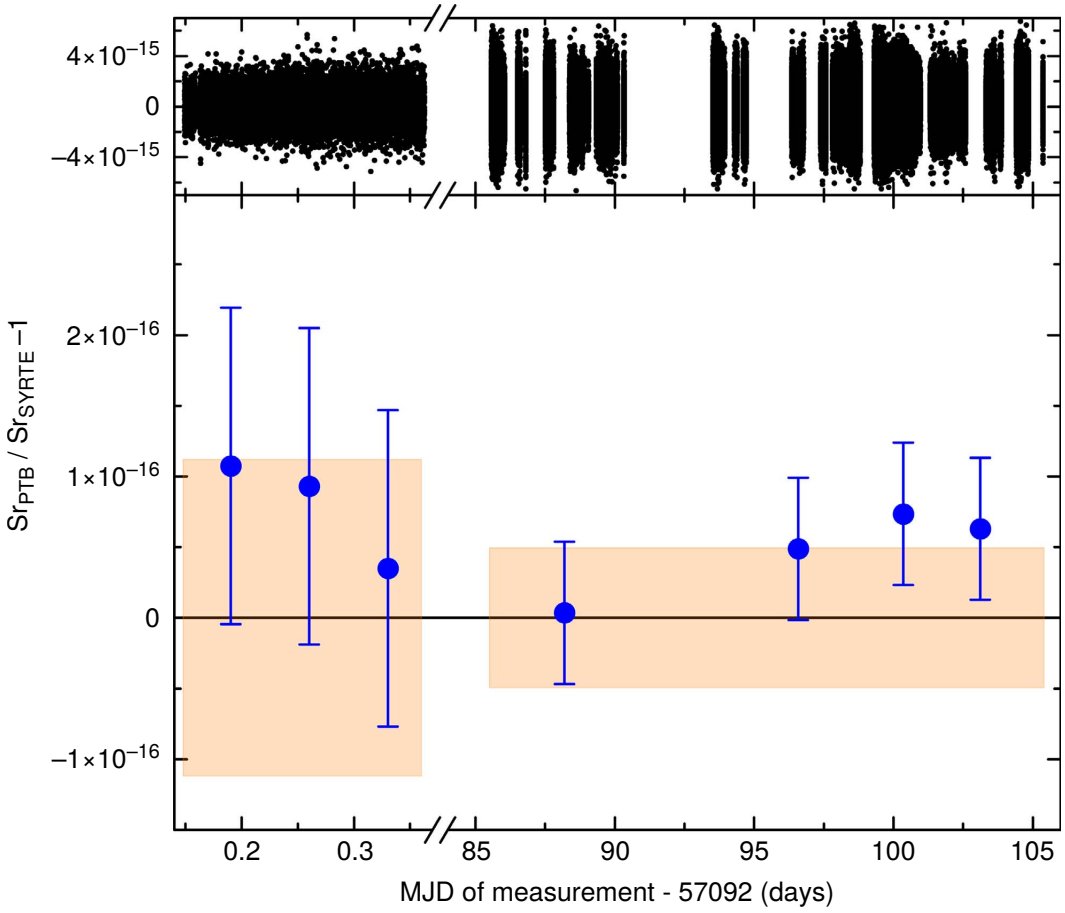

Figure 5.7.15. TOP: combined valid datasets of campaigns: 6000 s length for the first campaign and 125 000 s for the second campaign. BOTTOM: Frequency ratio between SYRTE and PTB clocks: ν_{PTB}/ν_{SYRTE}-1. The statistical and systematic uncertainties are included in the error bars (1σ). The orange shaded area represents $\pm 1\sigma$ range of uncertainty, which is shown in table 5.7.2.

The Allan deviation of frequency difference is already shown on figure 5.7.14 with a total overlapped up-time of 145 h (see figure 5.7.15) and a statistical uncertainty of 2×10^{-17} in the first campaign. The long term stability behaves as a white frequency noise at $1.2 \times 10^{-15}/\sqrt{\tau}$ for the first session and $3 \times 10^{-15}/\sqrt{\tau}$ for the second session. The fiber noise has negligible contribution, and it averages faster than clock signal. The stabilities of the first and second campaign are slightly different. It is most likely due to the magnetic field from Parisian metro station. The second campaign, in contrast to the first campaign, was performed rather during daytime over almost 3 weeks. The posteriori

analysis and additional measurements shown a similar instability behavior during the day, when the magnetic field is higher during the daily Parisian metro activity.

During both campaigns, the agreement between two completely independent and remote clocks was found within the combined uncertainties. The final frequency offset between the two completely independent Sr clocks during the second longer campaign is $(4.7 \pm 5.0) \times 10^{-17}$ (see figure 5.7.15). It is the first international comparison of remote optical clocks without limitations due to the transfer link. This result is among the best obtained frequency ratio in the world. The comparison with two Al^+ ion clocks shown agreement at $(-1.8 \pm 0.7) \times 10^{-17}$ level [185]. Among other Sr clocks, the best agreement is reached by prof. Katori's group, whose two Sr clocks agree to within $(-1.1 \pm 1.6) \times 10^{-18}$ uncertainty level [48]. But these comparisons were performed in one location and was limited to a single team, and by using similar equipment. Here the demonstrated comparisons are an effect of the efforts of two independent remote groups.

That state-of-the-art all-optical comparison shows an exceptional precision between two entirely independent Sr OLCs which makes a step forward for the future re-definition of the SI second and opens new opportunities in Geo-science and fundamental physics.

5.8 SYRTE-NPL

In a similar fashion as in the case of the comparison between SYRTE and PTB, SYRTE has compared the Sr OLCs against another Sr OLC at NPL in Teddington, UK in June 2016. In this comparison, only bidirectional amplifiers were used in a 812 km long cascaded fiber link. 3 amplifiers are placed in Great Britain and 6 in France. The connection point where the beat note of the two transfer lasers of both sides is measured is placed at LPL, Université Paris 13, by using a dedicated repeater laser station. The frequency is counted with respect to an ultra-low noise oscillator disciplined to GPS. The

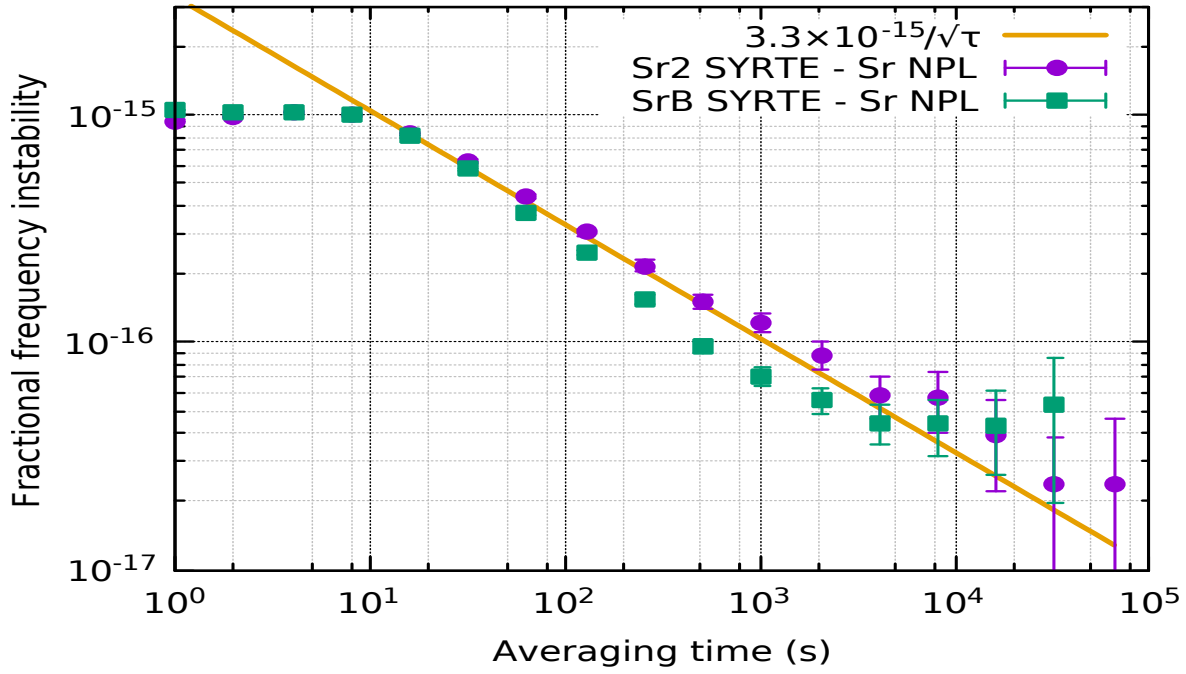

Figure 5.8.16. Frequency stability of two Sr OLCs at SYRTE and NPL. 10^{-17} level is reached after 3000 s.

Allan deviation of the frequency difference between clocks is shown on figure 5.8.16.

It is obtained from 60 hours of accumulated data. The long term stability averages like $3.3 \times 10^{-15}/\sqrt{\tau}$ where τ is the averaging time. The fractional frequency difference reachs low 10^{-17} level after few hours of measurement. As in the SYRTE-PTB comparison the contribution of the noise of the fiber link is negligible, and the frequency instability is limited by the clock signals. In the future, a common simultaneous comparison between clocks at SYRTE, PTB and NPL is planned. It will be an embodiment of design of a network of clocks.

5.9 Test of Special Relativity

By using the network of spatially separated clocks connected by phase coherent fiber link described above, it is possible to test the relative velocity time dilation by monitoring daily variations of the relative frequency difference [84] with unprecedented precision. This test establishes a new constraint on the Lorentz invariance parameter α, which improved by 2 orders of magnitude the previous limit obtained by clock comparisons [161], and it is 2 times better than the best constraint obtained by accelerated ions [160]. We hope that this test is the great beginning of forthcoming tests of modern physics with an improved and more dense optical network of optical lattice clocks in the near future. Unification theories describe the violation of Lorentz invariance in dynamical or kinematical frameworks (review [186]). In our case, because we compare 4 clocks of the same type, we can use the relatively simple Robertson-Mansouri-Sexl (RMS) framework to test LI [157,187–189]. The RMS framework describes only kinematic relations and says nothing about the dynamics, and relations between clocks and fundamental particles. It assumes that there exists some preferred frame Σ within which the constant speed of light c is isotropic and rectilinear in free space. In the experiment, the cosmological microwave background (CMB) rest frame is chosen. In the 3-D space, an observer at rest with respect to Σ can measure an event E by time and space intervals (4 coordinates $\vec{x}, t$).

The Lorentz transformations from frame Σ to some frame S, defined that $(\vec{x}, t)$ are in S. Frame S moves with constant velocity $\vec{w} = d\vec{x}/dt$ $(w < c)$ and is parametrized by the LI violation coefficients:

$$t' = a^{-1}(t - c^{-1}\vec{\epsilon} \cdot \vec{x}), \tag{5.9.11}$$

$$\vec{x}' = d^{-1}\vec{x} - (d^{-1} - b^{-1})\frac{\vec{w}(\vec{w} \cdot \vec{x})}{w^2} + \vec{w}t, \tag{5.9.12}$$

where parameters a, b, d are functions of the relative velocity w between the frames. In Special Relativity, they reduce to: $a = b^{-1}$ and $d = 1$. ϵ is a synchronization dependent arbitrary vector in frame S. In the experiment, S is geocentric frame which moves in the space with a speed of $w = 370$ km/s with respect to CMB. Regarding that the $a = b^{-1}$ and due to that the speed is much smaller than the speed of light, it is possible to expand a coefficient a in power series w:

$$a = 1 + c^{-2}(\alpha_{RMS} - \frac{1}{2})w^2 + \mathcal{O}(c^{-4}, w^4) \tag{5.9.13}$$

In our case, clocks are connected by fiber and they exchange in two ways the frequency signal. Frequency information is sent from clock A with proper frequency ν_0 to clock B which receives the proper frequency ν_1. Then, clock B immediately sends back the signal. Clock A receives the signal with frequency ν_2. This set-up corresponds to a two-way

frequency transfer in Λ configuration with the Einstein synchronization. The fractional frequency difference between the clocks is:

$$\frac{\Delta\nu}{\nu_0} = \frac{\nu_1 - \nu_0}{\nu_0} = \frac{\nu_2 - \nu_0}{2\nu_0} + \Delta, \tag{5.9.14}$$

where Δ includes all corrections, which de-syntonizate the frequency difference between the clocks, like the gravitational relativistic redshift effect due to the different altitudes of the clocks and the time variations of the gravity potential. The two-way Doppler signal $\nu_2 - \nu_0$ is stabilized through the whole link by implementation the Doppler cancellation method. Assuming a violation of LI, the term Δ includes a LI violation term. In the low-velocity limit Δ can be written as a simple composition of the redshift gravity effects term Δ_{cl} and the LI violating term Δ_α:

$$\Delta = \Delta_{cl} + \Delta_\alpha. \tag{5.9.15}$$

We find the parameter Δ_α with the aid of which we can describe the violation of Lorentz invariance:

$$\Delta_\alpha = \alpha c^{-2}[2\vec{w} \cdot (\vec{v}_A - \vec{v}_B) + (v_A^2 - v_B^2)] + \mathcal{O}(c^{-3}), \tag{5.9.16}$$

where $\vec{w}$ is the velocity of the Earth with respect to the preferred frame Σ. This velocity is composed of the movement of the Earth in the Solar System (by using Solar System Barycenter (SSB)) and the movement of the barycenter of the Solar System with respect to Σ (it means CMB). The orbital velocity of the Earth around the Sun is taken into account despite that it is 1 order of magnitude smaller than the velocity of the barycenter of the Solar System and the experiment is limited to only 3 weeks of the calendar year. The celestial coordinates of the velocity of the center of the mass of the Solar System with respect to CMB in galactic coordinates are 263.99° in longitude and 48.26° in latitude. Transformation to the geocentric celestial reference system (GCRS gives a right ascension of 11 h 11 m 36 s, and a declination of -6° 54' 00" and velocity of norm 369 km/s. The norm of velocity $\vec{w} \approx 340$km/s during June 2015 and 2016. $\vec{v}_A$ and $\vec{v}_B$ are the velocities of the clocks in the non-rotating GCRS (see figure 5.9.17). The velocities are calculated with the SOFA algorithm by transforming the fixed on the Earth's surface terrestrial coordinates of clocks. The difference $\nu_1 - \nu_0$ is measured by beating the clock lasers at each end of the link. $\nu_2 - \nu_0$ is fixed on a given value by the implementation of the Doppler cancellation. Clocks have different orientation of $\vec{v}$ (different longitudes) and as well norms of $\vec{v}$ (different latitudes). The term $(v_A^2 - v_B^2)$ of Δ_α gives a negligible contribution to the variations of the frequency ratio (at 10^{-20} level). Therefore, it is not taken into account in the calculations. Then, the fractional difference between the clocks can be written:

$$y(t) = \bar{y} + 2\alpha c^{-2}\vec{w} \cdot [\vec{v}_{\mathrm{A}}(t) - \vec{v}_{\mathrm{B}}(t)], \tag{5.9.17}$$

which can be approximated by a sine function:

$$y(t) = \bar{y} + 2c^{-2}\alpha \sin[2\pi(t - t_0)/T], \tag{5.9.18}$$

where T is the sidereal day and $t_0 = 57549.130$ (MJD). Therefore, the violation of LI can be interpreted as a daily periodic oscillation of the frequency ratio of the clocks. The comparisons were not performed simultaneously, therefore we always consider pairs of clocks. Then, clocks (SYRTE SrB, SYRTE Sr2, NPL Sr and PTB Sr) are composed in pairs: A: SYRTE Sr2 - NPL Sr, B: SrB - NPL Sr, C: SYRTE SrB & Sr2 - NPL Sr and

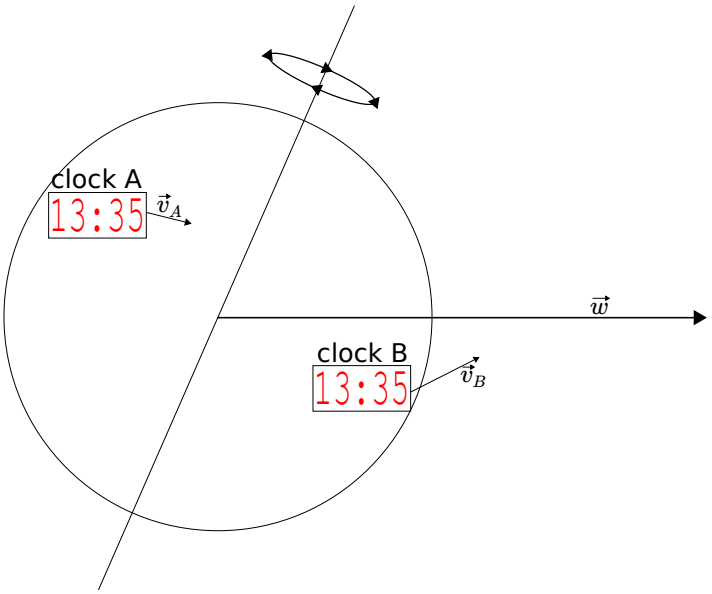

Figure 5.9.17. Relative velocity time dilation. Moving clocks have different orientations and norms of velocity vectors $\vec{v}_A$ and $\vec{v}_B$. The Earth moves with own velocity $\vec{w}$, much faster than the velocity of the clocks in the GCRS.

Table 5.9.3. α coefficient for given sets of clocks obtained from the fitting procedure.

	α (10^{-8})
A: SYRTE Sr2 - NPL Sr	+3.81 ± 8.41
B: SYRTE SrB - NPL Sr	-5.87 ± 7.78
C: SYRTE Sr2 & SrB - NPL Sr	-2.83 ± 6.19

D: SYRTE Sr2 - PTB Sr. For each pair, the violating parameter α and $\bar{y}$ are estimated as a fit parameters by using an affine invariant Markov Chain Monte Carlo ensemble sampler (MCMC) fitting method with 10^5 points. Clear and natural correlation like the flicker noise of the ultra-stable cavity in the short-term frequency stability of the clocks is included in the fitting procedure in the non-diagonal terms of the covariance matrix. In subset C, which combines data from SrB and Sr2, the correlations between these clocks are also included in the covariance matrix. The rest of correlation terms are less than 0.2.

Results for the comparison between SYRTE and NPL clocks are shown in table 5.9.3. They are obtained from 60 hours of useful data. The best constraint for the comparison between SYRTE and NPL is obtained from the C subset which includes the largest dataset: the combination of Parisian clocks and NPL Sr, for which the histogram and correlations of parameters are shown in figure 5.9.18

$$\alpha = (-2.83 \pm 6.19) \times 10^{-8}.$$

Analyzing the pair D of clocks (SYRTE Sr2 and PTB Sr) is more complicated. In a first analysis, similar to the analysis of the SYRTE-NPL comparison, the value of the LI violation parameter $\alpha = -4.5 \pm 0.9 \times 10^{-8}$ has resolved. It is the non-zero value with more than 5 σ and it could be interpreted as an oscillation of the LI violating signal. Therefore, it is necessary to investigate further, in order to exclude all systematic effects, which could be overlooked. As a first, the variations of the temperature were investigated. We include a temperature dependent term to the fit model with a scaling factor and a time lag as a free parameter, because the temperature measured in the

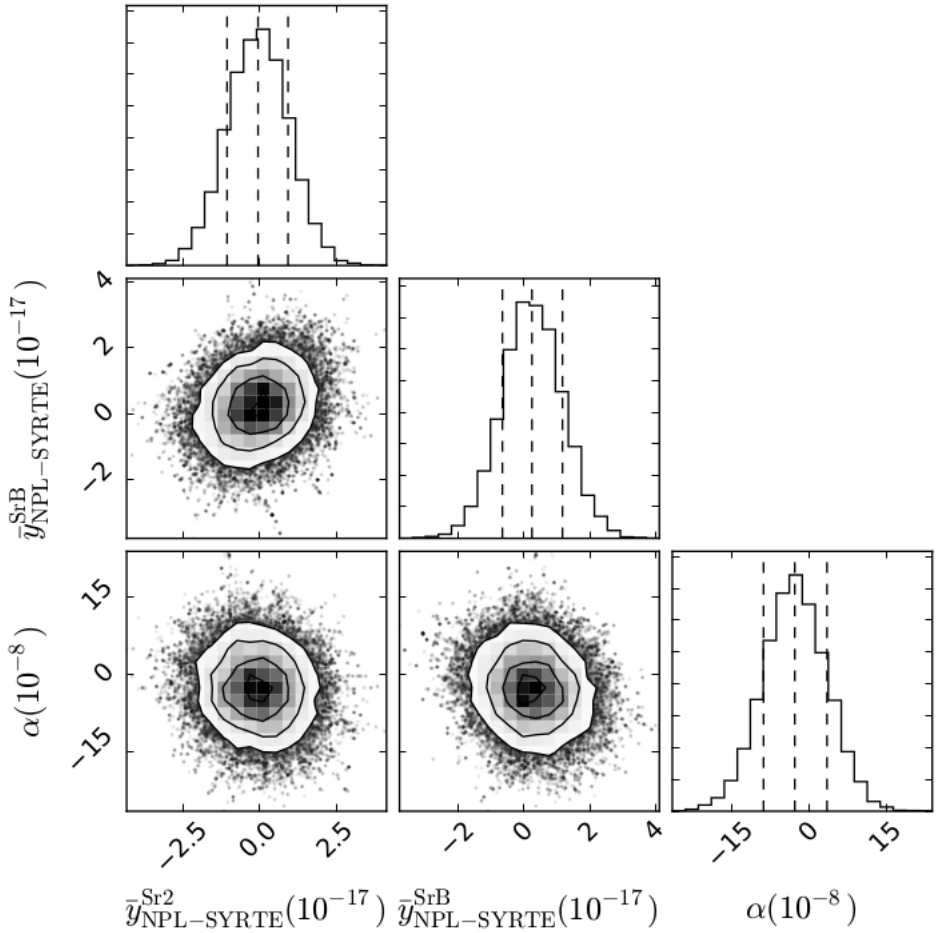

Figure 5.9.18. Histogram and correlations diagram of all data sets for SYRTE and NPL clock comparison.

Sr lab and the frequency difference between the clocks are significantly correlated, as depicted in figure 5.9.19, which shows all days of the comparison with averaged data and the model signal. Temperatures during these days increased really high as on June.

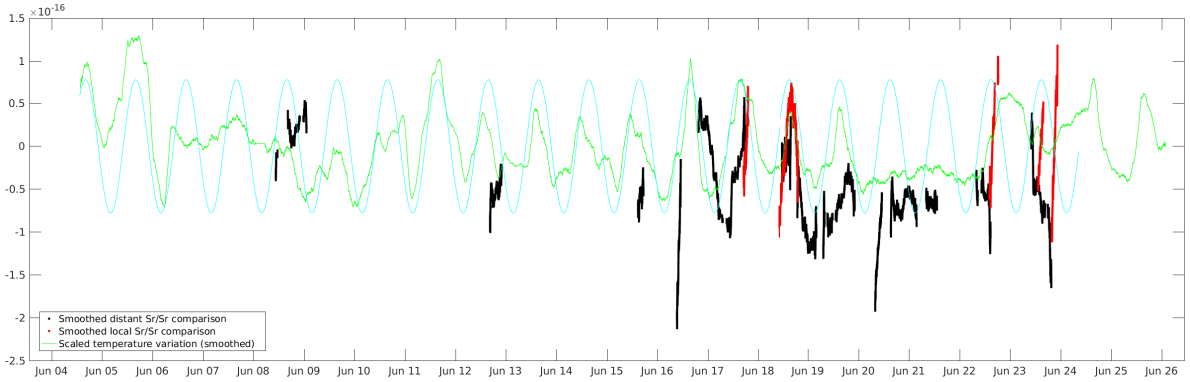

Figure 5.9.19. Simulated Lorentz violation oscillations (light blue oscillations), available data comparison (red and black) and temperature fluctuations (green) in the Sr laboratory during the campaign.

However, the temperature correction due to the black body radiation is applied to the clock frequency and the daily temperature variations should not have any contribution to the clock frequency difference. Moreover, the temperature of the science chamber,

where atoms are interrogated, is spread no more than 0.9 K. It corresponds to a 2 times smaller frequency shift than the observed signal. Nevertheless, the correlation is visible. Therefore, we introduce the temperature dependent coefficient α_T which influences the frequency ratio:

$$y_T(t) = \alpha_T[T_X(t - \delta t) - \bar{T}_X], \tag{5.9.19}$$

$T_X(t)$ is the temperature at location X and time t, $\bar{T}_X$ is the mean value of $T_X(t - \delta t)$ evaluated from comparison data times. The lag δt and α_T are given from fitting procedure. We apply this model to the frequency comparison and to the previous equation for the LI violation, we include the extra temperature dependent term $y_T(t)$:

$$y_D(t) = \bar{y}_D + y_T(t) + 2\alpha c^{-2}\vec{w} \cdot [\vec{v}_{\mathrm{SYRTE}}(t) - \vec{v}_{\mathrm{PTB}}(t)] \tag{5.9.20}$$

Using this model we obtained the following results: We can see that the temperature

Table 5.9.4. Fitting parameters for the pair D of clocks: Sr2 SYRTE- Sr PTB.

δt (hours)	α_T (1/K)	α
4.81 ± 0.25	$(1.76 \pm 0.12) \times 10^{-16}$	$-0.38 \pm 1.06 \times 10^{-8}$

data fit well with the frequency data and make the LI violation at 5 sigma disappear. It means that the temperature effect is the reason why we initially observed a violation, but it does not explain the physical source of the temperature variation. All collected data from this campaign does not give any clear evidence. Nevertheless, based on several facts, we can infer certain points. The effect does not come from PTB. The independent frequency ratio measurement between local Sr and Yb^+ at PTB performed at the same time did not show any temperature variation effects. It is in contrast to the data of the Sr clock laboratory at SYRTE, for which the temperature data fits better than any other temperature measurements. It seems that the effect might come from the Sr lab. On the other hand, there is a problem that the variations of the frequency of the clock comparison are shifted by 5-6 hours with respect to the model and temperature oscillations. This time lag does not correspond to the dynamics of any temperature effect. Even when we compare combinations of temperature series: inside the Sr SYRTE clock laboratory and the PTB clock, the clock laser and comb laboratories, outside laboratories (measured on the roof) and include a time difference in the solar day between Braunchweig and Paris. Temperature models do not explain the time lag. However, we do not have full information, because we have no temperature data from the comb laboratory at SYRTE.

Other possibilities are incorrectly applied de-drift to the ultra-stable cavity or an anomalous behavior of the clock laser. We focused on the longest quasi-continuous available data set from June 16 at 12 o'clock to June 18 at 4 o'clock, when the Sr clocks at SYRTE and PTB were working. Figures show the frequency difference between atoms and the ultra-stable cavity without applied de-drift 5.9.20, the frequency difference between atoms and the ultra-stable cavity with applied de-drift, its derivative 5.9.21. During that time, the frequency difference changed in total by 7000 Hz. The residual non compensated drift has opposite sign and it is smaller than ± 10 mHz/s, which is negligible at this level of precision. It seems that there is no correlation with the LI violating signal.

Moreover, during this longest quasi-continuous time interval, the Hg optical clock at SYRTE was partially operated and compared to the Sr clock. For this time interval Sr-Sr comparison, simulated LI and temperature variations and local Sr-Hg comparison data are depicted in figure 5.9.22. This local comparison data shows fluctuations with various time delays, which can not confirm the fact that the effect comes from the Sr lab.

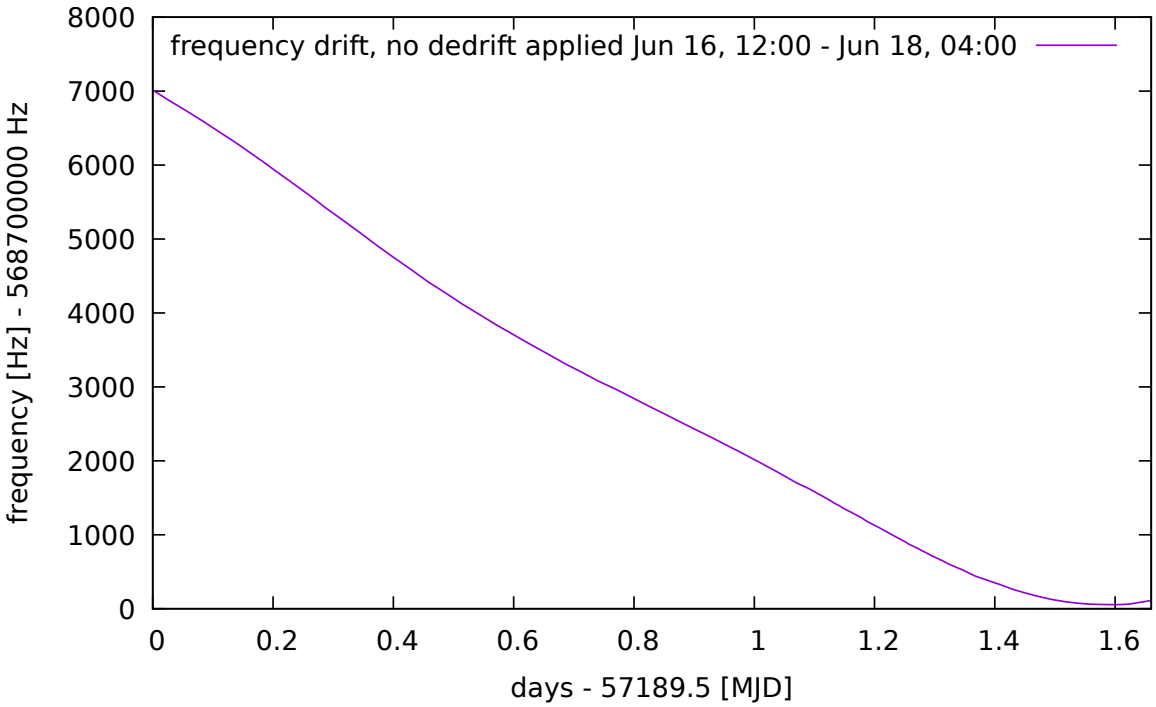

Figure 5.9.20. The frequency difference between atoms and the ultra-stable cavity with no applied de-drift.

The histogram and correlations of parameters are shown on figure 5.9.23.

It seems that only future comparisons can clarify and verify «the temperature effect», if it is a real temperature effect, another effect which was overlooked. In the future, with improved and more reliable optical clocks, fiber network and as well as better theoretical and more complex dynamical frameworks such as the Standard Extension Model or Dark Matter models, the results should set the new limit of LI violation.

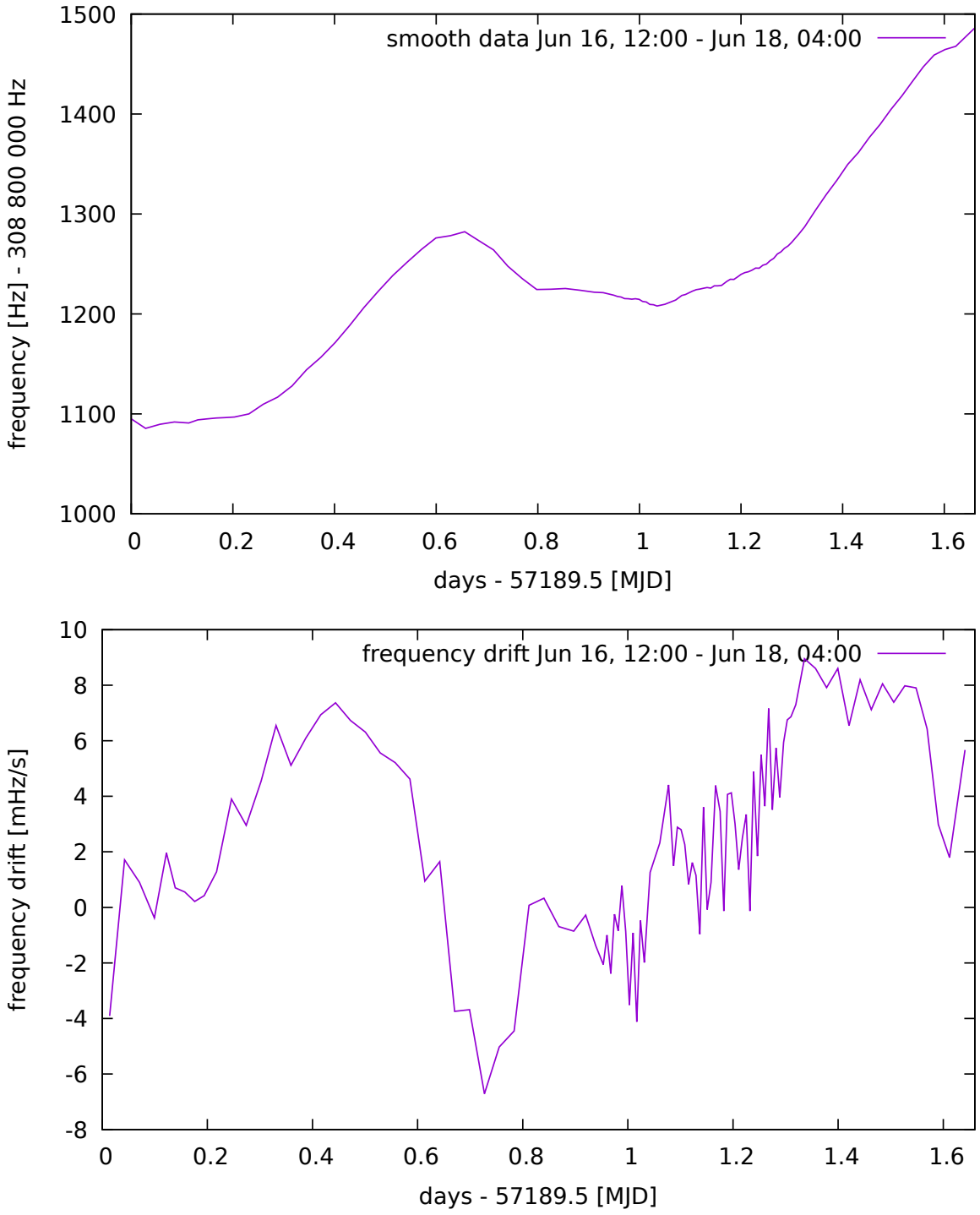

Figure 5.9.21. The frequency difference between atoms and the ultra-stable cavity with applied de-drift and its derivative.

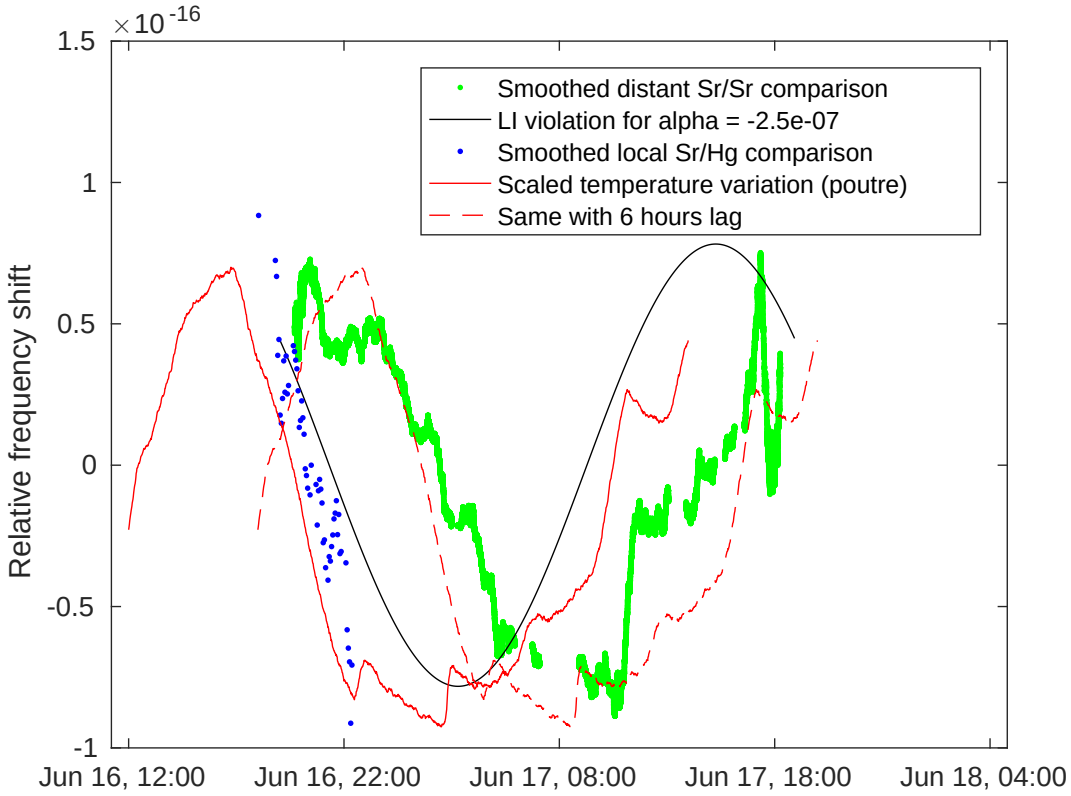

Figure 5.9.22. The longest and quasi-contiuous data slot for Sr-Sr comparison, simulated violating oscillations, temperature variations and local Sr-Hg comparison data.

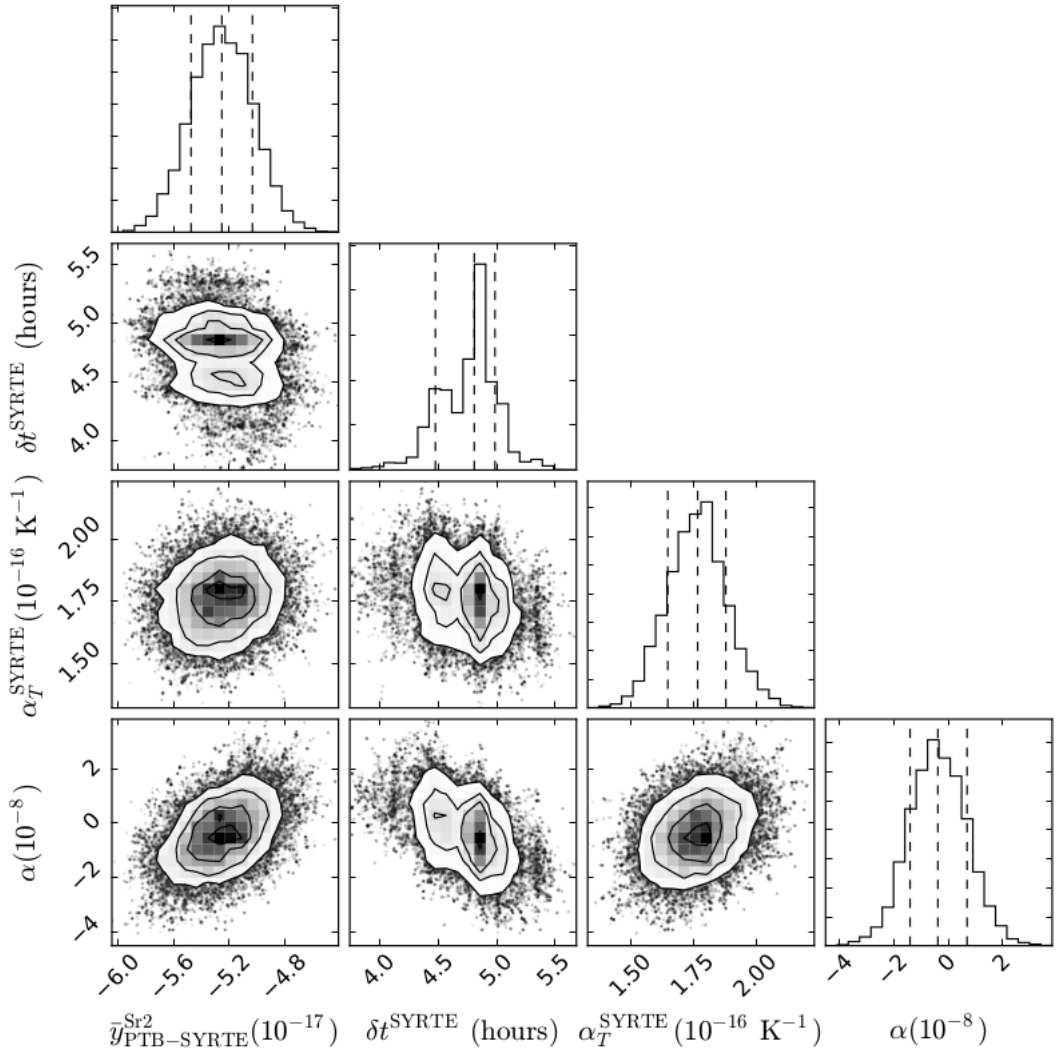

Figure 5.9.23. Histogram and correlations diagram of all data sets for SYRTE and PTB clock comparison.

CHAPTER 6

TEMPS ATOMIQUE INTERNATIONAL

Since 1955, when Essen and Parry calibrated the resonance frequency of the cesium standard with respect to Universal Time 2 (UT2, based on the most precise astronomical observations of Earth rotations), many institutions have started to develop, their own, local timescales, for instance the Greenwich Atomic (GA), A.1 of US Naval Observatory, which used atomic clocks for the daily calibration of quartz crystal clocks. In 1967 the Conférence Générale des Poids et Mesures (CGPM) defined the second as «the duration of 9 192 631 770 periods of the radiation corresponding to the transition between the two hyperfine levels of the ground state of the cesium 133 atom» [1,190,191]. The Bureau International de l'Heure (BIH) established timescale TA(BIH), initially limited to 3 contributed institutions, within the timescale institution TA(k), was able to track the time varying difference between the local timescale TA(k) and TA(BIH). The new timescale Temps Atomique International (TAI) has been established for the unification of time through an international atomic timescale, in order to coordinate time signals, compare different frequency standards in different places and times, and set a uniform time reference for astronomical objects. Beforehand, the unification was recommended by the International Astronomical Union (IAU) in 1967, the International Union of Radio Sciences in 1969 and the International Radio Consultative Committee (currently International Telecommunication Union) in 1970. TAI has been finally approved by Conférence Générale de Poids et Mesure (CGPM) in 1971 with the following definition: «The International Atomic Time is the time reference coordinate established by the Bureau International de l'Heure on the basis of the results given by the atomic clocks working in various establishments in accordance with the definition of the second, the time unit of the International System of Units». In 1980, the definition of TAI was clarified by the requirement of the relativistic approach: «TAI is a coordinate timescale defined in a geocentric reference frame with the SI second as realized on the rotating geoid as the scale unit.»

TAI is a uniform timescale based on the atomic second, but it is not disseminated directly. The reference timescale - Universal Coordinated Time (UTC) was defined as an international standard of timekeeping. UTC is a hybrid timescale. The class of «Universal Time» timescale includes timescales, synchronized to the mean solar day obtained from the Earth's rotation time. On the other hand, its definition is based on the SI second. Therefore (since 1972) UTC has combined different and unrelated values: UTC day and UTC second. Initially, UTC differed from TAI by ten seconds and over time in order to keep its time of day as close as possible to the Earth's rotation time, UTC must be

compensated by the insertion of, the so-called «leap seconds» [192]. It is a one-second adjustment predicted and announced by the International Earth Rotation and Reference System Service (IERS). The last, 27th «leap second» was implemented on December 31st 2016. Therefore, UTC is now shifted with respect to TAI by 37 seconds.

BIPM is the institution responsible for the calculation of UTC and TAI. The computation of UTC/TAI is based on the comparison (using GNSS or TWSTFT) between remote clocks spread worldwide. The participating institutions submit their own local realization of UTC(k) to BIPM. UTC is calculated from one-month long sets of data and presented in the form of [UTC - UTC(k)] in 5-day grids. The results are available in the BIPM Circular T with usual by 10 day delay after the last publication. UTC is not a «real time» timescale but an applied special model extrapolates of values of UTC from 10 days to 45 days. The process of calculation of UTC is divided into 3 steps, driven by a special algorithm, called ALGOS. In the first step, a weighted average of more than 450 contributing free running atomic clocks is calculated to establish the free atomic time scale EAL (échelle atomique libre). The difference $x_j(t)$ between EAL and a given contributing atomic clock obtained from ALGOS, is:

$$x_j(t) = \mathrm{EAL}(t) - h_j(t) = \sum_{i=1}^{N} w_i[h'_i(t) - x_{i,j}(t)], \tag{6.0.1}$$

$$x_{i,j}(t) = h_j(t) - h_i(t)$$

where N is the number of contributing clocks in a given month, w_i is the relative weight of clock H_i, $h_i(t)$ is the readout of clock H_i at time t, $h'_i(t)$ is the computed prediction of the readout of clock H_i and $x_{i,j}(t)$ is the time difference between the readouts of the clocks. The values w_i and $h'_i(t)$ are calculated by ALGOS. In the first case, this procedure optimizes and increases the long-term frequency stability of the EAL. An algorithm gives higher w_i and favors the clocks whose behavior is well predicted over time. In the second case, an algorithm counts the future behavior and frequency drift of clock $h'_i(t)$ with a monthly period. The number of clocks that contribute to the timescale varies from month to month. Then, by accurate predictions, we can avoid time and frequency jumps.

In the second step, to improve the accuracy of the timescale, EAL is compared to primary and secondary frequency standards in order to determine the relativistic frequency shift between the location of a given standard and a fixed point on the equipotential surface. Cesium primary frequency standards realize the SI second. Secondary frequency standards operate with other atoms than Cs, but their clock transition is accepted as a secondary representation of the SI second[1]. Then, a frequency steering correction is applied to EAL to be in agreement with the definition of the SI second. As a result, we get TAI. In order to keep an accurate and non-degrading long-term stability of TAI, the applied correction changes over time and it is regularly announced in advance in the BIPM Circular T. Therefore, the accuracy of TAI depends only on the performance of primary and secondary frequency standards.

In the last step, leap seconds are implemented to find agreement with UT1, the time based on the Earth's rotation. The new leap second is added when the difference between TAI and UT1 is more than 0.9 s. As the result we get UTC.

The high reliability and long term stability at the 10^{-16} level of UTC/TAI, better by one order of magnitude than a single commercial atomic clock, comes from the weighed average of the signals and the accumulation of as a large as possible number of contributing

[1] http://www.bipm.org/en/publications/mep.html

clocks, which are spread over the world, and connected by links which do not degrade the clock signals.

6.1 A Timescale with Optical Clocks

We mentioned that SYRTE is the department of the Laboratoire National de Métrologie et d'Essais (LNE) and it is the national institution responsible for the official national realization of UTC. Therefore, at LNE-SYRTE there are four H-masers and two microwave fountains: stationary and mobile fountains, based on Cs (FO1 and FOM) and one stationary dual Cs-Rb fountain (FO2-Cs and FO2-Rb). Fountains contribute to the elaboration of TAI under the direction of the Bureau International de Poids et Mesures: Cs fountains naturally as the primary representation of the SI second and Rb as a the secondary representation of the SI second. To realize the time scale UTC(OP), the system is equipped in 4 H-masers, among which one is chosen to be the reference H-maser H_{ref}. The phases of the other 3 H-masers are compared to H_{ref} with measurement interval 1 s. The ultra-stable microwave signal is provided by the free running cryogenic sapphire oscillator (CSO), which directly produces a 11.98 GHz signal, down-converted to 8.985 GHz, 1 GHz, 100 MHz signals. All signals are phase-locked to the H_{ref} which has an access to GNSS and TWSTFT satellite links. The optical-microwave metrology chain is described in the section 5.5. The down converted optical signal from the Sr clocks is connected with the 100 MHz signal from the H-maser via the 8.985 GHz signal generated from the CSO. The frequency ratio between H_{ref} and the ultra-stable laser is measured every second with a delay less than 10 μs and synchronized to the local time UTC(OP).

Since 2012, all microwave standards at LNE-SYRTE have contributed regularly to calibrations of TAI via continuous comparison to H_{ref} [193]. In general, nothing stands in the way to ask if optical clocks can contribute to TAI on the same rules as the secondary representation of the SI second - Rubidium [194], after a future re-definition of the SI second as the primary representation. Therefore, a contribution to TAI makes an important and essential step forward the re-definition of the SI second. We can expect that optical clocks, due to better accuracy and stability than microwave clocks, can improve current timescales. Unfortunately, problems with the reliability of optical clocks over several days makes hard to establish a timescale with optical clocks. Therefore, we have two options: implement for more reliable optical clocks (see the next section) or include intermittent-operated optical clocks into current timescales despite their short operating time [66, 170, 195]. In the latter case, intermittent optical clocks can be bridged by a local oscillator which can work over 5 days, for instance an H-maser. The most challenging part is an estimation of the uncertainty of the mean frequency of the H-maser during the time gaps when the clock is not operated. The lack of data need to be extrapolated, which causes the additional uncertainty. Because optical clocks reach the maser long term stability after a few minutes, theoretical simulations show that it is possible to achieve better performance of the timescale than by using continuously operated Cs fountains [195]. However, operating optical clocks during such small fraction of time (few minutes per day) requires reliable, predictable and extremely well behaved H-masers over a year. That H-masers are not commonly available in the time/frequency institutions. Nevertheless, the main benefit of using optical clocks is that the timescale is more predictable and the variations from UTC are much smaller [196].

Below, we show the first approach, in which optical clocks were operated and compared to H-maser in quasi continuous regime with uptimes up to 90%. The calibrations were

used to the first calibrations of TAI with optical clocks, which is an important step in the future possible optical architecture of the SI second.

6.2 Reliability of Clocks

For a practical realization of TAI with optical clocks, they must work reliably over longer time periods than the currently achievable few hours per day. It is not easy due to the high complexity of the optical clock system. To operate Sr OLCs, it is necessary to have 7 well-controlled lasers, the ultra-stable cavity and the optical frequency comb. These opto-electronical systems must be synchronized and work properly during all calibration periods. This is why, we equipped our clocks with intelligent systems, so that clocks can work over such long periods with minimum service. The most typical failures related with unlocking of lasers are detected, corrected by re-locking systems based on digital micro controllers, and the clock operation is restored to the right track. A correction of the drift of the ultra-stable cavity can be applied and it is matched automatically to the changing in time drift. Softwares collect, backs up all data. Information about the state of the clock, like number of atoms, transition probability, the difference between the clock frequency and the ultra-stable reference, temperature etc. are displayed in a graphical interface, which makes a monitoring of potential errors easier. The typical view of the interface is shown on figure 6.2.1. Data can be followed from remote localizations in real

Figure 6.2.1. The view of the monitoring software. In the left panel various colors indicate the difference states of parameters.

time. Another system is developed to analyze data. This software can show the frequency offset between Sr clocks, transition probability, etc. For selected data it can plot frequency stability represented by Allan deviation, Zeeman shift and 1st order lattice shift during the clock operation. The clocks can be operated in a frequency standard mode, providing

at each cycle a value for the ratio between the frequency of Sr clock transition and the frequency of the 100 MHz output of the H-maser in order to calibrate TAI.

We performed several calibrations of H_{ref} over at least 5 days of the conventional TAI grid:

- 10 days in October 2014 with Sr2 (MJD 56954 to 56964) with total up-time 93%,
- 22 days in June 2015 with Sr2 (MJD 57179 to 57199) with total up-time 83%,
- 10 days in March 2016 with Sr2 (MJD 57469 to 57479) with total up-time 66%,
- 15 days in June 2016 with Sr2 (MJD 57539 to 57554) with total up-time 66%.
- 15 days in June 2016 with SrB (MJD 57539 to 57554) with total up-time 74%

The traces of data presented on figures 6.2.2 and 6.2.3 show the best performance calibration campaign and the longest calibration campaign.

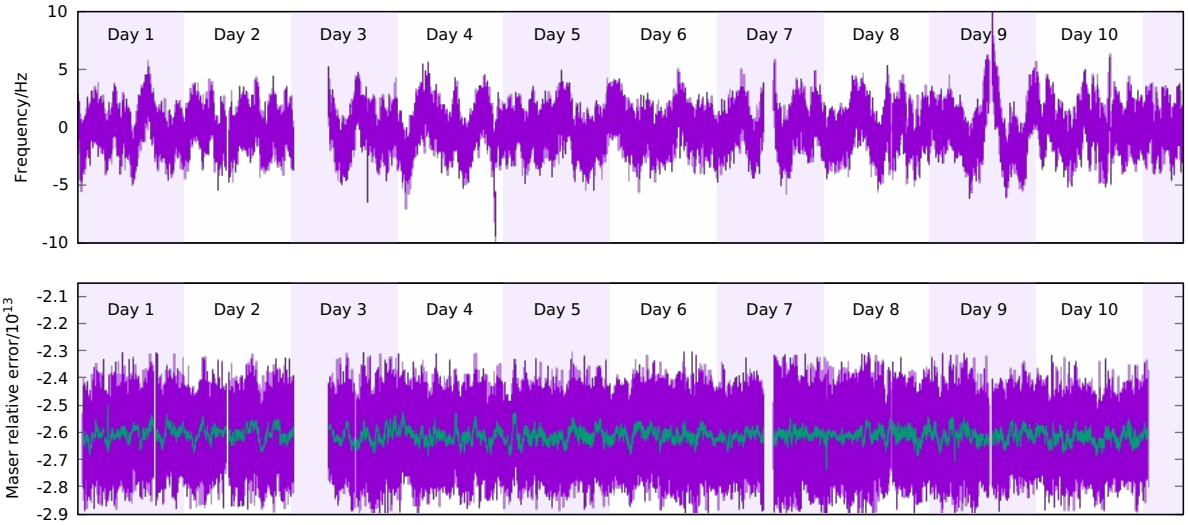

Figure 6.2.2. Campaign: October 24 2014 - November 02 2014 TOP: frequency difference between the clock (Sr2) and the resonance of the USC. The drift of cavity is removed by fitting by polynomial up to 5th order over successive intervals of 1 or 2 days. The residual fluctuations come from the thermal noise of the coatings of the ultra-stable cavity. BOTTOM: Hydrogen maser relative error (purple •) and its average over 100 s (green •) referenced against the Sr atoms via the frequency comb.

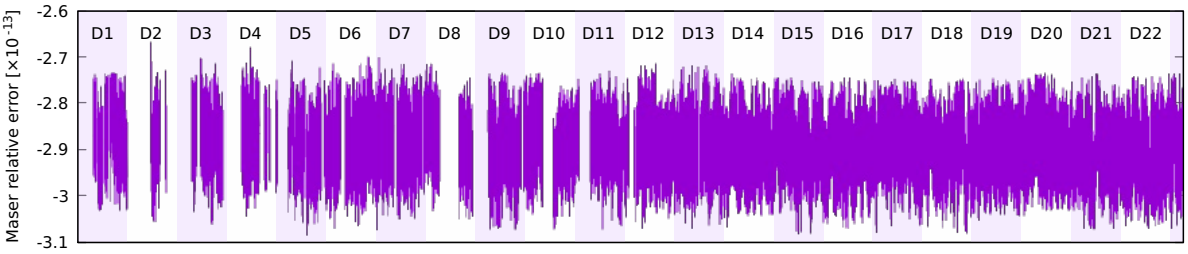

Figure 6.2.3. Campaign: June 4 - 25 June 2015. H-maser relative error referenced against the Sr atoms.

The system allows that clocks work unattended during the nights and the usual service can be done at day. Using developed system, our clocks run in nearly continuous regime.

Figure 6.2.4 shows the uptime of clock hour by hour with the fraction of valid points for the 10-day campaign in October 2014. The limitations of the clock operation are

Day	UTC	Points	Uptime
24/10	00:00	291	8,08%
	01:00	2081	57,81%
	02:00	3301	91,69%
	03:00	3364	93,44%
	04:00	3261	90,58%
	05:00	3348	93,00%
	06:00	2943	81,75%
	07:00	3289	91,36%
	08:00	3387	94,08%
	09:00	3375	93,75%
	10:00	3455	95,97%
	11:00	3416	94,89%
	12:00	3460	96,11%
	13:00	3505	97,36%
	14:00	3501	97,25%
	15:00	3476	96,56%
	16:00	3595	99,86%
	17:00	2032	56,44%
	18:00	3595	99,86%
	19:00	3597	99,92%
	20:00	3598	99,94%
	21:00	3596	99,89%
	22:00	3597	99,92%
	23:00	3599	99,97%
25/10	00:00	3599	99,97%
	01:00	3600	100,00%
	02:00	3600	100,00%
	03:00	3600	100,00%
	04:00	3593	99,81%
	05:00	3588	99,67%
	06:00	3600	100,00%
	07:00	3600	100,00%
	08:00	3594	99,83%
	09:00	2732	75,89%
	10:00	2565	71,25%
	11:00	3599	99,97%
	12:00	3592	99,78%
	13:00	3599	99,97%
	14:00	3591	99,75%
	15:00	3600	100,00%
	16:00	3600	100,00%
	17:00	3599	99,97%
	18:00	3600	100,00%
	19:00	3600	100,00%
	20:00	3080	85,56%
	21:00	3600	100,00%
	22:00	3596	99,89%
	23:00	3599	99,97%
	Total	160588	92,93%

Day	UTC	Points	Uptime
26/10	00:00	3090	85,83%
	01:00	0	0,00%
	02:00	0	0,00%
	03:00	0	0,00%
	04:00	0	0,00%
	05:00	0	0,00%
	06:00	0	0,00%
	07:00	0	0,00%
	08:00	704	19,56%
	09:00	2766	76,83%
	10:00	3594	99,83%
	11:00	3580	99,44%
	12:00	3597	99,92%
	13:00	3594	99,83%
	14:00	2686	74,61%
	15:00	3199	88,86%
	16:00	3585	99,58%
	17:00	3264	90,67%
	18:00	3596	99,89%
	19:00	3593	99,81%
	20:00	3593	99,81%
	21:00	3596	99,89%
	22:00	3594	99,83%
	23:00	3596	99,89%
27/10	00:00	3595	99,86%
	01:00	3598	99,94%
	02:00	3595	99,86%
	03:00	3594	99,83%
	04:00	3597	99,92%
	05:00	3590	99,72%
	06:00	3598	99,94%
	07:00	3374	93,72%
	08:00	3598	99,94%
	09:00	3587	99,64%
	10:00	3600	100,00%
	11:00	3597	99,92%
	12:00	3594	99,83%
	13:00	3569	99,14%
	14:00	3598	99,94%
	15:00	3590	99,72%
	16:00	3590	99,72%
	17:00	3600	100,00%
	18:00	3599	99,97%
	19:00	3592	99,78%
	20:00	3596	99,89%
	21:00	3592	99,78%
	22:00	3480	96,67%
	23:00	3600	100,00%
	Total	141150	81,68%

Day	UTC	Points	Uptime
28/10	00:00	3597	99,92%
	01:00	3600	100,00%
	02:00	3599	99,97%
	03:00	3599	99,97%
	04:00	3600	100,00%
	05:00	3600	100,00%
	06:00	3599	99,97%
	07:00	3600	100,00%
	08:00	3559	98,86%
	09:00	3598	99,94%
	10:00	3571	99,19%
	11:00	3600	100,00%
	12:00	3599	99,97%
	13:00	3597	99,92%
	14:00	3599	99,97%
	15:00	3599	99,97%
	16:00	3598	99,94%
	17:00	3600	100,00%
	18:00	3598	99,94%
	19:00	3600	100,00%
	20:00	3597	99,92%
	21:00	3591	99,75%
	22:00	3599	99,97%
	23:00	3599	99,97%
29/10	00:00	3569	99,14%
	01:00	3600	100,00%
	02:00	3600	100,00%
	03:00	3600	100,00%
	04:00	3600	100,00%
	05:00	3600	100,00%
	06:00	3600	100,00%
	07:00	3600	100,00%
	08:00	3594	99,83%
	09:00	3592	99,78%
	10:00	3600	100,00%
	11:00	3600	100,00%
	12:00	3600	100,00%
	13:00	3593	99,81%
	14:00	3599	99,97%
	15:00	3596	99,89%
	16:00	3594	99,83%
	17:00	3600	100,00%
	18:00	3595	99,86%
	19:00	3594	99,83%
	20:00	3591	99,75%
	21:00	3422	95,06%
	22:00	3596	99,89%
	23:00	3600	100,00%
	Total	172433	99,79%

Day	UTC	Points	Uptime
30/10	00:00	3600	100,00%
	01:00	3600	100,00%
	02:00	3598	99,94%
	03:00	3599	99,97%
	04:00	3600	100,00%
	05:00	3594	99,83%
	06:00	3594	99,83%
	07:00	3600	100,00%
	08:00	3599	99,97%
	09:00	3600	100,00%
	10:00	2481	68,92%
	11:00	0	0,00%
	12:00	0	0,00%
	13:00	3298	91,61%
	14:00	3590	99,72%
	15:00	3574	99,28%
	16:00	3580	99,44%
	17:00	3597	99,92%
	18:00	3595	99,86%
	19:00	3596	99,89%
	20:00	3568	99,11%
	21:00	3589	99,69%
	22:00	3595	99,86%
	23:00	3598	99,94%
31/10	00:00	3588	99,67%
	01:00	3594	99,83%
	02:00	3600	100,00%
	03:00	3597	99,92%
	04:00	3598	99,94%
	05:00	3592	99,78%
	06:00	3595	99,86%
	07:00	3593	99,81%
	08:00	3598	99,94%
	09:00	3595	99,86%
	10:00	3595	99,86%
	11:00	3594	99,83%
	12:00	3600	100,00%
	13:00	3453	95,92%
	14:00	3593	99,81%
	15:00	2318	64,39%
	16:00	3600	100,00%
	17:00	3596	99,89%
	18:00	3178	88,28%
	19:00	3598	99,94%
	20:00	3595	99,86%
	21:00	3596	99,89%
	22:00	3599	99,97%
	23:00	3600	100,00%
	Total	162110	93,81%

Day	UTC	Points	Uptime
01/11	00:00	3599	99,97%
	01:00	3600	100,00%
	02:00	3594	99,83%
	03:00	3596	99,89%
	04:00	3598	99,94%
	05:00	3599	99,97%
	06:00	3596	99,89%
	07:00	3600	100,00%
	08:00	3597	99,92%
	09:00	3598	99,94%
	10:00	3594	99,83%
	11:00	3590	99,72%
	12:00	3600	100,00%
	13:00	1515	42,08%
	14:00	2733	75,92%
	15:00	3600	100,00%
	16:00	3600	100,00%
	17:00	3600	100,00%
	18:00	3600	100,00%
	19:00	3600	100,00%
	20:00	3600	100,00%
	21:00	3599	99,97%
	22:00	3600	100,00%
	23:00	3600	100,00%
02/11	00:00	3599	99,97%
	01:00	3600	100,00%
	02:00	3600	100,00%
	03:00	3600	100,00%
	04:00	3600	100,00%
	05:00	3600	100,00%
	06:00	3591	99,75%
	07:00	3594	99,83%
	08:00	3600	100,00%
	09:00	3600	100,00%
	10:00	3599	99,97%
	11:00	3600	100,00%
	12:00	3600	100,00%
	13:00	3600	100,00%
	14:00	3540	98,33%
	15:00	3600	100,00%
	16:00	3119	86,64%
	17:00	3599	99,97%
	18:00	3600	100,00%
	19:00	3599	99,97%
	20:00	3599	99,97%
	21:00	3598	99,94%
	22:00	3595	99,86%
	23:00	3598	99,94%
	Total	169238	97,94%

Total	805519	93,23%

Figure 6.2.4. Fraction of valid points during the campaign October 24 2014 to November 2 2014.

related with the misalignment of drain laser beams, the optimization of the number of atoms in the trap, or the amplitude noise of the pump laser (Coherent Verdi V10) of the TiSa laser. The first problems can be solved only manually and require interruptions, but it can be done during other services. The latter problem was partially solved by an external service, but random and accidental behavior of this amplitude noise is hard to control. Nevertheless, the clocks are only one part of the whole chain and other problems could limit the performance of calibrations for instance the optical frequency comb. The distribution of interruptions is shown on figure 6.2.5, and it is clear that for this campaign the majority of problems does not come from the clock.

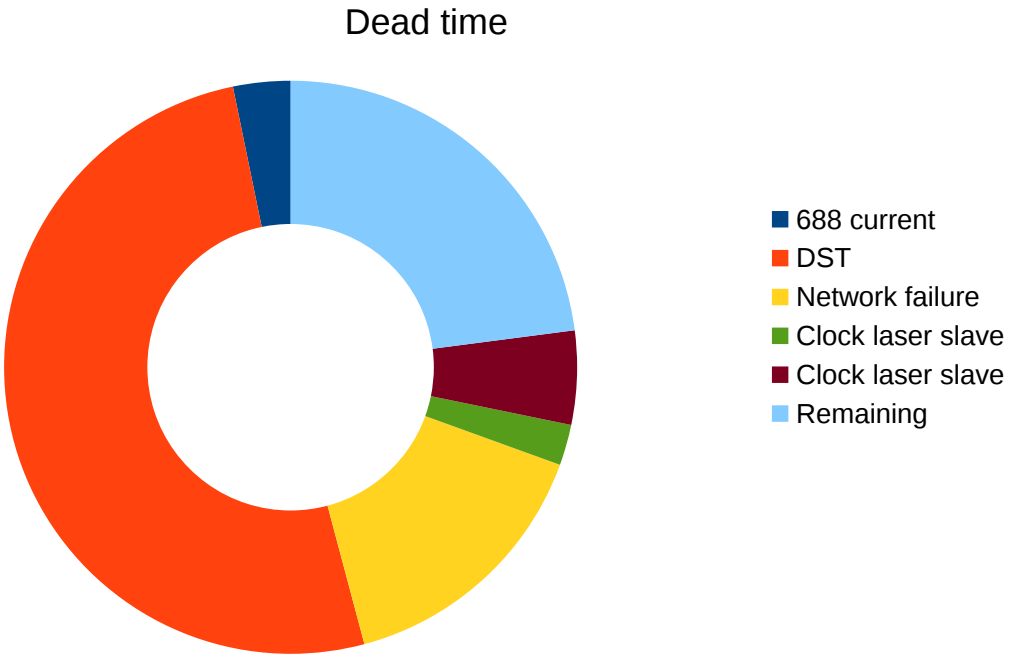

Figure 6.2.5. Distribution of interruptions during the campaign October 24 2014 to November 2 2014. DST - Daylight saving time, Clock laser slave for Sr1 and Clock laser slave for Sr2.

6.3 Estimation of Uncertainty of Dead Times

The estimation of the average frequency of the frequency standard, reference H-maser (H_{ref}), is required after each five-day TAI grid. The total average frequency of the H-maser is given at the middle of estimation time and it is determined from the averaged points with the unweighted linear drift of H-maser removed. Despite the excellent performance of our optical clocks over time, there are time intervals in which clocks are off and are not compared to the H-maser. Therefore, it is necessary to estimate the additional uncertainty due to these dead times. The method used to estimate this uncertainty is based on two publications [197, 198]. Let us consider that we have two time intervals: A and B: $\tau_A = t_2 - t_1$ and $\tau_B = t_4 - t_3$. During the time interval A, the frequency standard is calibrated. During the time interval B, we want to estimate an average frequency, based on information from interval A. The time intervals A and B are separated by some time gap t, the so-called «dead time», as shown on figure 6.3.6. In general, the time interval B can be earlier than the calibration interval A or it can partially or totally overlap the interval A. Therefore, $t = t_3 - t_2$ can be not only positive but also negative (when τ_A and τ_B are overlapped). The indefinite integral over $y(t)$, the so-called «phase» of the frequency standard relative to an ideal standard, is defined as $x(t) = \int_0^t y(t')dt'$. For a calibration interval τ_A and an estimation interval τ_B, the simplest and usually the best estimator is an average of the reference standard relative to an ideal standard, for instance, for interval A: $[t_1, t_2]$:

$$\bar{y}_A = \frac{x(t_2) - x(t_1)}{t_2 - t_1}. \tag{6.3.2}$$

The estimation of the frequency of the interval B requires to include the additional uncertainty caused by the average-frequency transfer process, because during interval t, the value of the frequency is unknown. In such process, it corresponds to the variance, which

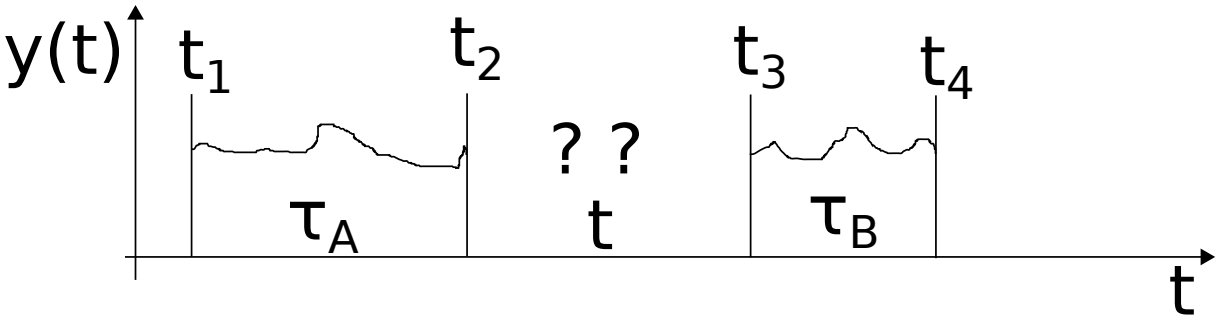

Figure 6.3.6. Frequency calibration with one dead time.

is the mean-square difference between frequencies of period t_A and t_B:

$$U^2 = \left\langle \left[\frac{x(t_4) - x(t_3)}{t_4 - t_3} - \frac{x(t_2) - x(t_1)}{t_2 - t_1} \right]^2 \right\rangle = \langle (\bar{y}_B - \bar{y}_A)^2 \rangle. \tag{6.3.3}$$

To properly evaluate the uncertainty of the transfer process, we need to know the noise characteristics of our oscillator. For each class of noise, the variance must be evaluated separately and the total variance for the process can be expressed as:

$$U^2(\tau_A, \tau_B, t) = \sum_{-2}^{2} s^2_{y[\alpha]} \mathcal{F}_{AB[\alpha]}, \tag{6.3.4}$$

where summation indexes indicate the class of noise $\alpha = \{-2, -1, 0, 1, 2\}$ according to the power law noise, $s^2_{y[\alpha]}$ is the Allan deviation for a given class of noise. $\mathcal{F}$ is the $A - B$ structure factors which describe the limiting ratio of the variance U^2 to the Allan variance $\sigma^2_y(\tau_0)$. $\mathcal{F}$ describes how much the variance of the estimation interval is larger than the Allan variance of the calibration interval.

In calibrations to TAI, we are interested in measuring the average frequency of the reference standard and an estimation of its uncertainty for the whole time interval. It means that the estimation interval τ_B takes 5 days (or a multiply of 5). During calibration, we have several live measurements τ_A and dead time intervals t, which both are part of t_B. Let us consider, we have N live measurements and $N - 1$ dead times in interval τ_A, as shown in figure 6.3.7. According to our notation, the dead time t is negative and time intervals τ_A and τ_B are overlapped. In this case, due to the number of calibration intervals, the variance must include additionally normalized weights a_i:

$$U^2 = \left\langle \left[\sum_{i=1}^{N} a_i y_i - y_B \right]^2 \right\rangle, \tag{6.3.5}$$

where y_i is a frequency measured during a given calibration interval A, y_B is the frequency of the estimation interval. For the stationary signal, equation 6.3.5 evolves to the case with the distributed live measurements:

$$U^2 = \sum_{i}^{N} a_i \langle (y_i - y_B)^2 \rangle - \frac{1}{2} \sum_{i,j=1}^{N} a_i a_j \langle (y_i - y_j)^2 \rangle \tag{6.3.6}$$

The part $\langle (y_i - y_B)^2 \rangle$ in the first term is just the variance of the transfer process, shown in the equations 6.3.3. The second part of the equation is the covariance term of all possible

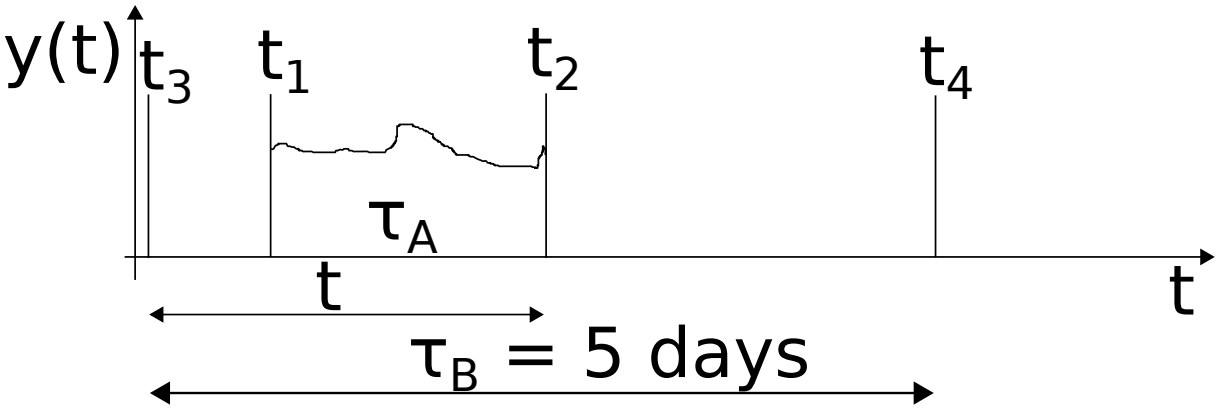

Figure 6.3.7. Frequency calibration over 5 days at SYRTE.

combinations between two live measurements. The total uncertainty is a combination of uncertainties a_i, $\langle (y_i - y_T)^2 \rangle$ and $\langle (y_i - y_j)^2 \rangle$ and they can be found in [199]. We can simply assume that all live measurements are equivalent and then, all a_i are the same. But to have the minimum uncertainty of the estimation interval, weights a_i should not be the same. To find the minimum of the variance U^2 we can use the method of Lagrange multipliers, known from mechanics. According to this method, we build the Lagrange function defined by:

$$\mathcal{L} = U^2 + \lambda \left(\sum_{i=1}^{N} a_i - 1 \right) \tag{6.3.7}$$

The minimum can be found by solving $\nabla_{a_i,\lambda} \mathcal{L} = 0$:

$$\frac{\partial \mathcal{L}}{\partial a_i} = \langle (y_i - y_B)^2 \rangle - \sum_{j=1}^{N} a_j \langle (y_i - y_j)^2 \rangle + \lambda = 0, \tag{6.3.8}$$

$$\frac{\partial \mathcal{L}}{\partial \lambda} = \sum_{i=1}^{N} a_i - 1 = 0. \tag{6.3.9}$$

We obtain the optimum of the whole $N+1$ weights from $N+1$ equations. Yu et al. [198] show that the uncertainty is smaller for distributed and scattered dead times than for one lumped dead time (on order of days), even when the overall time duration in both cases is the same.

Presented method, correct and elegant on the mathematical point of view, is based only on the theoretical model of the H-maser. At SYRTE, it is hard to build a model with combined CSO and H-maser microwave chain, therefore, the used conservative method always overestimates the uncertainty. For now, 3 applied models show slightly different values of the uncertainty by a factor of 2 between them. So far, we used alternative method. The estimation of the additional uncertainty due to the dead time was based on the empirical data of the H_{ref} and another H-maser. During the whole time of comparison with Sr clock the phase of the H_{ref} is compared with the phase of the other H-maser - number 140 0809. Then, the uncertainty due to the dead times $\sigma_{y_{DT}}$ is obtained from the normalized phase difference $\sigma^2_{x_j}$ of each dead time i with the removed linear frequency drift and divided by total time T of the estimation interval:

$$\sigma_{y_{DT}} = \frac{\sqrt{\sum_i \sigma^2_{x_j}}}{T}. \tag{6.3.10}$$

Nevertheless, a well behaved and characterized H-maser, for which an application of the model is easy, makes easier the calibration process. At NICT, an optical clock calibrates an excellent H-maser. By having such H-maser, it is possible for intermittent measurements, during which the local optical clock is operated only by 3 hours per day. The obtained uncertainty associated with the dead time (deterministic and stochastic parts) is comparable with our results [170]. On the other hand, the noise characteristics of the H-maser can evolve over time and to avoid such possible problems, at SYRTE, the reference H-maser is, typically, calibrated by Sr optical clock during a time interval at least ten days (two TAI grids) with as large as possible uptime. The dead time is defined as a time interval longer than 600 s. For the reference H-maser is applied a noise characterization expressed as a Allan deviation: white frequency noise $s^2_{y,[0]} = 2 \times 10^{-16}$ at one day, flicker frequency noise $s^2_{y,[-1]} = 1.2 \times 10^{-15}$ and random walk $s^2_{y,[-2]} = 0$. The uncertainties due to the dead times for both methods are similar and are as follows: 1×10^{-16} using the noise model and 0.5×10^{-16} using the empirical data. Dead times on order of one hour contribute the most to the uncertainty in both cases.

6.4 Contribution to TAI

The calibrations presented above constitute a first contribution of optical clock to TAI as a secondary representation of SI second. After each comparison, a report was prepared with the H-maser calibrations and the evaluation of uncertainties. Such reports together, with a summary, were submitted to BIPM on August 2016. The summary includes 5 pub-

3 - Duration of the TAI scale interval *d*.

Table 1: Estimate of *d* by individual PSFS measurements and corresponding uncertainties.
All values are expressed in 10^{-15} and are valid only for the stated period of estimation.

Standard	Period of Estimation	*d*	u_A	u_B	$u_{l/lab}$	$u_{l/Tai}$	*u*	$u_S$rep	Ref(u_S)	Ref(u_B)	u_B(Ref)	Steer	Note
PTB-CS1	57784 57809	-18.71	6.00	8.00	0.00	0.15	10.00	PFS/NA		T148	8.	Y	(1)
PTB-CS2	57784 57809	-0.28	3.00	12.00	0.00	0.15	12.37	PFS/NA		T148	12.	Y	(1)
SYRTE-FO2	57784 57809	-1.30	0.40	0.32	0.11	0.32	0.61	PFS/NA		T301	0.23	Y	(2)
SYRTE-FORb	57784 57809	-0.91	0.20	0.29	0.11	0.32	0.49	0.7 [1]		T328	0.34	Y	(2)
SYRTE-SR2	56954 56964	0.81	0.20	0.04	0.10	0.53	0.57	0.5 [1]		[2]	0.05	N	(3)
SYRTE-SR2	57179 57199	0.46	0.20	0.04	0.10	0.28	0.36	0.5 [1]		[2]	0.05	N	(3)
SYRTE-SR2	57469 57479	-1.39	0.25	0.20	0.11	0.53	0.63	0.5 [1]		[2]	0.05	N	(3)
SYRTE-SR2	57539 57554	-1.24	0.30	0.04	0.11	0.37	0.49	0.5 [1]		[2]	0.05	N	(3)
SYRTE-SRB	57539 57554	-1.22	0.25	0.05	0.10	0.37	0.46	0.5 [1]		[2]	0.05	N	(3)
PTB-CSF2	57779 57809	-1.36	0.09	0.20	0.03	0.13	0.26	PFS/NA		T287	0.41	Y	(4)

Notes:
(1) Continuously operating as a clock participating to TAI
(2) Report 03 MAR. 2017 by LNE-SYRTE
(3) Report 16 AUG. 2016 by LNE-SYRTE
(4) Report 02 MAR. 2017 by PTB
[1] CIPM Recommendation 2 (CI-2015) : Updates to the list of standard frequencies in Proces-Verbaux des Seances du Comite International des Poids et Mesures, 104th meeting (2015), 2016, 47 p.
[2] Optical to microwave clock frequency ratios with a nearly continuous strontium optical lattice clock. Lodewyck J., Bilicki S., Bookjans E., Robyr J.L., Shi C., Vallet G., Le Targat R., Nicolodi D., Le Coq Y., Guena J., Abgrall M., Rosenbusch P. and Bize S.. Metrologia 53(4), 1123, 2016.

Figure 6.4.8. Calibration data reported to BIMP in April 2017 Circular T350.

lications containing all information about the performance, reproducibility and agreement of the LNE-SYRTE Sr clocks with various microwave and optical clocks [46, 61, 105, 106]. This submission was reviewed by the Working Group on Primary and Secondary Fre-

quency Standards (WGPSFS). In April 2017, after a positive recommendation, the BIPM published the first calibrations of TAI with optical clocks in the BIPM Circular T350 [107] (the screen shot presented on figure 6.4.8). LNE-SYRTE plans to contribute regularly to TAI with both Sr clocks with a minimum of two calibrations of 10 days per year. These first contributions to TAI show that the ultra-narrow optical resonance in Sr atoms is no longer a candidate to be the a new frequency primary standard but has already evolved to be it. Moreover, optical clocks made progress toward replacing the currently microwave time and frequency architecture which realize the SI second.

6.5 SYRTE-NICT

We have shown above that TAI is used as a timescale with a 10^{-16} accuracy level, because for most of the time cesium fountains provide a calibration service of the frequency of TAI. Using a satellite-based link to TAI and a commercial H-maser we can compare clocks. But for clock comparisons, we use TAI as a flywheel. During June 2016, from MJD 57539 to 57549 (two 5-day grids), Sr1 and Sr2 at SYRTE and another Sr clock at NICT in Tokyo in Japan calibrated own their H-masers. Synchronously calibration of TAI has an advantage that its noise and inaccuracy cancel out, up to the performances of the satellite links. The calibration procedure at LNE-SYRTE is described above. At NICT it was performed in a different way than at LNE-SYRTE. In contrast, NICT did not operate their Sr clock in a quasi-continuous regime. Because the Japanese H-maser is well characterized, the Japanese clock can be intermittently operated during 10^3 to 10^4 s each day, and based on this short-time calibration time, the deterministic and stochastic behaviors of the H-maser were evaluated for the whole 10 days [170, 196]. The deterministic features are obtained by applying a linear fit to the 10 days results. The stochastic behavior is evaluated based on the phase noise characteristics of the H-maser. To improve the link uncertainty of the measurement, the campaign was extended to two 5-day grids, instead of 1 grid, and as well as by employing a combination of two H-masers. At each institute, the H-maser provides the local reference to the GPS receiver, therefore both H-masers can be directly compared via GPS IPPP method [176]. This protocol counts the phase data integer ambiguities at the un-differenced level. It needs not only a precise GPS satellite orbits and clock data but also the determination of wide lane satellite biases. SYRTE and NICT are effectively connected because both institutions send to BIPM data about 1) the frequency comparison of their H-maser and Sr clock and 2) information about the time difference and the frequency transfer of GPS. Based on this information, and using special algorithms, BIPM can calculate the frequency ratio of clocks.

The general scheme is shown on figure 6.5.9. The optical frequency of Sr clocks at each institute is down-converted to 100 MHz via the optical frequency comb. Then the 100 MHz signal is compared to the 100 MHz signal of the H-maser, which has an access to the satellite link. More details about the TAI chain at LNE-SYRTE is described in the previous sections. The details about NICT can be found in [68, 170], but in principle they are similar. The main difference is that the Japanese clock is effectively compared with two H-masers during its operation, when at SYRTE the data of second H-maser is used during dead times of Sr clock.

The frequency offset between two Sr clocks obtained by G. Petit from BIPM is:

$$\mathcal{C} = \frac{\nu_{\mathrm{LNE-SYRTE}} - \nu_{\mathrm{NICT}}}{\nu^0_{Sr}} = (-4.8 \pm 8) \times 10^{-16}.$$

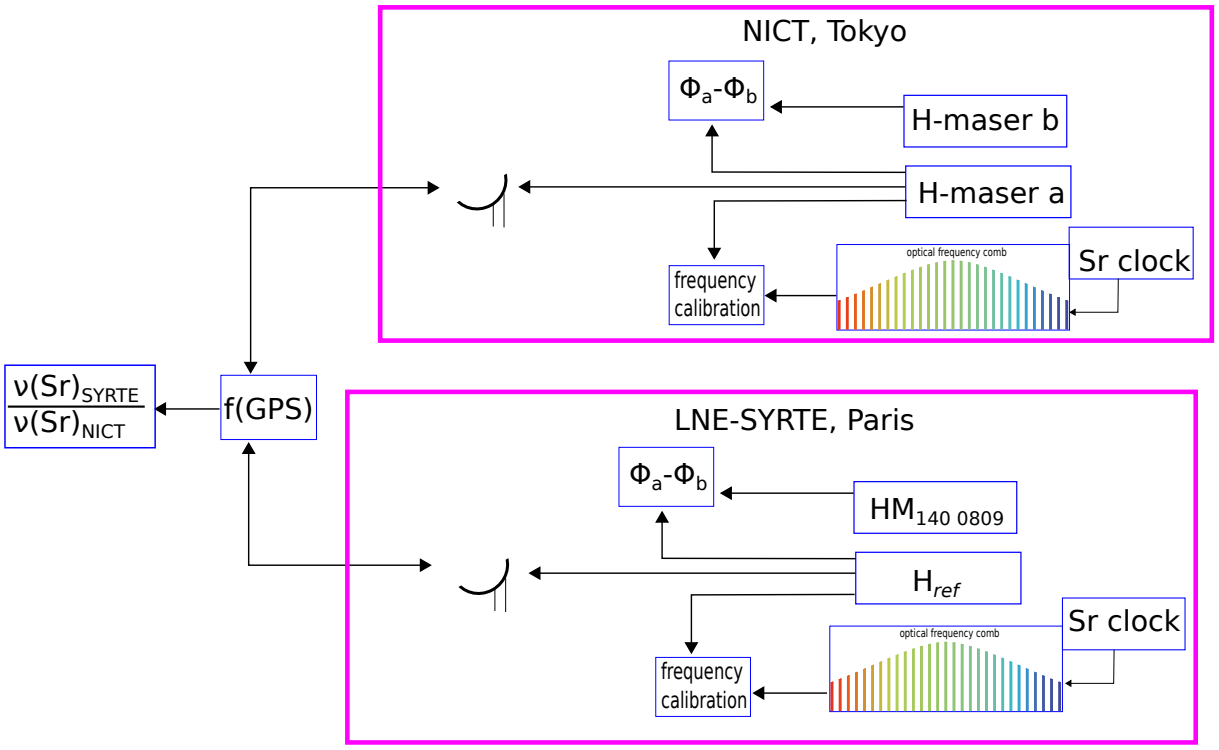

Figure 6.5.9. Basic conception of the common calibration. Using optical frequency comb Sr clock at each institute is connected to own H-maser, which is the source of the local realization of UTC during the measurement.

Table 6.5.1. Uncertainty budget in 10^{-17} of common calibration of TAI for each institute in June 2016.

		SYRTE	NICT
Strontium	systematic	4.4	6
Gravity		1	2
H-maser	deterministic	30	18
	dead time	4	10
TOTAL		**31**	**21**

The measurement is limited by the evaluation of the frequency of the H-maser and satellite link, which can be evaluated with a few parts at the 10^{-16} level, even when the most precise GPS IPPP method is applied. The uncertainties of two clocks are negligible. Nevertheless, we found an agreement within combined uncertainties between two completely independent clocks. Currently, it is the only way to directly compare optical clocks at intercontinental scale. In the future, we will be able to perform better comparisons when the Pharao/ACES program is finished.

CHAPTER 7

A LATTICE WITH SEMICONDUCTOR SOURCES

Sr OLCs promise to become a powerful tool for relativistic geodesy. In order to exploit the full potential of OLCs in geosciences, OLCs should be transportable, and consequently a miniaturization of the apparatus is required. One of the largest problems with the miniaturization is the lattice laser source at 813 nm. Because the lattice light is continuously on during the clock cycle, it is essential that the light source is spectrally pure, because any incoherent background detuned from the magic wavelength would induce a light shift. In most experiments, a Titanium-Sapphire (TiSa) laser is used to generate the lattice potential, as it guarantees a high spectral purity with an uncertainty at the 10^{-18} level [61]. Unfortunately, TiSa lasers occupy a lot of space and power (compared to the other clock components). On the other hand, semiconductor sources look promising in view of their volume, but tests on clocks that were carried out with these sources show a frequency shift due to the incoherent background [132, 200, 201] (see figure 7.0.1). It was identified that the Amplified Spontaneous Emission (ASE) coming from semiconductor sources induces a shift at the Hz level. This shift depends on a given TA chip, and it changes with the aging of the chip. Then, an extrapolation of the light-shift to zero trap depth can be error prone, giving wrong results up to several 10^{-15}. To avoid these problems, we decided to resign from using the semiconductor source and replace it with a Titanium-Sapphire laser. But this does not solve the problem in the miniaturization point of view. In order to reach uncertainties in the 10^{-17} range, we need a quantitative study to determine the systematic uncertainty of the frequency shifts induced by the incoherent background of different possible laser sources.

In this chapter, we will describe my studies of this problem. We have tried to understand the behavior of the incoherent part of the spectrum of semiconductor sources, and apply filtering systems to have a better spectral purity. The chapter is organized as follows: first, we present the experimental set-up, describe experimental conditions and characterize optical filters that can be used to reach a better spectral purity. Second, we propose a theoretical method for the estimation of the light shift, based on the spectral distributions, and we show the experimental differential comparison to measure directly the ASE induced light shift. Next, we characterized all available lattice laser sources in our laboratory: TiSa laser and semiconductor sources. The obtained spectral distributions were extrapolated in a broad frequency range and are used in the theoretical model. In the last part of this chapter, the estimated theoretical light shifts are compared to the experimental results, including various experimental conditions. These measurements

allow us to understand the light-shifts induced by the ASE and to determine systematic effects for all sources and test if the TA can be a suitable light source for the optical lattice.

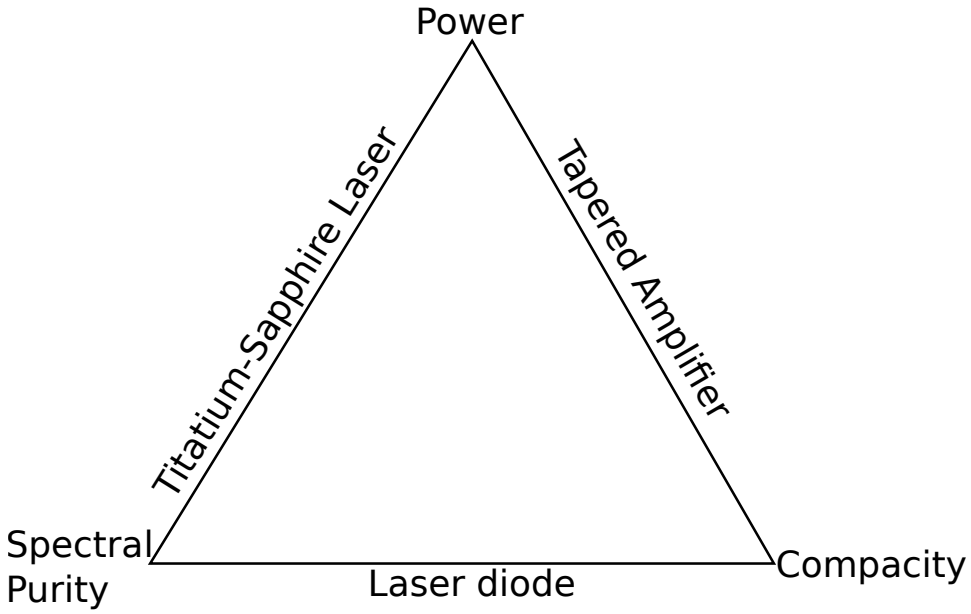

Figure 7.0.1. The miniaturization problem of the lattice laser. No laser meets all requirements for mobile OLCs. The feature in front of a given laser is the weak point of this laser.

7.1 Methods

The lattice laser system in the Sr laboratory is already described in details in section 3.2, and comprised both semiconductor lasers and a TiSa laser. The simplified experimental set-up is shown in figure 7.1.2. The semiconductor based setup is composed

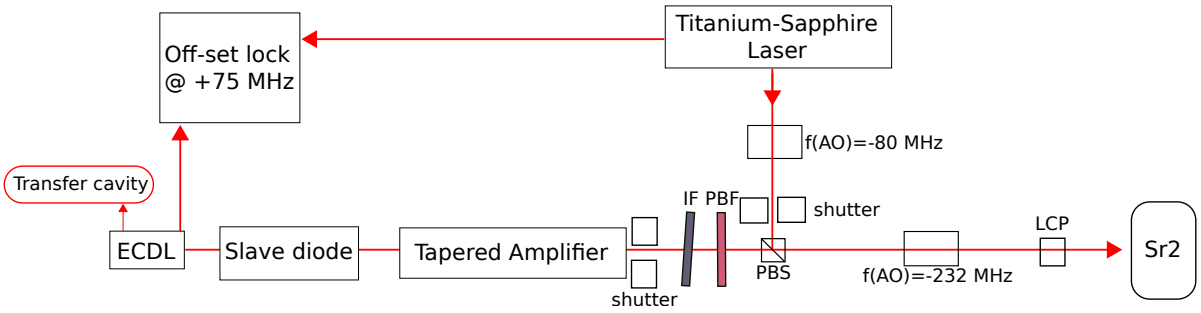

Figure 7.1.2. Scheme of 813 nm light distribution. A master ECDL laser at 813 nm seeds slave laser diode. Then the injected light of the slave seeds a Tapered Amplifier (TA) that can generate 2 W of optical power. IF: Interference Filter, PBF: Premium Band Filter

of a slave diode injected by a home-made ECDL laser (master laser), a tapered amplifier amplifying the slave laser light, and a filtering system - interference filter (IF) and premium band filter (PBF) to reach a better spectral purity. The characteristics of this filtering system is described in subsection 7.1.3. The master laser is locked to a transfer cavity whose length is reference to the narrow $^1S_0 - ^3P_1$ transition. The TiSa light is

directly transfered to atoms and its frequency is offset locked to the master ECDL. To characterize the light shift induced by the background of the ASE, we used two methods. We have measured the spectral distributions of available sources in our lab by using an optical spectrum analyzer (OSA). The obtained spectral distributions will be used to a estimate the frequency shift induced by the incoherent background using the theoretical polarizability of the Sr clock transition. In the second method, we have performed differential light shift measurements on a single clock, alternating between a configuration in which the lattice light is generated by the TiSa laser and a configuration in which the light is generated by the semiconductor sources.

7.1.1 Coherent Light in the Cavity

The spectral distributions measured with the OSA have to be adapted in order to reproduce the conditions in the optical cavity where the atoms are trapped during the usual clock operation. Spectral distributions which we collect and show in the next sections are taken before the cavity by using the same fiber that we actually use to transfer the lattice light to the atoms. We need to take into account that in the optical cavity where the Sr atoms are trapped and interrogated in the deep lattice, coherent and incoherent part of the spectrum can behave differently. In this subsection, we want to briefly describe how the coherent and incoherent light behave inside the optical cavity.

We consider a simple two mirror stable optical cavity as shown in figure 7.1.3. Mirrors are the same and have field reflection and transmission coefficient – r and t, and intensity reflection and transmission coefficients - R and T respectively, where $r^2 = R$ and $T = t^2 = 1 - R$. Taking into account all round trips of the light in the cavity, we obtain an

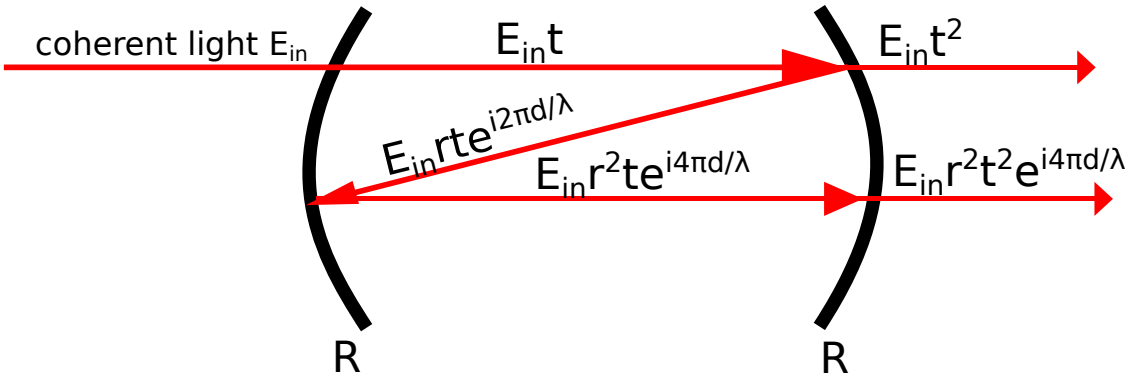

Figure 7.1.3. A two mirror optical cavity. The field E_{in} is incident on the cavity and the field is transmitted and reflected by the mirrors.

infinite sum and the circulating field in the cavity can be written as follows:

$$E = E_{in}t + E_{in}tr^2e^{i2\pi d/\lambda} + ... + E_{in}tr^{2n}e^{2n(i2\pi d/\lambda)} + ... = E_{in}t\sum_{0}^{\infty} r^{2n}e^{2n(i2\pi d/\lambda)} \quad (7.1.1)$$

and using the formula for the sum of a geometric series, the circulating field can be written:

$$E = E_{in}\frac{t}{1 - r^2e^{i4\pi d/\lambda}} \quad (7.1.2)$$

At the resonance, the term $\exp(i4\pi d/\lambda) = 1$, then the circulating field is as follows:

$$\frac{E}{E_{in}} = \frac{t}{1 - r^2} = \frac{t}{t^2} = \frac{1}{t}. \quad (7.1.3)$$

Using the relation between field coefficients and intensities and assume that $1 - R \ll 1$, the coherent intensity I inside the cavity is:

$$\frac{I}{I_{in}} = |\frac{1}{t}|^2 = \frac{1}{T} = \frac{1}{1-R} = \frac{\mathcal{F}}{\pi}, \tag{7.1.4}$$

where $\mathcal{F}$ is the finesse of the cavity. For our mirrors with $R = 0.975$ at 813.4 nm, it is 40 times larger than the intensity of the incident light. In our calculation, we therefore must include that the power in the carrier is 40 times larger than the power incoming on the cavity. Note that this factor is taken into account in the calculations for all types of lasers.

7.1.2 Incoherent Light in the Cavity

The coherent light is amplified in the cavity by factor of 40. Now, we need to know how the incoherent part of spectrum behaves in the cavity. Incoherent light is a light whose phase difference between two photons is random and not constant. In this case, we do not need to count the electric field but just intensities in a similar fashion as before. Again, shown on figure 7.1.4 circulating intensity can be described by the superposition

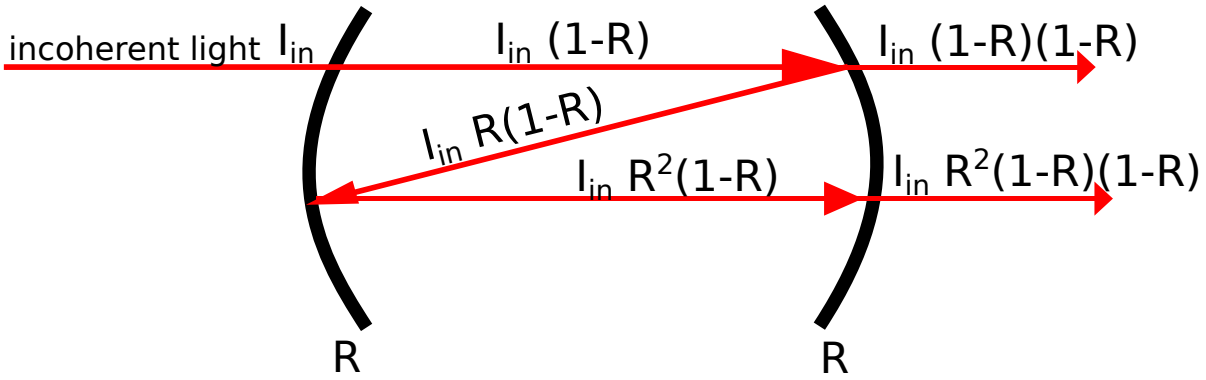

Figure 7.1.4. A two mirror optical cavity. a broadband incoherent light with intentisty I_{in} enters the cavity.

of the incident light I_{in}:

$$I = I_{in}(1-R) + I_{in}(1-R)R + ... + I_{in}(1-R)R^n = I_{in}(1-R)\sum_{i=0}^{\infty} R^n. \tag{7.1.5}$$

It is the same type of geometric series as in case of the coherent light, then by using the same maths, the sum is the following:

$$I = I_{in}. \tag{7.1.6}$$

It means that the intensity of the incoherent light inside cavity is not amplified nor filtered. Because it is impossible to measure directly the intensity inside the cavity, to verify our model, we measured the intensity transmitted by the cavity. The sum of the transmitted light I_{out} for the coherent light for locked cavity is equal to incident light I_{in}:

$$I_{out} = I_{in}. \tag{7.1.7}$$

For incoherent light, the sum of the transmitted intensity is:

$$I_{out} = I_{in}\frac{1-R}{1+R}. \tag{7.1.8}$$

The model is compatible with the measured transmitted spectra as is shown on figure. 7.1.5. The intensity of the carriers of incident and transmitted light are scaled to the same value.

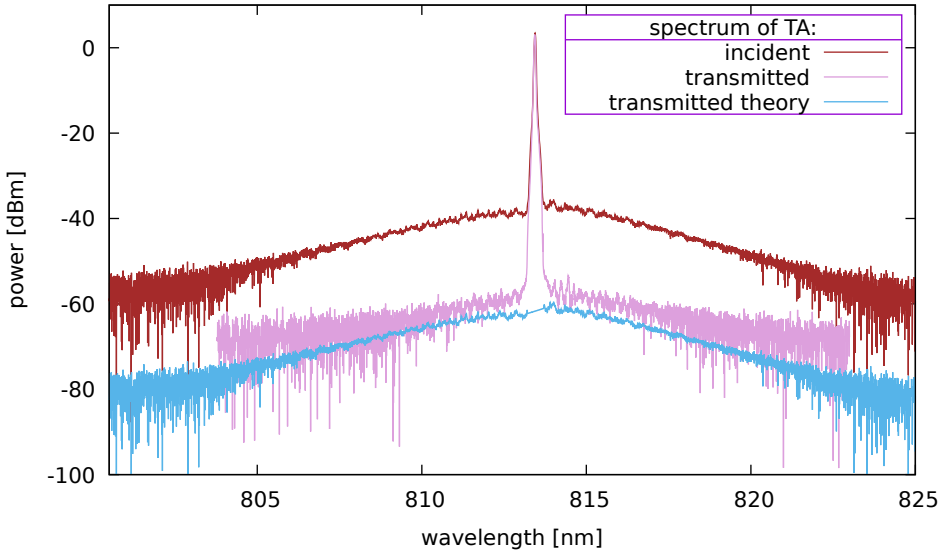

Figure 7.1.5. Spectrum distributions of the TA taken by the OSA before cavity, transmitted by locked cavity and computed from theory model (in the calculations, the coherent carrier is cut).

As we can see, the cavity amplifies the coherent carrier, in our case by factor of 40, but does not amplify the incoherent background. Therefore, the cavity acts as an additional filter for the incoherent background. This filtering effect is included in all calculations, including the result of the light shift induced by incoherent background of the TiSa laser. Additionally, we take into account the coupling efficiency to the cavity $\eta = 0.8$.

7.1.3 Filtering System

We are interested to apply a filtering system such that the ASE will be dwarfed from the spectral distribution of the tapered amplifier. For this, we have used two types of filters:

- interference filter (IF) manufactured by REO,
- Premium Hard-Coated Bandpass Filter (PBF) manufactured by Thorlabs (model FBH810-10)

We have characterized the spectral response of the IF filter using the TiSa laser because its wavelength can be continously tuned from 725 nm to 925 nm. Nevertheless, we have chosen the spectral range from 726.4 nm to 900.4 nm in order to have the magic wavelength at the center. The TiSa laser beam is divided in two parts. One part goes to the arm with the IF, the second part is the reference beam. We measured the optical power in both arms with a Thorlabs powermeter (Thorlabs S130C) and a homemade 10k photodiode

as a reference. The Thorlabs power is used because of its large dynamic range. To be independent of the spectral sensitivity of the photodiode we have normalized the transfer function of the IF by repeating the measurement without the IF in any beam. The sketch is depicted on figure 7.1.6. The transmission of the IF is shown on figure 7.1.7. We can

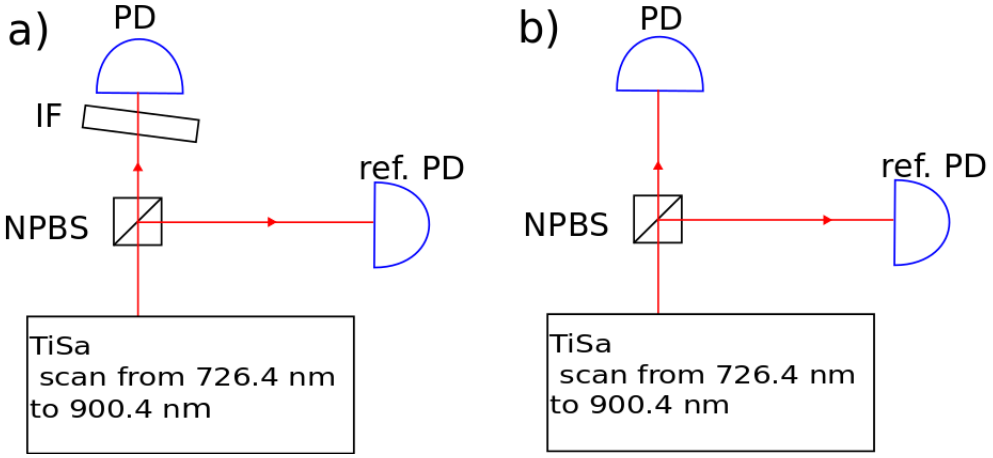

Figure 7.1.6. To be independent of the wavelength dependence of NPBS and photodiodes (PD), we measured signal with the same PD with (a) and without IF (b) with respect with a reference photodiode.

see 3 main transmission windows. Between these regions, the IF filters the incoming beam by about 10^{-3}. The transmission windows are fitted by a Lorentz profile:

$$\mathcal{L} = \frac{a}{1 + l^2}, \tag{7.1.9}$$

where a is the maximum transmission of the window and

$$l = \frac{x_0 - x}{w/2},$$

x_0 is the position of the maximum and w is the full width at half maximum (FWHM). The results of the fitting are shown of figures 7.1.8 and 7.1.9.

The fitting parameters are shown in table 7.1.1. We can see that the widths of the windows are not the same. The right peak is more than 2 times broader than the other peaks. The transmitted amplitude also differs. The main peak is not in the center between the right and left peaks. The distance left-central is 51 nm and right-center is 57 nm. The central value of the peak depends on the angle of the filter. Due to the fact that the

Table 7.1.1. Parameters of the fit for given transfer window.

peak	x_0 [nm]	w [nm]	a
left	763	0.25(11)	0.67
central	814	0.20(2)	0.90
right	871	0.55(3)	0.78

peaks are far detuned from the magic wavelength and they are not symmetric, the part of the light transmitted by the IF can possibly contribute to the total light-shift induced by the incoherent background. To filter these residual transfer windows, we have used the band pass filter mentioned above. We have not calibrated the PBF ourselves, but rely on the specification sheet delivered by Thorlabs. The calibration was performed in a broader

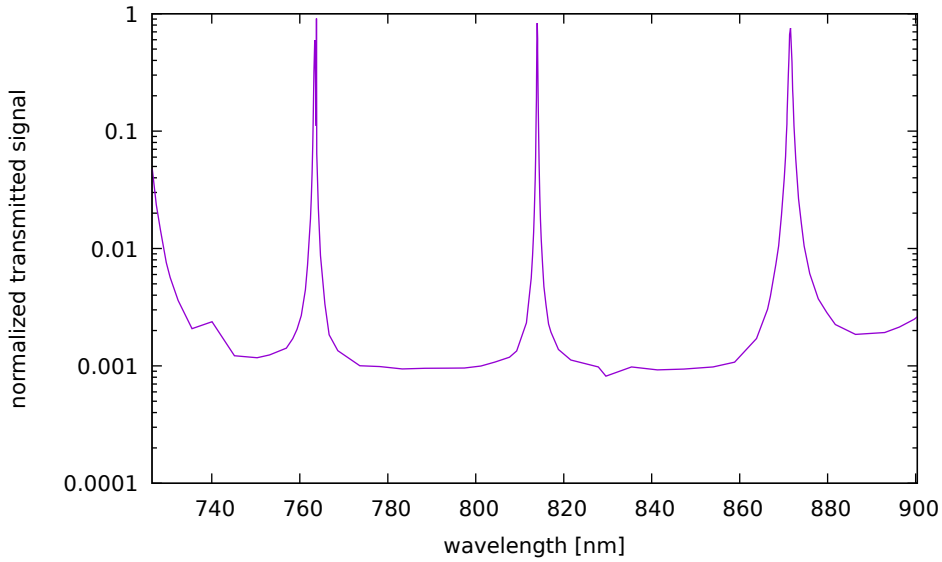

Figure 7.1.7. Calibration of the IF in the 726.4 nm - 900.4 nm range. The TiSa laser can be tuned between 725 nm - 925 nm but due to the symmetry with respect to 813.4 nm, we choose to scan between 726.4 nm and 900.4 nm. For an incident power of 1 mW, the optical power between transmission windows is at the 1μW level. The background that comes from the residual ambient light is at the 0.01μW level.

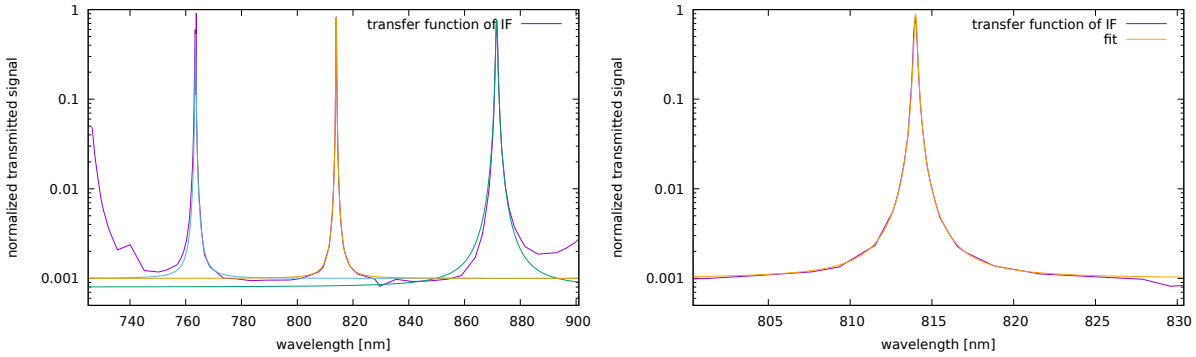

Figure 7.1.8. (left) Transfer function of the IF with the 3 fit functions. (right) Zoom on the central peak and the fit function.

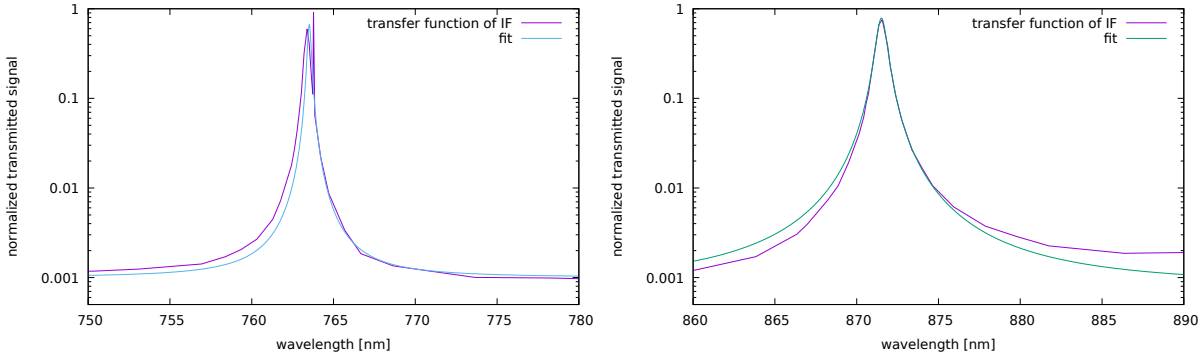

Figure 7.1.9. (left) Zoom on the left peak and its fit function and (right) Zoom on the right peak and fit function.

range than it is possible to measure in our laboratory. The transfer function of the PBF is shown on figure 7.1.10. Its linewidth is 10 nm around the central wavelength of 810 nm. It has a very good suppression in its rejection region - at the 10^{-7} level, which enables us

to remove the residual transfer windows of the IF. We can see that the magic wavelength

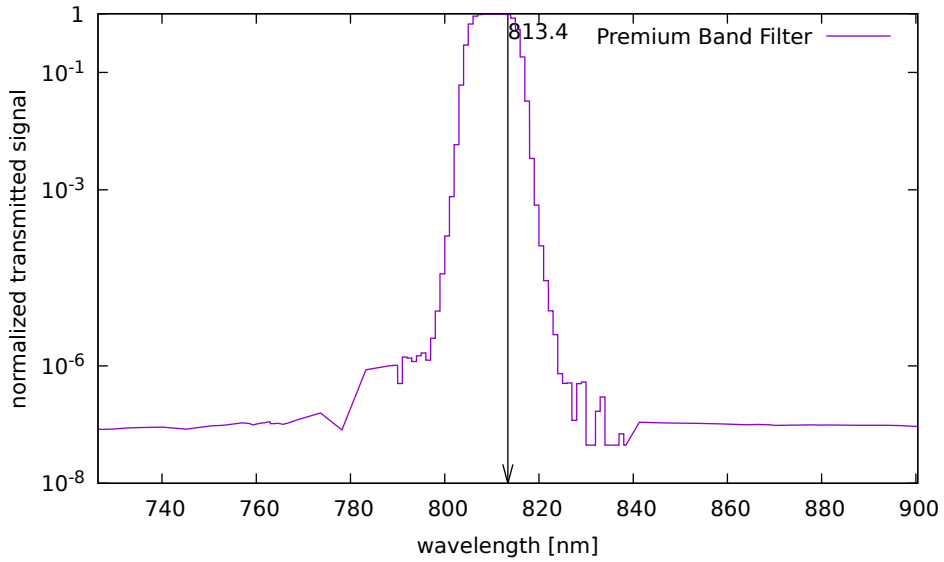

Figure 7.1.10. Transmission of the Premium Band Filter (PBF), Thorlabs FBH810-10 in the 726.4 nm - 900.4 nm range based on the specification sheet from Thorlabs.

813.4 nm is not on the center of the transfer window, meaning that the filtering of the ASE spectrum is not symmetric. The total transmission window of both filters (H(IF) · H(PBF)) is depicted on figure 7.1.11. Far detuned regions with the residual transfer windows are well suppressed below the 10^{-6} level. Only the region of the transfer window of the PBF is dwarfed at the 10^{-3} level.

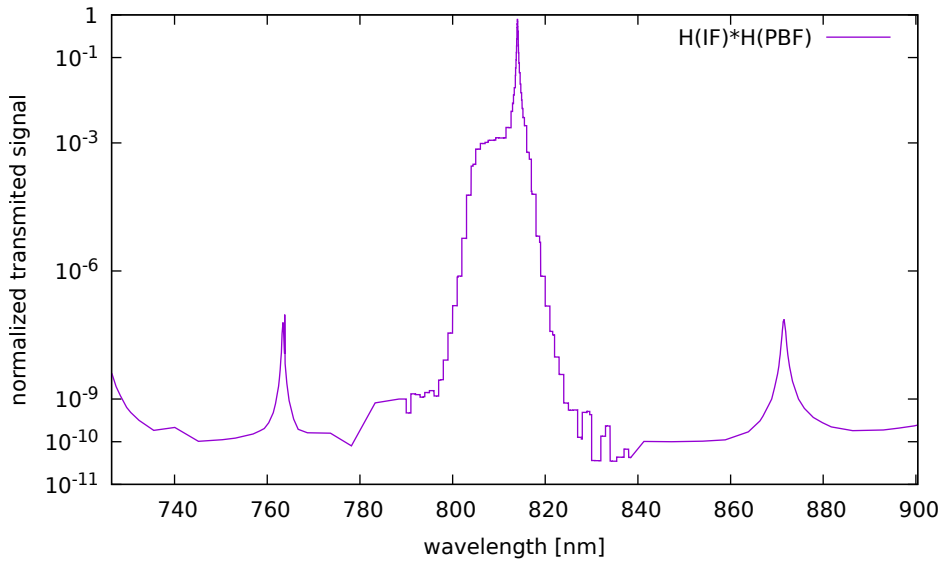

Figure 7.1.11. Cumulated transmission of the interference filter and the premium band filter.

7.1.4 Theory

To estimate the total light shift associated with the ASE background, we use a theoretical model of the atomic polarizability. According to equation 4.3.5, the total frequency

shift induced by the incoherent ASE background can be expressed as the sum of light shifts derived over the whole optical spectrum:

$$h\Delta\nu = -\sum_i \Delta\alpha^s(\lambda_i)\left|\frac{\mathcal{E}_i^{\text{intra}}}{2}\right|^2, \tag{7.1.10}$$

where the sum runs over the acquisition points of the optical spectrum. $\Delta\alpha^s(\lambda_i)$ is the differential scalar dipole polarizability for wavelength λ, $\mathcal{E}_i^{\text{intra}}$ is amplitude of the ith point of the incoherent background laser field inside the cavity. Because during the measurement, the light intensity of the carrier is measured rather than the intensity of the ASE background, the light shift can be expressed as:

$$h\Delta\nu = -\sum_i \Delta\alpha^s(\lambda_i)\frac{I_i^{\text{intra}}}{I_{\text{carrier}}^{\text{intra}}}\left|\frac{\mathcal{E}_{\text{carrier}}^{\text{intra}}}{2}\right|^2, \tag{7.1.11}$$

where the relation between the measured power in a given point i, I_i^{intra}, the power in the carrier $I_{\text{carrier}}^{\text{intra}}$ and the corresponding laser electric fields: $\mathcal{E}_i^{\text{intra}}$ and $\mathcal{E}_{\text{carrier}}^{\text{intra}}$, is:

$$\frac{I_i^{\text{intra}}}{I_{\text{carrier}}^{\text{intra}}} = \left|\frac{\mathcal{E}_i^{\text{intra}}}{\mathcal{E}_{\text{carrier}}^{\text{intra}}}\right|^2. \tag{7.1.12}$$

Considering that the power of the incoherent part is not amplified, $I_i^{\text{intra}} = I_i^{\text{in}}$, and that the carrier inside the cavity is amplified by a factor of $I_{\text{carrier}}^{\text{intra}} = \eta\frac{\mathcal{F}}{\pi}I_{\text{carrier}}^{\text{in}}$, where η is the coupling efficiency to the cavity, equation 7.1.11 becomes:

$$h\Delta\nu = -\sum_i \Delta\alpha^s(\lambda_i)\frac{I_i^{\text{in}}}{\eta\frac{\mathcal{F}}{\pi}I_{\text{carrier}}^{\text{in}}}\left(\frac{\mathcal{E}_{\text{carrier}}^{\text{intra}}}{2}\right)^2. \tag{7.1.13}$$

Therefore, during the measurement, the light shift induced by the ASE background can be expressed as a combination of known experimental factors:

$$\Delta\nu = \sum_i \Delta\kappa^s(\lambda_i)\frac{I_i^{\text{in}}}{\eta\frac{\mathcal{F}}{\pi}I_{\text{carrier}}^{\text{in}}}U_0, \tag{7.1.14}$$

where $\Delta\kappa^s$ is the scaled scalar light shift introduced in chapter 4:

$$\Delta\kappa^s = -\frac{\Delta\alpha^s(\lambda_i)}{h\alpha^s(\lambda_m)}, \tag{7.1.15}$$

where λ_m is the magic wavelength and U_0 is the measured trap depth:

$$U_0 = \alpha^s(\lambda_m)\left|\frac{\mathcal{E}_{\text{carrier}}^{\text{intra}}}{2}\right|^2. \tag{7.1.16}$$

The dependence of $\Delta\kappa^s$ as a function of λ is shown in figure 7.1.12.

7.1.5 Experiment

The light shift is determined in two different ways. First, we have measured the spectral distributions of all sources (TiSa, TA, slave diode) using the OSA. For each laser

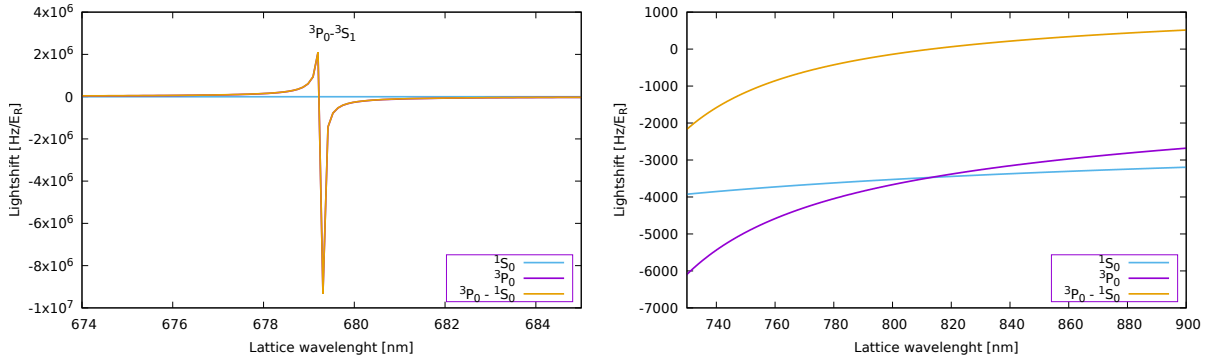

Figure 7.1.12. $\kappa^s(\lambda)$ for both clock states and the differential $\Delta\kappa^s(\lambda)$ as a function of the wavelength: around the $^3P_0$-$^3S_1$ transition (left) and around the magic wavelength at 813.4 nm (right).

spectra, we computed the frequency light shift induced by the ASE background by using above theoretical model in the range determined in the next section.

The second method is based on a differential light-shift measurement using a configuration in which the lattice light is generated by the TiSa laser and a configuration in which the light is generated by the TA for different trap depths for two laser sources. TiSa and semiconductor lasers with two optical set-ups that are used as a source of lattice light are combined and the induced light shifts are compared using a single clock. To combine the two optical paths, we used a polarized cube splitter. To actively switch the polarization of the beams during the clock cycle, a half-wave liquid crystal retarder (LCP) - Thorlabs LCC1111-B is inserted. The combined beams are transferred by a fiber and after it, a polarized beam splitter selects only one polarization and the beams go to the vacuum chamber where the Sr atoms are trapped. The scheme of this set-up is shown on figure 7.1.2. We use the TiSa laser to load the atoms because of its better stability and performance. The frequency of the TiSa is detuned by 114 MHz from the magic wavelength to reach the effective magic wavelength that cancels the sum of the scalar and tensor light shifts (see section chapter 4). For an identical frequency of both lasers, strong interferences appear during the switching between the two sources, and the atoms are lost from the trap. Therefore, the frequency difference between TiSa and TA is set to 5 MHz to suppress this interference effect. This frequency difference induces a different light shift, that is taken into account in the data analysis. The Tisa laser is used as a reference laser in this comparison experiment.

7.2 Titanium-Sapphire Laser

The Titanium-Saphire laser used for the daily operation in the lab is manufactured by M Squared (SolsTiS model) and it is pumped by a Verdi laser at 532 nm with 10 W output power manufactured by Coherent. It is the common laser system for both Sr clocks.

The direct measurement of the spectrum of the lasing TiSa is not possible because the ASE background is too low as compared to the lasing carrier. Therefore, the spectrum is measured when the laser is not lasing. For this, the TiSa laser is equipped with an intra-cavity shutter that blocks the laser emission without blocking the pumping laser nor the ASE. When the shutter blocks the TiSa cavity, we measured the optical power transmitted from the laser to the atoms. To estimate an upper limit on the uncertainty of the light-shift induced by the incoherent background of the TiSa, we take this situation

as the worst case scenario, because the spontaneous emission is larger than during the proper lasing operation. As shown on figure 7.2.13, when the cavity is blocked, the output of the TiSa laser is composed of two beams: the first one is a 10 μW green beam coming from the Verdi pump laser and the second is a 5 μW infrared beam coming from the ASE of the pumped crystal. The green beam is present independently of whether the laser cavity is blocked or TiSa works normally or not. It is filtered by the optics in the optical path between the laser and the atoms. Indeed, before the fiber which transfers the light to the atoms, the green beam is not visible by the CCD camera nor by eye. The infrared beam goes through the fiber with a very low efficiency but at the end of the optical path, 4 nW (from the initial 5 μW) of optical power goes to the build up cavity where the atoms are located. The total power of the spontaneous emission that can induce a frequency light-shift, is at least 89 dB below the power of the lasing TiSa (1.2 W).

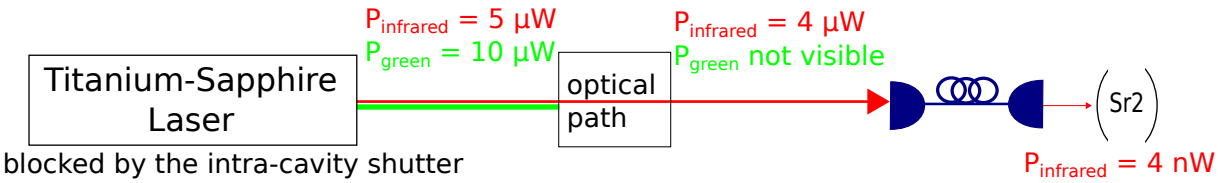

Figure 7.2.13. Scheme of the TiSa light distribution. The blocked laser cavity emits 5 μW of infrared light and 10 μW of green light. The green light is the residual light coming from the Verdi pump laser and is independent of whether the laser cavity is blocked or not.

To evaluate the total light-shift of the spontaneous emission of the TiSa, we have measured its spectral distribution using the OSA. Due to the very low power in the infrared beam, 5 μW, we used a multi-mode fiber in order to transfer enough light to the OSA and to be able to observe a signal (3 μW). The spectral distribution is shown on figure 7.2.14 and includes the working wavelength range of the TiSa laser between 726.4 nm and 900.4 nm (813.4 nm is the central wavelength of this range).

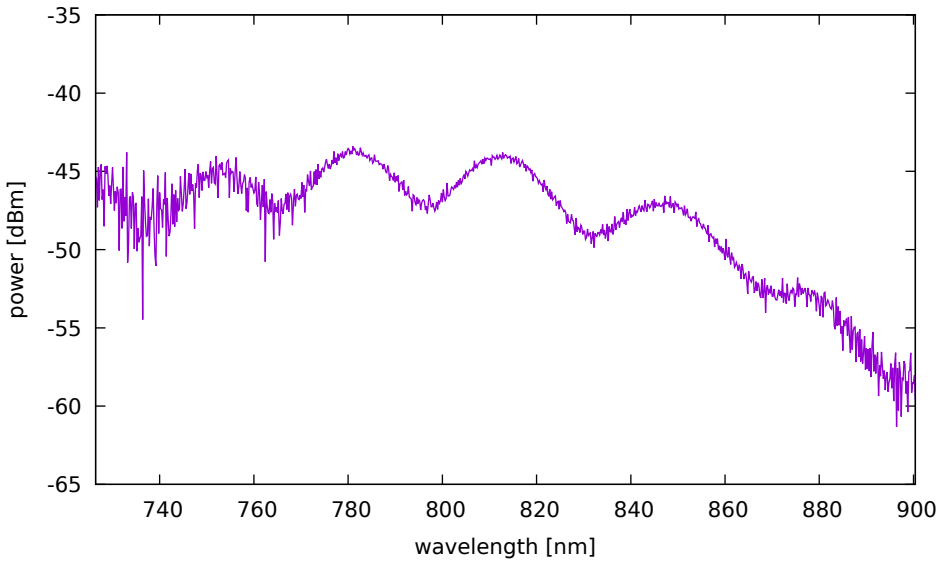

Figure 7.2.14. Spectrum distribution of the incoherent background of the TiSa laser with blocked cavity in 726.4 nm - 900.4 nm range.

We calculated the light shift induced by the ASE background shown on figure 7.2.14 by using equation 7.1.14 in which we consider that the optical power in the carrier is 35 mW which corresponds to a trap depth of 100 E_r. These are typical working conditions during the interrogation of the atoms. The spectrum is scaled down to the total power 4 nW. The total frequency shift induced by the spontaneous emission of the TiSa is lower than 10^{-18} in fractional units for a trap depth of 100 E_r.

7.3 Slave Diodes

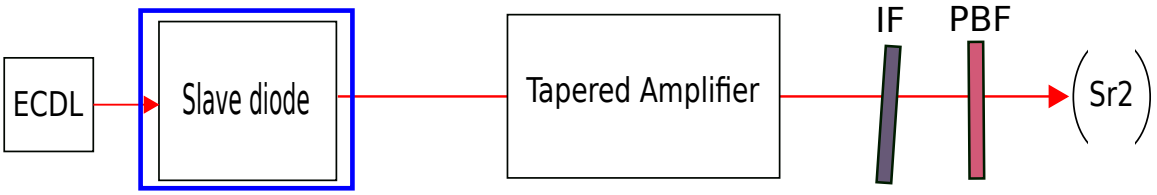

Figure 7.3.15. General scheme of the set-up based on semiconductor sources.

In addition to the TiSa laser, we have an independent setup based on semiconductor sources. The general scheme is presented on figure 7.3.15. Semiconductor lasers are equipped with two types of filters (IF and PBF, which are already described in subsection 7.1.3). In this section, we will focus on the spectral distributions of slave diodes [blue rectangle on picture 7.3.15]. We measured the spectral distributions of the injected slave diodes without any filtering system because with the filtering system in place, no background of diodes is observed by using the OSA. However, the filtered spectrum can be deduced from the unfiltered spectrum using the transfer function of the filters described in subsection 7.1.3. In the set-up, there are two different slave laser diodes. The first diode is

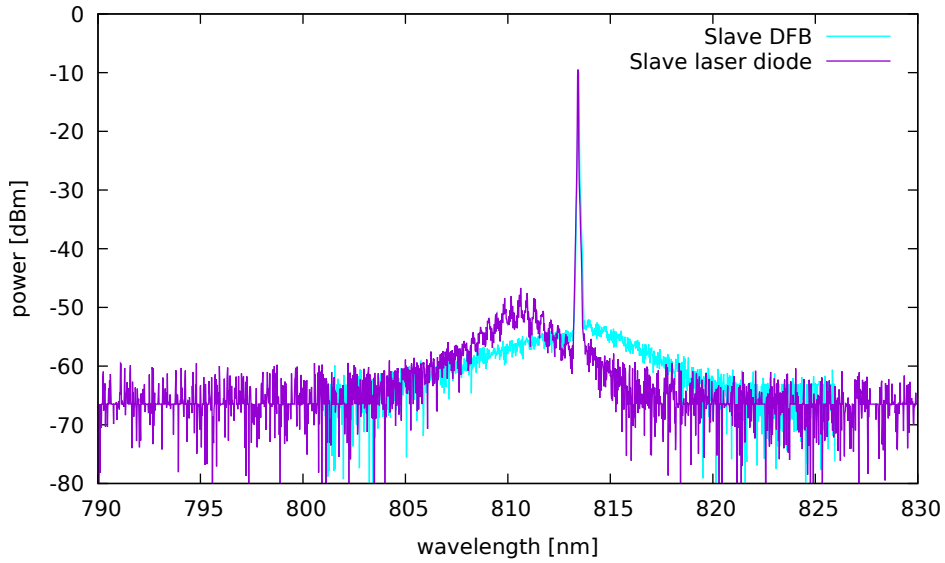

Figure 7.3.16. Spectra distribution of two types of laser diode without filtering system that is used as a slave.

a distributed feedback laser (DFB), the second diode is a standard Fabry-Pérot (FP) laser diode (manufactured by SDL/JDSUniphase). To transfer the light to the OSA, we have

used a single-mode fiber (Thorlabs P3-780PM-FC-5). The typical spectral distributions are shown on figure 7.3.16. Around the carrier, we can see an incoherent background induced by Amplified Spontaneous Emission (ASE). It is clearly visible that the shape of spectral distribution depends on the type of diode. Because the ASE pedestal sits on both sides of the carrier, the light-shift induced by the red-detuned component partly cancels the light-shift induced by the blue-detuned component. However, the incoherent background of the «slave laser diode» is more unbalanced than the pedestal of the «slave DFB» meaning that the light shift can change significantly from diode to diode. The far-detuned parts of the spectrum is limited by the noise of the optical spectral analyzer and we have no information about the shape of the background. To be sure that the pedestal does not come from the ECDL master laser, we measured the spectral distribution of the master. There is no visible background higher than the noise of the OSA. Also, the spectrum of slave diodes does not change when an interference filter is inserted in the injecting beam that goes to the slave diode. The light coming from the slave diode is amplified by a tapered amplifier. And such amplifier light is used to trap the atoms.

7.4 Tapered Amplifier

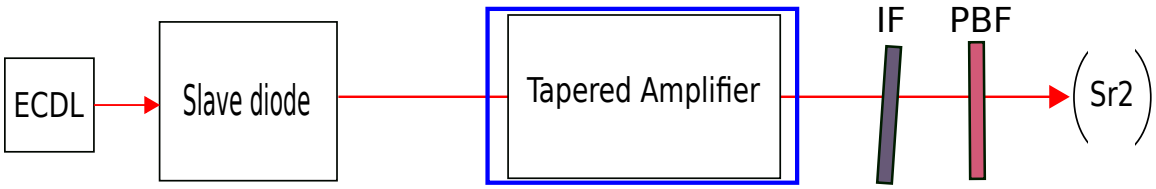

In this section we will focus on the spectrum of the tapered amplifier (TA) that can be used to trap the atoms. Figure 7.4.17 shows a typical spectral distribution of the tapered amplifier seeded by the injected slave DFB. As in the case of the distribution of the slave diodes, the spectrum shows an ASE pedestal around the carrier. The visible part of the ASE background extends from 804 nm to 824 nm. Beyond this range, we are limited by the noise of the OSA. Hence we need to model the far detuned parts of spectrum to characterize the incoherent background and to apply the filtering system in a broader spectral range. The extrapolation is necessary because, although the optical power is low in this domain, below the detection limit of the OSA, its contribution is enhanced because it is far detuned from the magic wavelength, especially because it may reach the nearby transition $^3P_0$-$^3S_1$ at 679 nm.

We have taken spectra of the TA when the PBF and IF are inserted in the optical path. It is shown in figure 7.4.18. When we insert the PBF, we can clearly see the transmitted part of this filter and it is consistent with the calibration provided by the manufacturer. However, when we insert the IF, we are limited by the noise and resolution of the OSA and we gain no information about the width of the transfer window and rejected parts of the spectrum.

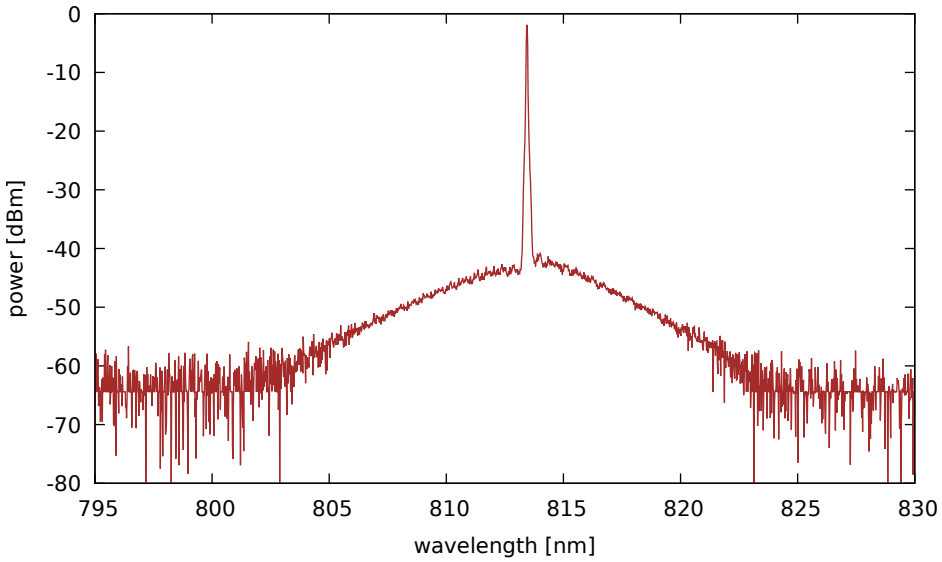

Figure 7.4.17. Spectra distribution of the TA without filters.

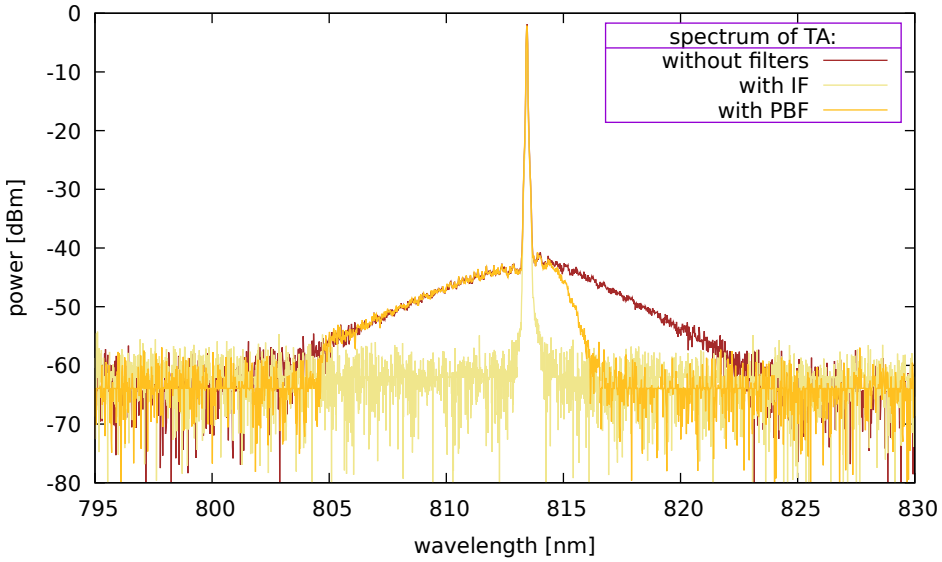

Figure 7.4.18. Spectra distribution of the TA with IF and PBF.

7.4.1 Model of the ASE Background

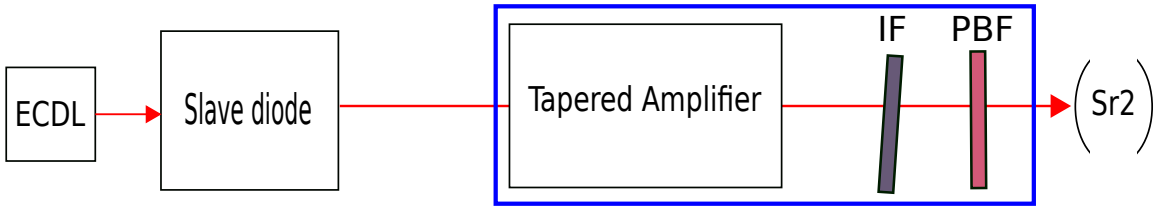

As we can see, the collected spectra of the TA are limited by the noise of the OSA in the far-detuned parts from the magic wavelength. But because we have characterized filters in a broad spectral range, we are able to extrapolate and model the spectrum of the TA. We assume two scenarios. In the first, realistic case, the pedestal decreases exponentially.

For this, we fit the ASE background in log scale with the function $f(\lambda) = a_1\lambda + b_1$ for the blue and red detuned parts. The fit functions are shown on figure 7.4.19 and their parameters in table 7.4.2. The crossing point of the fit of functions is λ_c=813.916 nm, y_c=-40.64 dBm. In the second, the worst case scenario, we consider that the ASE background of the unfiltered TA is equal to the OSA background noise. For these two models

Table 7.4.2. Parameters of the exponential fit of the pedestal.

fit	a_1 [dBm/nm]	b_1 [dBm]
green	1.64	-1379
blue	-2.12	1685

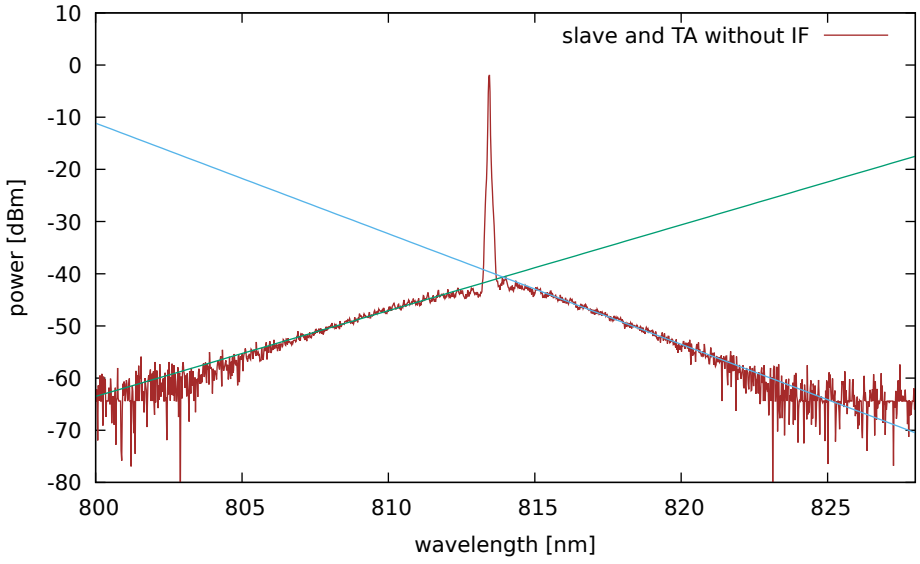

Figure 7.4.19. Spectral distribution of the TA without IF and fit curves to background.

of incoherent background, we insert «virtual» filters - IF and BF. By multiplying the extrapolated TA spectral distributions in the broad range from 726.4 nm to 900.4 nm by the transfer functions of the filters, we obtain the total spectral distributions limited by

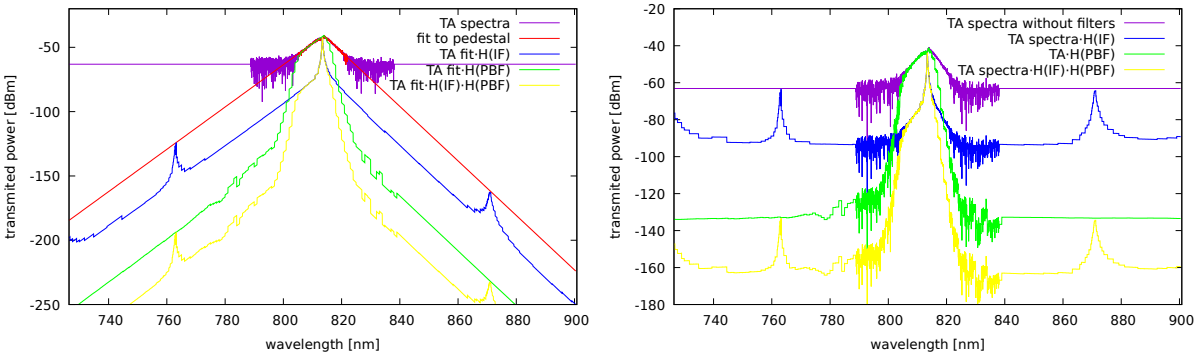

Figure 7.4.20. Extrapolation of the distribution of the pedestal of the TA: (left) fitted by an exponential function in the full range, (right) limited by the OSA,

the OSA and fitted exponentially, which are shown on figure 7.4.20, respectively.

First, we focus only on the unfiltered spectrum extrapolated by the exponential function. Figure 7.4.21 shows the spectral distribution of the light shift in a band of 0.02 nm. This plot shows a large contribution of the part of the spectrum close to the carrier, but due to the symmetric shape of the ASE pedestal around the carrier, this contribution may cancel out. This is why this plot does not tell whether its the far detuned (small but broad) part of the spectrum or the part (big but limited to a small range) that contributes most to the light shift. To discriminate these two cases, we rather calculate the cumulative light shift. At a wavelength λ, this cumulative light shift is defined as the integrated light-shift for all wavelengths smaller than λ. The total light shift is therefore the rightmost value of the cumulative light shift.

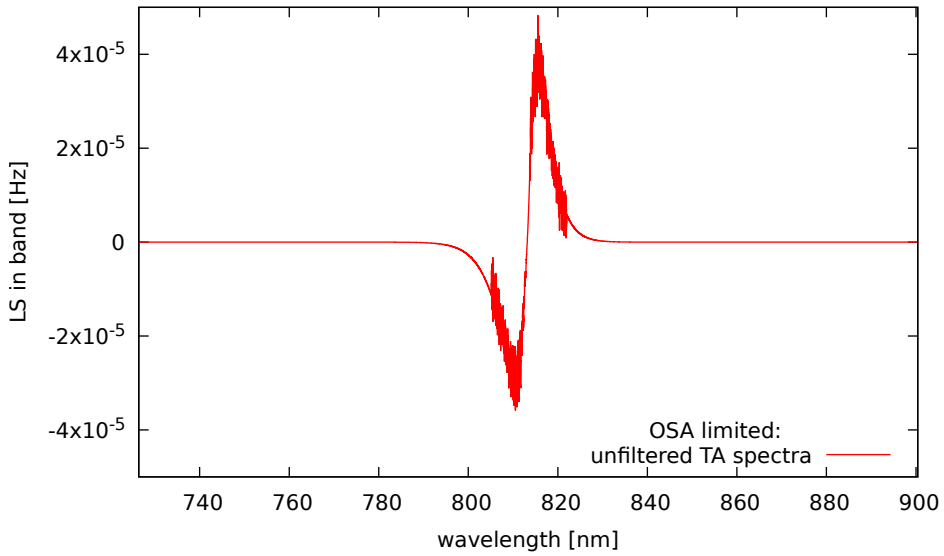

Figure 7.4.21. The light shift in band of 0.02 nm for the exponential fit of the unfiltered spectrum of the TA (for 1 E_r). Contribution from the far-detuned wings of the fit are negligible.

Using formula 7.1.14, we have counted the cumulative light-shift for both models instead of calculating the total light-shift, in order to see which parts of the spectrum gives the largest contribution. It is shown on figure 7.4.22.

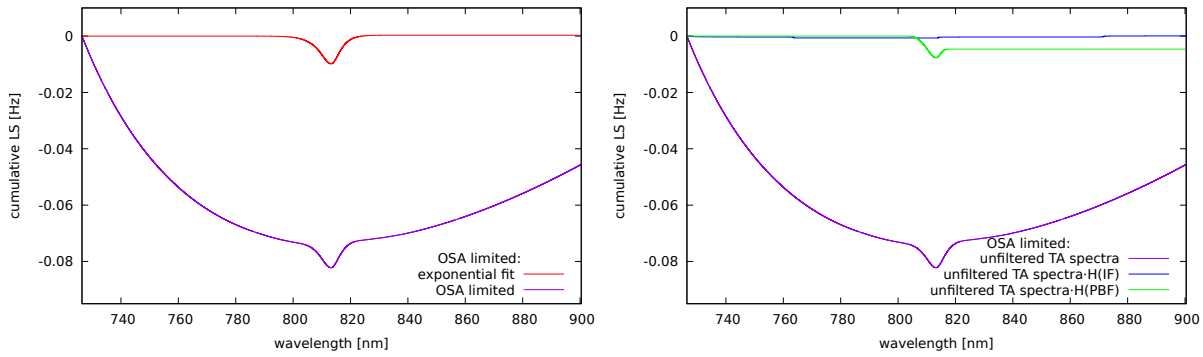

Figure 7.4.22. (left) Cumulative light shift of the unfiltered spectra of the TA for exponential fit of the pedestal of the TA and limited for the OSA (for 1 E_r). (right) Cumulative light shift of unfiltered spectra of the TA for the OSA limited model. The large contribution of the far-detuned parts of the unfiltered spectra is reduced by using one of the filter (for 1 E_r).

In the first model, we assume that the ASE pedestal decreases exponentially with the detuning. The largest contribution in the total light shift is in the part close to the

magic wavelength. Far-detuned wings of the spectrum have negligible contributions. In the second model, the far-detuned parts in the model limited by the OSA have a large contribution in the total light shift. It means that the near-detuned part of the ASE that we can physically observe by the OSA has negligible contribution and the most of the light-shift comes from the far-detuned parts that we can not distinguish from the OSA noise. Please note that OSA limited model, the blue-detuned and red-detuned parts of the light shift are not equal although the broad range was centered at magic wavelength. Due to the non-physical behavior, the model limited by OSA is rejected in further analysis. Nevertheless, the large contribution of the total light shift of the far-detuned parts is cancel out by using the filtering system. Therefore, if the ASE background has another shape than the exponential decay modeled here, the contribution to the total light shift is negligible with applied filtering system.

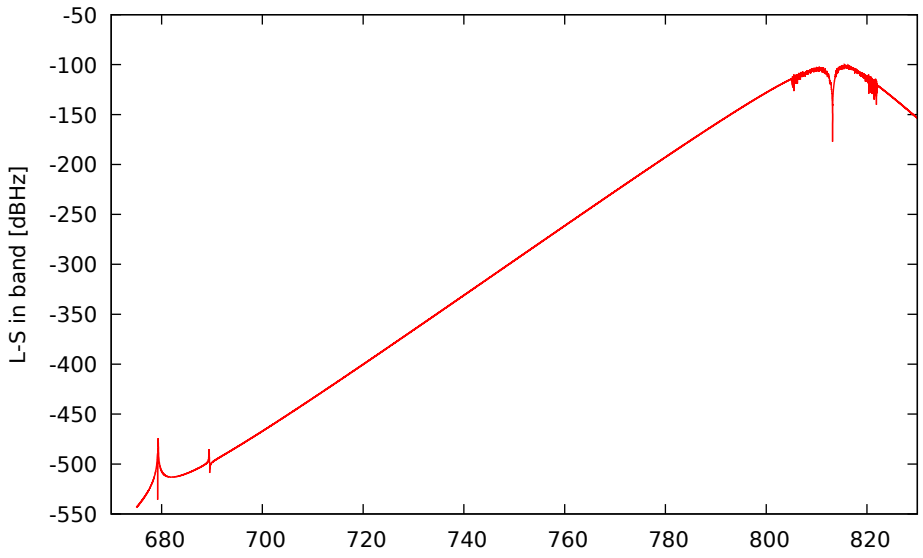

Figure 7.4.23. The light shift in a band of 0.02 nm for the exponential fit of the pedestal in a large range in logarithmic scale. The $^3P_0 - ^3S_1$ transition around 679 nm does not contribute significantly to the light shift.

The polarizability is not linear with the wavelength because the presence of the $^3P_0 - ^3S_1$ transition at 679 nm. This transition is relatively close to the lower limit of the ASE range. Its contribution must be evaluated because it can induce a large light shift, larger than the closer detuned parts. As shown on figure 7.4.23, the contribution of this transition in the total light-shift for the exponential fit is negligible. It is 400 dBHz less than the visible part of the ASE background.

Because far detuned parts of the spectrum contribute less than 1% of the red-detuned and blue-detuned light shift, we can reject these parts in the calculations to save calculation time. Therefore, we use the more practical range from 790.98 nm to 827.812 nm in all calculations presented in the next section.

7.5 Results

In this section, we will show the results of the theoretical calculations of the light shift induced by the ASE background calculated from spectral measurement with the OSA, and differential light shift measurement performed with the atoms. The experiment was

performed for different temperatures of the TA chip and various combinations of the filters in the optical path (including the optical path of the slave diode and TA). Using the exponential model of the ASE background, the calculated theoretical values for given trap depths will be compared with the corresponding obtained experimental results.

7.5.1 Dependence on Temperature

The shape of the ASE background of a TA varies with the temperature of a given chip. First, without using any filters, we changed the temperature over the maximum range of the controller of the chip: from 23.9 °C to 26.6 °C, in order to see a difference in the shape of the incoherent ASE pedestal.

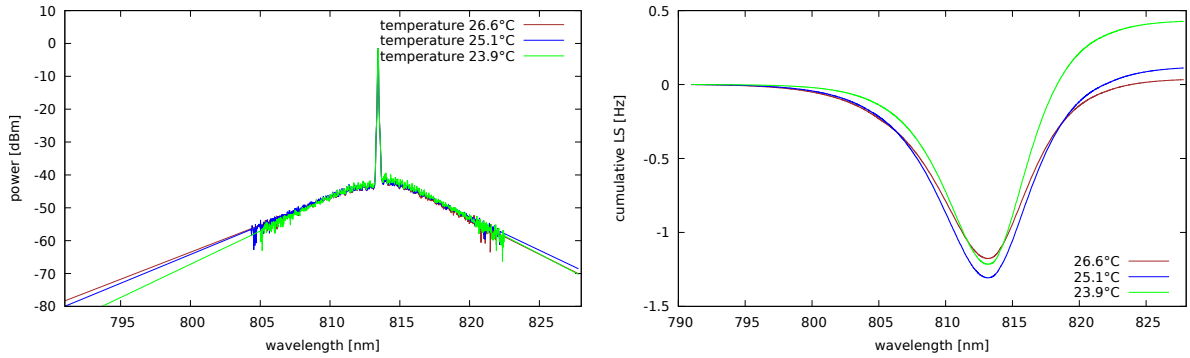

Figure 7.5.24. (left) Spectral distribution of the TA and (right) calculated cumulative light shifts (for 120 E_r) for a given temperature of the chip.

As we can see on figure 7.5.24 left it is possible to observe differences for spectral distributions. The green spectra is more unbalanced than the brown spectra. Theoretical calculations, shown in table 7.5.3, suggest that around 26.6 °C is a point where the light shift is lower than for other temperatures and is close to zero. On the other hand, the light shift increases for lower temperatures because the spectrum becomes more unbalanced in the red detuned part as shown on figure 7.5.24 right. This high sensitivity to the shape of the TA spectrum on temperature of the chip makes hard precise measurements without accurate controlling of the temperature of the chip. We have performed several light shift differential measurements for various temperatures of the chip but the results show unclear shift of the ASE and are mixed within the statistical resolution.

Table 7.5.3. Calculated light shifts (LS, expressed in Hertz and fractional units) based on spectral distributions measured by the OSA for a given trap depth and a temperature of the TA.

	LS at $U_0 = 120\ E_r$		LS at $U_0 = 270\ E_r$	
Temperature [°C]	[Hz]	$[10^{-16}]$	[Hz]	$[10^{-16}]$
26.6	+0.03	+0.77	+0.07	+1.72
25.1	+0.11	+2.61	+0.35	+8.05
23.9	+0.43	+9.96	+1.32	+30.71

7.5.2 Filtering of the Slave Spectrum

In the next step, we have filtered the ASE background of the slave diode, using one or both filters as is shown in figure 7.5.25. For each configuration, we performed differential

measurement. Distributions of the slave (blue) and seeded TA (brown) by this slave show that the TA amplifies the ASE background of the slave. The shape and the fit of these ASE pedestals behave similarly. For the next two distributions, we can see that inserting the PBF in a situation when we have already inserted IF does not change the spectrum significantly. It seems that the extra filter does not make any change and the violet and yellow ASE backgrounds come from the TA only. By inserting an extra IF in the optical path after the TA, we filter the background such that we are beyond the OSA resolution. The expected light shift for all configuration are shown in table 7.5.4. It shows that the configurations with IF in the optical path of the slave diode are expected to show a larger light shift. This conter-intuitive results comes from the different balance between the red-detuned and blue-detuned parts of the spectrum.

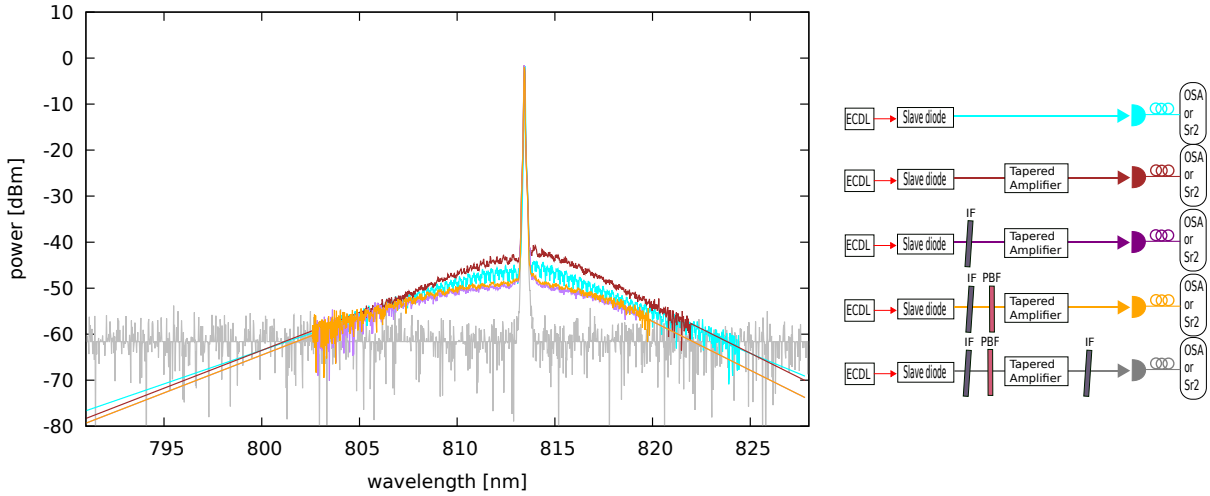

Figure 7.5.25. (left) Spectra distribution of the slave diode laser and TA (right) for given position of filters.

Table 7.5.4. Light shifts (expressed in Hertz and fractional units) calculated from spectra distributions measured by the OSA for a given trap depth.

	LS at $U_0 = 120\ E_r$		LS at $U_0 = 270\ E_r$	
Configuration	[Hz]	[10^{-16}]	[Hz]	[10^{-16}]
slave without IF	–0.20	–4.73	–0.46	–10.64
slave and TA without filters	+0.03	+0.77	+0.07	+1.72
slave with IF	–0.26	–6.13	–0.59	–13.80
slave with IF and PBF	–0.32	–7.49	–0.72	–16.85

The summary of the differential measurement is shown on figure 7.5.28. As the frequency difference, we take the difference between the corrected TA frequency and value of the expected light shift (which is the linear fit of the TiSa points) for the same trap depth as TA point (see figures 7.5.26 and 7.5.27). We can see that for configurations with IF frequency differences are positive when our theory model predicts something opposite. When we insert extra IF after TA to clean spectrum we reach the same frequency different as for not filtered spectrum. Generally, the comparison measurement gives the frequency difference within the statistical resolution as for the dependence with the temperature. Therefore, the expected light shift of the ASE background model must be overestimated, because it would be able to resolve a shift on the order of 10^{-15} for at least higher trap

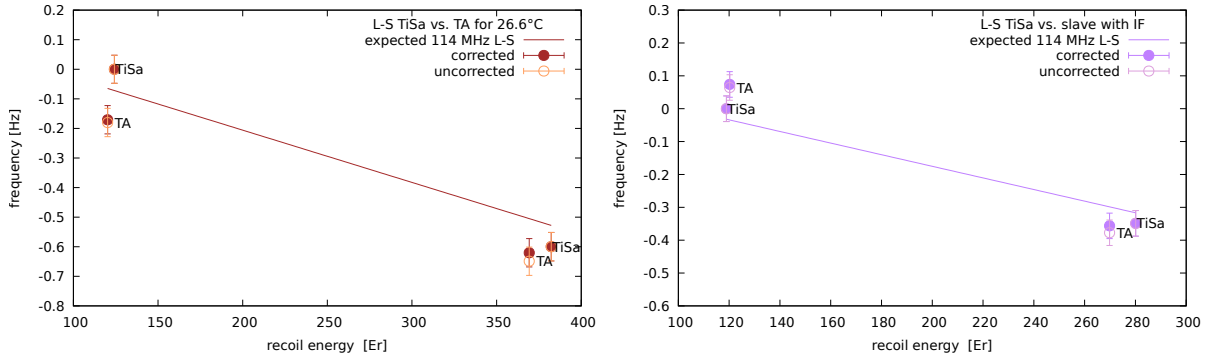

Figure 7.5.26. Differential light-shift measurement for 2 trap depths for TiSa and TA for a given configuration of filters. Corrected points include the 5 MHz difference between TA and TiSa. To the «TiSa points» linear function is fitted $f(x) = ax + b$ where a means the sensitivity of the relative scalar polarizability with trapping light and it is equal -15.5 μHz/E_r/MHz. Only parameter b is obtain from the fit.

depths. In order to actually observe a light shift associated with the ASE background, in the next section, the ASE background will be strongly unbalanced by the PBF inserted in the TA optical path.

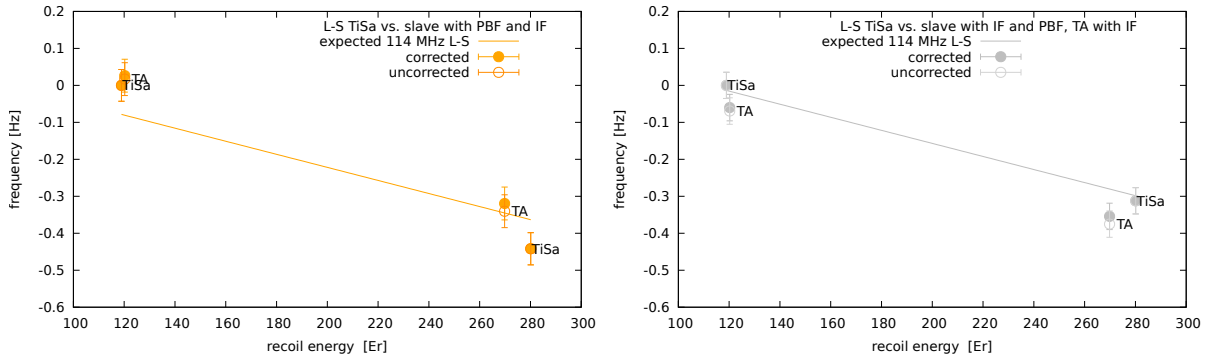

Figure 7.5.27. Differential light-shift measurement for 2 trap depths for TiSa and TA for a given configuration of filters. Corrected points include the 5 MHz difference between TA and TiSa.

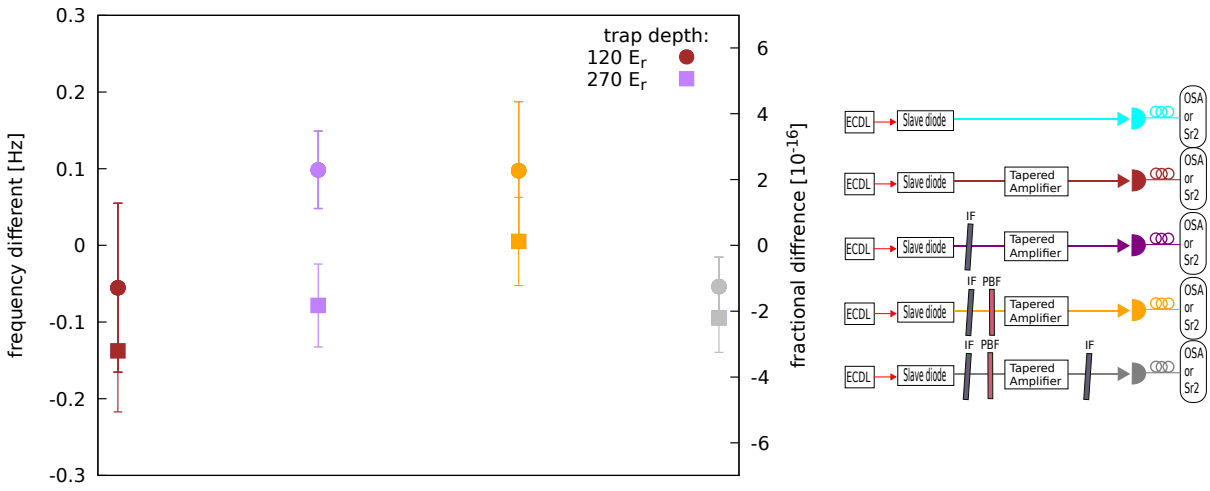

Figure 7.5.28. Frequency difference between TA and expected value of light shift from TiSa for 120 E_r and 270 E_r.

7.5.3 Filtering by Band Filter

In the next step, we investigate configurations with PBF. For this filter, the magic wavelength of 813.4 nm is not a central wavelength of the band. By using this filter, we can cut the red detuned part of the spectra and produce the strongly unbalanced ASE spectra as is shown on figure 7.5.29. Parts of spectra which are limited by the OSA noise, are hard to fit (spectra yellow and red). Therefore, we multiplied them by the transfer function of the PBF. Using the PBF, we should be able to induce larger frequency shifts

Table 7.5.5. Light shifts (expressed in Hertz and fractional units) calculated from spectra distributions taken from the OSA for given trap depth.

	LS at $U_0 = 120\ E_r$		LS at $U_0 = 270\ E_r$	
Configuration	[Hz]	[10^{-16}]	[Hz]	[10^{-16}]
slave and TA without filters	+0.03	+0.77	+0.07	+1.72
slave with PBF, TA without filters	–0.46	–10.8	–1.04	–24.25
slave without filters, TA with PBF	–0.76	–17.8	–1.71	–39.65
slave with IF, TA with PBF	–0.44	–10.3	–0.99	–23.2

than in the previous subsections. We can see in table 7.5.5, the expected light shift is 2-3 times larger than in previous subsections, which makes the light shift resolvable in our experimental conditions. The differential measurement with atoms, depicted on figures 7.5.30, 7.5.31 and summarized on figure 7.5.32, shows the differences at the same order of magnitude as the theoretical model predicts, and is consistent that the largest shift should be for configuration with PBF after TA (yellow). The frequency difference for the red spectrum should be smaller than similar yellow spectrum and its value is comparable to the value of the pink spectrum. We can reproduce qualitatively this trend in the differential measurement comparisons. The light shift obtained from the measurement with atoms is smaller than the predictions derived from the theoretical model but the difference is smaller than 1 order of magnitude. This measurement validates the theoretical model that is used to calculate the ASE but our model overestimates the frequency shift.

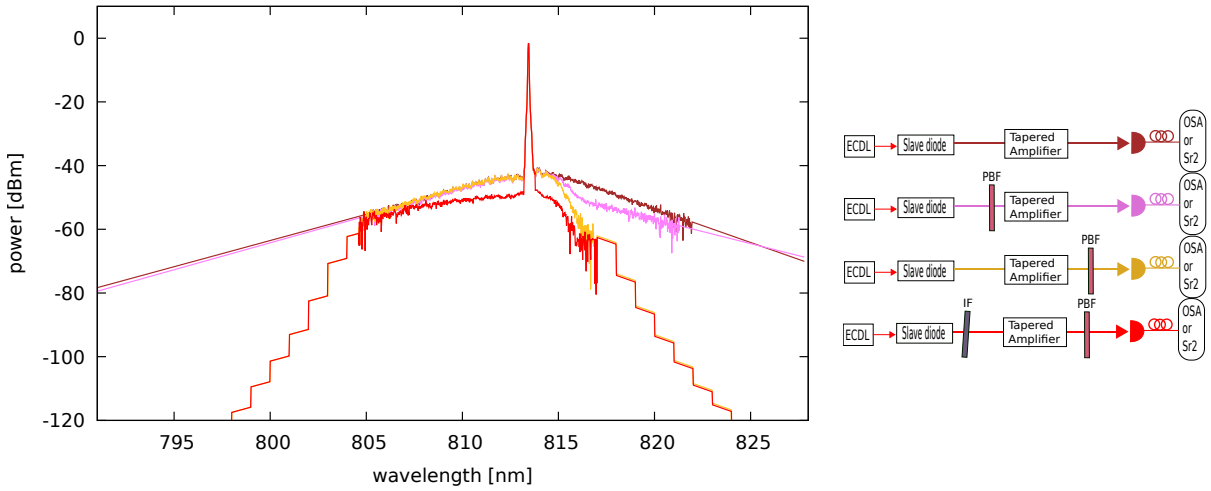

Figure 7.5.29. (left) Spectra distribution of the slave diode laser and TA (right) for given position of filters. The parts of yellow and red curves, beyond the OSA resolution, are obtained by multiplying by the measured transfer function of the PBF instead of fitting the spectrum.

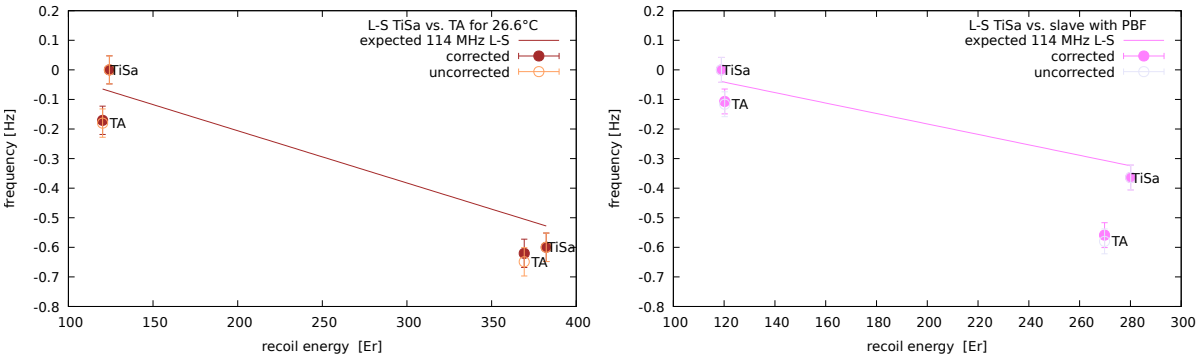

Figure 7.5.30. Differential light-shift measurement for 2 trap depths for TiSa and TA for given configuration of filters. Corrected points include the 5 MHz difference between TA and TiSa.

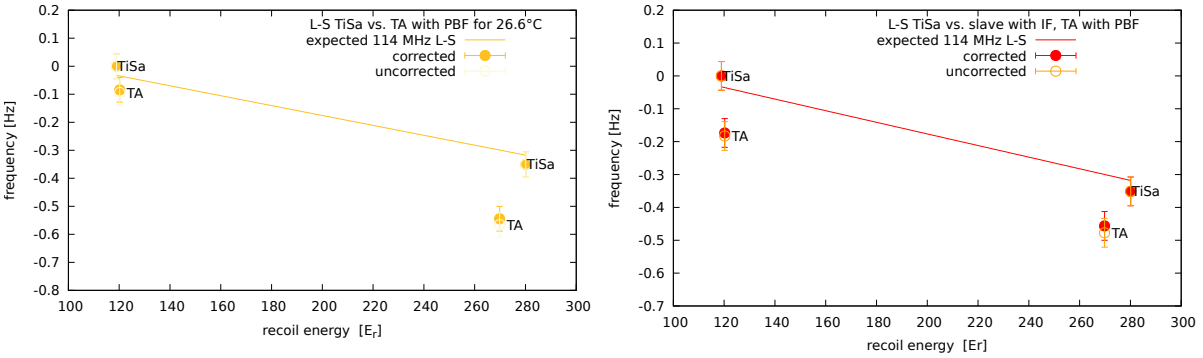

Figure 7.5.31. Differential light-shift measurement for 2 trap depths for TiSa and TA for given configuration of filters. Corrected points include the 5 MHz difference between TA and TiSa.

7.5.4 Filtering of the TA Spectrum

Finally, we have measured spectral distributions of filtered spectra of the TA for which the ASE background is lower than the noise of the OSA. In this case, we can see only the carrier whose width is an artifact of the apparatus and is not real. Inserting an additional IF should not change the spectrum. But as is shown on figure 7.5.33, for configurations

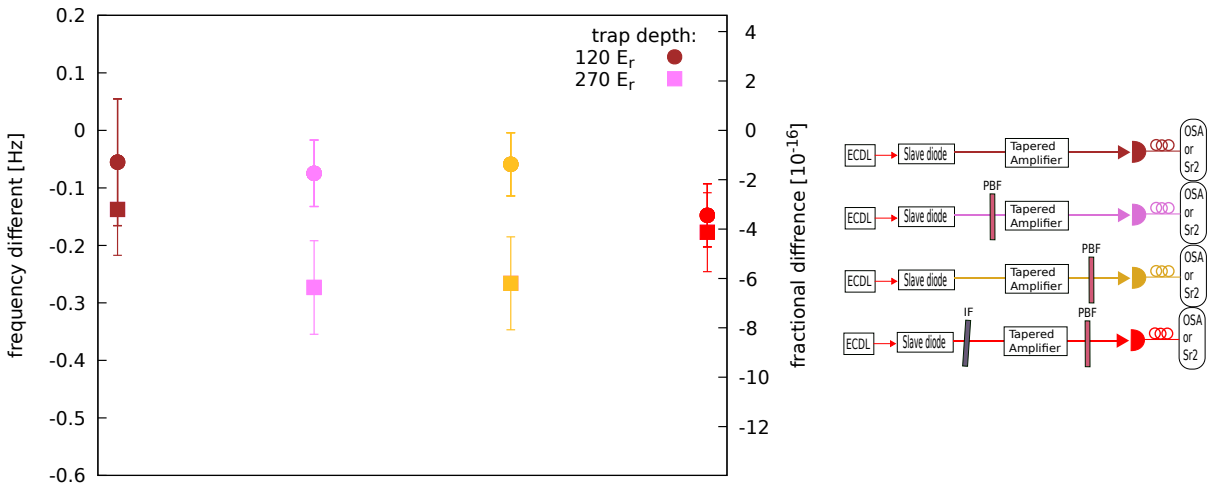

Figure 7.5.32. Frequency difference between TA and expected value of light shift from TiSa for 120 E_r and 270 E_r.

where only one IF is used in the optical path (khaki, pink and olive spectra) the level of the signal around 814 nm is higher than for the configurations with double IF (gray and blue). In the blue detuned part, such a difference is less visible. Because there is no visible ASE incoherent background in the whole range, we have not calculated the light shift based on the spectral distributions. Instead, we calculated the light shift of the virtually filtered TA spectra for various detuning of the central transmission wavelength of the IF, λ_c, from the magic wavelength λ_m. As is shown on figure 7.5.34, the light shift stays at the 10^{-17} level even if the position of the IF peak moves by the filter linewidth (0.2 nm). Because the optimal position is rather arbitrary, the aligning of the IF introduces the uncertainty on the angle of the IF that is on the same order of the expected light shift derived from the spectral distributions. Therefore, we present only results of differential measurements.

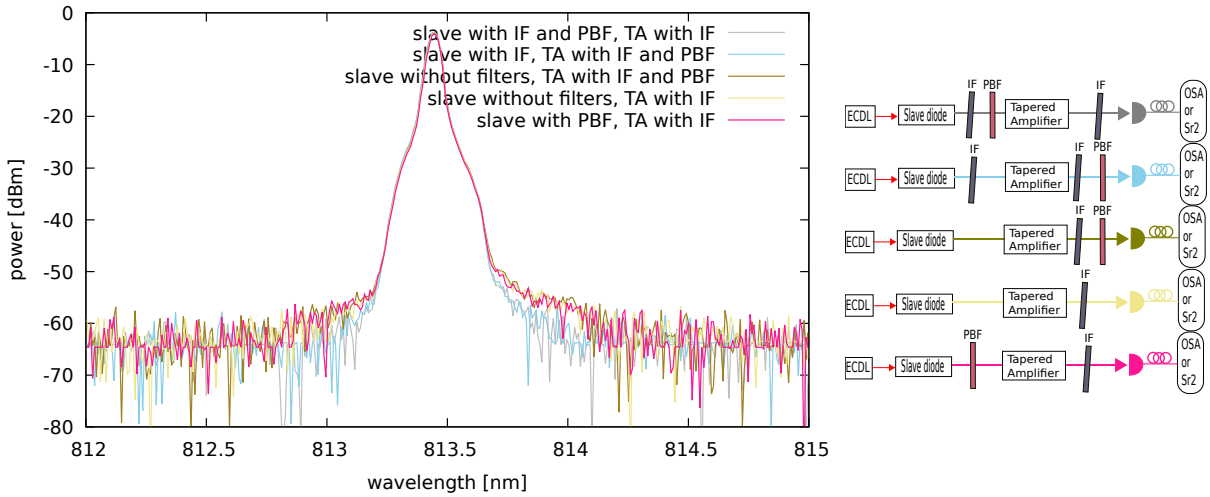

Figure 7.5.33. (left) Spectra distribution of the slave diode laser and TA (right) for given position of filters.

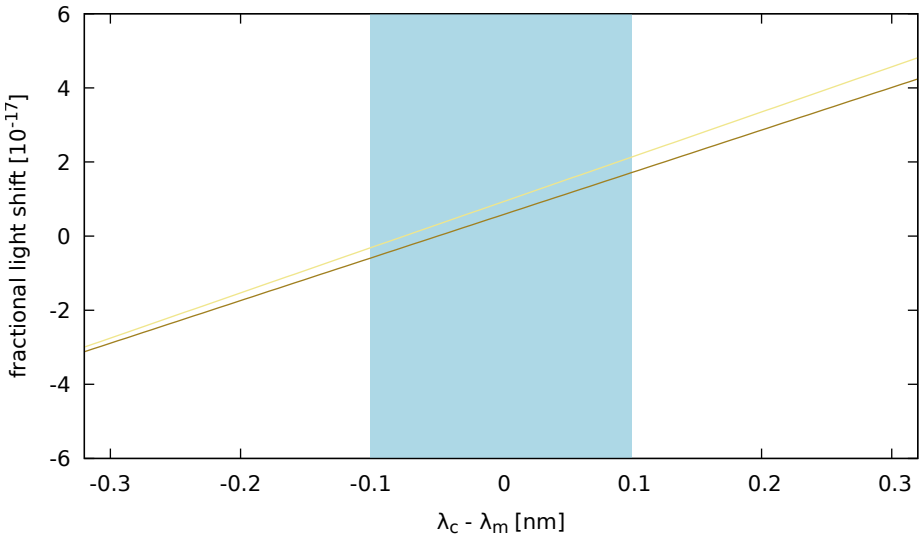

Figure 7.5.34. The fractional light shift as a function of the difference between the central transmission wavelength of the IF, λ_c, and magic wavelength λ_m (for 120 E_r). The light blue area represents the bandwidth of the IF.

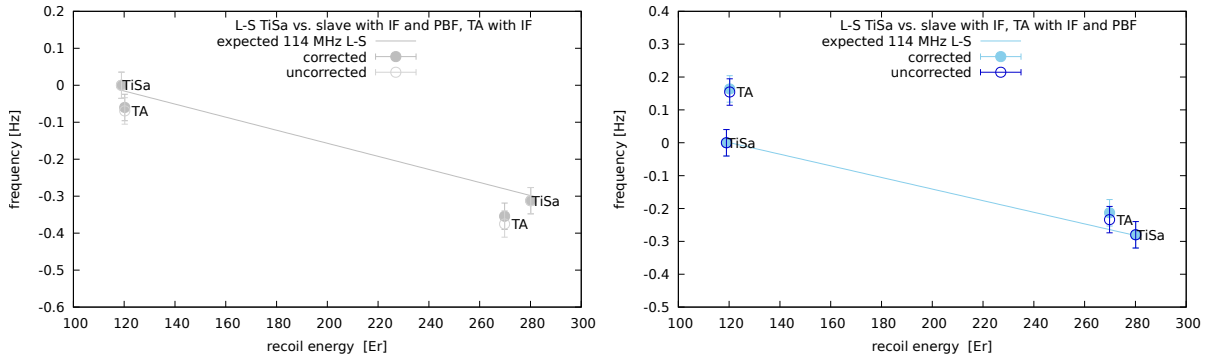

Figure 7.5.35. Differential light-shift measurement for 2 trap depths for TiSa and TA for given configuration of filters. Corrected points include the 5 MHz difference between TA and TiSa.

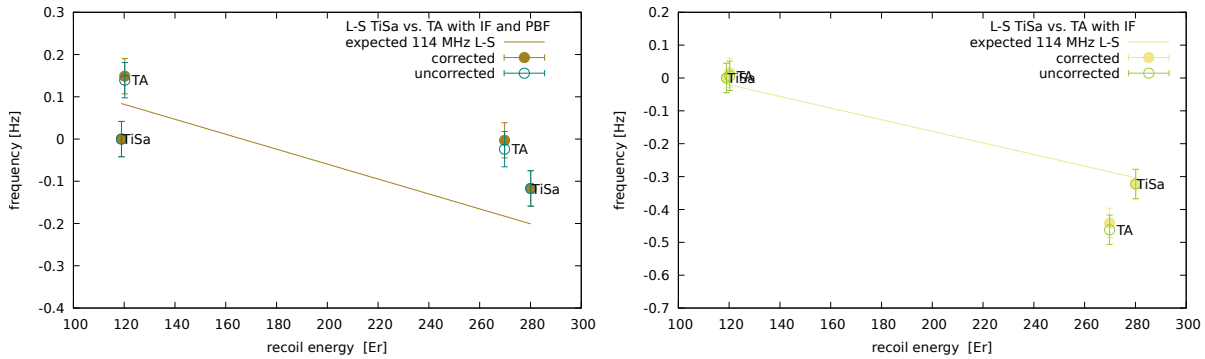

Figure 7.5.36. Differential light-shift measurement for 2 trap depths for TiSa and TA for given configuration of filters. Corrected points include the 5 MHz difference between TA and TiSa.

In the differential measurements with the atoms, we do not observe any clear shift of the ASE background beyond statistical fluctuations at the 10^{-16} level, in contrast to the previous subsection where by using a PBF, we could clearly see an effect with the atoms. The results of these measurements are shown on figures 7.5.35, 7.5.36, 7.5.37 and

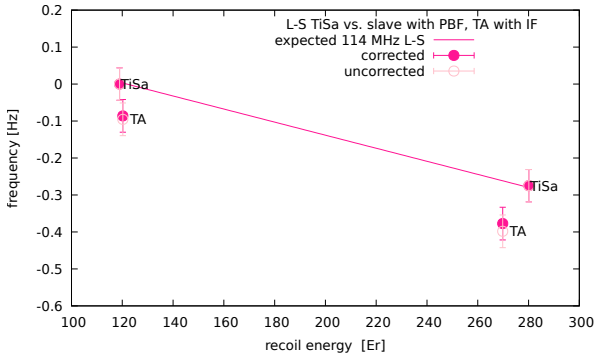

Figure 7.5.37. Differential light-shift measurement for 2 trap depths for TiSa and TA for given configuration of filters. Corrected points includes the 5 MHz difference between TA and TiSa.

summarized on figure 7.5.38 These results are consistent with the theoretical calculations which show shift at the level of a few of 10^{-17} for 120 E_r. As shown in the previous

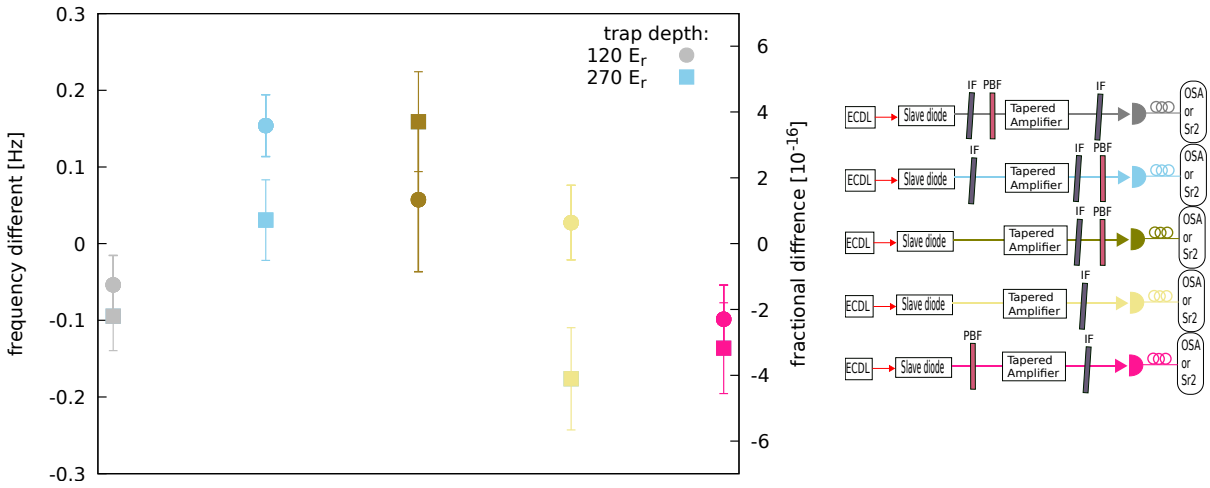

Figure 7.5.38. Frequency different between TA and expected value of light shift from TiSa for 120 E_r and 270 E_r.

subsection, our model overestimates the shift by a factor 3, therefore the real light shift is rather expected at about 10^{-17} for 120 E_r. Because the residual light shift is due to the ASE within the IF bandwidth, filtering of the spectral distribution beyond the 10^{-17} level can be only reached by using more narrow filters than the filter used in these measurements (0.2 nm) which is technically challenging. Another possible option is to employ an optical cavity that filters out the ASE background because the carrier is transmitted by the cavity while the incoherent background is attenuated, as shown by equation 7.1.8.

CHAPTER 8

SUMMARY

In this manuscript, I have presented the work I have done at LNE-SYRTE during my Ph.D. studies on the optical lattice clock with strontium atoms from October 2014 to September 2017.

During this period, our group has performed regular comparisons between our clocks and various frequency standards. These comparisons show unprecedented agreements and reproducibility of the obtained frequency ratios. The first international optical-to-optical measurement between two independent Sr clocks in Paris and Braunschweig is the first demonstration of the full frequency agreement (within the clock's uncertainty) of remote optical clocks at continental scale. The frequency stability of the comparison was not limited by the noise of the fiber link, for any integration time. Second, the first local optical-to-optical comparison between the optical clocks based on Sr and Hg at SYRTE is in excellent agreement with the same ratio obtained by the RIKEN group in Japan. These results confirm the reproducibility of optical lattice clocks beyond the realization of the SI second by Cs fountains. By regular comparisons with primary microwave standards, the absolute Sr frequency was proven to be stable and fully reproducible over long time period within the uncertainty of the microwave fountains.

The installation of auto-relocking systems, that can detect and restore the clock to its operational state, allows us to minimize the clock's maintenance and operate them over long periods of time, ranging from 10 to 20 days. During these measurement campaigns, it was possible to reach a quasi-continuous operational regime of the clocks with up to 90% of the total uptime, which starts to be comparable with the robustness of the microwave frequency standards. Such reliable systems are useful for many applications that require long term acquisitions or a high reliability, such as the clock comparisons mentioned above, or the calibration of timescales.

A decisive step forward a re-definition of the SI second was achieved with the first contribution to Atomic International Time by using optical clocks, accepted by BIPM. This contribution made that the Sr optical clock has evolved to be a strong candidate of the primary frequency standard of the future and it shows the progress towards replacing the microwave time and frequency architecture currently realizing the SI second.

Remote optical clocks connected by a connection with a noise and accuracy better than the clock's performances are a new tool to explore fundamental physics, astronomy and geoscience. Optical clocks provide a highly stable signal that makes possible to monitor daily variations of the frequency difference between remote clocks with an exceptional

precision which allows us to establish a new constraint in the search of a possible violation of the Lorentz invariance. The new bound we derive on this violation is two orders of magnitude better than the previous measurement based on clocks, and it is 2 times better than the best current limit based on accelerated ions. We hope that in the near future, other tests of fundamental physics will be performed with denser clock networks.

In addition to these comparisons, we studied the evaluation of new effects that can shift the clock transition. The impact of the incoherent background of the trapping laser was estimated for a TiSa laser and semiconductor sources. For the TiSa laser, which is widely used in OLCs the upper limit on the light-shift is below 10^{-18}. For tapered amplifiers the light shift associated with the ASE background can be filtered to reach a systematic uncertainty in the low 10^{-17} level.

The status of the optical frequency standards described here, using SYRTE Sr clock as an example, shows the continuous progress in the accuracy and the stability of optical clocks. The current clock performance is better and better than the primary microwave frequency standards. In the near future, the best optical clocks should reach the level below 10^{-18}, with a better evaluation of the lattice light shift and of the black body radiation. At SYRTE, a new vacuum environment under study for the Sr2 clock should reduce the BBR uncertainty below 10^{-18}. A novel non-destructive detection method for the transition probability will significantly reduce the clock cycle's dead time, and therefore reduce the Dick effect currently limiting the clock stability [15]. The success of OLCs makes them prime candidates for a possible redefinition of the SI second. With better clock performance, the next optical clocks should massively contribute to TAI, replacing microwave standards in timescales. Optical clocks connected in a fast developing fiber network will provide highly stable signal, initiating new applications and services.

In 2018, a revision of the SI[1] is planned, such that «four of the SI base units - namely the kilogram, the ampere, the kelvin and the mole - will be redefined in terms of constants; the new definitions will be based on fixed numerical values of the Planck constant (h), the elementary charge (e), the Boltzmann constant (k_B), and the Avogadro constant (N_A), respectively.» All revised units will therefore derive directly from the SI second.

[1] http://www.bipm.org/en/measurement-units/rev-si/

Appendices

APPENDIX A

LIST OF PUBLICATIONS

G. Vallet, E. Bookjans, U. Eismann *et al.*
A noise-immune cavity-assisted non-destructive detection for an optical lattice clock in the quantum regime
New Journal of Physics **19** (2017) 083002
https://doi.org/10.1088/1367-2630/aa7c84

P. Delva, J. Lodewyck, S. Bilicki *et al.*
Test of special relativity using a fiber network of optical clocks
Physical Review Letters **118**, 221102, (2017)
https://doi.org/10.1103/PhysRevLett.118.221102

M. Witkowski, N.Nagórny, R. Muñoz-Rodriguez *et al.*
Dual Hg-Rb magneto-optical trap
Optics Express **25**, No. 4, 3165-3179 (2017)
https://doi.org/10.1364/OE.25.003165

R. Tyumenev, M. Favier, S. Bilicki *et al.*
Comparing a mercury optical lattice clock with microwave and optical frequency standards
New Journal of Physics **18** (2016) 113002
http://doi.org/10.1088/1367-2630/18/11/113002

Ch. Lisdat, G. Grosche, N. Quintin *et al.*
A clock network for geodesy and fundamental science
Nature Communications **7**:12443 (2016)
http://www.nature.com/articles/ncomms12443

J. Lodewyck, S. Bilicki, E. Bookjans *et al.*
Optical to microwave clock frequency ratios with a nearly continuous strontium optical lattice clock
Metrologia **53**, (2016) 1123-1130
http://dx.doi.org/10.1088/0026-1394/53/4/1123

APPENDIX B

RÉSUMÉ

Dans la passé, l'astronomie a été responsable du chronométrage, car le temps a été déterminé à partir des changements diurnes dans l'apparition du ciel. Mais la stabilité du temps fourni par la Terre est limitée en raison de l'uniformité insuffisante de sa vitesse de rotation. Donc, la communauté scientifique a dû choisir une autre caractéristique physique plus stable que la rotation de la Terre. Une transition atomique a le potentiel pour devenir une bonne norme de fréquence grâce à leurs propriétés d'invariance et de résonance. En 1955 la transition de l'atome de césium-133 a été calibrée avec ± 20 Hz d'incertitude au Physical National Laboratory (NPL) par L. Essen et J.V.L Parry. En 1967, la 13ème Conférence Générale des Poids et Mesures (CGPM) a accepté la second déterminé par la transition atomique et a défini la seconde comme «la durée de 9 192 631 770 périodes de la radiation correspondant à la transition entre les deux niveaux hyperfins de l'état fondamental de l'atome de césium 133». Au cours des décennies suivantes, la seconde basée sur la transition du césium a été réalisée avec une précision de plus en plus grande. Aujourd'hui, après 50 années de développements et d'expériences, la fontaine atomique au césium, qui utilise un nuage d'atomes refroidis par laser, réalise l'état l'art de l'étalon de fréquence micro-ondes avec une exactitude au niveau de quelques 10^{-16} et une stabilité limitée par le bruit de projection quantique. Elles sont utilisées couramment pour calibrer les échelles de temps internationales (le temps universel coordonné UTC et temps atomique international TAI) via des comparaisons satellitaires, ainsi que pour réaliser la définition de la seconde du système international d'unités (SI).

Aujourd'hui, pour réaliser de meilleurs étalons de fréquences, une nouvelle génération d'étalons basés sur des transitions dans la domaine optique, se développe rapidement dans plusieurs laboratoires dans le monde. Deux pistes son poursuivies : d'une part les horloges piégeant un ion unique dans un champ électromagnétique radiofréquence, et d'autre part les horloges à réseau optique piégeant des atomes neutres dans une onde laser stationnaire par la force dipolaire. Ces dernières, de par leur meilleur rapport signal à bruit résultant du grand nombre d'atomes qu'on peut interroger simultanément, sont récemment devenues les meilleures horloges atomiques, aussi bien en termes de stabilité de fréquence au niveau de $2 \times 10^{-16}/\sqrt{\tau}$ oú τ est le temps d'intégration exprimé en secondes, que sur le contrôle des effets systématiques perturbateurs au niveau de 2×10^{-18}. Ce progrès a été initié par les peignes de fréquences optiques, qui relient le domaine micro-onde accessible à l'électronique et le domaine optique des fréquences des transitions des atomes. Ce transfert se réalise sans dégradation la stabilité du signal. Ainsi, des horloges

à réseau optiques au strontium, ytterbium et mercure ont été construites et elles déjà ont surpassé les étalons de fréquence micro-ondes de deux ordres de grandeur en termes d'exactitude et de stabilité.

Dans le futur proche, une redéfinition la seconde SI est attendue via les transitions des horloges optique. Le groupe de travail des étalons de fréquence (Working Group of Frequency Standards - WGFS) formé en 2001, a recommandé et défini des «représentations secondaires de la seconde» qui peuvent réaliser la seconde SI en parallèle du standard primaire au césium. Cette recommandation fait que plusieurs transitions peuvent servir d'étalons de fréquence. En 2006, le Comité International des Poids et Mesures (CIPM) a officiellement adopté les cinq premières représentations secondaires. En 2015, la liste a été mise à jour.

Cette thèse est consacrée aux progrées récents des horloges à réseau optique au strontium du LNE-SYRTE, Observatoire de Paris. L'incertitude systématique et la stabilité des horloges optiques sont 2 ordres de grandeur meilleures que les horloges atomiques micro-ondes au cesium qui réalisent la seconde SI, bénéficiant maintenent a des applications en physique fondamentale, astronomie et géosciences. Dans un futur proche, une redéfinition de la seconde SI est attendue, quand les horloges optiques se seront révélées aussi fiables et reproductibles que les horloges a micro-ondes. La thèse présente trois étapes décisives dans cette direction. Nous présentons un fonctionnemment operation quasi-continu de nos horloges Sr pendant plusieurs semaines. Des comparaisons de fréquences locales et à distance avec diverses références de fréquence micro-ondes et optiques montrent que les horloges optiques sont reproductibles par des laboratoires independants. Nous avons démontré un premier réseau tout optique entre des horloges optiques à l'échelle continentale. Les horloges au Sr ont été utilisées pour préparer 5 rapports de calibration du Temps Atomique International (TAI) qui ont été validés par le BIPM comme première contribution au TAI par des horloges optiques. Certains de ces résultats ont été utilisés pour borner l'amplitude d'une possible violation de l'invariance de Lorentz analysant les comparaisons d'horloges distantes. Enfin, nous avons effectué une caractérisation complète des déplacements de fréquence associés aux sources laser à semiconducteur utilisées pour le piégeage des atomes dans l'optique d'applications pour des horloges transportables et spatiales.

B.1 Principe de fonctionnement

Les horloges sont constituées de deux composants principaux. D'abord le système atomique proprement dit, constitué d'une enceinte à vide dans laquelle sont préparés les atomes froids de strontium piégés, entourée d'un système de laser pour la capture et la manipulation des atomes. Ensuite, les atomes son interrogés par un laser de très petite largeur de raie (inférieure à 1 Hz), obtenu par la stabilisation d'une diode laser sur une cavité Fabry-Perot ultra-stable.

Le refroidissement laser des atomes est réalisé par le ralentissement d'un jet de strontium collimaté issu d'un four chauffé à 550°C par un ralentisseur Zeeman, puis capturé et refroidit à une température de 3 mK dans un piège magnéto-optique (PMO), en utilisant la transition intense $^1S_0$-$^1P_1$ à longueur d'onde de 461 nm. Quelques 10^6 atomes de ^{87}Sr sont ainsi capturés.

La réseau optique est formé par une onde laser stationnaire à la longueur d'onde magique ($\lambda_m = 813$ nm) dans une cavité optique d'environ 4 cm de longueur placée dans l'enceinte à vide. En utilisant la méthode du drain atomique dans laquelle les atomes qui

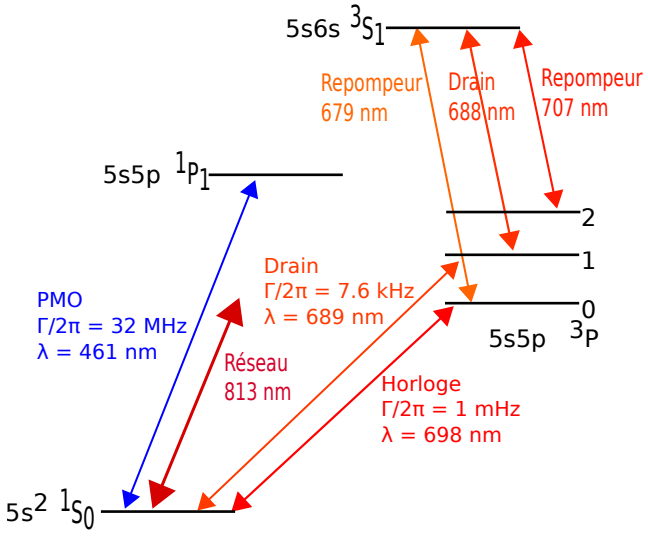

Figure B.1.1. Niveaux d'énergie de l'atome de strontium. La résonance $^1S_0$-$^3P_0$ avec une largeur de raie de l'ordre du millihertz est adaptée pour la transition d'horloge.

se trouvent au niveau de réseau optique sont pompés dans les états métastables $^3P_0$ et $^3P_2$ par deux faisceaux laser à 689 nm et 688 nm, on parvient à transférer environ 1% des atomes du PMO vers le réseau optique. La température de ces atomes est encore trop importante, donc ils sont refroidis en utilisant la raie d'inter-combinaison $^1S_0$-$^3P_1$, soit par refroidissement Doppler dans les deux directions transverses au réseau jusqu'à une température de 10μK, soit par refroidissement sur bandes latérales motionelles dans la direction longitudinale jusqu'à une température de quelques microkelvins. Pour obtenir des résonance étroites et contrasté, il convient de préparer l'état interne de ces atomes via pomper des atomes dans les états magnétiques extrêmes ($m_F = \pm 9/2$).

Les atomes sont ensuite interrogés avec un laser d'horloge à 698 nm pendant une durée de 200 ms, limitée par le temps de cohérence de ce laser. Enfin, la probabilité de transition associée à cette interaction est mesurée en détectant à l'aide d'une camera la fluorescence des atomes restés dans l'état fondamental soumis à un faisceau laser à 461 nm.

B.2 Évaluation des effets systématiques

Nous avons établi le bilan d'exactitude de l'horloge Sr2 au niveau 4×10^{-17}, reproduit dans le tableau B.2.1.

La principale contribution vient du rayonnement du corps noir. L'amélioration de cet effet nécessite la conception d'une nouvelle chambre à vide dans lequel la température est bien connu et plus homogène. Les autres effets sont limités par la statistique. Le bilan exactitude de l'horloge a été réévalué en Juin 2017 au niveau 2×10^{-17}, grâce à une meilleure statistique sur certains effets comme le déplacement lumineux du réseau, la distorsion de la résonance et les collisions atomes froids) mais aussi une meilleure homogénéité de la température de la chambre à vide.

Table B.2.1. Bilan exactitude de l'horloge Sr2 en valeur relative en Juin 2016.

Effet	Correction $[10^{-18}]$	Incertitude $[10^{-18}]$
Rayonnement du corps noir	5208	20
Effet Zeeman quadratique	1317	12
Déplacement lumineux du réseau	-30	20
Spectre du réseau	0	1
Collisions atomes froids	0	8
Distorsion de la résonance	0	20
Déplacement lumineux de la sonde	0.4	0.4
Dérive de phase dans les MAO	-4	4
Erreur de l'intégrateur	0	3
Charges statiques	0	1.5
Rayonnement du corps noir four	0	10
Collisions atomes chauds	0	8
TOTAL	6487.4	41

B.3 Comparaisons d'horloges

Les comparaisons d'horloges sont un élément clé dans l'exploitation des horloges atomiques. D'abord, elles sont nécessaires pour confirmer les performances affichées : la comparaison entre deux horloges donne directement la stabilité de fréquence combinée de ces deux horloges. De plus, si les deux horloges utilisent la même espèce atomique, l'égalité entre leurs fréquences confirmera le bilan d'exactitude. Si les horloges utilisent deux espèces atomiques différentes, la reproductibilité dans le temps et l'espace du rapport de fréquence entre les horloges devra être compatible avec le bilan d'exactitude combiné des horloges.

Ensuite, ce sont des comparaisons entre horloges que découlent la plupart de leurs applications. Elles sont déjà en cours d'exploration dans les instituts nationaux de métrologie dans le monde et elles sont basées sur la surveillance l'évolution relative dans le temps du rapport de fréquence entre différentes espèces atomiques. Il s'agit de détecter une hypothétique dérive des constantes fondamentales, d'explorer les variations spatiales du potentiel gravitationnel de la Terre, détecter la matière noire, effectuer des vérifications la relativité générale ou restreinte. D'autres applications utilisent la grande stabilité des horloges optique, comme la réalisation d'échelles de temps et en astronomie.

B.3.1 Comparaison locale de deux horloges au strontium

Nous avons comparé deux horloges au strontium non synchronisées. La stabilité de l'écart de fréquence entre ces deux horloges est au niveau 1.0×10^{-15} à 1 s et descend au niveau du bas 10^{-17} après une heure d'intégration. La différence entre les horloges est compatible avec le bilan d'incertitude combiné des deux horloges au niveau de $(2.3 \pm 7.1) \times 10^{-17}$. Cet accord a permis de confirmer le bilan d'incertitude des horloges, et donne une indication forte que les effets systématiques des horloges à réseau optique sont effectivement maîtrisés avec une meilleure incertitude que les horloges micro-onde.

Cette comparaison a montré que les comparaisons locales entre horloges de même nature sont essentielles : au cours de la caractérisation des horloges, la mesure de la différence de fréquence entre les horloges nous a permis d'identifier deux effets systématiques

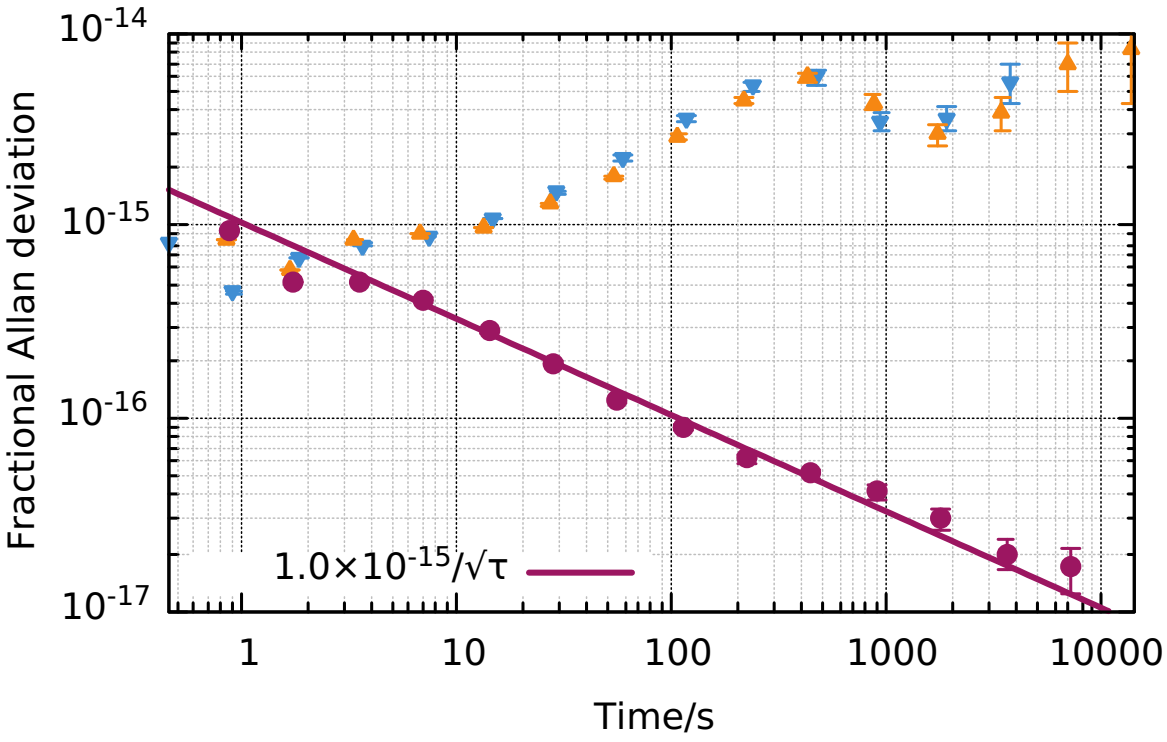

Figure B.3.2. Stabilité de fréquence du laser d'horloge, comparée à l'horloge SrB (bleu) et Sr2 (orange). Le bruit de fréquence long terme du laser d'horloge s'élimine lorsque l'on compare les deux horloges (violet). La stabilité de cette comparaison reste toutefois limitée par l'effet Dick.

qui n'avaient pas été pris en compte par le passé pour les horloges à réseau optique, et qui peuvent induire des déplacements de fréquence supérieurs à 10^{-15}. Ces deux effets sont le déplacement de fréquence dû à la présence de charges statiques et le déplacement lumineux induit par le spectre incohérent issu des sources laser semiconducteurs (section 1.5).

B.3.2 Comparaisons locales d'horloges d'espèces différentes

Le LNE-SYRTE dispose d'un ensemble d'horloges atomiques micro-onde et une horloge optique au mercure, qui peuvent être comparées aux horloges au strontium via un peigne de fréquences généré par un laser femto-seconde fibré. Cet ensemble d'horloges nous a permis de réaliser des mesures répétées du rapport de fréquence entre l'horloge au strontium et les étalons primaires au césium. Au cours des dernières années, plusieurs campagnes de comparaison ont été réalisées. La stabilité de ces comparaisons de l'ordre de $3 \times 10^{-14}/\sqrt{\tau}$ est limitée par bruit de projection quantique des horloges de type fontaines atomiques. L'exactitude, 2.6×10^{-16} est également limitée par l'exactitude des fontaines. Ces mesures, qui constituent la meilleure détermination d'une fréquence absolue à ce jour, sont reproductibles sur plusieurs années avec un écart inférieur à l'incertitude systématique, ce qui indique une excellente maîtrise des effets systématiques sur les deux horloges. La moyenne de la fréquence absolue de la transition horloge obtenue à partir de toutes les campagnes de mesure est :

$$\nu_{Sr} = 429228004229872.92(12) \text{ Hz}.$$

De plus, elles sont en très bon accord avec des mesures similaires effectuées aux autres

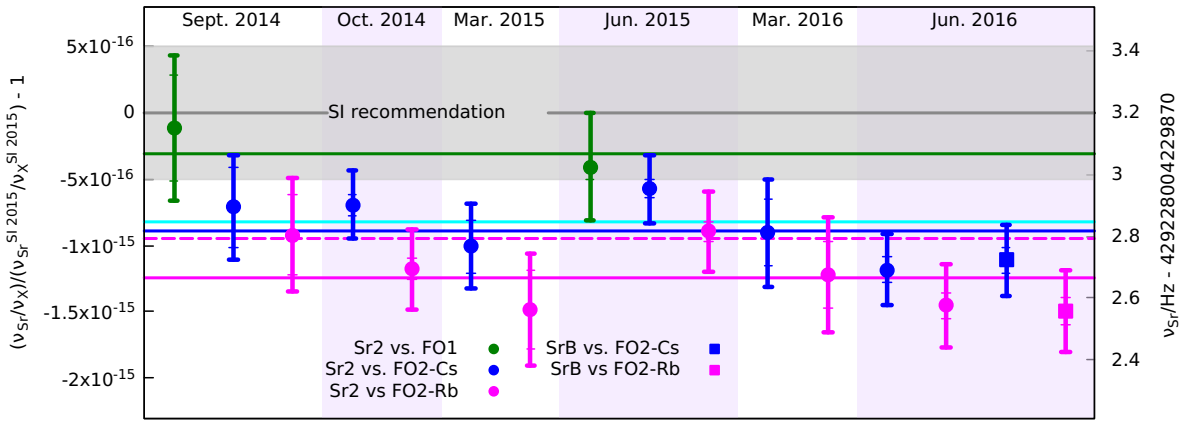

Figure B.3.3. Rapport de fréquence entre la résonance des horloges du strontium et la fréquence des horloges au césium et la rubidium, relativement aux rapport recommandés par le comité consultatif temps fréquence (CCTF) (labellisés SI2015). Les horloges impliquées dans cette mesure sont la fontaine atomique au césium FO1 et la fontaine mixte au rubidium et au césium FO2. Pour les comparaisons entre les horloges au strontium et au césium, l'échelle de droite indique la fréquence absolue correspondante pour la fréquence de l'horloge au strontium dans le SI. Les barres d'erreur grasses indiquent l'incertitude totale.

instituts nationaux de métrologie. Plus récemment, nous avons mesuré pour la première fois le rapport de fréquence entre les horloges au strontium et au rubidium, avec une incertitude comparable. Enfin, les premières comparaisons tout optique entre les horloges à réseau optique au strontium et au mercure conduites au LNE-SYRTE permettent de s'affranchir des étalons micro-onde, et ainsi de démontrer une stabilité de fréquence dix fois meilleure, à quelques 10^{-15} avec la précision au-delà la seconde SI limite. Le rapport de fréquence obtenu à ces mesures est :

$$\mathcal{R} = 2.62931420989890915(46).$$

Ce résultat est 1 ordre de grandeur meilleur que le dernier rapport obtenu en 2012 qui avait été mesuré via une fontaine au césium. Notre nouveau rapport est en très bon accord avec le même rapport indépendamment mesuré par l'équipe japonaise du RIKEN.

B.3.3 Comparaisons intracontinentales

Les comparaisons d'horloges distantes, par exemple en vue de réaliser des échelles de temps internationales, utilisent à ce jour des méthodes satellitaires. Pourtant, même les meilleures d'entre elles ne permettent pas de comparer des horloges avec une résolution meilleure que quelques 10^{-16} après quelques semaines, incompatible avec la résolution des horloges optiques de l'ordre de 10^{-17}. Pour comparer des horloges à réseau optique distantes sans dégrader leur stabilité de fréquence, de nouveaux moyens de comparaison utilisant des fibres optiques dont les fluctuations d'indice sont compensées ont été mises en place et caractérisées. Un lien connectant le LNE-SYRTE, la PTB (Braunschweig, Allemagne) et le NPL (Londres, grande Bretagne), plus récemment mis en place, a permis de comparer les horloges à réseau optique au strontium des trois instituts. Depuis 2014, les horloges (en 2014 et 2015 les horloges du LNE-SYRTE et de PTB seulement) sont été impliquées dans les campagnes de comparaisons d'horloges par ce lien optique. La stabilité de la comparaison est entièrement limitée par les horloges, et a permis de démontrer une

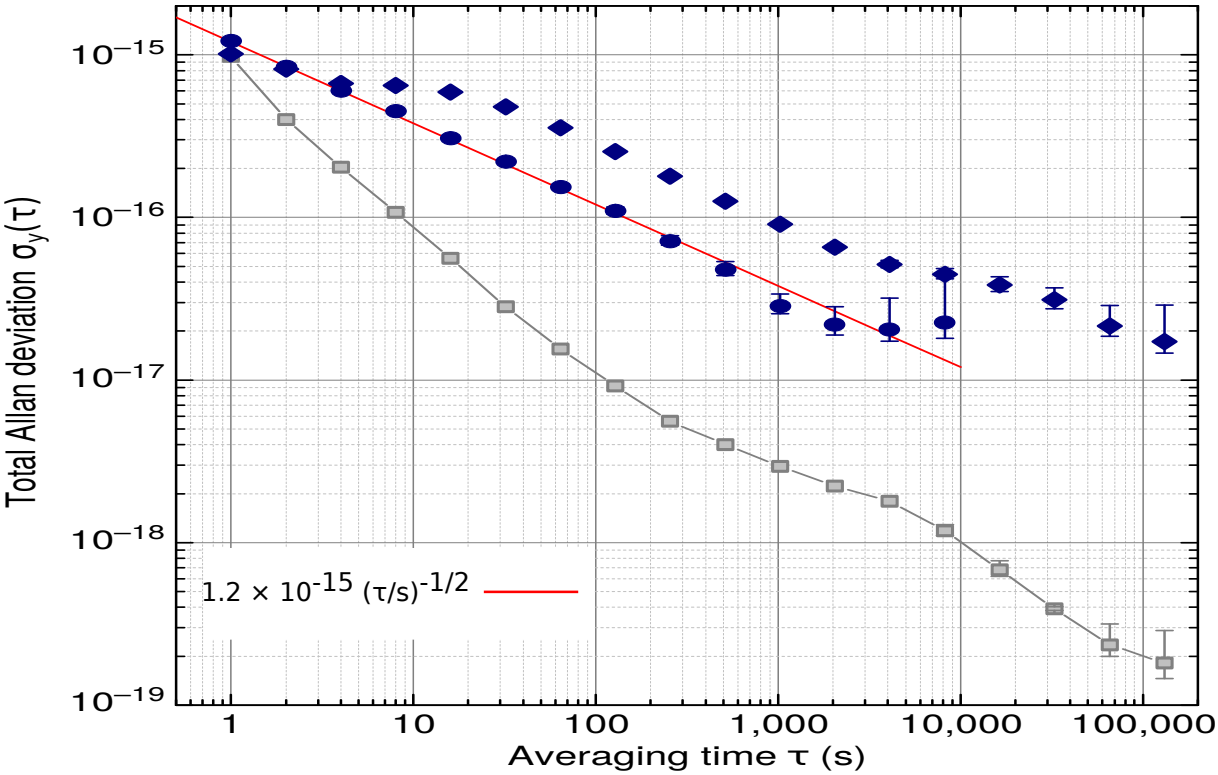

Figure B.3.4. Stabilité de fréquence entre des horloges du SYRTE et de la PTB en utilisant le lien optique pour deux comparaisons (bleu). La stabilité de cette comparaison n'est pas limitée par le bruit du transfert de fréquence (gris).

résolution statistique de 2×10^{-17} après 1 heure d'intégration. Cette résolution est un ordre de grandeur meilleure que celle offerte par les méthodes satellitaires, atteinte après un temps d'intégration deux ordres de grandeur plus petit. De plus, les performances du lien sont compatibles avec les progrès attendus pour les horloges à réseau optique dans la gamme des 10^{-19}. La différence de fréquence entre les deux horloges du LNE-SYRTE et de PTB est $(4.7 \pm 5.0) \times 10^{-17}$, compatible avec zéro. Ce la première comparaison dans la gamme 10^{-17} entre deux horloges à réseau optique complètement indépendantes, développées par des équipes différentes. Cette expérience démontre donc pleinement la reproductibilité des horloges à réseau optique.

Certains de ces résultats ont été utilisés pour tester la dilation de temps de vitesse relative par analyse de la stabilité de fréquence entre ces horloges connectées par lien optique. Ce test établit une nouvelle contrainte du paramètre de l'invariance de Lorentz α, que améliore des deux ordres de grandeur les derniers résultats obtenus par comparaisons d'horloge, et il est 2 fois meilleur que la meilleur contrainte obtenu par des mesures sur des ions relativistes. Dans le futur proche, le réseau ds liens optiques va s'agrandir en connectant de nouveaux laboratoires (en France, Allemagne mais aussi Italie ou Pologne), ce qui permettra de faire un réseau dense et d'effectuer de nouveaux tests de physique fondamentale.

B.4 Vers une redéfinition de la seconde fondée sur une transition optique

Comme les horloges au césium sont maintenant surpassées par les horloges optiques, il est envisagé de redéfinir l'unité de temps sur la base d'une horloge optique. De nombreuses transitions optiques, dont plusieurs sont déjà recommandées par le Comité international des poids et mesures (CIPM) comme représentations secondaires de la seconde, pourront être choisies pour cette redéfinition. Parmi ces transitions optiques, celle du strontium est un bon candidat car sa réalisation pratique est parmi les plus simples, et il est à ce jour l'étalon de fréquence optique le plus répandu et le mieux reproduit dans les laboratoires de métrologie.

B.4.1 Horloges au strontium opérationnelles

La contribution aux échelles de temps internationales, notamment au TAI, est une première étape vers la redéfinition de la seconde avec un étalon optique. Une telle contribution consiste en la calibration d'un oscillateur local - en l'occurrence un maser à hydrogène - réalisant une échelle de temps locale - pour le LNE-SYRTE, il s'agit d'UTC(OP). Pour qu'une telle contribution soit représentative, il faut d'une part des mesures longues capables de calibrer l'oscillateur local en continu sur plusieurs jours, et d'autre part des mesures répétées pour avoir un poids significatif. Ainsi, il est nécessaire de faire fonctionner les horloges optiques sur des intervalles de 5 à 10 jours, correspondant à des plages de calibration du TAI fixées par le Bureau International des Poids et Mesures, avec un taux de remplissage typique supérieur à 80% pour pouvoir détecter de façon fiable les fluctuations de fréquence de l'oscillateur. C'est pourquoi une telle contribution nécessite la démonstration d'horloges opérationnelles. Malgré le haut taux de remplissage de notre horloges, il y a des intervalles de temps pendant lequel les horloges ne fonctionnent pas et le maser n'est pas calibré. Pour cette raison, il est nécessaire d'estimer l'incertitude additionnelle due à ce temps mort. Au LNE-SYRTE, le temps mort est défini comme un intervalle de temps plus long que 600 s. Les temps morts de l'ordre d'une heure constituent la contribution la plus grande. L'incertitude associé avec cet effet est estimée au niveau de 1×10^{-16}.

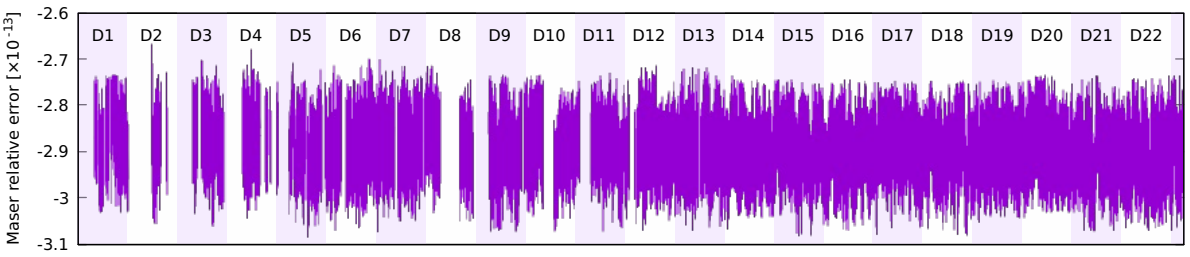

Figure B.4.5. En juin 2015, l'horloges Sr2 a fonctionné pendant 21 jours avec taux de remplissage de 83%. Cette figure montre le différence de fréquence entre l'horloge au strontium et le maser utilisé pour générer UTC(OP).

B.4.2 Contribution au TAI

Nous avons effectué un travail de fiabilisation des horloges au strontium du LNE-SYRTE afin de pouvoir réaliser cet objectif. Ce développement s'est conclu par la démonstration de mesures longues et quasi-continues, avec une assistance humaine limitée. Il est possible d'atteindre une durée de 10 jours avec un taux de remplissage de 93.8 %. Cette mesure est donc compatible avec une contribution au TAI. Nous avons répété cette démonstration en juin 2015, mars 2016, et juin 2016, sur des périodes allant jusqu'à 21 jours avec un taux de remplissage entre 66% et 83%. L'ensemble de ces mesures a été récemment adressé au BIPM, qui a validé ces rapports. La première contribution d'une horloge optique au TAI a donc été constituée en avril 2017 et a été publiée dans la Circulaire T350. Dans le futur, le LNE-SYRTE veut contribuer régulièrement avec les deux horloges au strontium, au rythme de deux étalonnage de dix jours par an.

B.4.3 Comparaisons intercontinentales

À ce jour, il n'existe pas de moyen de comparaison permettant de comparer des horloges optiques à l'échelle mondiale avec une résolution meilleure que 10^{-16}. Malgré cela, en juin 2016, les horloges Sr du SYRTE et un autre horloge au strontium au NICT au Japon ont été comparées de façon synchrone en utilisant le TAI comme moyen de transfert. Dans ce cas, le bruit du TAI s'annule jusqu'à la performance de lien satellitaire. Deux masers étalonnés sont comparés par la méthode GPS IPPP qui apporte la meilleure précision. La différence de fréquence entre les deux horloges au strontium est : $(-4 \pm 8) \times 10^{-16}$, limitée par le lien satellitaire.

B.5 Un réseau optique avec des sources semi-conducteurs

Le strontium est l'espèce atomique la plus couramment choisie pour les horloges à réseau optique, notamment du fait de l'accessibilité des sources laser nécessaires au refroidissement et au piégeage des atomes. Ainsi, l'horloge au strontium est considérée comme une horloge transportable ou spatiale dans la futur. Pour cela, un équipement compact et fiable est nécessaire. Un des plus grands problèmes est la miniaturisation du laser à 813 nm pour générer le réseau optique. Ce laser de piégeage doit fournir aussi une haute puissance optique (1 W) et une haute pureté du spectre afin de piéger les atomes sans perturbations. Des sources semi-conducteurs (comme des diode lasers ou des amplificateurs optiques) semblent prometteur en termes de volume. Mais nous avons pu montrer que les sources semi-conducteurs peuvent induire un déplacement de fréquence de plus de 10^{-15} associé avec l'émission spontanée amplifiée. Donc il est nécessaire de prendre en compte l'ensemble de la lumière qui est émise par la source utilisée pour générer le réseau optique, notamment en dehors du spectre d'émission laser. Ce fond spectral peut se situer à plusieurs centaines de nm de la longueur d'onde magique, oú même une faible puissance peut induire un large effet systématique. Quantitativement, il est nécessaire que toute la puissance située hors de l'émission laser soit 80 dB plus faible que cette dernière pour atteindre une exactitude de 10^{-18} . Cette condition est satisfaite pour notre source - un laser titane saphir - que est utilisé couramment au laboratoire.

Nous proposons une caractérisation complète du déplacement de fréquence associé aux sources semi-conducteurs, y compris la mesure optique en utilisant un analyseur du

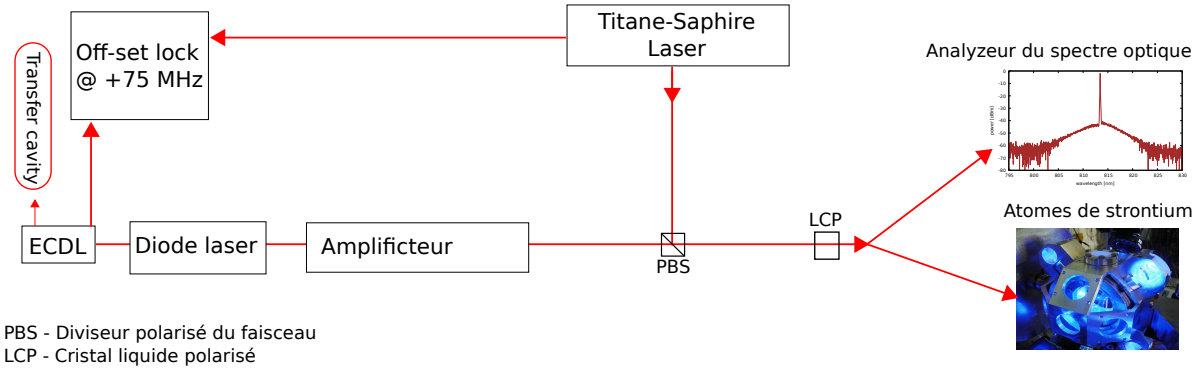

Figure B.5.6. Système de distribution des lasers piégeages qui sont utilisés sur l'expérience. La lumière des lasers est mesurée par un analyseur du spectre optique ou les atomes de strontium.

spectre optique, mais aussi la mesure du déplacement de fréquence par des atomes. Nous proposons aussi une stratégie de filtration afin d'obtenir un déplacement de fréquence au niveau plus bas que 10^{-17}. Afin de mesurer directement le déplacement associé avec l'émission spontanée amplifié, nous avons mesuré le déplacement de fréquence dû aux lasers piégeages en alternant la configuration nominale d'horloge (dans laquelle le titane saphir est utilisé) et une situation dans laquelle le réseau optique est généré par les sources semi-conducteurs. Nous pouvons résoudre un déplacement au niveau 10^{-16} pour un spectre très déséquilibré en utilisant un filtre passe bande. Le résultat de l'expérience est cohérent avec un modèle théorique.

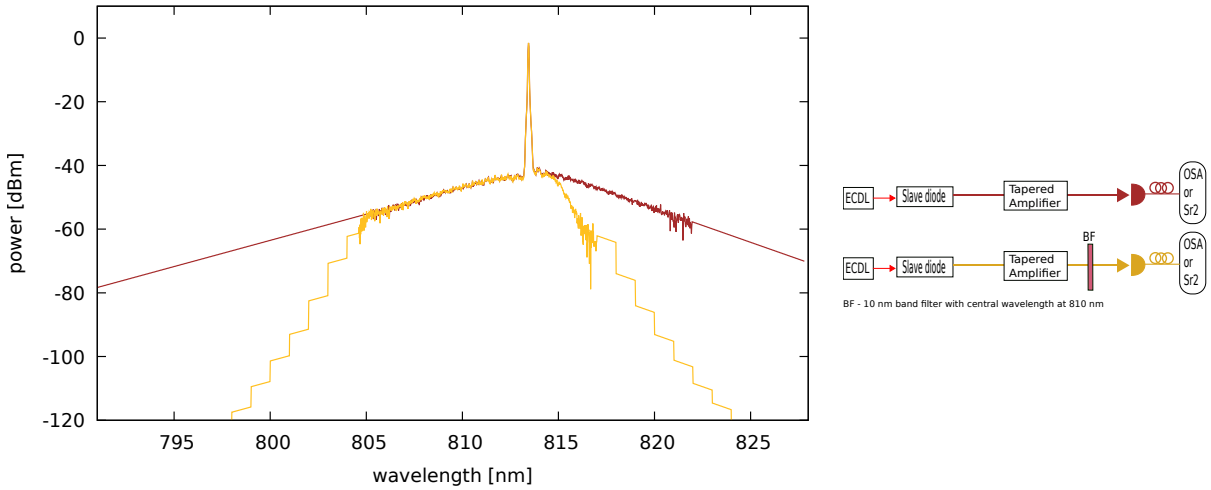

Figure B.5.7. (gauche) Distribution du spectre optique des diodes laser et amplificateur TA (à droite) pour un position donnée du filtre.

B.6 Conclusion

Les horloges à réseau optique ont maintenant largement surpassé les horloges micro-onde, et mènent, encore talonnées par les horloges optiques à ion, la course à l'exactitude. Le développement de nombreuses horloges à réseau optique à travers le monde a démontré leur reproductibilité dans la gamme des 10^{-17} , donnant une solide crédibilité aux performances annoncées. À court terme, les horloges à réseau optique devraient contribuer à

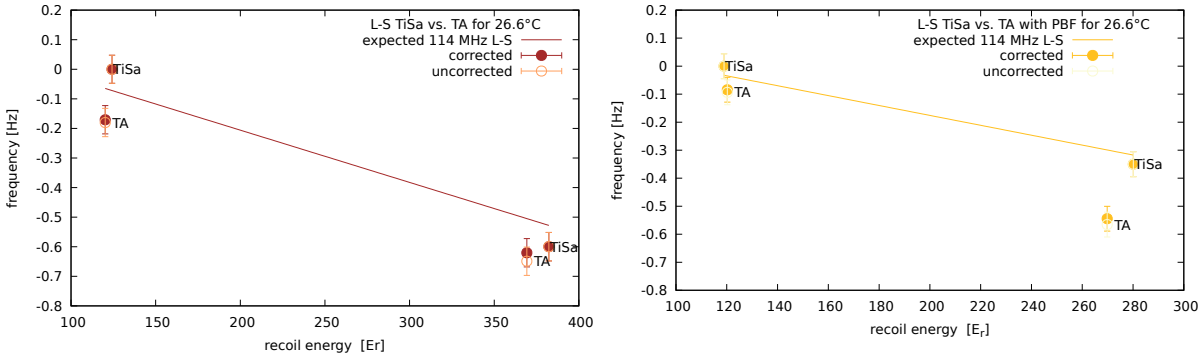

Figure B.5.8. Mesure différentielle du déplacement lumineux pour 2 profondeurs de piégeage du laser titane saphir et de l'amplificateur TA pour une configuration donnée du filtre. Les points corrigés comprennent la différence de fréquence de 5 MHz introduite entre les deux lasers.

l'élaboration d'échelles de temps internationales en grande partie, ce qui est une première étape vers une redéfinition de la seconde, unité de temps dans le SI. Pourtant, malgré ces rapides avancées, les performances ultimes de ces horloges sont encore floues. Les progrès attendus dans la stabilisation de la fréquence des lasers, avec des cavités de référence cryogéniques ou des méthodes de stabilisation innovantes, laissent entrevoir des stabilités au niveau du bruit de projection quantique, de l'ordre de $10^{-17}/\sqrt{\tau}$. Avec une telle stabilité, l'évaluation des effets systématiques au niveau de 10^{-19} est tout à fait envisageable. À un tel niveau de performances, les applications des horloges à réseau optique en géodésie et en physique fondamentale seront possibles.

BIBLIOGRAPHY

[1] Dennis D McCarthy. Evolution of timescales from astronomy to physical metrology. *Metrologia*, 48(4):S132, 2011. http://stacks.iop.org/0026-1394/48/i=4/a=S03.

[2] W. Snyder. Lord Kelvin on atoms as fundamental natural standards (for base units). *IEEE Transactions on Instrumentation and Measurement*, 22(1):99–99, March 1973. http://ieeexplore.ieee.org/document/4314109/.

[3] L. Essen and J.V.L. Parry. An atomic standard of frequency and time interval: a cesium resonator. *Nature*, 176(4476):280–282, 1955. http://dx.doi.org/10.1038/176280a0.

[4] W. Markowitz, R. Glenn Hall, L. Essen, and J. V. L. Parry. Frequency of cesium in terms of ephemeris time. *Phys. Rev. Lett.*, 1:105–107, Aug 1958. https://link.aps.org/doi/10.1103/PhysRevLett.1.105.

[5] J. Guéna *et al*. Progress in atomic fountains at LNE-SYRTE. *IEEE Trans. Ultrasonics Ferroelectr. Freq. Control*, 59, 391-409, 2012. ieeexplore.ieee.org/iel5/58/6174170/06174184.pdf.

[6] T.L. Nicholson, S.L. Campbell, R.B. Hutson, G.E. Marti, B.J. Bloom, R.L. McNally, W. Zhang, M.D. Barrett, M.S. Safronova, G.F. Strouse, W.L. Tew, and J. Ye. Systematic evaluation of an atomic clock at 2×10^{-18} total uncertainty. *Nature Communications*, 6, (6896), 2016. http://dx.doi.org/10.1038/ncomms7896.

[7] H. Schnatz, B. Lipphardt, J. Helmcke, F. Riehle, and G. Zinner. First phase-coherent frequency measurement of visible radiation. *Phys. Rev. Lett.*, 76:18–21, Jan 1996. https://link.aps.org/doi/10.1103/PhysRevLett.76.18.

[8] Theodor W. Hänsch. Nobel lecture: Passion for precision. *Rev. Mod. Phys.*, 78:1297–1309, Nov 2006. https://link.aps.org/doi/10.1103/RevModPhys.78.1297.

[9] John L. Hall. Nobel lecture: Defining and measuring optical frequencies. *Rev. Mod. Phys.*, 78:1279–1295, Nov 2006. https://link.aps.org/doi/10.1103/RevModPhys.78.1279.

[10] BIPM. https://www.bipm.org/en/publications/mises-en-pratique/standard-frequencies.html.

[11] W.J. Riley. *Handbook of Frequency Stability Analysis*. NIST Special Publication 1065, 2008.

[12] W. M. Itano, J. C. Bergquist, J. J. Bollinger, J. M. Gilligan, D. J. Heinzen, F. L. Moore, M. G. Raizen, and D. J. Wineland. Quantum projection noise: Population fluctuations in two-level systems. *Phys. Rev. A*, 47:3554–3570, May 1993. https://link.aps.org/doi/10.1103/PhysRevA.47.3554.

[13] G J. Dick. Local oscillator induced instabilities in trapped ion frequency standards. *Proc. of Precise Time and Time Interval*, page 16, 12 1987. http://tycho.usno.navy.mil/ptti/1987papers/Vol19_13.pdf.

[14] Jérôme Lodewyck, Philip G. Westergaard, and Pierre Lemonde. Nondestructive measurement of the transition probability in a Sr optical lattice clock. *Phys. Rev. A*, 79:061401, Jun 2009. https://link.aps.org/doi/10.1103/PhysRevA.79.061401.

[15] G. Vallet, E. Bookjans, U. Eismann, S. Bilicki, R. Le Targat, and J. Lodewyck. A noise-immune cavity-assisted non-destructive detection for an optical lattice clock in the quantum regime. *New Journal of Physics*, 19(8):083002, 2017. http://stacks.iop.org/1367-2630/19/i=8/a=083002.

[16] D. J. Wineland, J. J. Bollinger, W. M. Itano, and D. J. Heinzen. Squeezed atomic states and projection noise in spectroscopy. *Phys. Rev. A*, 50:67–88, Jul 1994. https://link.aps.org/doi/10.1103/PhysRevA.50.67.

[17] Onur Hosten, Nils J. Engelsen, Rajiv Krishnakumar, and Mark A. Kasevich. Measurement noise 100 times lower than the quantum-projection limit using entangled atoms. *Nature*, 529:505–508, 2016. http://dx.doi.org/10.1038/nature16176.

[18] T. L. Nicholson, M. J. Martin, J. R. Williams, B. J. Bloom, M. Bishof, M. D. Swallows, S. L. Campbell, and J. Ye. Comparison of two independent Sr optical clocks with 1×10^{-17} stability at 10^3 **s**. *Phys. Rev. Lett.*, 109:230801, Dec 2012. https://link.aps.org/doi/10.1103/PhysRevLett.109.230801.

[19] Sebastian Häfner, Stephan Falke, Christian Grebing, Stefan Vogt, Thomas Legero, Mikko Merimaa, Christian Lisdat, and Uwe Sterr. 8×10^{-17} fractional laser frequency instability with a long room-temperature cavity. *Opt. Lett.*, 40(9):2112–2115, May 2015. http://ol.osa.org/abstract.cfm?URI=ol-40-9-2112.

[20] Schioppo M., Brown R. C., McGrew W. F., Hinkley N., Fasano R. J., Beloy K., Yoon T. H., Milani G., Nicolodi D., Sherman J. A., Phillips N. B., Oates C. W., and Ludlow A. D. Ultrastable optical clock with two cold-atom ensembles. *Nat. Photon.*, 11, 2016. http://dx.doi.org/10.1038/nphoton.2016.231.

[21] Kessler T., Hagemann C., Grebing C., Legero T., Sterr U., Riehle F., Martin M. J., Chen L., and Ye J. A sub-40-mHz-linewidth laser based on a silicon single-crystal optical cavity. *Nat. Photon.*, 6, 2012. http://dx.doi.org/10.1038/nphoton.2012.217.

[22] D. G. Matei, T. Legero, S. Häfner, C. Grebing, R. Weyrich, W. Zhang, L. Sonderhouse, J. M. Robinson, J. Ye, F. Riehle, and U. Sterr. 1.5 μm lasers with sub-10 mhz linewidth. *Phys. Rev. Lett.*, 118:263202, Jun 2017. https://link.aps.org/doi/10.1103/PhysRevLett.118.263202.

[23] Sana Amairi, Thomas Legero, Thomas Kessler, Uwe Sterr, Jannes B. Wübbena, Olaf Mandel, and Piet O. Schmidt. Reducing the effect of thermal noise in optical cavities. *Applied Physics B*, 113(2):233–242, Nov 2013. https://doi.org/10.1007/s00340-013-5464-8.

[24] Garrett D. Cole, Wei Zhang, Michael J. Martin, Jun Ye, and Markus Aspelmeyer. Tenfold reduction of brownian noise in high-reflectivity optical coatings. *Nat. Photon.*, 7, 2013. http://dx.doi.org/10.1038/nphoton.2013.174.

[25] Qun-Feng Chen, Andrei Troshyn, Ingo Ernsting, Steffen Kayser, Sergey Vasilyev, Alexander Nevsky, and Stephan Schiller. Spectrally narrow, long-term stable optical frequency reference based on a Eu^{3+}:Y_2SiO_5 crystal at cryogenic temperature. *Phys. Rev. Lett.*, 107:223202, Nov 2011. https://link.aps.org/doi/10.1103/PhysRevLett.107.223202.

[26] David R. Leibrandt, Michael J. Thorpe, Chin-Wen Chou, Tara M. Fortier, Scott A. Diddams, and Till Rosenband. Absolute and relative stability of an optical frequency reference based on spectral hole burning in Eu^{3+}:Y_2SiO_5. *Phys. Rev. Lett.*, 111:237402, Dec 2013. https://link.aps.org/doi/10.1103/PhysRevLett.111.237402.

[27] R. Kohlhaas, A. Bertoldi, E. Cantin, A. Aspect, A. Landragin, and P. Bouyer. Phase locking a clock oscillator to a coherent atomic ensemble. *Phys. Rev. X*, 5:021011, Apr 2015. https://link.aps.org/doi/10.1103/PhysRevX.5.021011.

[28] D. Meiser, Jun Ye, D. R. Carlson, and M. J. Holland. Prospects for a millihertz-linewidth laser. *Phys. Rev. Lett.*, 102:163601, Apr 2009. https://link.aps.org/doi/10.1103/PhysRevLett.102.163601.

[29] Jérôme Lodewyck, Philip G Westergaard, Arnaud Lecallier, Luca Lorini, and Pierre Lemonde. Frequency stability of optical lattice clocks. *New Journal of Physics*, 12(6):065026, 2010. http://stacks.iop.org/1367-2630/12/i=6/a=065026.

[30] G. W. Biedermann, K. Takase, X. Wu, L. Deslauriers, S. Roy, and M. A. Kasevich. Zero-dead-time operation of interleaved atomic clocks. *Phys. Rev. Lett.*, 111:170802, Oct 2013. https://link.aps.org/doi/10.1103/PhysRevLett.111.170802.

[31] M. Meunier, I. Dutta, R. Geiger, C. Guerlin, C. L. Garrido Alzar, and A. Landragin. Stability enhancement by joint phase measurements in a single cold atomic fountain. *Phys. Rev. A*, 90:063633, Dec 2014. https://link.aps.org/doi/10.1103/PhysRevA.90.063633.

[32] M. G. Raizen, J. M. Gilligan, J. C. Bergquist, W. M. Itano, and D. J. Wineland. Ionic crystals in a linear paul trap. *Phys. Rev. A*, 45:6493–6501, May 1992. https://link.aps.org/doi/10.1103/PhysRevA.45.6493.

[33] T. Rosenband, D. B. Hume, P. O. Schmidt, C. W. Chou, A. Brusch, L. Lorini, W. H. Oskay, R. E. Drullinger, T. M. Fortier, J. E. Stalnaker, S. A. Diddams, W. C. Swann, N. R. Newbury, W. M. Itano, D. J. Wineland, and J. C. Bergquist. Frequency ratio of Al^+ and Hg^+ single-ion optical clocks; metrology at the 17th decimal place. *Science*, 319(5871):1808–1812, 2008. http://science.sciencemag.org/content/319/5871/1808.

[34] M. Chwalla, J. Benhelm, K. Kim, G. Kirchmair, T. Monz, M. Riebe, P. Schindler, A. S. Villar, W. Hänsel, C. F. Roos, R. Blatt, M. Abgrall, G. Santarelli, G. D. Rovera, and Ph. Laurent. Absolute frequency measurement of the $^{40}Ca^+$ $4s\ ^2s_{1/2} - 3d\ ^2d_{5/2}$ clock transition. *Phys. Rev. Lett.*, 102:023002, Jan 2009. https://link.aps.org/doi/10.1103/PhysRevLett.102.023002.

[35] K. Matsubara *et al*. Direct comparison of a Ca^+ single-ion clock against a Sr lattice clock to verify the absolute frequency measurement. *Opt. Express*, 20(22034-22041), 2012. https://doi.org/10.1364/OE.20.022034.

[36] H. Margolis *et al*. Hertz-level measurement of the optical clock frequency in a single $^{88}Sr^+$ ion. *Science*, 306, 1355-1358, 2004. http://science.sciencemag.org/content/306/5700/1355.

[37] Alan A. Madej, Pierre Dubé, Zichao Zhou, John E. Bernard, and Marina Gertsvolf. $^{88}Sr^+$. *Phys. Rev. Lett.*, 109:203002, Nov 2012. https://link.aps.org/doi/10.1103/PhysRevLett.109.203002.

[38] J. von Zanthier, Th. Becker, M. Eichenseer, A. Yu. Nevsky, Ch. Schwedes, E. Peik, H. Walther, R. Holzwarth, J. Reichert, Th. Udem, T. W. Hänsch, P. V. Pokasov, M. N. Skvortsov, and S. N. Bagayev. Absolute frequency measurement of the In^+ clock transition with a mode-locked laser. *Opt. Lett.*, 25(23):1729–1731, Dec 2000. https://doi.org/10.1364/OL.25.001729.

[39] R.M. Godun *et al*. Frequency ratio of two optical clock transitions in $^{171}Yb^+$ and constraints on the time variation of fundamental constants. *Phys. Rev. Lett.*, 113, 210801, 2014. https://link.aps.org/doi/10.1103/PhysRevLett.113.210801.

[40] N. Huntemann, M. Okhapkin, B. Lipphardt, S. Weyers, Chr. Tamm, and E. Peik. High-accuracy optical clock based on the octupole transition in $^{171}Yb^+$. *Phys. Rev. Lett.*, 108:090801, Feb 2012. https://link.aps.org/doi/10.1103/PhysRevLett.108.090801.

[41] N. Huntemann, C. Sanner, B. Lipphardt, Chr. Tamm, and E. Peik. Single-ion atomic clock with 3×10^{-18} systematic uncertainty. *Phys. Rev. Lett.*, 116:063001, Feb 2016. https://link.aps.org/doi/10.1103/PhysRevLett.116.063001.

[42] W. H. Oskay, S. A. Diddams, E. A. Donley, T. M. Fortier, T. P. Heavner, L. Hollberg, W. M. Itano, S. R. Jefferts, M. J. Delaney, K. Kim, F. Levi, T. E. Parker, and J. C. Bergquist. Single-atom optical clock with high accuracy. *Phys. Rev. Lett.*, 97:020801, Jul 2006. https://link.aps.org/doi/10.1103/PhysRevLett.97.020801.

[43] Hidetoshi Katori, Masao Takamoto, V. G. Pal'chikov, and V. D. Ovsiannikov. Ultrastable optical clock with neutral atoms in an engineered light shift trap. *Phys. Rev. Lett.*, 91:173005, Oct 2003. https://link.aps.org/doi/10.1103/PhysRevLett.91.173005.

[44] Masao Takamoto and Hidetoshi Katori. Spectroscopy of the $^1s_0$–$^3p_0$ clock transition of ^{87}Sr in an optical lattice. *Phys. Rev. Lett.*, 91:223001, Nov 2003.

[45] Masao Takamoto, Feng-Lei Hong, Ryoichi Higashi, and Hidetoshi Katori. An optical lattice clock. *Nature*, 435(321-324), 2005. http://dx.doi.org/10.1038/nature03541.

[46] R. Le Targat *et al*. Experimental realization of an optical second with strontium lattice clocks. *Nat. Commun.*, 4:2109, 2013. http://dx.doi.org/10.1038/ncomms3109.

[47] S. Falke, N. Lemke, C. Grebing, B. Lipphardt, S. Weyers, V. Gerginov, N. Huntemann, C. Hagemann, A. Al-Masoudi, S. Häfner, S. Vogt, U. Sterr, and C. Lisdat. A strontium lattice clock with 3×10^{-17} inaccuracy and its frequency. *New Journal of Physics*, 16(7):073023, 2014. http://stacks.iop.org/1367-2630/16/i=7/a=073023.

[48] I. Ushijima, M. Takamoto, M. Das, T. Ohkubo, and H. Katori. Cryogenic optical lattice clocks. *Nat Photon*, 9:185–189, 2015. http://dx.doi.org/10.1038/nphoton.2015.5.

[49] D. Akamatsu *et al*. Spectroscopy and frequency measurement of the ^{87}Sr clock transition by laser linewidth transfer using an optical frequency comb. *Appl. Phys. Express*, 7(012401), 2014. http://stacks.iop.org/1882-0786/7/i=1/a=012401.

[50] Marcin Bober, Piotr Morzyński, Agata Cygan, Daniel Lisak, Piotr Masłowski, Mateusz Prymaczek, Piotr Wcisło, Piotr Ablewski, Mariusz Piwiński, Szymon Wójtewicz, Katarzyna Bielska, Dobrosława Bartoszek-Bober, Ryszard S. Trawiński, Michał Zawada, Roman Ciuryło, Jerzy Zachorowski, Marcin Piotrowski, Wojciech Gawlik, Filip Ozimek, and Czesław Radzewicz. Strontium optical lattice clocks for practical realization of the metre and secondary representation of the second. *Measurement Science and Technology*, 26(7):075201, 2015. http://stacks.iop.org/0957-0233/26/i=7/a=075201.

[51] N. Hinkley, J. A. Sherman, N. B. Phillips, M. Schioppo, N. D. Lemke, K. Beloy, M. Pizzocaro, C. W. Oates, and A. D. Ludlow. An atomic clock with 10^{-18} instability. *Science*, 341(6151):1215–1218, 2013. http://science.sciencemag.org/content/341/6151/1215.

[52] T. L. Bloom, B. J.and Nicholson, J. R. Williams, S. L. Campbell, M. Bishof, X. Zhang, W. Zhang, S. L. Bromley, and J. Ye. An optical lattice clock with accuracy and stability at the 10^{-18} level. *Nature*, 506:71–75, 2014. http://dx.doi.org/10.1038/nature12941.

[53] Takuya Kohno, Masami Yasuda, Kazumoto Hosaka, Hajime Inaba, Yoshiaki Nakajima, and Feng-Lei Hong. One-dimensional optical lattice clock with a fermionic

^{171}Yb isotope. *Applied Physics Express*, 2(7):072501, 2009. http://stacks.iop.org/1882-0786/2/i=7/a=072501.

[54] Chang Yong Park, Dai-Hyuk Yu, Won-Kyu Lee, Sang Eon Park, Eok Bong Kim, Sun Kyung Lee, Jun Woo Cho, Tai Hyun Yoon, Jongchul Mun, Sung Jong Park, Taeg Yong Kwon, and Sang-Bum Lee. Absolute frequency measurement of $^1S_0$ (F = 1/2) - $^3P_0$ (F = 1/2) transition of ^{171}Yb atoms in a one-dimensional optical lattice at KRISS. *Metrologia*, 50(2):119, 2013. http://stacks.iop.org/0026-1394/50/i=2/a=119.

[55] Marco Pizzocaro, Pierre Thoumany, Benjamin Rauf, Filippo Bregolin, Gianmaria Milani, Cecilia Clivati, Giovanni A Costanzo, Filippo Levi, and Davide Calonico. Absolute frequency measurement of the $^1S_0$ - $^3P_0$ transition of ^{171}Yb. *Metrologia*, 54(1):102, 2017. http://stacks.iop.org/0026-1394/54/i=1/a=102.

[56] H. Hachisu, K. Miyagishi, S. G. Porsev, A. Derevianko, V. D. Ovsiannikov, V. G. Pal'chikov, M. Takamoto, and H. Katori. Trapping of neutral mercury atoms and prospects for optical lattice clocks. *Phys. Rev. Lett.*, 100:053001, Feb 2008. https://link.aps.org/doi/10.1103/PhysRevLett.100.053001.

[57] L. Yi, S. Mejri, J. J. McFerran, Y. Le Coq, and S. Bize. Optical lattice trapping of ^{199}Hg and determination of the magic wavelength for the ultraviolet $^1S_0 \leftrightarrow ^3P_0$ clock transition. *Phys. Rev. Lett.*, 106:073005, Feb 2011. https://link.aps.org/doi/10.1103/PhysRevLett.106.073005.

[58] M.M. Boyd *et al.* Nuclear spin effects in optical lattice clocks. *Phys. Rev. A*, 76:022510, 2007. https://link.aps.org/doi/10.1103/PhysRevA.76.022510.

[59] P. G. Westergaard, J. Lodewyck, L. Lorini, A. Lecallier, E. A. Burt, M. Zawada, J. Millo, and P. Lemonde. Lattice-induced frequency shifts in Sr optical lattice clocks at the 10^{-17} level. *Phys. Rev. Lett.*, 106:210801, May 2011. https://link.aps.org/doi/10.1103/PhysRevLett.106.210801.

[60] C. Shi, J.-L. Robyr, U. Eismann, M. Zawada, L. Lorini, R. Le Targat, and J. Lodewyck. Polarizabilities of the ^{87}Sr clock transition. *Phys. Rev. A*, 92:012516, Jul 2015. https://link.aps.org/doi/10.1103/PhysRevA.92.012516.

[61] J. Lodewyck, S. Bilicki, E. Bookjans, J.-L. Robyr, C. Shi, G. Vallet, R. Le Targat, D. Nicolodi, Y. Le Coq, J. Guéna, M. Abgrall, P. Rosenbusch, and S. Bize. Optical to microwave clock frequency ratios with nearly continuous strontium optical lattice clock. *Metrologia*, 53(1123-1130), 2016. http://stacks.iop.org/0026-1394/53/i=4/a=1123.

[62] X. Baillard, M. Fouché, and R. Le Targat *et al.* An optical lattice clock with spin-polarized ^{87}Sr atoms. *Eur. Phys. J. D*, 48(11), 2008. https://doi.org/10.1140/epjd/e2007-00330-3.

[63] G. K. Campbell *et al.* The absolute frequency of the ^{87}Sr optical clock transition. *Metrologia*, 45:539, 2008. http://stacks.iop.org/0026-1394/45/i=5/a=008.

[64] S. Blatt *et al.* New limits on coupling of fundamental constants to gravity using ^{87}Sr optical lattice clocks. *Phys. Rev. Lett.*, 100(140801), 2008. https://link.aps.org/doi/10.1103/PhysRevLett.100.140801.

[65] F.-L. Hong, M. Musha, M. Takamoto, H. Inaba, S. Yanagimachi, A. Takamizawa, K. Watabe, T. Ikegami, M. Imae, Y. Fujii, M. Amemiya, K. Nakagawa, K. Ueda, and H. Katori. Measuring the frequency of a Sr optical lattice clock using a 120 km coherent optical transfer. *Opt. Lett.*, 34(5):692–694, Mar 2009. https://doi.org/10.1364/OL.34.000692.

[66] C. Grebing *et al*. Realization of a timescale with an accurate optical lattice clock. *Optica*, 3(563-569), 2015. https://doi.org/10.1364/OPTICA.3.000563.

[67] S. Falke *et al*. The ^{87}Sr optical frequency standard at PTB. *Metrologia*, 48(399), 2011. http://stacks.iop.org/0026-1394/48/i=5/a=022.

[68] H. Hachisu and T. Ido. Intermittent optical frequency measurements to reduce the dead time uncertainty of frequency link. *Japan. J. Appl. Phys.*, 54(112401), 2015. http://stacks.iop.org/1347-4065/54/i=11/a=112401.

[69] A. Yamaguchi *et al*. Stability transfer between two clock lasers operating at two different wavelengths for absolute frequency measurement of clock transition in ^{87}Sr. *Appl. Phys. Express*, 5(022701), 2012. http://stacks.iop.org/1882-0786/5/i=2/a=022701.

[70] T. Tanebe *et al*. Improved frequency measurement of the $^1S_0$–$^3P_0$ clock transition in ^{87}Sr using a Cs fountain clock as a transfer oscillator. *J. Phys. Soc. Japan*, 84(115002), 2015. https://doi.org/10.7566/JPSJ.84.115002.

[71] L. Yi-Ge *et al*. First evaluation and frequency measurement of the strontium optical lattice clock at NIM. *Chin. Phys. Lett.*, 32(090601), 2015. http://stacks.iop.org/0256-307X/32/i=9/a=090601.

[72] Martin M. Boyd, Andrew D. Ludlow, Sebastian Blatt, Seth M. Foreman, Tetsuya Ido, Tanya Zelevinsky, and Jun Ye. ^{87}Sr lattice clock with inaccuracy below 10^{-15}. *Phys. Rev. Lett.*, 98:083002, Feb 2007. https://link.aps.org/doi/10.1103/PhysRevLett.98.083002.

[73] H. Hachisu, M. Fujieda, S. Nagano, T. Gotoh, A. Nogami, T. Ido, St. Falke, N. Huntemann, C. Grebing, B. Lipphardt, Ch. Lisdat, and D. Piester. Direct comparison of optical lattice clocks with an intercontinental baseline of 9000 km. *Opt. Lett.*, 39(14):4072–4075, Jul 2014. https://doi.org/10.1364/OL.39.004072.

[74] C. Daussy, O. Lopez, A. Amy-Klein, A. Goncharov, M. Guinet, C. Chardonnet, F. Narbonneau, M. Lours, D. Chambon, S. Bize, A. Clairon, G. Santarelli, M. E. Tobar, and A. N. Luiten. Long-distance frequency dissemination with a resolution of 10^{-17}. *Phys. Rev. Lett.*, 94:203904, May 2005. https://link.aps.org/doi/10.1103/PhysRevLett.94.203904.

[75] K. Predehl, G. Grosche, S. M. F. Raupach, S. Droste, O. Terra, J. Alnis, Th. Legero, T. W. Hänsch, Th. Udem, R. Holzwarth, and H. Schnatz. A 920-kilometer optical fiber link for frequency metrology at the 19th decimal place. *Science*, 336(6080):441–444, 2012. http://science.sciencemag.org/content/336/6080/441.

[76] N. Chiodo *et al*. Cascaded optical fiber link using the Internet network for remote clocks comparison. *Opt. Express*, 23(33927-33937), 2015. https://doi.org/10.1364/OE.23.033927.

[77] S. M. F. Raupach, A. Koczwara, and G. Grosche. Brillouin amplifiacation supports 10^{-20} accuracy in optical frequency transfer over 1400 km of underground fibre. *Phys. Rev. A*, 92(021801(R)), 2015. https://link.aps.org/doi/10.1103/PhysRevA.92.021801.

[78] D. Calonico, E. K. Bertacco, C. E. Calosso, C. Clivati, G. A. Costanzo, M. Frittelli, A. Godone, A. Mura, N. Poli, D. V. Sutyrin, G. Tino, M. E. Zucco, and F. Levi. High-accuracy coherent optical frequency transfer over a doubled 642-km fiber link. *Applied Physics B*, 117(3):979–986, Dec 2014. https://doi.org/10.1007/s00340-014-5917-8.

[79] Łukasz Śliwczyński, Przemysław Krehlik, Albin Czubla, Łukasz Buczek, and Marcin Lipiński. Dissemination of time and rf frequency via a stabilized fibre optic link over a distance of 420 km. *Metrologia*, 50(2):133, 2013. http://stacks.iop.org/0026-1394/50/i=2/a=133.

[80] Ph. Laurent, D. Massonnet, L. Cacciapuoti, and C. Salomon. The ACES/PHARAO space mission: La mission spacial ACES/Pharao. *C.R. Physique*, 16(540-552), 2015. https://doi.org/10.1016/j.crhy.2015.05.002.

[81] *Development of a strontium optical lattice clock for the SOC mission on the ISS*, volume 9900, 990003-12. Proc. of SPIE, 2016. http://dx.doi.org/10.1117/12.2229473.

[82] M. D. Swallows, G. K. Campbell, A. D. Ludlow, M. M. Boyd, J. W. Thomsen, M. J. Martin, S. Blatt, T. L. Nicholson, and J. Ye. Precision measurement of fermionic collisions using an ^{87}Sr optical lattice clock with 1×10^{-16} inaccuracy. *IEEE Transactions on Ultrasonics, Ferroelectrics, and Frequency Control*, 57(3):574–582, March 2010. http://dx.doi.org/10.1109/TUFFC.2010.1449.

[83] Matthew D. Swallows, Michael Bishof, Yige Lin, Sebastian Blatt, Michael J. Martin, Ana Maria Rey, and Jun Ye. Suppression of collisional shifts in a strongly interacting lattice clock. *Science*, 331(6020):1043–1046, 2011. http://science.sciencemag.org/content/331/6020/1043.

[84] P. Delva, J. Lodewyck, S. Bilicki, E. Bookjans, G. Vallet, R. Le Targat, P.-E. Pottie, C. Guerlin, F. Meynadier, C. Le Poncin-Lafitte, O. Lopez, A. Amy-Klein, W.-K. Lee, N. Quintin, C. Lisdat, A. Al-Masoudi, S. Dörscher, C. Grebing, G. Grosche, A. Kuhl, S. Raupach, U. Sterr, I. R. Hill, R. Hobson, W. Bowden, J. Kronjäger, G. Marra, A. Rolland, F. N. Baynes, H. S. Margolis, and P. Gill. Test of special relativity using a fiber network of optical clocks. *Phys. Rev. Lett.*, 118:221102, Jun 2017. https://link.aps.org/doi/10.1103/PhysRevLett.118.221102.

[85] P. Wcisło, P. Morzyński, M. Bober, A. Cygan., D. Lisak, R. Ciuryło, and M. Zawada. Experimental constraint on dark matter detection with optical lattice clocks. *Nature Astronomy*, 1(0009), 2016. http://dx.doi.org/10.1038/s41550-016-0009.

[86] Tetsushi Takano, Ray Mizushima, and Hidetoshi Katori. Precise determination of the isotope shift of 88 sr– 87 sr optical lattice clock by sharing perturbations. *Applied Physics Express*, 10(7):072801, 2017. http://stacks.iop.org/1882-0786/10/i=7/a=072801.

[87] Xavier Baillard, Mathilde Fouché, Rodolphe Le Targat, Philip G. Westergaard, Arnaud Lecallier, Yann Le Coq, Giovanni D. Rovera, Sebastien Bize, and Pierre Lemonde. Accuracy evaluation of an optical lattice clock with bosonic atoms. *Opt. Lett.*, 32(13):1812–1814, Jul 2007. https://doi.org/10.1364/OL.32.001812.

[88] Ch. Lisdat, J. S. R. Vellore Winfred, T. Middelmann, F. Riehle, and U. Sterr. Collisional losses, decoherence, and frequency shifts in optical lattice clocks with bosons. *Phys. Rev. Lett.*, 103:090801, Aug 2009. https://link.aps.org/doi/10.1103/PhysRevLett.103.090801.

[89] Tomoya Akatsuka, Masao Takamoto, and Hidetoshi Katori. Three-dimensional optical lattice clock with bosonic ^{88}Sr atoms. *Phys. Rev. A*, 81:023402, Feb 2010. https://link.aps.org/doi/10.1103/PhysRevA.81.023402.

[90] Rodolphe Le Targat. *Horloge à réseau optique au Strontium : une 2ème génération d'horloges à atomes froids*. PhD thesis, Ecole Nationale Supérieure des Télécommunications, 2007. https://tel.archives-ouvertes.fr/tel-00170038/.

[91] Xavier Baillard. *Horloge à réseau optique à atomes de Strontium*. PhD thesis, Université de Paris VI, 2008. https://tel.archives-ouvertes.fr/tel-00267252/.

[92] Andrew D. Ludlow. *The Sr Optical Lattice Clock: Optical Spectroscopy with sub-Hertz Accuracy*. PhD thesis, University of Colorado, 2008. https://jila.colorado.edu/yelabs/sites/default/files/uploads/theses_2008_AndrewLudlow.pdf.

[93] Sebastian Blatt. *Ultracold Collisions and Fundamental Physics with Strontium*. PhD thesis, University of Colorado, 2011. https://jila.colorado.edu/publications/ultracold-collisions-and-fundamental-physics-strontium.

[94] Philip G. Westergaard. *Horloge à réseau optique au Strontium : en quête de perfomance ultime*. PhD thesis, Ecole Nationale Supérieure des Télécommunications, 2010. https://tel.archives-ouvertes.fr/tel-00541420/.

[95] Benjamin J. Bloom. *Building a Better Atomic Clock*. PhD thesis, University of Colorado, 2014. https://jila.colorado.edu/publications/37314/building-better-atomic-clock.

[96] Travis L. Nicholson. *A new record in atomic clock performance*. PhD thesis, University of Colorado, 2015. https://jila.colorado.edu/yelabs/sites/default/files/uploads/nicholson_thesis_5.pdf.

[97] H. S. Margolis. Optical frequency standards and clocks. *Contemporary Physics*, 51(1):37–58, 2010. http://dx.doi.org/10.1080/00107510903257616.

[98] Andrei Derevianko and Hidetoshi Katori. Colloquium: Physics of optical lattice clocks. *Rev. Mod. Phys.*, 83:331–347, May 2011. https://link.aps.org/doi/10.1103/RevModPhys.83.331.

[99] N. Poli, C.W. Oates, P. Gill, and G.M. Tino. Optical atomic clocks. *La rivista del Nuovo Cimento*, 36:555–624, 2013. https://doi.org/10.1393/ncr/i2013-10095-x.

[100] Fritz Riehle. Towards a redefinition of the second based on optical atomic clocks. *Comptes Rendus Physique*, 16(5):506 – 515, 2015. https://doi.org/10.1016/j.crhy.2015.03.012.

[101] Andrew D. Ludlow and Jun Ye. Progress on the optical lattice clock. *Comptes Rendus Physique*, 16(5):499 – 505, 2015. https://doi.org/10.1016/j.crhy.2015.03.008.

[102] Andrew D. Ludlow, Martin M. Boyd, Jun Ye, E. Peik, and P. O. Schmidt. Optical atomic clocks. *Rev. Mod. Phys.*, 87:637–701, Jun 2015. https://link.aps.org/doi/10.1103/RevModPhys.87.637.

[103] Rodolphe Le Targat, Xavier Baillard, Mathilde Fouché, Anders Brusch, Olivier Tcherbakoff, Giovanni D. Rovera, and Pierre Lemonde. Accurate optical lattice clock with ^{87}Sr atoms. *Phys. Rev. Lett.*, 97:130801, Sep 2006. https://link.aps.org/doi/10.1103/PhysRevLett.97.130801.

[104] J. Lodewyck, M. Zawada, L. Lorini, M. Gurov, and P. Lemonde. Observation and cancellation of a perturbing dc stark shift in strontium optical lattice clocks. *IEEE Transactions on Ultrasonics, Ferroelectrics, and Frequency Control*, 59(3):411–415, March 2012. http://ieeexplore.ieee.org/document/6174185/.

[105] R. Tyumenev, M. Favier, S. Bilicki, E. Bookjans, R. Le Targat, J. Lodewyck, D. Nicolodi, Y. Le Coq, J. Guéna, M. Abgrall, L. De Sarlo, and S. Bize. Comparing a mercury optical lattice clock with microwave and optical frequency standard. *New. J. Phys.*, 18(113002), 2016. http://stacks.iop.org/1367-2630/18/i=11/a=113002.

[106] C. Lisdat *et al*. A clock network for geodesy and fundamental science. *Nat. Commun.*, 7:12443, 2016. http://dx.doi.org/10.1038/ncomms12443.

[107] BIPM. Circular T. ftp://ftp2.bipm.org/pub/tai//Circular-T/cirthtm/cirt.350.html.

[108] M. Abgrall, B. Chupin, L. De Sarlo, J. Guéna, Ph. Laurent, Y. Le Coq, R. Le Targat, J. Lodewyck, M. Lours, P. Rosenbusch, G. D. Rovera, and S. Bize. Atomic fountains and optical clocks at SYRTE: Status and perspectives. *Comptes Rendus Physique*, 16(5):461 – 470, 2015. https://doi.org/10.1016/j.crhy.2015.03.010.

[109] R. Grimm, M. Weidemuller, and Y. B. Ovchinnikov. Optical dipole traps for neutral atoms. *Adv. At. Mol. Opt. Phys.*, 42(95), 2000. https://doi.org/10.1016/S1049-250X(08)60186-X.

[110] V D Ovsyannikov, Vitalii G Pal'chikov, H Katori, and M Takamoto. Polarisation and dispersion properties of light shifts in ultrastable optical frequency standards. *Quantum Electronics*, 36(1):3, 2006. http://stacks.iop.org/1063-7818/36/i=1/a=A02.

[111] Fam Le Kien, Philipp Schneeweiss, and Arno Rauschenbeutel. Dynamical polarizability of atoms in arbitrary light fields: general theory and application to cesium. *The European Physical Journal D*, 67(5):92, May 2013. https://doi.org/10.1140/epjd/e2013-30729-x.

[112] S. G. Porsev, Andrew D. Ludlow, Martin M. Boyd, and Jun Ye. Determination of Sr properties for a high-accuracy optical clock. *Phys. Rev. A*, 78:032508, Sep 2008. https://link.aps.org/doi/10.1103/PhysRevA.78.032508.

[113] A. V. Taichenachev, V. I. Yudin, V. D. Ovsiannikov, V. G. Pal'chikov, and C. W. Oates. Frequency shifts in an optical lattice clock due to magnetic-dipole and electric-quadrupole transitions. *Phys. Rev. Lett.*, 101:193601, Nov 2008. https://link.aps.org/doi/10.1103/PhysRevLett.101.193601.

[114] Andrew D. Ludlow, Martin M. Boyd, Tanya Zelevinsky, Seth M. Foreman, Sebastian Blatt, Mark Notcutt, Tetsuya Ido, and Jun Ye. Systematic study of the ^{87}Sr clock transition in an optical lattice. *Phys. Rev. Lett.*, 96:033003, Jan 2006. https://link.aps.org/doi/10.1103/PhysRevLett.96.033003.

[115] Anders Brusch, Rodolphe Le Targat, Xavier Baillard, Mathilde Fouché, and Pierre Lemonde. Hyperpolarizability effects in a Sr optical lattice clock. *Phys. Rev. Lett.*, 96:103003, Mar 2006. https://link.aps.org/doi/10.1103/PhysRevLett.96.103003.

[116] A. D. Ludlow, T. Zelevinsky, G. K. Campbell, S. Blatt, M. M. Boyd, M. H. G. de Miranda, M. J. Martin, J. W. Thomsen, S. M. Foreman, Jun Ye, T. M. Fortier, J. E. Stalnaker, S. A. Diddams, Y. Le Coq, Z. W. Barber, N. Poli, N. D. Lemke, K. M. Beck, and C. W. Oates. Sr lattice clock at 1 $\times 10^{-16}$ fractional uncertainty by remote optical evaluation with a Ca clock. *Science*, 319(5871):1805–1808, 2008. http://science.sciencemag.org/content/early/2008/02/14/science.1153341.

[117] Pierre Lemonde and Peter Wolf. Optical lattice clock with atoms confined in a shallow trap. *Phys. Rev. A*, 72:033409, Sep 2005. https://link.aps.org/doi/10.1103/PhysRevA.72.033409.

[118] R. H. Dicke. The effect of collisions upon the doppler width of spectral lines. *Phys. Rev.*, 89:472–473, Jan 1953. https://link.aps.org/doi/10.1103/PhysRev.89.472.

[119] M. J. Martin, M. Bishof, M. D. Swallows, X. Zhang, C. Benko, J. von Stecher, A. V. Gorshkov, A. M. Rey, and Jun Ye. A quantum many-body spin system in an optical lattice clock. *Science*, 341(6146):632–636, 2013. http://science.sciencemag.org/content/341/6146/632.

[120] Thierry Chanelière, Jean-Louis Meunier, Robin Kaiser, Christian Miniatura, and David Wilkowski. Extra-heating mechanism in doppler cooling experiments. *J. Opt. Soc. Am. B*, 22(9):1819–1828, Sep 2005. https://doi.org/10.1364/JOSAB.22.001819.

[121] Thomas H. Loftus, Tetsuya Ido, Andrew D. Ludlow, Martin M. Boyd, and Jun Ye. Narrow line cooling: Finite photon recoil dynamics. *Phys. Rev. Lett.*, 93:073003, Aug 2004. https://link.aps.org/doi/10.1103/PhysRevLett.93.073003.

[122] Seth M. Foreman, Kevin W. Holman, Darren D. Hudson, David J. Jones, and Jun Ye. Remote transfer of ultrastable frequency references via fiber networks. *Review of Scientific Instruments*, 78(2):021101, 2007. https://doi.org/10.1063/1.2437069.

[123] K. Beloy, N. Hinkley, N. B. Phillips, J. A. Sherman, M. Schioppo, J. Lehman, A. Feldman, L. M. Hanssen, C. W. Oates, and A. D. Ludlow. Atomic clock with 1×10^{-18} room-temperature blackbody stark uncertainty. *Phys. Rev. Lett.*, 113:260801, Dec 2014. https://link.aps.org/doi/10.1103/PhysRevLett.113.260801.

[124] Thomas Middelmann, Stephan Falke, Christian Lisdat, and Uwe Sterr. High accuracy correction of blackbody radiation shift in an optical lattice clock. *Phys. Rev. Lett.*, 109:263004, Dec 2012. https://link.aps.org/doi/10.1103/PhysRevLett.109.263004.

[125] Joint Commitee for Guides in Metrology 2008 JCGM 100: evaluation of measurement data – guide to the expression of uncertainty in measurement. Technical Reports JCGM www.bipm.org/utils/common/documents/jcgm/JCGM_100_2008_E.pdf.

[126] G. K. Campbell, M. M. Boyd, J. W. Thomsen, M. J. Martin, S. Blatt, M. D. Swallows, T. L. Nicholson, T. Fortier, C. W. Oates, S. A. Diddams, N. D. Lemke, P. Naidon, P. Julienne, Jun Ye, and A. D. Ludlow. Probing interactions between ultracold fermions. *Science*, 324(5925):360–363, 2009. https://doi.org/10.1126/science.1169724.

[127] N. D. Lemke, J. von Stecher, J. A. Sherman, A. M. Rey, C. W. Oates, and A. D. Ludlow. p-wave cold collisions in an optical lattice clock. *Phys. Rev. Lett.*, 107:103902, Aug 2011. https://link.aps.org/doi/10.1103/PhysRevLett.107.103902.

[128] M. Bishof, M. J. Martin, M. D. Swallows, C. Benko, Y. Lin, G. Quéméner, A. M. Rey, and J. Ye. Inelastic collisions and density-dependent excitation suppression in a ^{87}Sr optical lattice clock. *Phys. Rev. A*, 84:052716, Nov 2011. https://link.aps.org/doi/10.1103/PhysRevA.84.052716.

[129] V. I. Yudin, A. V. Taichenachev, C. W. Oates, Z. W. Barber, N. D. Lemke, A. D. Ludlow, U. Sterr, Ch. Lisdat, and F. Riehle. Hyper-ramsey spectroscopy of optical clock transitions. *Phys. Rev. A*, 82:011804, Jul 2010. https://link.aps.org/doi/10.1103/PhysRevA.82.011804.

[130] Kurt Gibble. Scattering of cold-atom coherences by hot atoms: Frequency shifts from background-gas collisions. *Phys. Rev. Lett.*, 110:180802, May 2013. https://link.aps.org/doi/10.1103/PhysRevLett.110.180802.

[131] A. Hees, J. Guéna, M. Abgrall, S. Bize, and P. Wolf. Searching for an oscillating massive scalar field as a dark matter candidate using atomic hyperfine frequency comparisons. *Phys. Rev. Lett.*, 117:061301, Aug 2016. https://link.aps.org/doi/10.1103/PhysRevLett.117.061301.

[132] R. Le Targat, L. Lorini, M. Gurov, M. Zawada, R.Gartman, B. Nagórny, P. Lemonde, and J. Lodewyck. Comparison of two strontium optical lattice clocks in agreement at the 10^{-16} level. *European Frequency and Time Forum*, pp 19-22, 2012. http://ieeexplore.ieee.org/document/6243652/.

[133] K. Yamanaka *et al*. Frequency ratio of ^{199}Hg and ^{87}Sr optical lattice clocks beyond the SI limit. *Phys. Rev. Lett.*, 114(230801), 2015. https://link.aps.org/doi/10.1103/PhysRevLett.114.230801.

[134] Jean-Philippe Uzan. The fundamental constants and their variation: observational and theoretical status. *Rev. Mod. Phys.*, 75:403–455, Apr 2003. http://link.aps.org/doi/10.1103/RevModPhys.75.403.

[135] V. A. Dzuba, V. V. Flambaum, and J. K. Webb. Calculations of the relativistic effects in many-electron atoms and space-time variation of fundamental constants. *Phys. Rev. A*, 59:230–237, Jan 1999. http://link.aps.org/doi/10.1103/PhysRevA.59.230.

[136] R. Srianand, H. Chand, P. Petitjean, and B. Aracil. Limits on the time variation of the electromagnetic fine-structure constant in the low energy limit from absorption lines in the spectra of distant quasars. *Phys. Rev. Lett.*, 92:121302, Mar 2004. https://link.aps.org/doi/10.1103/PhysRevLett.92.121302.

[137] John K. Webb, Victor V. Flambaum, Christopher W. Churchill, Michael J. Drinkwater, and John D. Barrow. Search for time variation of the fine structure constant. *Phys. Rev. Lett.*, 82:884–887, Feb 1999. https://link.aps.org/doi/10.1103/PhysRevLett.82.884.

[138] J. K. Webb, J. A. King, M. T. Murphy, V. V. Flambaum, R. F. Carswell, and M. B. Bainbridge. Indications of a spatial variation of the fine structure constant. *Phys. Rev. Lett.*, 107:191101, Oct 2011. https://link.aps.org/doi/10.1103/PhysRevLett.107.191101.

[139] J. Guéna, M. Abgrall, D. Rovera, P. Rosenbusch, M. E. Tobar, Ph. Laurent, A. Clairon, and S. Bize. Improved tests of Local Position Invariance using ^{87}Rb and ^{133}Cs fountains. *Phys. Rev. Lett.*, 109:080801, Aug 2012. https://link.aps.org/doi/10.1103/PhysRevLett.109.080801.

[140] V. A. Dzuba, V. V. Flambaum, and M. V. Marchenko. Relativistic effects in Sr, Dy, Yb II, and Yb III and search for variation of the fine-structure constant. *Phys. Rev. A*, 68:022506, Aug 2003. http://link.aps.org/doi/10.1103/PhysRevA.68.022506.

[141] Feng Luo, Keith A. Olive, and Jean-Philippe Uzan. Gyromagnetic factors and atomic clock constraints on the variation of fundamental constants. *Phys. Rev. D*, 84:096004, Nov 2011. https://link.aps.org/doi/10.1103/PhysRevD.84.096004.

[142] N. Huntemann *et al.* Improved limit on a temporal variation of m_p/m_e from comparison of Yb^+ and Cs atomic clocks. *Phys. Rev. Lett.*, 113, 210802, 2014. https://link.aps.org/doi/10.1103/PhysRevLett.113.210802.

[143] T. M. Fortier, N. Ashby, J. C. Bergquist, M. J. Delaney, S. A. Diddams, T. P. Heavner, L. Hollberg, W. M. Itano, S. R. Jefferts, K. Kim, F. Levi, L. Lorini, W. H. Oskay, T. E. Parker, J. Shirley, and J. E. Stalnaker. Precision atomic spectroscopy for improved limits on variation of the fine structure constant and local position invariance. *Phys. Rev. Lett.*, 98:070801, Feb 2007. https://link.aps.org/doi/10.1103/PhysRevLett.98.070801.

[144] Gianfranco Bertone, Dan Hooper, and Joseph Silk. Particle dark matter: evidence, candidates and constraints. *Physics Reports*, 405(5-6):279 – 390, 2005. https://doi.org/10.1016/j.physrep.2004.08.031.

[145] Dmitry Budker, Peter W. Graham, Micah Ledbetter, Surjeet Rajendran, and Alexander O. Sushkov. Proposal for a cosmic axion spin precession experiment (CASPEr). *Phys. Rev. X*, 4:021030, May 2014. https://link.aps.org/doi/10.1103/PhysRevX.4.021030.

[146] Y. V. Stadnik and V. V. Flambaum. Searching for dark matter and variation of fundamental constants with laser and maser interferometry. *Phys. Rev. Lett.*, 114:161301, Apr 2015. https://link.aps.org/doi/10.1103/PhysRevLett.114.161301.

[147] Y. V. Stadnik and V. V. Flambaum. Enhanced effects of variation of the fundamental constants in laser interferometers and application to dark-matter detection. *Phys. Rev. A*, 93:063630, Jun 2016. https://link.aps.org/doi/10.1103/PhysRevA.93.063630.

[148] A. Derevianko and M. Pospelov. Hunting for topological dark matter with atomic clocks. *Nature Physics*, 10(933-936), 2014. http://dx.doi.org/10.1038/nphys3137.

[149] Y. V. Stadnik and V. V. Flambaum. Can dark matter induce cosmological evolution of the fundamental constants of nature? *Phys. Rev. Lett.*, 115:201301, Nov 2015. https://link.aps.org/doi/10.1103/PhysRevLett.115.201301.

[150] H. Schuh and D. Behrend. Vlbi: A fascinating technique for geodesy and astrometry. *Journal of Geodynamics*, 61:68 – 80, 2012. https://doi.org/10.1016/j.jog.2012.07.007.

[151] M. Rioja, R. Dodson, Y. Asaki, J. Hartnett, and S. Tingay. The impact of frequency standards on coherence in VLBI at the highest frequencies. *The Astronomical Journal*, 144(4):121, 2012. http://stacks.iop.org/1538-3881/144/i=4/a=121.

[152] N. R. Nand, J. G. Hartnett, E. N. Ivanov, and G. Santarelli. Ultra-stable very-low phase-noise signal source for very long baseline interferometry using a cryocooled sapphire oscillator. *IEEE Transactions on Microwave Theory and Techniques*, 59(11):2978–2986, Nov 2011. http://ieeexplore.ieee.org/abstract/document/6032721/.

[153] Neill A. et al. VLBI2010: current and future requirements for geodetic VLBI systems. Report of working group 3 to the IVS Directing Board, 2005. ftp://ivscc.gsfc.nasa.gov/pub/memos/ivs-2006-008v01.pdf.

[154] Cecilia Clivati, Roberto Ambrosini, Thomas Artz, Alessandra Bertarini, Claudio Bortolotti, Matteo Frittelli, Filippo Levi, Alberto Mura, Giuseppe Maccaferri, Mauro Nanni, Monia Negusini, Federico Perini, Mauro Roma, Matteo Stagni, Massimo Zucco, and Davide Calonico. A VLBI experiment using a remote atomic clock via a coherent fibre link. *Scientific Reports*, 7(40992), 2017. http://dx.doi.org/10.1038/srep40992.

[155] P. Krehlik, L. Buczek, J. Kolodziej, M. Lipinski, L. Sliwczynski, J. Nawrocki, P. Nogas, A. Marecki, E. Pazderski, P. Ablewski, M. Bober, R. Ciurylo, A. Cygan, D. Lisak, P. Maslowski, P. Morzynski, M. Zawada, R. M. Campbell, J. Pieczerak, and *et al*. Fibre-optic delivery of time and frequency to VLBI station. *A&A*, 603:A48, 2017. https://doi.org/10.1051/0004-6361/201730615.

[156] A. Einstein. Zur elektrodynamik bewegter körper. *Annalen der Physik*, 322(10):891–921, 1905.

[157] H. P. Robertson. Postulate versus observation in the special theory of relativity. *Rev. Mod. Phys.*, 21:378–382, Jul 1949. https://link.aps.org/doi/10.1103/RevModPhys.21.378.

[158] V. Fock. Three lectures on relativity theory. *Rev. Mod. Phys.*, 29:325–333, Jul 1957. https://link.aps.org/doi/10.1103/RevModPhys.29.325.

[159] Sascha Reinhardt, Guido Saathoff, Henrik Buhr, Lars A. Carlson, Andreas Wolf, Dirk Schwalm, Sergei Karpuk, Christian Novotny, Gerhard Huber, Marcus Zimmermann, Ronald Holzwarth, Thomas Udem, Theodor W. Hansch, and Gerald Gwinner. Test of relativistic time dilation with fast optical atomic clocks at different velocities. *Nat. Phys.*, 3, 861 - 864, 2007. http://dx.doi.org/10.1038/nphys778.

[160] Benjamin Botermann, Dennis Bing, Christopher Geppert, Gerald Gwinner, Theodor W. Hänsch, Gerhard Huber, Sergei Karpuk, Andreas Krieger, Thomas Kühl, Wilfried Nörtershäuser, Christian Novotny, Sascha Reinhardt, Rodolfo Sánchez, Dirk Schwalm, Thomas Stöhlker, Andreas Wolf, and Guido Saathoff. Test of time dilation using stored Li^+ ions as clocks at relativistic speed. *Phys. Rev. Lett.*, 113:120405, Sep 2014. https://link.aps.org/doi/10.1103/PhysRevLett.113.120405.

[161] Peter Wolf and Gérard Petit. Satellite test of special relativity using the global positioning system. *Phys. Rev. A*, 56:4405–4409, Dec 1997. https://link.aps.org/doi/10.1103/PhysRevA.56.4405.

[162] Michael Edmund Tobar, Peter Wolf, Sébastien Bize, Giorgio Santarelli, and Victor Flambaum. Testing local Lorentz and position invariance and variation of fundamental constants by searching the derivative of the comparison frequency between a cryogenic sapphire oscillator and hydrogen maser. *Phys. Rev. D*, 81:022003, Jan 2010. https://link.aps.org/doi/10.1103/PhysRevD.81.022003.

[163] R. F. C. Vessot, M. W. Levine, E. M. Mattison, E. L. Blomberg, T. E. Hoffman, G. U. Nystrom, B. F. Farrel, R. Decher, P. B. Eby, C. R. Baugher, J. W. Watts, D. L. Teuber, and F. D. Wills. Test of relativistic gravitation with a space-borne hydrogen maser. *Phys. Rev. Lett.*, 45:2081–2084, Dec 1980. http://link.aps.org/doi/10.1103/PhysRevLett.45.2081.

[164] J.C Hafele and R.E Keating. Around-the-World atomic clocks: predicted relativistic time gains. *Science*, 177,166, 1972. http://www.jstor.org/stable/1734833.

[165] H. Müller, A. Peters, and S. Chu. A precision measurement of the gravitational redshift by the interference of mater waves. *Nature*, 463, 926-929, 2010. http://dx.doi.org/10.1038/nature08776.

[166] Grotti J. et al. Geodesy and metrology with a transportable optical clock. *preprint:arXiv*, 1705:04089, 2017.

[167] M. Vermeer, 1983.

[168] P. Delva and J. Lodewyck. Atomic clocks: new prospects in metrology and geodesy. *Acta Futura*, 7, (67-78), 2013. https://arxiv.org/pdf/1308.6766.

[169] T. Takano *et al*. Geopotential measurements with synchronously linked optical lattice clocks. *Nature Photonics*, 10(662-666), 2016. http://dx.doi.org/10.1038/nphoton.2016.159.

[170] Hidekazu Hachisu, Gérard Petit, Fumimaru Nakagawa, Yuko Hanado, and Tetsuya Ido. Si-traceable measurement of an optical frequency at the low 10^{-16} level without a local primary standard. *Opt. Express*, 25(8):8511–8523, Apr 2017. https://doi.org/10.1364/OE.25.008511.

[171] A. Bauch. Time and frequency comparisons using radiofrequency signals from satellites. *C. R. Physique*, 16(471-479), 2015. https://doi.org/10.1016/j.crhy.2015.02.006.

[172] A. Bercy *et al*. Two-way optical frequency comparisons at 5×10^{-21} relative stability over 100-km telecommunication network fibers. *Phys. Rev. A*, 90(061802(R)), 2014. https://link.aps.org/doi/10.1103/PhysRevA.90.061802.

[173] Schibli T.R., Hartl I., Yost D.C., Martin M.J., Marcinkevicius A., Fermann M.E., and Ye J. Optical frequency comb with submillihertz linewidth and more than 10 w average power. *Nat Photon*, 2:355–359, 2008. http://dx.doi.org/10.1038/nphoton.2008.79.

[174] Long-Sheng Ma, Zhiyi Bi, Albrecht Bartels, Lennart Robertsson, Massimo Zucco, Robert S. Windeler, Guido Wilpers, Chris Oates, Leo Hollberg, and Scott A. Diddams. Optical frequency synthesis and comparison with uncertainty at the 10^{-19} level. *Science*, 303(5665):1843–1845, 2004. http://science.sciencemag.org/content/303/5665/1843.

[175] S. Droste, C. Grebing, J. Leute, S. Raupach, A. Matveev, T.W. Hánsch, A. Bauch, R. Holzwarth, and G. Grosche. Characterization of a 450 km baseline GPS carrier-phase link using an optical fiber link. *New Journal of Physics*, 17(8):083044, 2015. http://stacks.iop.org/1367-2630/17/i=8/a=083044.

[176] G. Petit *et al*. 1×10^{-16} frequency transfer by GPS PPP with integer ambiguity resolution. *Metrologia*, 52(301-309), 2015. http://stacks.iop.org/0026-1394/52/i=2/a=301.

[177] O. Lopez, A. Amy-Klein, M. Lours, C. Chardonnet, and G. Santarelli. High-resolution microwave frequency dissemination on an 86-km urban optical link. *Applied Physics B*, 98(4):723–727, 2010. https://doi.org/10.1007/s00340-009-3832-1.

[178] Olivier Lopez, Fabien Kéfélian, Haifeng Jiang, Adil Haboucha, Anthony Bercy, Fabio Stefani, Bruno Chanteau, Amale Kanj, Daniele Rovera, Joseph Achkar,

Christian Chardonnet, Paul-Eric Pottie, Anne Amy-Klein, and Giorgio Santarelli. Frequency and time transfer for metrology and beyond using telecommunication network fibres. *Comptes Rendus Physique*, 16(5):531 – 539, 2015. https://doi.org/10.1016/j.crhy.2015.04.005.

[179] O. Lopez *et al*. Ultra-stable long distance optical frequency distribution using the Internet fiber network. *Opt. Express*, 20(23518-23526), 2012. https://doi.org/10.1364/OE.20.023518.

[180] C. J. Buczek, R. J. Freiberg, and M. L. Skolnick. Laser injection locking. *Proceedings of the IEEE*, 61(10):1411–1431, Oct 1973. http://ieeexplore.ieee.org/abstract/document/1451224/.

[181] J. J. McFerran, L. Yi, S. Mejri, W. Zhang, S. Di Manno, M. Abgrall, J. Guéna, Y. Le Coq, and S. Bize. Statistical uncertainty of 2.5×10^{-16} for the ^{199}Hg $^1S_0$–$^3P_0$ clock transition against a primary frequency standard. *Phys. Rev. A*, 89:043432, Apr 2014. https://link.aps.org/doi/10.1103/PhysRevA.89.043432.

[182] L De Sarlo, M Favier, R Tyumenev, and S Bize. A mercury optical lattice clock at LNE-SYRTE. *Journal of Physics: Conference Series*, 723(1):012017, 2016. http://stacks.iop.org/1742-6596/723/i=1/a=012017.

[183] J. McFerran, L. Yi, S. Mejri, S. Di Manno, W. Zhang, J. Guéna, Y. Le Coq, and S. Bize. Erratum: Neutral atom frequency reference in the deep ultraviolet with fractional uncertainty = 5.7×10^{-15}. *Phys. Rev. Lett.*, 115(219901), 2015. https://link.aps.org/doi/10.1103/PhysRevLett.115.219901.

[184] D. Nicolodi, B. Argence, W. Zhang, Le Targat R., G. Santarelli, and Le Coq. Spectral purity transfer between optical wavelengths at the 10^{-18} level. *Nat Photon*, 8:219–223, 2014. http://dx.doi.org/10.1038/nphoton.2013.361.

[185] C. W. Chou, D. B. Hume, J. C. J. Koelemeij, D. J. Wineland, and T. Rosenband. Frequency comparison of two high-accuracy Al^+ optical clocks. *Phys. Rev. Lett.*, 104:070802, Feb 2010. http://link.aps.org/doi/10.1103/PhysRevLett.104.070802.

[186] David Mattingly. Modern tests of lorentz invariance. *Living Reviews in Relativity*, 8(1):5, 2005. https://doi.org/10.12942/lrr-2005-5.

[187] Reza Mansouri and Roman U. Sexl. A test theory of special relativity: I. simultaneity and clock synchronization. *General Relativity and Gravitation*, 8(7):497–513, 1977. https://doi.org/10.1007/BF00762634.

[188] Reza Mansouri and Roman U. Sexl. A test theory of special relativity: Ii. first order tests. *General Relativity and Gravitation*, 8(7):515–524, 1977. https://doi.org/10.1007/BF00762635.

[189] Reza Mansouri and Roman U. Sexl. A test theory of special relativity: Iii. second-order tests. *General Relativity and Gravitation*, 8(10):809–814, 1977. https://doi.org/10.1007/BF00759585.

[190] E F Arias, G Panfilo, and G Petit. Timescales at the BIPM. *Metrologia*, 48(4):S145, 2011. http://stacks.iop.org/0026-1394/48/i=4/a=S04.

[191] G. Petit, F. Arias, and G. Panfilo. International atomic time: Status and future challenges. *Comptes Rendus Physique*, 16(5):480–488, 2015. https://doi.org/10.1016/j.crhy.2015.03.002.

[192] R A Nelson, D D McCarthy, S Malys, J Levine, B Guinot, H F Fliegel, R L Beard, and T R Bartholomew. The leap second: its history and possible future. *Metrologia*, 38(6):509, 2001. http://stacks.iop.org/0026-1394/38/i=6/a=6.

[193] G. D. Rovera, S. Bize, B. Chupin, J. Guéna, Ph. Laurent, P. Rosenbusch, P. Uhrich, and M. Abgrall. UTC(OP) based on LNE-SYRTE atomic fountain primary frequency standards. *Metrologia*, 53(3):S81, 2016. http://stacks.iop.org/0026-1394/53/i=3/a=S81.

[194] J. Guéna, M. Abgrall, A. Clairon, and S. Bize. Contributing to TAI with a secondary representation of the SI second. *Metrologia*, 51(1):108, 2014. http://stacks.iop.org/0026-1394/51/i=1/a=108.

[195] J. Yao, T. Parker, N. Ashby, and J. Levine. Incorporating an optical clock into a time scale. *arXiv*, 1704.06323, 2017.

[196] G Panfilo and P Tavella. Atomic clock prediction based on stochastic differential equations. *Metrologia*, 45(6):S108, 2008. http://stacks.iop.org/0026-1394/45/i=6/a=S16.

[197] R. J. Douglas and J-S. Boulanger. Standard uncertainty for average frequency traceability. *Proc. 11th European Frequency and Time Forum*, pp:345–9, 1997.

[198] Dai-Hyuk Yu, Marc Weiss, and Thomas E Parker. Uncertainty of a frequency comparison with distributed dead time and measurement interval offset. *Metrologia*, 44(1):91, 2007. http://stacks.iop.org/0026-1394/44/i=1/a=014.

[199] Derek Morris, Robert James Douglas, and Jean-Simon Boulanger. The role of the hydrogen maser for frequency transfer from cesium fountains. *Japanese Journal of Applied Physics*, 33(3S):1659, 1994. http://stacks.iop.org/1347-4065/33/i=3S/a=1659.

[200] N. Poli, M. Schioppo, S. Vogt, St. Falke, U. Sterr, Ch. Lisdat, and G.M. Tino. Transportable Sr optical lattice clock. *Applied Physics B*, 117(1107-1116), 2014. https://doi.org/10.1007/s00340-014-5932-9.

[201] S. Koller, J. Grotti, S. Vogt, A. Al-Masoudi, S. Dörscher, S. Häfner, U. Sterr, and Ch. Lisdat. Transportable optical lattice clock with 7×10^{-17} uncertainty. *Physical Review Letter*, 118(073601), 2017. https://link.aps.org/doi/10.1103/PhysRevLett.118.073601.

Résumé

Cette thèse est consacrée aux progrées récents des horloges à réseau optique au strontium du LNE-SYRTE, Observatoire de Paris. L'incertitude systématique et la stabilité des horloges optiques sont 2 ordres de grandeur meilleures que les horloges atomiques micro-ondes au cesium qui réalisent la seconde SI, bénéficiant maintenent a des applications en physique fondamentale, astronomie et géosciences. Dans un futur proche, une redéfinition de la seconde SI est attendue, quand les horloges optiques se seront révélées aussi fiables et reproductibles que les horloges a micro-ondes. La thèse présente trois étapes décisives dans cette direction. Nous présentons un fonctionnemment operation quasi-continu de nos horloges Sr pendant plusieurs semaines. Des comparaisons de fréquences locales et à distance avec diverses références de fréquence micro-ondes et optiques montrent que les horloges optiques sont reproductibles par des laboratoires independants. Nous avons démontré un premier réseau tout optique entre des horloges optiques à l'échelle continentale. Les horloges au Sr ont été utilisées pour préparer 5 rapports de calibration du Temps Atomique International (TAI) qui ont été validés par le BIPM comme première contribution au TAI par des horloges optiques. Certains de ces résultats ont été utilisés pour borner l'amplitude d'une possible violation de l'invariance de Lorentz analysant les comparaisons d'horloges distantes. Enfin, nous avons effectué une caractérisation complète des déplacements de fréquence associés aux sources laser à semiconducteur utilisées pour le piégeage des atomes dans l'optique d'applications pour des horloges transportables et spatiales.

Mots-clés : horloges à réseau optique, spectroscopie, atomes froids, comparaisons d'horloges optiques, échelles de temps, emission spontanée amplifiée

Abstract

This thesis describes the latest progresses regarding the Sr optical lattice clocks at LNE-SYRTE, Observatoire de Paris. Nowadays, the systematic uncertainty and stability of optical clocks are 2 orders of magnitude better than cesium microwave fountains currently realizing the SI second, with applications in fundamental physics, astronomy and geoscience. In the near future, a re-definition of the SI second is expected, once optical clocks are proven to be as reliable and reproducible as their microwave counterparts. The thesis presents three decisive steps in this direction. First, we demonstrate nearly continuous Sr clocks over several weeks. Second, local and remote frequency comparisons against various microwave and optical frequency standards show that OLCs are reproducible over time, and by independent laboratories. We notably demonstrated the first all-optical agreement between optical clocks at continental scale. Third, the Sr clocks were used to calibrate the Temps Atomique International (TAI). The five calibration reports, which we produced, were validated by the BIPM, as the first contribution to TAI with optical clocks. In addition, some of these results were used to improve bounds on a putative violation of the Lorentz invariance by testing the stability of the frequency ratio between remote clocks. Finally, we conducted a full characterization of the frequency shifts associated with semi-conductor laser sources for the trapping light, including optical measurements and frequency shifts measurements, with applications for transportable and space clocks.

Key words: optical lattice clock, spectroscopy, ultracold atoms, optical clock comparisons, timescales, amplified spontaneous emission